EBM
Experimental
Biology and
Medicine

Volume 250 | Issue 1

Experimental Biology and Medicine

Editor in Chief

Nicola Conran
University of Campinas,
Brazil

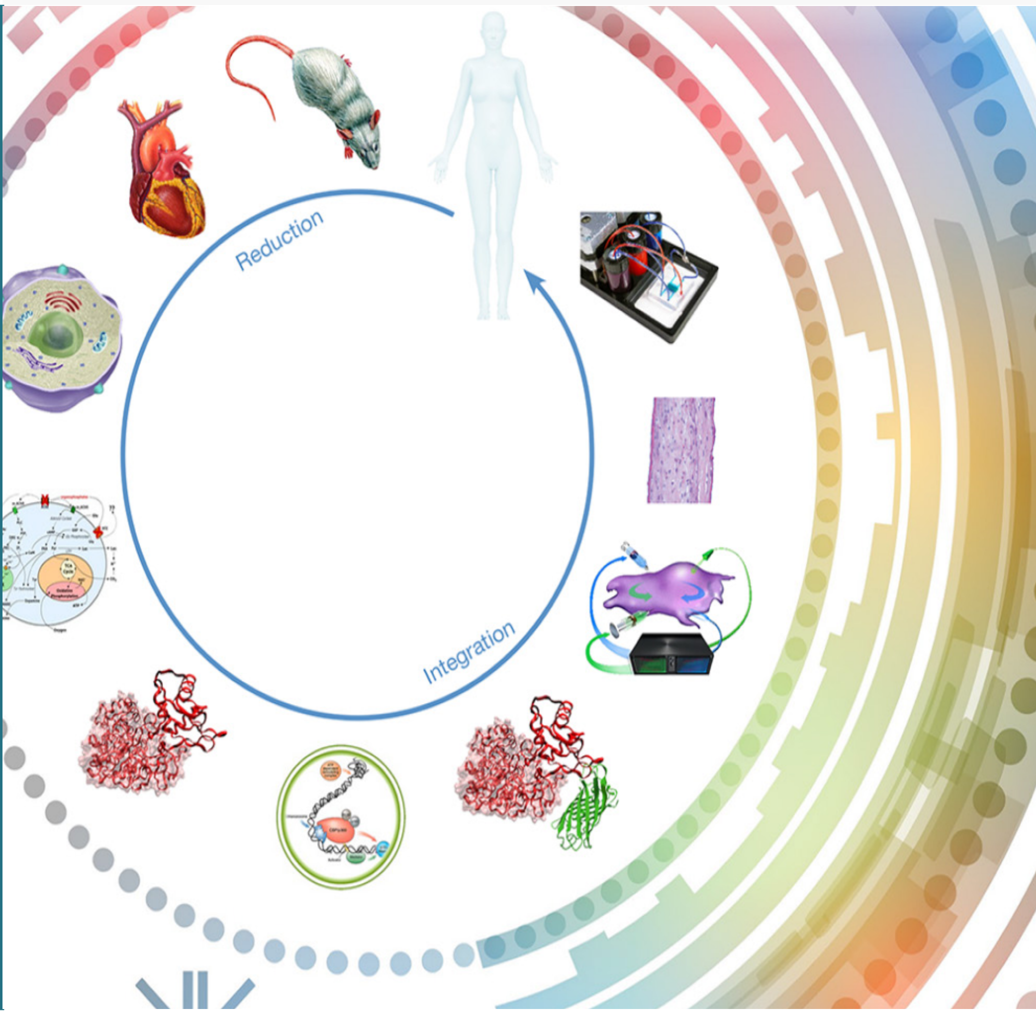

ISBN 978-2-8325-5968-0
DOI 10.3389/978-2-8325-5968-0

frontiers | Publishing Partnerships

SEBM Executive Council

Publication Committee

Society for Experimental Biology and Medicine
3220 N Street NW, #179
Washington DC 20007, USA
Executive Director – ed@sebm.org
Assistant to Editor-in-Chief – bzimmer@sebm.org

www.sebm.org

Editorial Board

EDITOR IN CHIEF
Nicola Conran
University of Campinas

DEPUTY EDITOR
Sulev Kõks
Murdoch University

GLOBAL EDITORS

Africa
Gordon Awandare
University of Ghana

Asia
Shaw-Jenq Tsai
National Cheng Kung University

Europe
Farzin Farzaneh
King's College London

Americas
Nicola Conran
University of Campinas

Australia/Oceana
Sulev Kõks
Murdoch University

Anatomy/Pathology

Associate Editor

Ian Zagon
Penn State University College of Medicine

William Banks
Alexander V. Ljubimov
Patricia J. McLaughlin
Artur Pasternak

Artifical Intelligence/Machine Learning Applications to Biomedical Research

Associate Editor

Huixiao Hong
US Food and Drug Administration

Xiaohui Fan
Ping Gong
Ruili Huang
Jie Liu
Fred Prior
Paul Rogers
Tieliu Shi
Wei Shi
Wenming Xiao

Biochemistry and Molecular Biology

Associate Editor

Muriel A. Lambert
Rutgers New Jersey Medical School

Brian D Adams
Bin Guo
J. Patrick O'connor

Bioimaging

Associate Editor

Shuliang Jiao
Florida International University

Kamran Avanaki
Zygmunt Gryczynski
Xinmai Yang
Xincheng Yao
Baohong Yuan
Weizhao Zhao

Biomedical Engineering

Associate Editor

F. Kurtis Kasper
University of Texas Health Science Center at Houston

Angela Pannier

Bionanoscience

Associate Editor

Juan Melendez
University of Albany

Nathaniel Cady
Hassan A. Elfawal
Jonathan F Lovell
Ya-Ping Sun
Maria Tomassone
Siyang Zheng

Cell and Developmental Biology

Associate Editor

Lidiane Torres
Albert Einstein College of Medicine

David Dean
Leszek Kotula
Harold I Saavedra
Yigang Wang
Warren Zimmer

Clinical Trials

Giuseppe Pizzorno
Daniel Vaena

Endocrinology and Nutrition

Co Associate Editors

Clint Allred and Keith Erikson
University of North Carolina Greensboro

Demin Cai
Sam Dagogo-Jack
Weiqun Wang
Malcolm Watford
Chia-Shan Wu

Environmental Health/Biomarkers/Precision Medicine

Associate Editor

William Slikker, Jr.
Retired

Gary Steven Friedman
Donald Johann
Igor Pogribny

Genomics, Proteomics, and Bioinformatics

Associate Editor

Sulev Kõks
Murdoch University

Mark Geraci
Paul Potter
John P Quinn
Giovanni Stracquadanio

Immunology/Microbiolog/Virology

Associate Editor

Flávio Guimarães Da Fonseca
Federal University of Minas Gerais

Andrea Doria
Farzin Farzaneh
Kam Hui
Francois Villinger

Mechanisms of Aging

Associate Editor

Shigemi Matsuyama
Case Western Reserve University

Ricki Colman
Aolin Allen Hsu
Akihiro Ikeda
Masaru Miyagi
Vincent Monnier

Neuroscience

Associate Editor

Michael Neal Lehman
Kent State University

Lique M. Coolen
Terrence Deak
Max L Fletcher
Sandra Mooney
Gregg Stanwood
Richard M Xu

Pharmacology/Toxicology

Associate Editor

Santosh Kumar
University of Tennessee Health Science Center

Guzel Bikbova
Pawel Brzuzan
Laetitia Dou
Jianxiong Jiang
Youngmi Jung
Li-Fu Li
Jonathan Shannahan
Manish Tripathi
Chaowu Xiao
Wuxiang Xie
Qihe Xu

Physiology and Pathophysiology

Associate Editor

Robert T. Mallet
University of North Texas Health Science Center

Rong Ma
Gabor Tigyi
Shaw-Jenq Tsai
Samuel Verges
Lei Xi
Chunyu Zeng

Population Health

Associate Editor

Ashish Joshi
School of Public Health, University of Memphis

Stem Cell Biology

Associate Editor

Jian Feng
State University of New York at Buffalo

Vania Broccoli
Jose Cibelli
Guoping Fan
Antonis Hatzopoulos
Dan S. Kaufman
Chun-Li Zhang

Structural Biology

Associate Editor

Tom Thompson
University of Cincinnati

Andrew P. Hinck
James Horn
Rhett Kovall
Vincent Luca
Rick Page

Synthetic Biology

Tara Deans
Ahmad Khalil
Aditya M. Kunjapur
Kevin Solomon

Systems Biology and Microphysiological Systems

Salman Khetani
Deok-Ho Kim
Andre Levchenko

Translational Research

Associate Editor

Chia-Ching (Josh) Wu
National Cheng Kung University

Jing An
Pan Pan Chong
Hyacinth Idu Hyacinth
Monica M. Jablonski
Chulso Moon
Esther Obeng
Athena Starland-Davenport

EBM eBook Copyright Statement

The copyright in the text of individual articles in this eBook is the property of their respective authors or their respective institutions or funders. The copyright in graphics and images within each article may be subject to copyright of other parties. In both cases this is subject to a license granted to Frontiers.

The compilation of articles constituting this eBook is the property of Frontiers.

Each article within this eBook, and the eBook itself, are published under the most recent version of the Creative Commons CC-BY licence. The version current at the date of publication of this eBook is CC-BY 4.0. If the CC-BY licence is updated, the licence granted by Frontiers is automatically updated to the new version.

When exercising any right under the CC-BY licence, Frontiers must be attributed as the original publisher of the article or eBook, as applicable.

Authors have the responsibility of ensuring that any graphics or other materials which are the property of others may be included in the CC-BY licence, but this should be checked before relying on the CC-BY licence to reproduce those materials. Any copyright notices relating to those materials must be complied with.

Copyright and source acknowledgement notices may not be removed and must be displayed in any copy, derivative work or partial copy which includes the elements in question.

All copyright, and all rights therein, are protected by national and international copyright laws. The above represents a summary only. For further information please read Frontiers' Conditions for Website Use and Copyright Statement, and the applicable CC-BY licence.

ISSN 1535-3699
ISBN 978-2-8325-5968-0
DOI 10.3389/978-2-8325-5968-0

Table of contents

Artificial Intelligence/Machine Learning Applications to Biomedical Research

Highlight

Original Research 07 Integrating machine learning with bioinformatics for predicting idiopathic pulmonary fibrosis prognosis: developing an individualized clinical prediction tool
Hongmei Ruan and Chunnian Ren

Artificial Intelligence/Machine Learning Applications to Biomedical Research

Review 20 Integrating artificial intelligence in strabismus management: current research landscape and future directions
Dawen Wu, Xi Huang, Liang Chen, Peixian Hou, Longqian Liu and Guoyuan Yang

Biochemistry and Molecular Biology

Original Research 30 Dysregulated transfer RNA-derived small RNAs as potential gastric cancer biomarkers
Jie Yuan, Wenchao Gu, Tianxin Xu, Yan Zhang, Lei Shen, Jianliang Yan, Xi Guan, Haidan Chu, Ruoyu Yuan and Shaoqing Ju

Endocrinology and Nutrition

Highlight

Original Research 42 Berberine alleviates AGEs-induced ferroptosis by activating NRF2 in the skin of diabetic mice
Chunjie Jiang, Guojuan Lao, Jianmin Ran and Ping Zhu

Endocrinology and Nutrition

Original Research 55 Increased hip fracture risk in the patients with type 2 diabetes mellitus is correlated with urine albumin-to-creatinine ratio (ACR) and diabetes duration in men
Huiru Ding, Hongxia Wang, Guanghui Liu, Yu Wang, Dongxu Han, Xiaoya Zhang and Lige Song

Genomics, Proteomics and Bioinformatics

Original Research
66 Function of formyl peptide receptor 2 in adriamycin resistance of breast cancer
Landi Su, Jingjing Li, Li Qin, Yang Feng and Dingwen Xu

Translational Research

Original Research
74 Neuroinflammation underlies the development of social stress induced cognitive deficit in male sickle cell mice
S'Dravious A. DeVeaux, Sofiya Vyshnya, Katherine Propsom, Oluwabukola T. Gbotosho, Asem S. Singh, Robert Z. Horning, Mihika Sharma, Anil G. Jegga, Liang Niu, Edward A. Botchwey and Hyacinth I. Hyacinth

Retraction

87 Retraction: Pyridoxal 5′ phosphate protects islets against streptozotocin-induced beta-cell dysfunction – *in vitro* and *in vivo*
EBM Editorial Office

EBM Experimental Biology and Medicine

TYPE Original Research
PUBLISHED 23 December 2024
DOI 10.3389/ebm.2024.10215

Check for updates

OPEN ACCESS

*CORRESPONDENCE
Chunnian Ren,
✉ chunnian0328@foxmail.com

RECEIVED 26 April 2024
ACCEPTED 11 December 2024
PUBLISHED 23 December 2024

CITATION
Ruan H and Ren C (2024) Integrating machine learning with bioinformatics for predicting idiopathic pulmonary fibrosis prognosis: developing an individualized clinical prediction tool. *Exp. Biol. Med.* 249:10215. doi: 10.3389/ebm.2024.10215

Integrating machine learning with bioinformatics for predicting idiopathic pulmonary fibrosis prognosis: developing an individualized clinical prediction tool

Hongmei Ruan[1] and Chunnian Ren[2]*

[1]Department of Pediatric Neurology, Chengdu Women's and Children's Central Hospital, School of Medicine, University of Electronic Science and Technology of China, Chengdu, China, [2]Department of Pediatric Surgery, Chengdu Women's and Children's Central Hospital, School of Medicine, University of Electronic Science and Technology of China, Chengdu, China

Abstract

Idiopathic pulmonary fibrosis (IPF) is a chronic interstitial lung disease with a poor prognosis. Its non-specific clinical symptoms make accurate prediction of disease progression challenging. This study aimed to develop molecular-level prognostic models to personalize treatment strategies for IPF patients. Using transcriptome sequencing and clinical data from 176 IPF patients, we developed a Random Survival Forest (RSF) model through machine learning and bioinformatics techniques. The model demonstrated superior predictive accuracy and clinical utility, as shown by the concordance index (C-index), the area under the operating characteristic curve (AUC), Brief scores, and decision curve analysis (DCA) curves. Additionally, a novel prognostic staging system was introduced to stratify IPF patients into distinct risk groups, enabling individualized predictions. The model's performance was validated using a bleomycin-induced pulmonary fibrosis mouse model. In conclusion, this study offers a new prognostic staging system and predictive tool for IPF, providing valuable insights for treatment and management.

KEYWORDS

idiopathic pulmonary fibrosis, machine learning, prediction model, random survival forest, hub gene

Impact statement

The lack of specificity of the clinical symptoms of IPF makes it difficult to predict the prognosis of IPF patients by clinical symptoms, and the establishment of a prediction model by identifying prognostic genes has become another possible method to determine the prognosis of IPF patients. To establish a prediction model with higher predictive performance, we compared the predictive performance of the conventional model and machine learning model, identified a prediction model with the best predictive performance, and developed it into a prediction tool. The current study provides a new tool for individualized treatment of IPF.

Introduction

IPF is a chronic, progressive interstitial lung disease defined by fibrosis, inflammation, and lung structure destruction [1, 2]. Predominantly affecting the elderly and middle-aged, IPF carries a poor prognosis [3], with a median survival time of 2–4 years post-diagnosis [3]. The current therapeutic mainstays, pirfenidone and nintedanib, offer only symptomatic relief by slowing the fibrotic progression [4, 5]. Identifying effective methods to understand the disease progression and prognosis of IPF patients is crucial for clinicians to enhance the management of IPF patients and formulate individualized treatment regimens. However, the non-specific clinical symptoms of IPF, such as dyspnea and cough, overlap with many other diseases, rendering the prediction of disease progression unreliable based on respiratory function and imaging examination alone. Therefore, there is a need to explore molecular-level biomarkers and develop an accurate prognostic model tool to track and evaluate the prognosis of IPF.

Recently, machine learning-based prediction models have emerged as potential tools for disease progression prediction [6, 7]. These models are believed to better handle complex, high-dimensional data relationships and more accurately reflect the associations between variables and outcomes compared to traditional linear models such as the Cox model. However, no studies have yet established a machine learning-based prognostic model for IPF, and the comparative predictive efficacy of traditional versus machine learning models in IPF remains unclear.

Given the non-specificity clinical manifestations in patients with IPF, prediction models based on these clinical manifestations, respiratory function, and imaging examinations have shown limited predictive power. With advancements in bioinformatics, molecular-level understanding of disease prognosis has been applied across various diseases. Identifying differentially expressed genes (DEGs) in IPF patients can aid clinicians in accurately determining the individualized prognosis by selecting prediction models with superior predictive performance. Additionally, establishing a prognostic staging system based on the most accurate predictive model can more precisely identify high-risk IPF patients.

The essence of IPF, a chronic progressive interstitial lung disease, lies in the fibrotic process, which involves tissue fibrosis, epithelial cell damage, and aberrant tissue repair [8, 9]. While previous studies have highlighted the role of immune cell infiltration in fibrotic injury and repair [8–10], few have investigated the molecular mechanisms that differentiate IPF patients across various risk groups. Our study employs enrichment analysis to identify pathways specifically enriched in different risk groups of IPF patients and to explore the extent of immune cell infiltration in the high-risk groups, potentially enhancing our understanding of the molecular mechanisms in high-risk IPF populations.

Materials and methods

Data acquisition and normalization

The GSE70866 dataset comprises gene expression profiles and clinical data from 176 bronchoalveolar lavage cells of IPF patients. It includes gene expression data from 112 IPF patients collected using the GPL14550 platform (Agilent-028004 SurePrint G3 Human GE 8 × 60 K Microarray, Agilent Technologies) and from 64 IPF patients using the GPL17077 platform (Agilent-039494 SurePrint G3 Human GE v2 8 × 60 K Microarray). We merged the data from these two platforms using inSilicoMerging and subsequently performed batch effect removal analysis to generate a consolidated expression matrix [11]. To verify the effectiveness of the batch effect removal, we conducted Principal Component Analysis (PCA) on the dataset's expression matrix both before and after the removal process. PCA is a dimensionality reduction technique that extracts key feature vectors from high-dimensional data, transforming it into a lower-dimensional representation and visualizing these features in 2D or 3D graphs.

Variance analysis

The "limma" package was used to identify DEGs between 176 IPF and 20 normal samples [12]. The Benjamin-Hochberg method was used to adjust original p-values, while the false discovery rate (FDR) procedure was employed to determine fold-changes (FC). Expressions with $|\log FC|>1.5$ and $FDR<0.05$ were considered significantly different. Heat maps and volcano maps were constructed to show the details of the variance analysis.

Weighted correlation network analysis (WGCNA)

To investigate the co-expression relationships among genes and their association with phenotypes, we constructed a gene co-expression network utilizing the "WGCNA" package in R software [13]. For all calculation of pair-wise genes, Pearson's correlation were performed. Using the TOM (Topological Overlap Matrix) model, average linkage hierarchical clustering was performed on Genes with similar expression profiles to classify them into Gene modules. Modules with a distance under 0.25 were combined, resulting in 24 co-expression modules.

Enrichment analysis

Gene Ontology (GO) [14] analysis is a common method to perform large-scale functional enrichment studies. The Kyoto Encyclopedia of Genes and Genomes (KEGG) [15] is a widely used database that stores information about genomes, biological pathways, diseases, and drugs. The biological process enrichment of hub genes was performed by the R package clusterprofiler with input filtering criteria of p.adj <0.05 and FDR value (q.value) < 0.5 statistically significant. Gene set enrichment analysis (GSEA) is a calculation method that determines whether a set of prior defend genes show statistically significant and consistent differences between two biological states [16]. In this study, GSEA was employed to discern the biological processes and signaling pathways that varied between the high-risk and low-risk IPF groups using the R package clusterProfiler. Significance was determined with a p-value threshold of less than 0.05.

Identification of prognostic genes

The Least Absolute Shrinkage and Selection Operator (LASSO) is a linear regression technique that incorporates shrinkage, making it suitable for survival analysis with high-dimensional data. In this study, we employed the R package glmnet, which facilitates LASSO regression analysis, to identify the most influential variables among the hub genes in our train set. Subsequently, we conducted a multivariate Cox regression analysis using the variables selected by the LASSO regression analysis.

The development and evaluation of model

Model development are performed based on the scikit-survival module for the Python platform, including algorithm optimization and training. For the RSF model, we employed grid search for algorithm optimization and utilized the RSF algorithm within ML for model training. Grid search fine-tuned the RSF model's hyperparameters, which included the number of estimators (10, 100, and 500), minimum of samples split (3, 5, 6, and 10), minimum of samples leaf (1, 2, 4, and 10), and maximum depth (2, 5, 10, and None). Model performance was assessed using the test set, with evaluations based on the C-index and AUC at 1, 2, and 3 years. The C-index is a widely recognized metric that quantifies the ability of a model to predict outcomes. A model with an AUC greater than 0.75 is generally considered to exhibit excellent discrimination [7]. Calibration was appraised using the Brier score at the same time points; a Brier score of 0.25 or less signifies favorable model calibration [17]. DCA was conducted to determine the clinical net benefit, a method that calculates the net benefit under a risk threshold and is primarily employed to assess the clinical utility of the model [18].

The interpretation of model

Clinicians require a straightforward method to elucidate how the model predicts patient survival. The Shapley Additive Explanations (SHAP) plot serves as an effective tool for this purpose. This game-theoretic approach to model output interpretation reveals the contribution of each variable to the predicted outcome [19]. The SHAP plot is generated utilizing the scikit-survival module within the Python environment.

Prognostic staging system for IPF patients

The X-tile is a bio-informatics tool utilized for biomarker assessment and optimization of outcome-based cut-points [20]. Kaplan Meier (KM) curve analysis serves as the method to analyze and infer patient survival times from the data, examining the relationship between survival times, outcomes and the influence of various factors along with their relative impact. The individual risk score, derived from the output of the RSF model, stratified IPF patients in both the train and test sets into high-risk and low-risk groups. A comparison of overall survival between these two groups was conducted using KM curve survival analysis, with the log-rank test employed for statistical testing.

Immune function analysis

To identify immune characteristics of IPF and normal samples, as well as high-risk and low-risk groups, we analyzed their expression data using the Cell-type Identification By Estimating Relative Subsets Of RNA Transcripts (CIBERSORT) web portal[1]. The analysis was conducted iteratively 1,000 times to ascertain the relative percentages of 22 distinct immune cell types [21]. Subsequently, we compared these relative percentages across IPF and normal samples, in addition to high-risk and low-risk groups.

---

[1] http://CIBERSORT.stanford.edu/

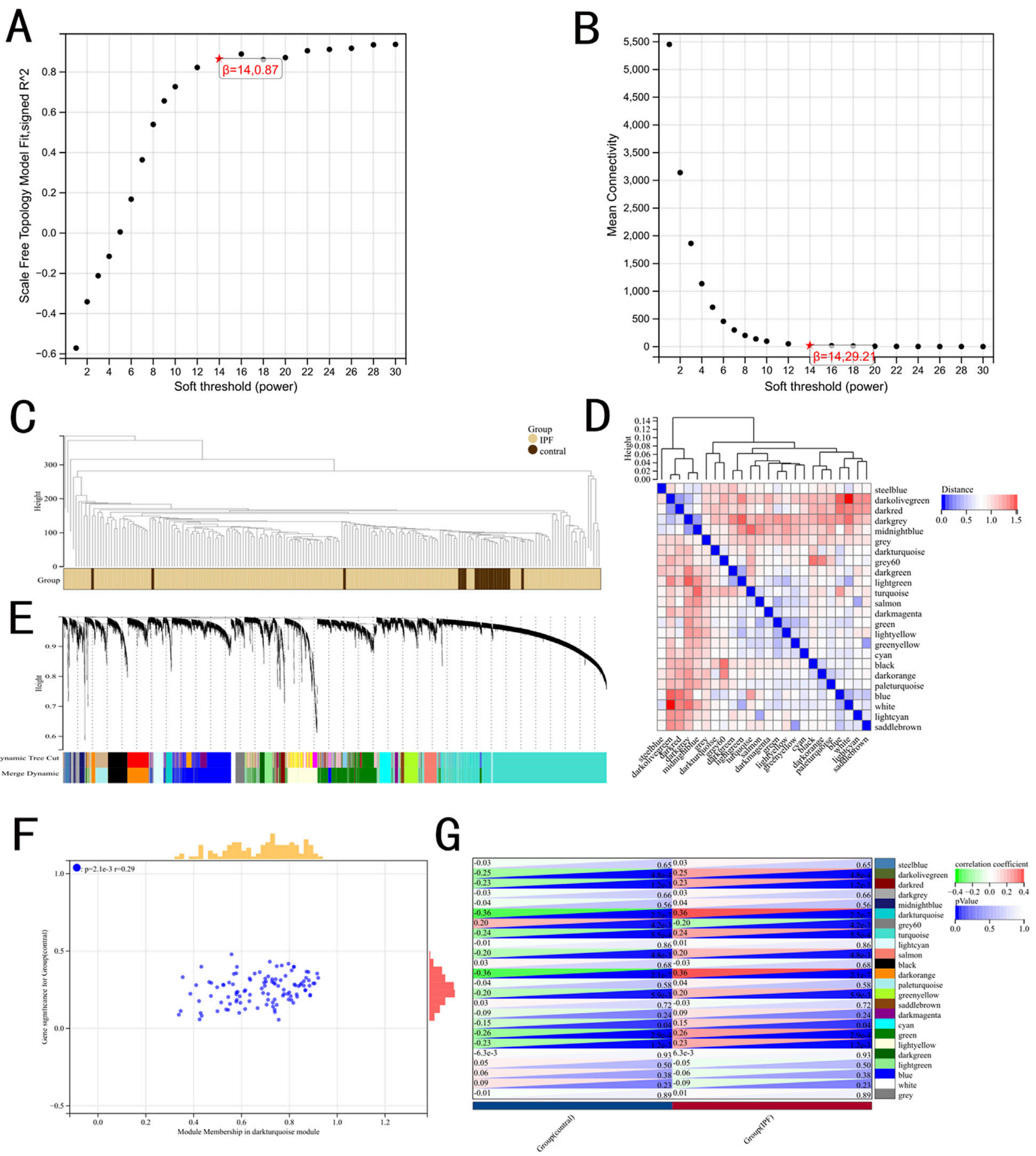

FIGURE 1
Results of the WGCNA. **(A)** The corresponding scale-free topological model fit indices at different soft threshold powers. **(B)** The corresponding mean connectivity values at different soft threshold powers. **(C)** Cluster dendrogram of samples. **(D)** Cluster dendrogram of module feature. **(E)** Cluster dendrogram of genes. **(F)** Correlations between different modules and clinical traits. **(G)** Correlation of module membership and gene significance in the darkturquoise module.

Validation of the PF model

The PF mouse model was established through a single intratracheal administration of Bleomycin (BLM) at a dosage of 2 mg/kg (MCE, USA) [22]. On day 14 post-administration, lung tissues were harvested from the sacrificed mice to proceed with further experiments. Lung fibrosis severity was evaluated through Masson's trichrome staining and Western blot analysis. Furthermore, the expression levels of hub genes integrated into the RSF model were validated using Quantitative Reverse Transcription-Polymerase Chain Reaction (qRT-PCR) assays.

Statistical analysis

For the statistical analysis, we employed R, a programming language and software environment for statistical computing (R Foundation for Statistical Computing, Vienna, Austria), and the Sangerbox platform. Model training was conducted using Python (Version 3.10), developed by Guido van Rossum in Scotts Valley, CA, United States. Both the Cox model and the RSF model were implemented utilizing the scikit-survival module (Version 0.19.0).

Results

Identification of hub genes in IPF

The flow chart of the study is shown in Supplementary Figure S1 mRNA expression data obtained from the GPL14550 platform and GPL17077 platform of GSE80776 were merged and subjected to a batch effect removal analysis to obtain a combined expression matrix with 176 IPF and 20 healthy people involving 19,531 Genes. After removing the batch effect we can observe a uniform distribution of the merged matrix (Supplementary Figure S2).

A total of 4,187 DEGs were obtained by variance analysis and included 3,970 upregulated and 217 downregulated genes (Supplementary Figure S3). The DEGs were visualized by the volcano map (Supplementary Figure S3A) and heatmap (Supplementary Figure S3B).

WGCNA was used to identify IPF-related hub genes. As shown in Figures 1A, B, the horizontal axis is the soft threshold and the vertical axis is the evaluation parameters of scale-free network. The higher the value of evaluation parameters, the more consistent the network is with the characteristics of scale-free network. The optimal soft-thresholding power was set as 14 with R square value of 0.87. Finally, 24 modules are identified by hierarchical clustering and optimal soft threshold capability (Figures 1C–E). The darkturquoise module, which exhibited the highest positive correlation with IPF, contained 28 genes (Figures 1F, G).

A venn diagram was utilized to identify DEGs selected in both variance analysis and WGCNA analysis. Consequently, 22 IPF-related hub genes were determined (Figure 2A). In IPF patients, heatmaps and boxplots revealed significant upregulation of these 22 genes (Figures 2B, C).

Functional enrichment analysis

GO and KEGG pathway enrichment analyses were conducted to deepen our understanding of the functions of the identified hub genes. The analysis of KEGG revealed that these hub genes were mainly associated with cell cycle, p53 signaling pathway, FoxO signaling pathway, and Cellular senescence (Supplementary Figures S4A, B). In addition, the analysis of GO enrichment revealed that these hub genes were primarily associated with the cell cycle, mitotic cell cycle, and cell cycle process (Supplementary Figure S4C).

Identification of prognostic genes

As shown in Figure 3A, we conducted LASSO regression analysis on 22 IPF-related hub genes screened and further screened 14 hub genes. Subsequently, proceeded with a multivariate Cox regression analysis, which led to the identification of four significant prognostic genes. Among these, one gene was identified as a potential risk gene, while the other three were recognized as potential protective genes (Figure 3B).

Model development and evaluation

We constructed both the Cox and RSF models using data from the train set. The RSF model's hyperparameters were optimized through grid search, with the final configuration set as follows: 10 estimators, 5 minimum of samples split and 1 minimum of samples leaf.

Model validation was conducted using the C-index, Brier score and AUC. The validation of the models in the test set is shown in Table 1. The results show that the C-index of RSF model is 0.840, which is obviously superior to Cox model. Similarly, the AUC (1-year, 2-year and 3-year) and Brier scores (1-year, 2-year and 3-year) also have better performance on the RSF model. Meanwhile, we used DCA to assess the potential clinical significance of the RSF model, the DCA regarding the RSF model showed fair clinical net benefits in 1, 2, and 3 years in Figure 4.

Model interpretation

The SHAP plot in Figure 5 was used to interpret visually the global importance of variables in the RSF model, the variables in

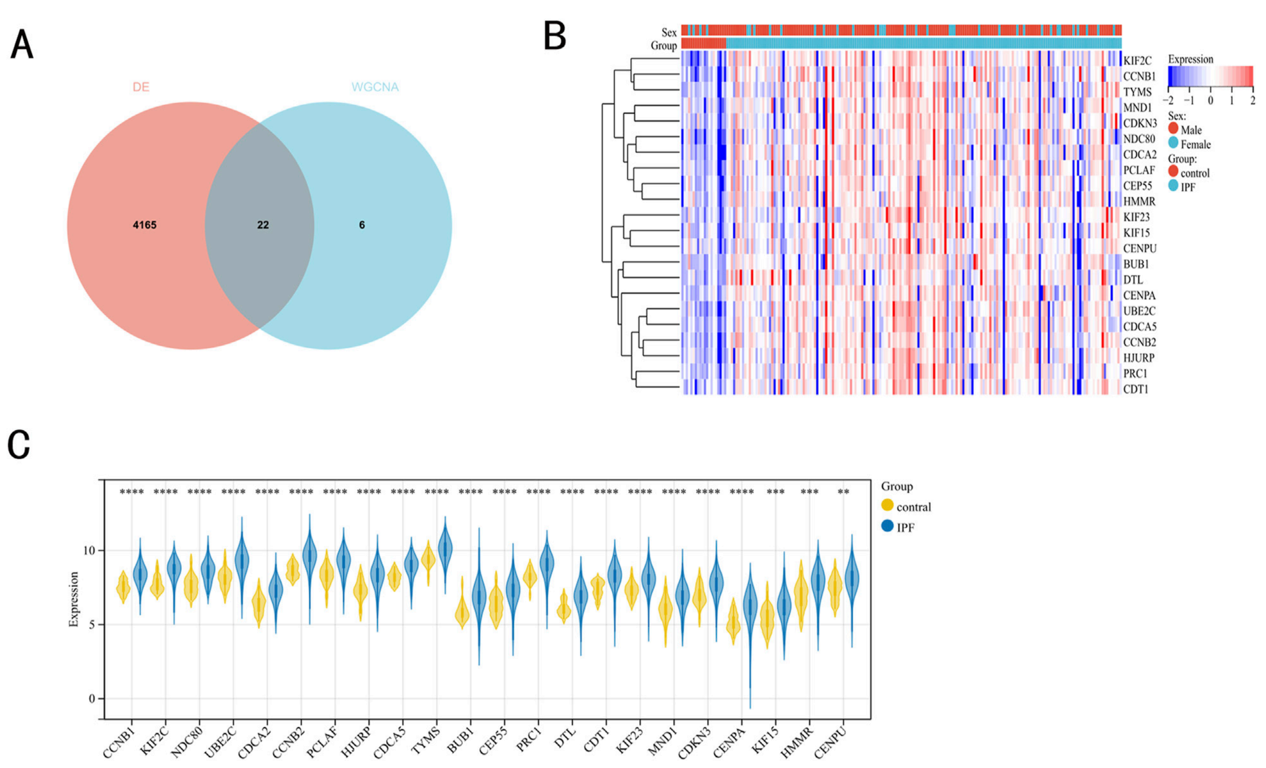

FIGURE 2
IPF-related hub genes. **(A)** 22 hub genes were obtained by taking the intersections of the DEGs, and darkturquoise module genes of the WGCNA. **(B, C)** Heatmaps and boxplots demonstrated the expression of 22 hub genes in IPF patients.

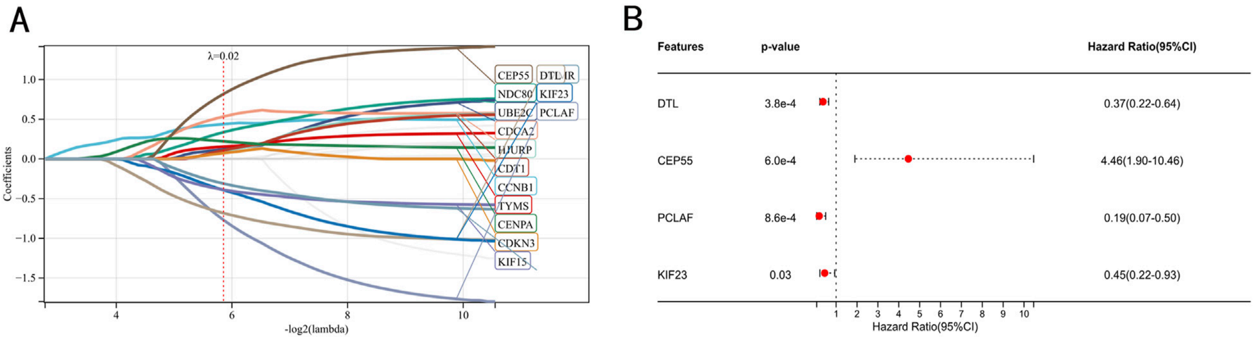

FIGURE 3
Identification of prognostic genes. **(A)** Screening of characteristic genes by LASSO regression analysis. **(B)** Multivariate Cox regression analysis to identification of prognostic genes in the train set.

the RSF model were listed in descending order of importance. As seen in Figure 5A, the contributions of all variables to the RSF model were quantified to establish their ranking. The distribution of the scatter plot in Figure 5B represents each variable across all samples in the RSF model. Among these, CEP55 emerged as the most influential variable, succeeded by KIF23, DTL and PCLAF.

Prognostic staging system for IPF patients

Patients within the train set were assigned scores by the RSF model, leading to the stratification of patients into high-risk (risk score>23.1) and low-risk (risk score<=23.1) groups. Meanwhile, the KM analysis and log-rank test results, which highlighted significant differences between the high-risk and low-risk groups, are displayed

TABLE 1 The validation of the models in the test set.

Model	C-index	AUC			Brier score		
		1-Year	2-Year	3-Year	1-Year	2-Year	3-Year
RSF model	0.840	0.941	0.942	0.958	0.099	0.120	0.007
Cox model	0.544	0.569	0.552	0.578	0.198	0.264	0.255

RSF, random survival forest.

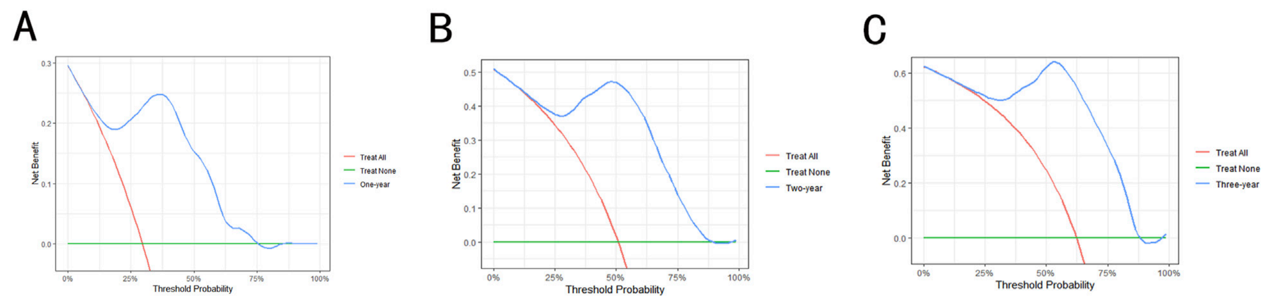

FIGURE 4
The decision analysis curves of RSF model. **(A)** The 1-year decision analysis curve of RSF model. **(B)** The 2-year decision analysis curve of RSF model. **(C)** The 3-year decision analysis curve of RSF model. In the decision analysis curve, the x-axis represented the threshold probability while the y-axis represented the clinical net benefits.

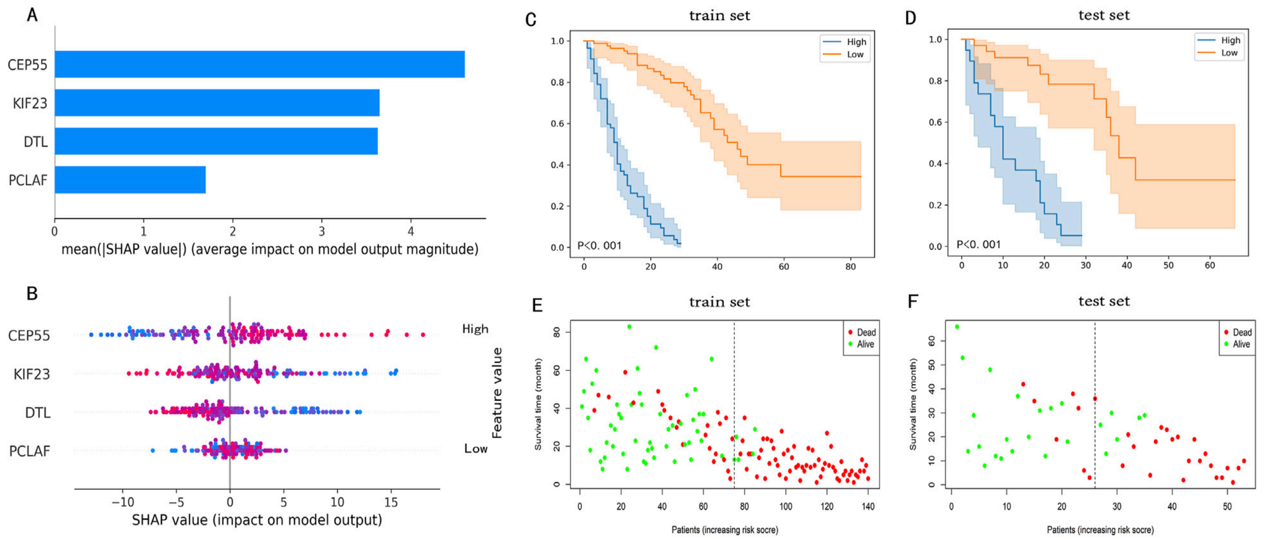

FIGURE 5
The SHAP plot of the RSF model and risk stratification of IPF patients. **(A)** A Shap plot after quantization of each variable. **(B)** A SHAP plot that includes the distribution of variables for all patients, the color of the dot symbolized the numerical value of the variable. In the SHAP plot, the length of the horizontal axis where each variable is located represents the variable's contribution to the outcome. For example, the variable (CEP55) is the most significant risk factor. The higher the expression of CEP55, the higher the probability of a poor prognosis. **(C)** KM survival curves after risk stratification of patients in the train set. **(D)** KM survival curves after risk stratification of patients in the test set. In KM survival plots, the blue line represents the high-risk group, the orange line represents the low-risk group, and the P-value in the plots is the log-rank test result. **(E)** The survival state distribution of the train set. **(F)** The survival state distribution of the test set.

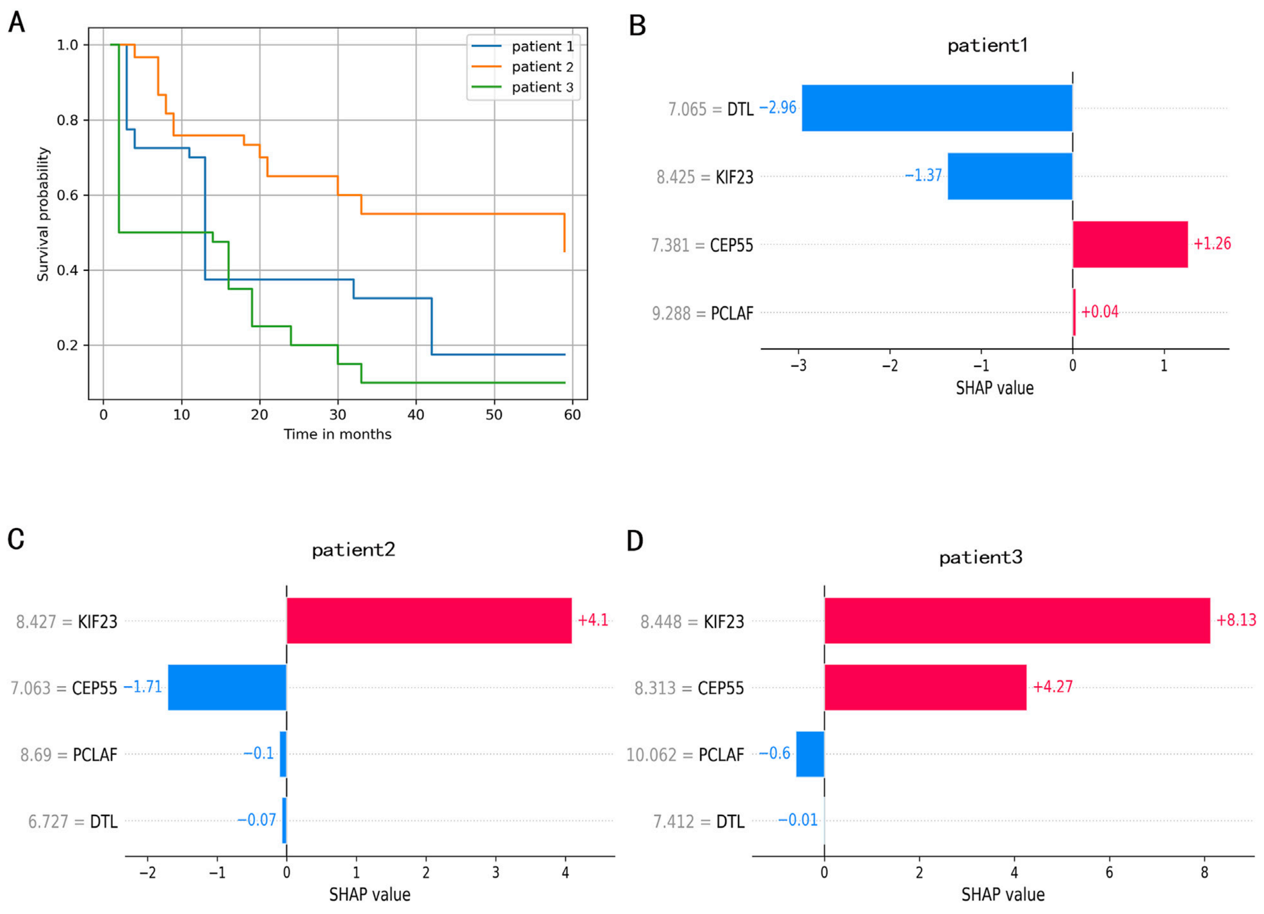

FIGURE 6
The individual survival prediction. **(A)** The estimated survival function of IPF patients. **(B)**. The individualized SHAP plot of the patient 1. **(C)** The individualized SHAP plot of the patient 2. **(D)** The individualized SHAP plot of the patient 3. In the individualized SHAP plot, red bands represent risk factors and promote poor prognosis, while blue bands are relative protective factors.

in Figures 5C, D which demonstrated a significant difference between the two groups. The distribution of survival states for both the train and test set is shown in Figures 5E, F. These findings indicate that the RSF model, based on four prognostic genes, can effectively predict IPF prognosis, demonstrating high accuracy in both the train and test sets.

Application of the RSF model in individual survival prediction

We randomly selected three patients to demonstrate individual survival prediction using the RSF model. Patient1: Expression levels of DTL, CEP55, PCLAF, and KIF23 were 6.727230, 7.063076, 8.690206, and 8.427149. Patient2: Expression levels of DTL, CEP55, PCLAF, and KIF23 were 7.064931, 7.381497, 9.288345, and 8.425116. Patient3: Expression levels of DTL, DTL, PCLAF, and KIF23 were 7.411715, 8.312722, 10.061563, and 8.447688. The individual predicted outcomes for these patients are shown in Figure 6. The personalized KM survival plots (Figure 6A) illustrate the survival probability for each individual at specific time points, while the individualized SHAP plots (Figures 6B–D) show the contribution of gene expression levels to each patient's prognosis.

To enable clinicians to use the RSF model and the prediction tools, relevant files of the model have been uploaded to[2]. It provides a quicker and more intuitive way of predicting.

GSEA enrichment analysis

The GSEA revealed that 32 pathways were significantly enriched in IPF compared to normal samples. In the high-risk group, 24 pathways were identified as enriched. After intersection

---

[2] https://github.com/Renrende0328/IPF-RSFmodel

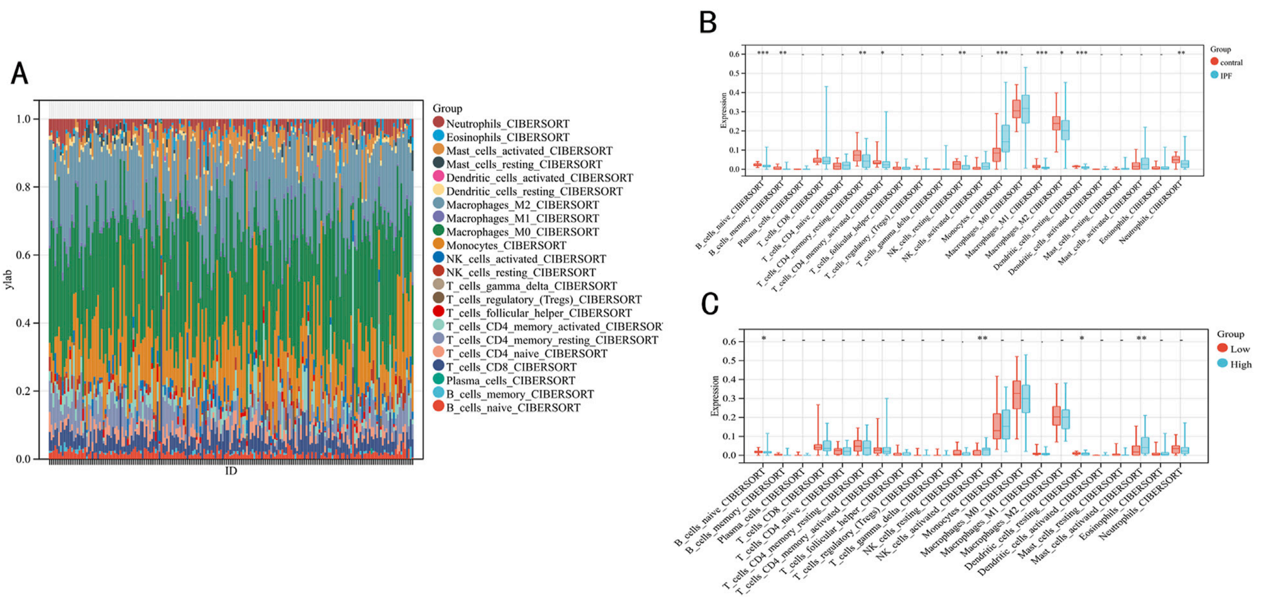

FIGURE 7
Immune infiltration between IPF and contral samples. **(A)** The relative percentage of 22 immune cells in each sample. **(B)** Differences in immune infiltration between IPF and contral samples. **(C)** Differences in immune infiltration between low-risk and high-risk groups.

analysis, we identified 7 pathways that were consistently enriched across both comparisons. The most significantly enriched pathways in the high-risk group included ECM receptor interaction, the MAPK signaling pathway, and focal adhesion, as illustrated in Supplementary Figure S4D.

Immune function analysis

To evaluate the impact of immune function on IPF, we employed the CIBERSORT algorithm to analyze differences in 22 types of infiltrating immune cells between IPF and normal samples (Figures 7A, B). We observed that the levels of B cell memory, B cells naive, T cells CD4 memory resting, T cells CD4 memory activated, NK cells resting, M1 macrophages, M2 macrophages, dendritic cells resting and neutrophils in the IPF were lower than those health samples, while the opposite was true for monocytes. Further analysis of the immune function of these differentially expressed immune cells within low-risk and high-risk groups revealed that the infiltration level of B cell naive ($P < 0.02$) and dendritic cells resting ($P < 0.03$) were significantly higher in the low-risk group than in the high-risk group (Figure 7C).

Validation of the PF model

Given the challenges in acquiring clinical samples from IPF patients, we endeavored to validate the four hub genes identified in this study using a PF mouse model. Given the challenges in acquiring clinical samples from IPF patients, we endeavored to validate the four hub genes identified in this study using a PF mouse model [22]. The successful construction of the PF mouse model was confirmed by Masson's trichrome staining and Western blot experiments (Figures 8A, B). RT-PCR was used to validate the expression of the hub genes incorporated into the RSF model and the results showed general agreement with the bioinformatics results (Figure 8C).

Discussion

IPF is a chronic and progressive interstitial lung disease characterized by a poor prognosis, and there is a current deficiency in specific treatments [1–3]. The clinical symptoms of IPF are nonspecific, complicating the assessment of disease progression and prognosis based on clinical manifestations and auxiliary examinations alone. Therefore, identifying biomarkers and establishing a prognostic prediction model for IPF patients at the molecular level could facilitate individualized treatment of IPF patients, and benefit clinicians for the management of IPF patients.

In this study, we used transcriptional profiling data of bronchoalveolar lavage fluid from IPF patients to explore the correlation between biomarker levels and patient prognosis. First, 22 hub genes were identified, meanwhile, a Cox model and an RSF model based on an ML algorithm were established, and the results indicated that the RSF model had better predictive

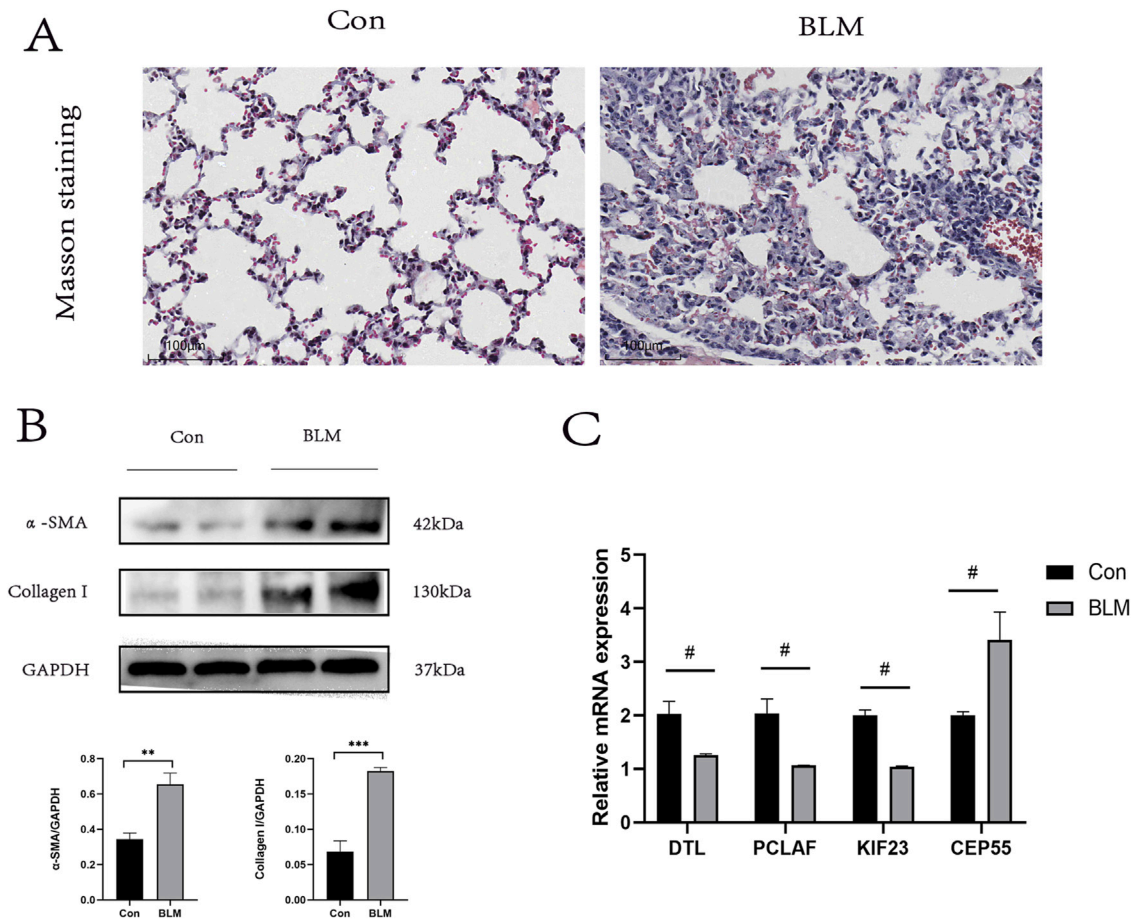

FIGURE 8
PF model sample validation. **(A)** Results of Masson staining, scale bar 100 µm. **(B)** In the lung tissue of PF mice protein levels of α- SAM, Collagen I (n = 3). **(C)** Expression levels of DTL, PCLAF, KIF23, and CEP55 were quantified using qRT-PCR analysis in lung tissue. *< 0.05, **< 0.01, ***P < 0.001 by t-test. #p < 0.05 versus Con, t-test was used in **(C)**.

performance. The RSF model was then used to establish a new prognostic staging system, which was able to discriminate IPF patients into high-risk and low-risk groups, and the KM curve showed that this prognostic staging system had better discriminatory power. Finally, to gain further insight into the molecular mechanisms underlying the high-risk group in IPF, we used GSEA enrichment analysis to identify their main enriched pathways and used the CIBERSORT algorithm to determine the level of immune cell infiltration in the high-risk group.

Differently expressed 22 hub genes were obtained between IPF and normal samples from the GSE70866 of the GEO dataset by the different analysis of the limma and WGCNA module methods. The 22 hub genes in IPF were all higher expressed than normal samples. Through the GO enrichment analysis, we found the 22 hub genes were significantly enriched in the cell cycle. In particular, KEGG enrichment analysis showed that the 22 hub genes were significantly enriched in p53 signaling pathway, FoxO signaling pathway, cellular senescence, and cell cycle. The p53 signaling pathway and FoxO signaling pathway have been proven to be closely related to the development of fibrosis. Huang et al. reported that the p53 signaling pathway could affect the EMT progression of silica-induced pulmonary fibrosis [23]. Wang et al. had a similar conclusion in the model of renal interstitial fibrosis induced by unilateral ureteral obstruction [24]. Ma et al. reported the role of FoxO3a signal pathway in pulmonary fibrosis [25]. The review by Parimon et al. systematically expounded on the regulatory role of cellular senescence in pulmonary fibrosis [26]. Lv et al. confirmed that cell cycle inhibitor P21 promotes the development of pulmonary fibrosis by suppressing lung alveolar regeneration, and further confirmed that cell cycle is involved in the process of fibrosis [24]. These studies further substantiate the relevance of the 22 identified hub genes to fibrogenesis and disease progression.

On the basis of 22 hub genes, four prognostic genes (DTL,CEP55,PCLAF,KIF23) were further identified. KIF23, a microtubule-associated movement protein, is crucial in mitosis and cytokinesis [27]. Chen et al. reported that the downregulation of MiR-17-5p alleviates renal fibrosis by targeting KIF23 [28], which is consistent with the role of our RSF model, indicating that KIF23 may be a potential protective factor in the process of pulmonary fibrosis. The autophagy gene Cep55 is associated with bleomycin-induced pulmonary fibrosis [29]. The model established in this study suggests that a reduction in CEP55 expression is beneficial to the survival of patients with IPF. Similarly, DTL and PCLAF were also considered potential protective factors in the process of pulmonary fibrosis in our study.

To develop a predictive model with enhanced accuracy and clinical relevance, we employed various algorithms to construct the model, selecting the one that demonstrated superior predictive capabilities. We compared the traditional model (Cox algorithm) and the RSF model (ML algorithm), and the results showed that the RSF model based on the ML algorithm had better prediction performance. Given the unique requirements of the medical field, high predictive performance alone is insufficient to guarantee clinical utility; thus, we sought an effective method to elucidate the relationship between model variables and outcomes. The "black box" nature of ML-based models, which obscures the interpretation of results, has been a significant barrier to their clinical application [30]. To address this, we used the SHAP algorithm to render our model interpretable [31, 32], thereby clarifying the contribution of each variable to the outcomes and enhancing the model's clinical utility. This high-performing prediction model facilitates the establishment of a more refined prognostic staging system for IPF patients, enabling more precise risk stratification and supporting the development of personalized treatment strategies. The RSF model has been refined into a user-friendly tool for individual survival prediction, providing risk scores, personalized Kaplan-Meier survival curves, and individualized SHAP plots. These features render individual predictions more intuitive and precise. In conclusion, we anticipate that this predictive tool will aid clinicians in evaluating patient prognoses to formulate tailored treatment plans. Furthermore, by quantifying individual prognosis risk levels, it is expected to enhance communication between clinicians and patients, thereby bolstering patient acceptance of prognostic information and treatment plans.

Patients with IPF could be divided into high-risk and low-risk groups based on prognostic staging systems. To deepen our understanding of the molecular pathways enriched in individuals at high risk for IPF, we performed GSEA on IPF patients and normal samples, as well as on high-risk and low-risk groups. This analysis identified seven significantly enriched pathways. Notably, ECM receptor interactions and MAPK signaling pathways have been reported to be closely associated with the development of pulmonary fibrosis. Han et al reported the role of ECM receptor interaction pathway in pulmonary fibrosis [33]. TGF-βs can regulate fibrosis via both canonical and non-canonical signaling pathways [34]. MAPK signaling pathway, as one of the non-canonical (non-Smad) signaling pathways, has demonstrated its role in pulmonary fibrosis [35]. Further exploration targeting these enriched pathways may be one of the directions to improve the prognosis of IPF.

Multiple studies have underscored the pivotal role of immunity in pulmonary diseases, including IPF [36]. Immune dysregulation is considered to be one of the bases of chronic lung diseases, including IPF [37]. Utilizing the CIBERSORT algorithm, we analyzed RNA-sequencing data to assess immune cell expression levels and derived the proportions of various immune cells within samples [38]. In this study, CIBERSORT was used to determine the level of immune cell infiltration between IPF and normal samples, as well as between high-risk and low-risk groups, and to determine two kinds of immune cells that may be related to the prognosis of high-risk IPF group, including B cell naive and dendritic cells resting. These two kinds of immune cell infiltration levels are lower in the high-risk group than in the low-risk group, indicating that they may be protective factors affecting the prognosis of pulmonary fibrosis.

Our research also has some limitations. First, the RSF model was established according to the GEO database, therefore, in order to validate our model, further clinical prospective studies are necessary. Second, functional experiments are needed to further reveal the potential mechanisms of hub genes in the future.

This study aims to establish a high-performance, clinically valuable prognostic prediction model at the molecular level, while also developing a new prognostic staging system that can understand the individualized prognosis of IPF patients and early identification of high-risk individuals. The study is based on the GSE70866 dataset, which has been reported in multiple studies, demonstrating its representativeness in IPF [39–43]. To establish a prognostic prediction model with universal applicability, unlike other previous studies that focused only on certain biological processes related to IPF, such as endoplasmic reticulum stress, autophagy, and immune-related genes [40, 42, 43], this study starts with all genes in IPF samples, aiming to screen out the most representative hub differential genes in IPF to establish a model. In addition, by constructing both traditional linear models and machine learning algorithm-based RSF models, the model with the best predictive performance was selected. Therefore, this study differs from currently reported studies in both variable selection and model algorithms. At the same time, the molecular mechanisms of high-risk individuals were further explored. Our findings provide a new and better tool for guiding individualized therapy in IPF and also provide new insights at a molecular level for improving the prognosis of IPF.

Author contributions

CR conducted the experiments, CR and HR wrote the manuscript. All authors contributed to the article and approved the submitted version.

Data availability

Publicly available datasets were analyzed in this study. This data can be found here: All datasets used in the research can be found in Gene Expression Omnibus (https://www.ncbi.nlm.nih.gov/geo/, containing dataset of GSE70866).

Ethics statement

The animal study was approved by the ethics committee of the Chengdu Women's and Children's Central Hospital, School of Medicine, University of Electronic Science and Technology of China. The study was conducted in accordance with the local legislation and institutional requirements.

Funding

The author(s) declare that no financial support was received for the research, authorship, and/or publication of this article.

Conflict of interest

The author(s) declared no potential conflicts of interest with respect to the research, authorship, and/or publication of this article.

Supplementary material

The Supplementary Material for this article can be found online at: https://www.ebm-journal.org/articles/10.3389/ebm.2024.10215/full#supplementary-material

References

1. Raghu G, Collard HR, Egan JJ, Martinez FJ, Behr J, Brown KK, et al. An official ATS/ERS/JRS/ALAT statement: idiopathic pulmonary fibrosis: evidence-based guidelines for diagnosis and management. *Am J Respir Crit Care Med* (2011) **183**(6):788–824. doi:10.1164/rccm.2009-040GL

2. Glass DS, Grossfeld D, Renna HA, Agarwala P, Spiegler P, DeLeon J, et al. Idiopathic pulmonary fibrosis: current and future treatment. *The Clin Respir J* (2022) **16**(2):84–96. doi:10.1111/crj.13466

3. Ley B, Collard HR, King TE, Jr. Clinical course and prediction of survival in idiopathic pulmonary fibrosis. *Am J Respir Crit Care Med* (2011) **183**(4):431–40. doi:10.1164/rccm.201006-0894CI

4. Wright WA, Crowley LE, Parekh D, Crawshaw A, Dosanjh DP, Nightingale P, et al. Real-world retrospective observational study exploring the effectiveness and safety of antifibrotics in idiopathic pulmonary fibrosis. *BMJ open Respir Res* (2021) **8**(1):e000782. doi:10.1136/bmjresp-2020-000782

5. Bargagli E, Piccioli C, Rosi E, Torricelli E, Turi L, Piccioli E, et al. Pirfenidone and Nintedanib in idiopathic pulmonary fibrosis: real-life experience in an Italian referral centre. *Pulmonology* (2019) **25**(3):149–53. doi:10.1016/j.pulmoe.2018.06.003

6. Bone C, Simmonds-Buckley M, Thwaites R, Sandford D, Merzhvynska M, Rubel J, et al. Dynamic prediction of psychological treatment outcomes: development and validation of a prediction model using routinely collected symptom data. *The Lancet Digital Health* (2021) **3**(4):e231–e240. doi:10.1016/S2589-7500(21)00018-2

7. D'Ascenzo F, De Filippo O, Gallone G, Mittone G, Deriu MA, Iannaccone M, et al. Machine learning-based prediction of adverse events following an acute coronary syndrome (PRAISE): a modelling study of pooled datasets. *Lancet (London, England)* (2021) **397**(10270):199–207. doi:10.1016/S0140-6736(20)32519-8

8. Jee AS, Sahhar J, Youssef P, Bleasel J, Adelstein S, Nguyen M, et al. Review: serum biomarkers in idiopathic pulmonary fibrosis and systemic sclerosis associated interstitial lung disease - frontiers and horizons. *Pharmacol and Ther* (2019) **202**:40–52. doi:10.1016/j.pharmthera.2019.05.014

9. Rieder F, Kessler SP, West GA, Bhilocha S, de la Motte C, Sadler TM, et al. Inflammation-induced endothelial-to-mesenchymal transition: a novel mechanism of intestinal fibrosis. *The Am J Pathol* (2011) **179**(5):2660–73. doi:10.1016/j.ajpath.2011.07.042

10. Steele MP, Luna LG, Coldren CD, Murphy E, Hennessy CE, Heinz D, et al. Relationship between gene expression and lung function in Idiopathic Interstitial Pneumonias. *BMC genomics* (2015) **16**:869. doi:10.1186/s12864-015-2102-3

11. Taminau J, Meganck S, Lazar C, Steenhoff D, Coletta A, Molter C, et al. Unlocking the potential of publicly available microarray data using inSilicoDb and inSilicoMerging R/Bioconductor packages. *BMC bioinformatics* (2012) **13**:335. doi:10.1186/1471-2105-13-335

12. Ritchie ME, Phipson B, Wu D, Hu Y, Law CW, Shi W, et al. Limma powers differential expression analyses for RNA-sequencing and microarray studies. *Nucleic Acids Res* (2015) **43**(7):e47. doi:10.1093/nar/gkv007

13. Langfelder P, Horvath S. WGCNA: an R package for weighted correlation network analysis. *BMC bioinformatics* (2008) **9**:559. doi:10.1186/1471-2105-9-559

14. The Gene Ontology Consortium. Gene Ontology consortium: going forward. *Nucleic Acids Res* (2015) **43**:D1049–D1056. doi:10.1093/nar/gku1179

15. Ogata H, Goto S, Sato K, Fujibuchi W, Bono H, Kanehisa M. KEGG: kyoto Encyclopedia of genes and genomes. *Nucleic Acids Res* (1999) **27**(1):29–34. doi:10.1093/nar/27.1.29

16. Subramanian A, Tamayo P, Mootha VK, Mukherjee S, Ebert BL, Gillette MA, et al. Gene set enrichment analysis: a knowledge-based approach for interpreting genome-wide expression profiles. *Proc Natl Acad Sci* (2005) **102**(43):15545–50. doi:10.1073/pnas.0506580102

17. Higgins AM, Neto AS, Bailey M, Barrett J, Bellomo R, Cooper DJ, et al. Predictors of death and new disability after critical illness: a multicentre prospective cohort study. *Intensive Care Med* (2021) **47**(7):772–81. doi:10.1007/s00134-021-06438-7

18. Van Calster B, Wynants L, Verbeek JFM, Verbakel JY, Christodoulou E, Vickers AJ, et al. Reporting and interpreting decision curve analysis: a guide for investigators. *Eur Urol* (2018) **74**(6):796–804. doi:10.1016/j.eururo.2018.08.038

19. Ogami C, Tsuji Y, Seki H, Kawano H, To H, Matsumoto Y, et al. An artificial neural network-pharmacokinetic model and its interpretation using Shapley additive explanations. *CPT: pharmacometrics and Syst Pharmacol* (2021) **10**(7):760–8. doi:10.1002/psp4.12643

20. Pan C, Wang X, Chen W, Tao C, Xu X, Jin L, et al. Reevaluation of glypican-3 as a prognostic marker in HCC using X-tile software. *Med Oncol (Northwood, Lond England)* (2015) **32**(1):359. doi:10.1007/s12032-014-0359-z

21. Newman AM, Steen CB, Liu CL, Gentles AJ, Chaudhuri AA, Scherer F, et al. Determining cell type abundance and expression from bulk tissues with digital cytometry. *Nat Biotechnol* (2019) **37**(7):773–82. doi:10.1038/s41587-019-0114-2

22. Ren C, Wang Q, Fan S, Mi T, Zhang Z, He D. Toll-like receptor 9 aggravates pulmonary fibrosis by promoting NLRP3-mediated pyroptosis of alveolar epithelial cells. *Inflammation* (2024) **47**(5):1744–61. doi:10.1007/s10753-024-02006-5

23. Huang R, Bai C, Liu X, Zhou Y, Hu S, Li D, et al. The p53/RMRP/miR122 signaling loop promotes epithelial-mesenchymal transition during the development of silica-induced lung fibrosis by activating the notch pathway. *Chemosphere* (2021) **263**:128133. doi:10.1016/j.chemosphere.2020.128133

24. Wang Y, Zuo B, Wang N, Li S, Liu C, Sun D. Calcium dobesilate mediates renal interstitial fibrosis and delay renal peritubular capillary loss through Sirt1/p53 signaling pathway. *Biomed and Pharmacother* (2020) **132**:110798. doi:10.1016/j.biopha.2020.110798

25. Ma Z, Yu R, Zhu Q, Sun L, Jian L, Wang X, et al. CXCL16/CXCR6 axis promotes bleomycin-induced fibrotic process in MRC-5 cells via the PI3K/AKT/FOXO3a pathway. *Int immunopharmacology* (2020) **81**:106035. doi:10.1016/j.intimp.2019.106035

26. Parimon T, Hohmann MS, Yao C. Cellular senescence: pathogenic mechanisms in lung fibrosis. *Int J Mol Sci* (2021) **22**(12):6214. doi:10.3390/ijms22126214

27. Neef R, Klein UR, Kopajtich R, Barr FA. Cooperation between mitotic kinesins controls the late stages of cytokinesis. *Curr Biol* (2006) **16**(3):301–7. doi:10.1016/j.cub.2005.12.030

28. Chen X, Gu L, Cheng X, Xing J, Zhang M. MiR-17-5p downregulation alleviates apoptosis and fibrosis in high glucose-induced human mesangial cells through inactivation of Wnt/β-catenin signaling by targeting KIF23. *Environ Toxicol* (2021) **36**(8):1702–12. doi:10.1002/tox.23280

29. Paun A, Lemay AM, Tomko TG, Haston CK. Association analysis reveals genetic variation altering bleomycin-induced pulmonary fibrosis in mice. *Am J Respir Cel Mol Biol* (2013) **48**(3):330–6. doi:10.1165/rcmb.2012-0078OC

30. Du M, Haag DG, Lynch JW, Mittinty MN. Comparison of the tree-based machine learning algorithms to Cox regression in predicting the survival of oral and pharyngeal cancers: analyses based on SEER database. *Cancers* (2020) **12**(10):2802. doi:10.3390/cancers12102802

31. Zou Y, Shi Y, Sun F, Liu J, Guo Y, Zhang H, et al. Extreme gradient boosting model to assess risk of central cervical lymph node metastasis in patients with papillary thyroid carcinoma: individual prediction using SHapley Additive exPlanations. *Computer Methods Programs Biomed* (2022) **225**:107038. doi:10.1016/j.cmpb.2022.107038

32. Fan YW, Liu WH, Chen YT, Hsu YC, Pathak N, Huang YW, et al. Exploring kinase family inhibitors and their moiety preferences using deep SHapley additive exPlanations. *BMC bioinformatics* (2022) **23**(Suppl. 4):242. doi:10.1186/s12859-022-04760-5

33. Han X, Yuan T, Zhang J, Shi Y, Li D, Dong Y, et al. FOXO4 peptide targets myofibroblast ameliorates bleomycin-induced pulmonary fibrosis in mice through ECM-receptor interaction pathway. *J Cell Mol Med* (2022) **26**(11):3269–80. doi:10.1111/jcmm.17333

34. Zhao M, Wang L, Wang M, Zhou S, Lu Y, Cui H, et al. Targeting fibrosis: mechanisms and clinical trials. *Signal Transduction Targeted Therapy* (2022) **7**(1):206. doi:10.1038/s41392-022-01070-3

35. Finnson KW, Almadani Y, Philip A. Non-canonical (non-SMAD2/3) TGF-β signaling in fibrosis: mechanisms and targets. *Semin Cel and Dev Biol* (2020) **101**:115–22. doi:10.1016/j.semcdb.2019.11.013

36. Li X, Cai H, Cai Y, Zhang Q, Ding Y, Zhuang Q. Investigation of a hypoxia-immune-related microenvironment gene signature and prediction model for idiopathic pulmonary fibrosis. *Front Immunol* (2021) **12**:629854. doi:10.3389/fimmu.2021.629854

37. Chen B, Khodadoust MS, Liu CL, Newman AM, Alizadeh AA. Profiling tumor infiltrating immune cells with CIBERSORT. *Methods Mol Biol (Clifton, N.J.)* (2018) **1711**:243–59. doi:10.1007/978-1-4939-7493-1_12

38. Kong J, Chen L. Gene expression profile analysis of severe influenza-based modulation of idiopathic pulmonary fibrosis. *Eur J Med Res* (2024) **29**(1):501. doi:10.1186/s40001-024-02107-9

39. Zhu H, Zhou A, Zhang M, Pan L, Wu X, Fu C, et al. Comprehensive analysis of an endoplasmic reticulum stress-related gene prediction model and immune infiltration in idiopathic pulmonary fibrosis. *Front Immunol* (2023) **14**:1305025. doi:10.3389/fimmu.2023.1305025

40. Luo H, Yan J, Zhou X. Constructing an extracellular matrix-related prognostic model for idiopathic pulmonary fibrosis based on machine learning. *BMC Pulm Med* (2023) **23**(1):397. doi:10.1186/s12890-023-02699-8

41. Huang G, Xu X, Ju C, Zhong N, He J, Tang XX. Identification and validation of autophagy-related gene expression for predicting prognosis in patients with idiopathic pulmonary fibrosis. *Front Immunol* (2022) **13**:997138. doi:10.3389/fimmu.2022.997138

42. Liu T, Ning J, Fan X, Wei H, Shi G, Fu QB. Identification of immune patterns in idiopathic pulmonary fibrosis patients driven by PLA2G7-positive macrophages using an integrated machine learning survival framework. *Scientific Rep* (2024) **14**(1):22369. doi:10.1038/s41598-024-73625-z

43. Lv X, Liu C, Liu S, Li Y, Wang W, Li K, et al. The cell cycle inhibitor P21 promotes the development of pulmonary fibrosis by suppressing lung alveolar regeneration. *Acta Pharmaceutica Sinica B* (2022) **12**(2):735–46. doi:10.1016/j.apsb.2021.07.015

EBM Experimental Biology and Medicine

TYPE Review
PUBLISHED 25 November 2024
DOI 10.3389/ebm.2024.10320

Check for updates

OPEN ACCESS

*CORRESPONDENCE
Guoyuan Yang,
31981077@qq.com

†These authors have contributed equally to this work

RECEIVED 19 July 2024
ACCEPTED 07 November 2024
PUBLISHED 25 November 2024

CITATION
Wu D, Huang X, Chen L, Hou P, Liu L and Yang G (2024) Integrating artificial intelligence in strabismus management: current research landscape and future directions.
Exp. Biol. Med. 249:10320.
doi: 10.3389/ebm.2024.10320

Integrating artificial intelligence in strabismus management: current research landscape and future directions

Dawen Wu[1,2†], Xi Huang[1,3†], Liang Chen[1,2], Peixian Hou[1,2], Longqian Liu[1,2] and Guoyuan Yang[1,2*]

[1]Department of Ophthalmology, West China Hospital, Sichuan University, Chengdu, China, [2]Laboratory of Optometry and Vision Sciences, West China Hospital, Sichuan University, Chengdu, China, [3]Laboratory of Macular Disease, West China Hospital, Sichuan University, Chengdu, China

Abstract

Advancements in artificial intelligence (AI) are transforming strabismus management through improved screening, diagnosis, and surgical planning. Deep learning has notably enhanced diagnostic accuracy and optimized surgical outcomes. Despite these advancements, challenges such as the underrepresentation of diverse strabismus types and reliance on single-source data remain prevalent. Emphasizing the need for inclusive AI systems, future research should focus on expanding AI capabilities with large model technologies, integrating multimodal data to bridge existing gaps, and developing integrated management platforms to better accommodate diverse patient demographics and clinical scenarios.

KEYWORDS

strabismus, artificial intelligence, deep learning, large model, multimodal, eye care

Impact statement

Early diagnosis and treatment of strabismus are crucial for preventing irreversible visual impairment and improving patient outcomes. This review explores the transformative potential of AI in strabismus management, highlighting significant advancements in screening, diagnosis, and surgical planning that have improved diagnostic accuracy and surgical outcomes. It addresses current challenges such as the underrepresentation of diverse strabismus types and reliance on single-source data, emphasizing the need for inclusive AI systems integrating multimodal data. As the first dedicated review on AI's role in strabismus, it provides valuable insights and guides future research. This new information highlights AI's potential to enhance patient outcomes, improve ophthalmic care, and contribute to societal welfare, setting the stage for further advancements in AI applications in strabismus management.

Introduction

Strabismus, a prevalent ocular disorder characterized by the misalignment of eyes [1], predominantly affects children, leading to rapid deterioration of binocular vision, monocular suppression, anomalous retinal correspondence, and ultimately, irreversible and permanent visual impairment. While primarily seen in children, strabismus can occur at any age, significantly impacting visual function, appearance, learning abilities, employment opportunities [2], and mental health [3], thus constituting a significant societal concern [4]. Delays in diagnosis and treatment often culminate in binocular vision dysfunction or irrevocable vision loss [5]. Given its subtle onset and diverse subtypes, early diagnosis significantly enhances recovery chances. Certain types of infantile strabismus, such as intermittent esotropia in infants under 6 months, may naturally improve by the age of one, advocating for close monitoring to circumvent premature surgical interventions [6]. In light of the above, implementing screening for high-risk groups and precisely diagnosing subtypes of strabismus, coupled with early and appropriate interventions (such as surgery), is of paramount importance. Screening refers to a binary classification process aimed at determining the presence or absence of strabismus, assisting in identifying cases that require referral for further evaluation. Diagnosis, on the other hand, involves multi-class classification to determine the specific subtype of strabismus, which is critical for deciding on appropriate treatment options. However, current strabismus screening and diagnosis are primarily conducted manually by strabismus and pediatric ophthalmologists using methods such as the corneal light reflex test and cover test, which heavily rely on patient cooperation and the physician's skill and experience.

Recent years have seen an exponential growth in artificial intelligence (AI) technology, encompassing research on all common ocular diseases, including anterior segment diseases like keratoconus [7] and cataracts [8], and posterior segment diseases such as retinal diseases [9] and optic nerve-related conditions [10]. The year 2023 witnessed unprecedented breakthroughs in medical AI capabilities, propelled by the transformative development of large models, such as ChatGPT [11]. Google's Med-PaLM [12], achieving expert-level performance on U.S. medical licensing examination questions, and the publication of foundational large model articles in prestigious journals like Nature [13], have underscored the emerging landscape of medical AI large models. The substantial potential of AI has markedly improved the accuracy of ocular disease screening and diagnosis, contributing to reduced healthcare workload, lower medical costs, and addressing the shortage of ophthalmologists, thereby striving for comprehensive healthcare resource coverage and enhanced public health. Notably, AI research in strabismus treatment and prognosis prediction has also been flourishing. This article, set against the backdrop of large model intelligence in medicine, primarily outlines the current state of research on AI applications in the screening, diagnosis, surgical parameter estimation, and prognosis prediction of strabismus, and provides a perspective on its research trends. Figure 1 and Table 1 summarize the relevant studies and applications discussed.

AI in strabismus screening and diagnosis

AI-driven strabismus detection using eye movement videos

The integration of videos with artificial intelligence (AI) in strabismus diagnosis represents a significant advancement in pediatric ophthalmology, offering a nuanced understanding of ocular misalignments through precise and dynamic assessment. This approach capitalizes on the temporal and spatial accuracy of eye tracking to capture subtle deviations in gaze behavior, which are often elusive in traditional examination settings. By harnessing the computational power of AI, these systems analyze complex eye movement patterns efficiently, uncovering diagnostic insights that transcend human observation. Furthermore, the ability to conduct these assessments in a non-invasive, patient-friendly manner reduces the stress associated with conventional diagnostic procedures, facilitating a more comfortable experience for pediatric patients. The amalgamation of eye-tracking technology and AI not only streamlines the diagnostic process but also enhances its accuracy, paving the way for early intervention strategies that are critical in mitigating the long-term visual consequences of strabismus.

In a groundbreaking study published in Nature Biomedical Engineering, Long et al. [14] investigated deep learning for diagnosing visually impaired infants, focusing on strabismus. Using a dataset of over 4,196 infants, they employed a temporal segment network on full-length videos to identify visual impairment patterns. The study highlighted Duane Syndrome and achieved high accuracy with area under the curve (AUC) metrics of 86.4%–93.0% for congenital conditions. This research validates deep learning's potential in diagnosing complex strabismus and underscores video-based behavioral analysis as a non-invasive pediatric ophthalmology tool [14]. Chen et al. [15] published a multicenter study in Nature Medicine, revealing a deep learning-based screening method for pediatric ophthalmic diseases, capable of diagnosing 16 common eye conditions in children, including strabismus. The study used cartoon videos to engage children, while advanced imaging recorded their head and eye movements. The neural network analyzed gaze patterns and facial features, distinguishing specific conditions. Using a dataset of 3,652 subjects and over 25 million video frames, the model achieved an AUC of 0.940 for internal validation and 0.843 for external validation [15].

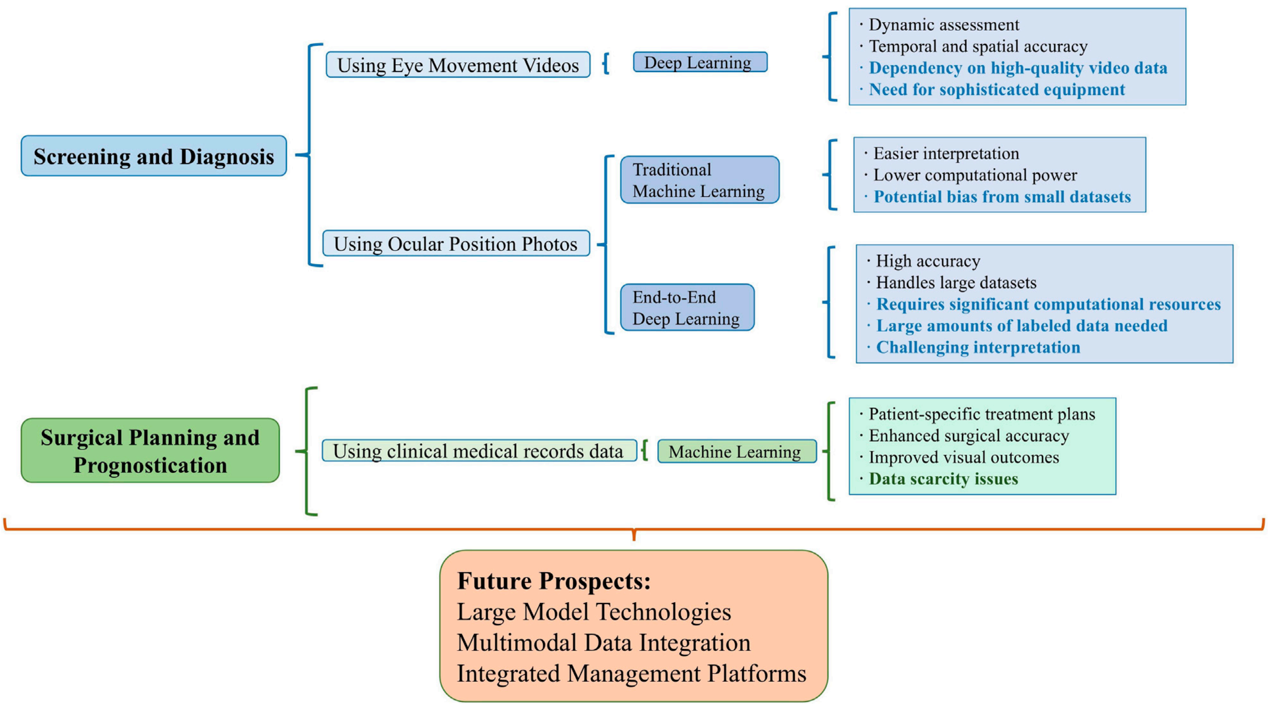

FIGURE 1
Overview of integrating AI in Strabismus management. This figure summarizes the use of different data modalities and AI algorithms in strabismus management tasks, highlighting their advantages and disadvantages. Disadvantages are indicated in bold.

While the studies mentioned offer significant insights into screening multiple pediatric eye diseases, including strabismus, their accuracy specifically for strabismus diagnosis highlights room for improvement. Given the potential of AI and eye-tracking technologies to advance strabismus diagnosis, automating this process presents a more accurate and efficient alternative to traditional methods. Therefore, previous studies have been published that focus specifically on AI-based strabismus screening and diagnosis using eye movement videos. Miao et al. [16] innovatively apply Virtual Reality (VR) to strabismus diagnosis, introducing a VR-based system that utilizes infrared cameras for measuring ocular deviation. In clinical trials, the VR system achieved a mean deviation of 0.4° ± 0.2° in orthotropic patients and 8.1° ± 5.5° in exotropic patients, closely mirroring doctor evaluations [16]. In the study by Saisara et al. [17], a novel strabismus screening approach combining eye tracking and gaming is proposed through the integration of the Gazepoint GP3 Eye Tracker with custom games. The system was tested on 50 volunteers, effectively identifying strabismus cases with a specific threshold value [17]. Chen et al. [18]'s study employs the Tobii X2-60 eye tracker to automate strabismus diagnosis. By contrasting object positions with eye fixations, their method identifies strabismus types. Precision is ensured through a 25-point calibration test, proving effective in diagnosing conditions like hypertropia [18]. Valente et al. [19] explore automated strabismus diagnosis through digital video analysis of the cover test. The study outlines an eight-step methodology culminating in a diagnostic accuracy of 93.33% for exotropia, with a specificity of 100% and a sensitivity of 80%. Furthermore, the system reported an average error of 2.57° in deviation measurement [19]. Chen et al. [20] developed a deep learning model capable of diagnosing strabismus by leveraging six different convolutional neural networks (CNNs) - AlexNet, VGG-S, VGG-M, VGG-16, VGG-F, and VGG-19. They collected eye-tracking data as participants looked at nine specific points, represented through gaze deviation (GaDe) images, from 42 subjects for model training and verification. Among the tested networks, VGG-S emerged as the most effective, demonstrating a specificity of 0.960 and sensitivity of 0.941 [20]. These findings highlight the tremendous potential of DL algorithms based on eye movement videos in the field of strabismus screening and subtype diagnosis.

AI-driven strabismus diagnosis using ocular position photos

While eye-tracking technology, with its spatial and temporal accuracy, excels at capturing subtle deviations in gaze behavior and leverages the AI for precise and dynamic evaluation of eye

TABLE 1 Summary of AI applications in strabismus management.

Authors, year	Task	Age, years	Disease type	Data type	Sample size	AI algorithm	Output
Strabismus Screening and Diagnosis							
Long 2019 [14]	Diagnosis	0–3	Visual impairment (including strabismus)	videos	4,196 subjects	Temporal Segment Networks	AUC = 0.816–0.930
Chen 2023 [15]	Screening	0–4	Visual impairment (including strabismus)	videos	3,652 subjects	EfficientNet-B4	AUC = 0.940 for internal validation AUC = 0.843 for external validation
Miao 2020 [16]	Ocular deviation measurement	>6	Exotropia	VR-based pupil tracking	17 subjects	stepwise approximation	Mean deviation of 0.4° ± 0.2° in orthotropia, 8.1° ± 5.5° in exotropia
Saisara 2017 [17]	Screening	7–50	Strabismus	Games and Eye tracking data	50 subjects	Gazepoint Analysis	Identified Dthreshold ≥0.05 for strabismus
Chen 2015 [18]	Diagnosis	3–63	Esotropia, Exotropia and Hypertropia	Eye tracking data	225 subjects	Eye-tracking with Tobii X2-60	Identified subjects' fixation accuracy
Valente 2017 [19]	Diagnosis	—	Exotropia	Eye tracking videos	15 videos of 7 strabismic subjects	Image processing	Sensitivity = 0.800 Specificity = 1.000 Accuracy = 0.933
Chen 2018 [20]	Screening	25–63	Recessive, intermittent, and manifest strabismus	Eye tracking images	42 subjects	AlexNet VGG-F VGG-M VGG-S VGG-16 VGG-17	VGG-S: Accuracy = 0.952 Specificity = 0.960 Sensitivity = 0.941
Ma 2020 [21]	Screening	8–10	Strabismus, myopia and anisometropia	Images	100 subjects	Image processing	Accuracy = 0.940 Specificity = 0.980 Sensitivity = 0.800
Kang 2022 [22]	Diagnosis	—	Strabismus	Images	828 subjects	U-Net	Sclera Segmentation: Accuracy = 0.998 Specificity = 0.975 Sensitivity = 0.999 DSC = 0.969 Limbus Segmentation: Accuracy = 0.999 Specificity = 0.956 Sensitivity = 0.999 DSC = 0.957
Almeida 2015 [23]	Diagnosis	—	Exotropia, Esotropia, Hypertropia and Hypotropia	Images	200 images of 40 strabismic subjects	SVM	Accuracy: 0.880 (ET) 1.000 (XT) 0.803 (HT) 0.833 (HoT)
de Oliveira Simoes 2019 [24]	Diagnosis	—	Exotropia, Esotropia, Hypertropia and Hypotropia	Images	225 images of 45 strabismic subjects	U-Net, ResNet	Accuracy = 0.966 Specificity = 1.000 Sensitivity = 0.958
Mesquita 2021 [25]	Diagnosis	5–15	Exotropia, Esotropia, Hypertropia and Hypotropia	Images	224 subjects	Image processing	Accuracy = 0.845 Specificity = 0.844 Sensitivity = 0.895 Kappa coefficient = 0.430
De Figueiredo 2021 [26]	Diagnosis	6–87	Exotropia and Esotropia	Images		ResNet50	Accuracy = 0.420–0.920 Precision = 0.250–0.840

(Continued on following page)

TABLE 1 (*Continued*) Summary of AI applications in strabismus management.

Authors, year	Task	Age, years	Disease type	Data type	Sample size	AI algorithm	Output
					990 images of 110 strabismic subjects		Recall = 0.380–0.920 F1 = 0.290–0.880 Val_Loss = 0.085–2.210
Huang 2021 [27]	Screening	—	Strabismus	Images	60 subjects	ResNet-12	Accuracy = 0.805 Specificity = 0.768 Sensitivity = 0.842
Zheng 2021 [28]	Screening	—	Exotropia and Esotropia	Images	7,026 images for training and 277 for External Validation	VGG16, Inception-V3, Xception	Inception-V3: AUC = 0.997 Accuracy = 0.968 Specificity = 0.993 Sensitivity = 0.940
Mao 2021 [29]	Screening	1–65	Exotropia	Images	5,797 subjects	InceptionResNetV2	AUC = 0.998 Accuracy = 0.990 Specificity = 0.983 Sensitivity = 0.991
Wu 2024 [30]	Screening	1–74	Exotropia, Esotropia and Vertical deviation	Images	6,194 images	VIT_16_224	AUC = 0.994, Accuracy = 0.967, Precision = 0.980, Specificity = 0.970, Sensitivity = 0.960, F1 = 0.975
Kim 2021 [31]	Diagnosis	—	Exotropia and Esotropia	Images	2023 subjects	CNN	Accuracy = 0.667
Strabismus Surgical Planning and Prognostication							
De Almeida 2015 [32]	Surgical planning	—	Exotropia and Esotropia	Clinical data	88 patients	SVR	Average error: medial rectus muscles: 0.500 mm for recoil, 0.700 for resection lateral rectus muscles: 0.600 for recoil, 0.800 for resection
Fernando 2021 [33]	Surgical planning	0.5–65	Exotropia and Esotropia	Clinical data	153 patients	DTR, RFR, ETR	MAE:0.448 – 1.038 mm RMSE = 1.496–2.447 mm
Tang 2022 [34]	Surgical planning	—	Strabismus	Clinical data	1,076 patients	WGAN-GP + lightGBM	AUC = 0.845
Mao 2021 [29]	Surgical planning	1–65	Exotropia	Images	1,070 images	InceptionResNetV2	accuracy of ±5.5° (11.5 PD) with a bias of −0.6°
Lou 2023 [35]	Surgical Planning	17.6 ± 12.7	Inferior oblique overaction	Images	106 eyes	GAR2U-Net	ICC = 0.975
Liu 2019 [36]	Surgical Prognostication	6–12.25	Intermittent exotropia	Clinical data	132 patients	SVM	Accuracy = 0.821

AI, artificial intelligence; AUC, area under curve; DSC, dice similarity coefficient; SVM, support vector machine; ET, esotropia; XT, exotropia; HT, hypertropia; HoT, hypotropia; CNN, convolutional neural network; SVR, support vector regression; DTR, decision tree regressor; RFR, random forest regressor; ETR, extra trees regressor; MAE, mean absolute error; RMSE, root mean squared error; LightGBM, light gradient-boosting machine; PD, prism diopter; ICC, intraclass correlation coefficient. This table summarizes various studies on AI applications in strabismus management, detailing the author and year, task, data type, sample size, AI algorithm, and key performance metrics.

movements in both "resting" and "task" states, facilitating the screening of multiple ocular diseases and identification of certain strabismus subtypes, the collection of eye movement videos often requires specialized equipment and is more time-consuming. Additionally, video processing demands substantial computational resources, unlike the convenience and lower computational requirements of ocular position photos. Merely a camera or even a smartphone can complete the image capture process. Instant uploads can return diagnostic results within milliseconds. Therefore, specifically for strabismus, AI systems based on ocular position photos continue to play a unique and indispensable role.

In the current realm of AI research for strabismus screening and diagnosis using ocular position photos, two main approaches prevail: algorithms for key eye region segmentation based on traditional stepwise learning, and classification algorithms based on end-to-end learning.

Traditional machine learning algorithms

Ma et al. [21] developed a smartphone app for the rapid screening of pediatric eye diseases, including strabismus. Utilizing image processing and AI, the app analyzes photos taken in dark rooms to evaluate facial landmarks, head tilt, and eye positions. It employs shape fitting techniques to estimate corneal light reflex and red reflex contours, quickly assessing risks of strabismus, myopia, and refractive errors in just 10 s. The app's sensitivity and specificity for detecting strabismus are 0.80 and 0.98, respectively, proving effective for early diagnosis [21]. Kang et al. [22] developed a deep learning model using U-Net architecture to detect strabismus by segmenting the cornea and scleral limbus from 828 gaze photographs across nine different gaze positions. The model demonstrated high segmentation accuracy: 0.9984 for the cornea and 0.9992 for the limbus, with Dice Similarity Coefficients of 0.9688 and 0.9571, respectively [22]. Almeida et al. [23] employed support vector machines (SVMs) for a machine learning-based diagnostic approach to strabismus. Analyzing 200 images from 40 patients with conditions like esotropias, exotropias, hypertropias, and hypotropias, their methodology involved face segmentation and eye region detection to precisely identify eye deviations. It achieved accuracy rates of 88% for esotropias, 100% for exotropias, and over 80% for vertical deviations, with errors closely matching specialist assessments [23]. de Oliveira Simoes et al. [24] adopted a similar experimental approach. Employing a private dataset of 225 images from 45 patients, the research aimed at evaluating ocular alignment by analyzing the distance between the limb centroid and a point between the eye corners, achieving an impressive accuracy of 96.6%, with a sensitivity of 95.8% and specificity of 100% [24]. Mesquita et al. [25] explored the concordance between expert ophthalmologist diagnoses and those made by an mHealth application for strabismus in 224 children aged 5–15. The app analyzed smartphone photos, incorporating steps like face segmentation, eye region detection, and alignment comparison of the Limbus center with brightness location. The app demonstrated a sensitivity of 89.47% and specificity of 84.39% at 6 PD, affirming its utility as a screening tool despite some misclassifications [25]. De Figueiredo et al. [26] developed an app based on the ResNet50 neural network to diagnose strabismus by identifying patients' different gaze positions in photographs from 110 patients. The model, trained to recognize combinations of left and right eyes in gaze positions ranging from 1 to 9 and version classifications from −4 to +4, achieved an overall accuracy between 0.42 and 0.92 and precision between 0.28 and 0.84 [26]. Huang et al. [27] developed a strabismus screening model with frontal facial images for face and eye region identification, and refining the detection with Otsu's binarization and the HSV color model. The model uses the least squares method to locate the pupil's center and assesses strabismus through eye positional similarity. Additionally, utilizing the ResNet-12 network for screening on images from 60 subjects, the team achieved diagnostic accuracy, sensitivity, and specificity of 0.805, 0.768, and 0.842, respectively [27].

End-to-end deep learning algorithms

Zheng et al. [28] leveraged the Inception-v3 architecture to train a model for identifying referable horizontal strabismus in children's primary gaze photos, excluding conditions like vertical and paralytic strabismus. It achieved an average AUC of about 0.99, with sensitivity at 94.0%, specificity at 99.3%, and accuracy at 96.8% in the external validation set, outperforming resident ophthalmologists [28]. Lin et al. [29] utilized the InceptionResNetV2 architecture for training a model aimed at diagnosing horizontal strabismus, deliberately excluding vertical strabismus and intermittent exotropia during the data collection phase. The training involved 1,561 photographs of horizontal strabismus (both esotropia and exotropia) and 2,496 of normal eyes. Tested on 356 horizontal strabismus and 514 normal eyes, the model achieved a sensitivity of 0.991, a specificity of 0.983, and an accuracy of 0.990 [29]. Wu et al. [30] constructed the largest corneal light-reflection photo dataset in the field to date and trained a model based on the Transformer architecture (VIT_16_224). Unlike previous studies that focused solely on pediatric patients and a limited number of strabismus subtypes, this study encompassed all age groups and a comprehensive range of strabismus subtypes, resulting in the development of the best-performing model. The VIT_16_224 architecture outperformed the models from the aforementioned studies on a shared dataset. On an independent test set, the model achieved an accuracy of 0.967, precision of 0.980, specificity of 0.960, sensitivity of 0.970, and an F1 score of 0.975, significantly improving the generalizability and practicality of the diagnostic model. Donghwan Kim et al. [31] introduced a Convolutional Neural Network (CNN)-based model for classifying strabismus into three categories: esotropia, exotropia, and normal eye alignment, leveraging a "9-photo" front view. The training set consisted of "9-photo" sets from 73 esotropia patients, 75 exotropia patients, and 72 individuals with normal alignment. Testing was conducted with "9-photo" sets from 10 patients in each group. The model achieved a final test accuracy of 66.7% [31]. These studies highlight the model's potential to streamline early strabismus diagnosis in young children.

Comparison of traditional machine learning and end-to-end deep learning algorithms

In comparing traditional machine learning algorithms and end-to-end deep learning algorithms for strabismus diagnosis, several key differences and similarities emerge. Traditional machine learning algorithms typically involve a series of preprocessing steps, feature extraction, and model training phases. Common techniques include Support Vector Machines (SVM), decision trees, and regression models. For eye region segmentation, researchers often use pre-trained facial detection models to extract key regions and calculate coordinates for critical areas like the pupil center and corneal light reflex points. By comparing these results to predetermined thresholds, the presence and subtype of strabismus can be determined. These methods are easier to interpret and require less computational power, allowing for fine-tuning at each stage. However, their performance heavily depends on the quality and relevance of manually extracted features and may struggle with high-dimensional data and complex patterns inherent in ocular position photos. Additionally, the selection of thresholds based on limited statistical data within smaller datasets may introduce bias, reducing the model's generalizability.

In contrast, end-to-end deep learning algorithms, such as convolutional neural networks (CNNs) and recurrent neural networks (RNNs), learn features and patterns directly from raw data, automating the feature extraction process. These models use extensive image datasets to enhance the model's generalization capability, handling large, high-dimensional datasets and capturing complex, non-linear relationships within the data. This leads to higher accuracy and robustness in predictions. However, they require significant computational resources and large amounts of labeled data for training, and their "black-box" nature can make interpretation and troubleshooting more challenging.

In conclusion, end-to-end deep learning models generally outperform traditional machine learning algorithms in accuracy and generalizability due to their ability to learn directly from data without manual feature extraction. Deep learning models scale better with increased data, improving performance as more data becomes available, whereas traditional methods may not show the same level of improvement due to the limitations of manual feature extraction. While traditional machine learning models are more interpretable, providing clearer insights into the decision-making process, deep learning models offer superior performance and scalability for strabismus diagnosis using ocular position photos. The choice between the two depends on the specific requirements and constraints of the clinical application, including the availability of computational resources and the need for model interpretability. This comparative understanding highlights the potential of integrating both approaches to optimize diagnostic accuracy and clinical applicability.

AI in strabismus surgical planning and prognostication

The application of AI in strabismus surgical planning and prognostication represents a transformative shift towards precision medicine in pediatric ophthalmology. Recent studies exemplify the integration of advanced machine learning models, such as Support Vector Regression (SVR) [37], multi-output regression trees [38], Light Gradient Boosting Machines (LightGBM) [34], convolutional neural networks (CNN) [39], and recurrent residual CNNs [40] with global attention gates, to refine surgical strategies for complex ocular deviations. These AI-driven tools process extensive clinical data, including visual acuity, type of deviation, binocular fixation, and ocular position, to predict the precise amounts of muscle resection and recoil needed in surgeries.

De Almeida et al. [32] conducted a regression study on 88 patients with horizontal strabismus using Support Vector Regression (SVR). The model aimed to accurately estimate the adjustments needed for medial and lateral rectus muscles. The SVR model achieved mean absolute errors of 0.5 mm for medial rectus recoil and 0.7 mm for resection, with 0.6 mm for lateral rectus recoil and 0.8 mm for resection [32]. Leite et al. [33] analyzed surgical planning for strabismus in 153 patients with horizontal deviations, primarily esotropia and exotropia. Utilizing comprehensive patient data including age, binocular fixation, and deviation from five ductions positions, the study applied a multi-output regression tree approach to predict necessary surgical adjustments for various muscles. The model accurately forecasted recoil and resection requirements for both medial and lateral rectus muscles, achieving a Mean Absolute Error (MAE) range of 0.448 mm–1.038 mm and a Root Mean Square Error (RMSE) of up to 1.496 mm [33]. Tang et al. [34] conducted a study involving 1,076 surgical cases of patients with various types of strabismus, including esotropia and exotropia, using patient data like age, dominant eye, and exodeviation angles. They developed a model using the Light Gradient Boosting Machine (LightGBM) architecture, which initially achieved a 69.32% accuracy in predicting surgical adjustments such as muscle movement amount and direction. To address data scarcity and improve model performance, the Wasserstein Generative Adversarial Network with Gradient Penalty (WGAN-GP) was applied, enhancing accuracy to 84.52% [34]. Mao et al. [29] developed an Operation Advice System using corneal light-reflection photos from 56 exotropia patients who had successfully undergone initial surgeries. The retrospective test set included 160 subjects, predominantly with intermittent exotropia, and demonstrated a high positive correlation ($r = 0.86$, $P < 0.001$) between the predicted and actual surgical angles, with an accuracy of ±5.5° (11.5 PD) and a slight bias of -0.6° [29]. Lou et al. [35] developed a recurrent residual CNN based on GAR2U-Net to evaluate Inferior Oblique Overaction (IOOA) in a study involving 106 eyes of 72 patients. The technique focused on measuring the height difference between the inferior corneal limbus of both eyes, a key indicator of IOOA, which was clinically graded from +1 to +4. The study found significant correlations between automated photographic measurements and clinical gradings, and excellent agreement with manual measurements, indicated by intraclass correlation coefficients (ICCs) of 0.975.

This study demonstrates advanced neural networks' ability to offer cost-effective, accurate, and scalable IOOA assessments using simple photographs [35]. Liu et al. [36] conducted a prospective cross-sectional study on 132 patients with intermittent exotropia, using a support vector machine (SVM) to determine the optimal timing for surgical interventions. The study utilized preoperative factors like deviation angle, binocular vision, and stereoacuity to predict the best moment for surgery. Post a 6-month follow-up, the SVM achieved an 82.1% accuracy rate, with an overall success rate of 63.6%, identifying the initial postoperative deviation angle as a crucial predictor of successful alignment. This research highlights the effectiveness of SVM in enhancing surgical outcomes for exotropia through precise timing based on detailed clinical data [36].

The aforementioned study illustrate that AI integration refines surgical planning and prognostication. By leveraging these technologies, ophthalmologists can achieve significantly improved accuracy in surgical outcomes, enhancing patient-specific treatment plans. Notably, these models facilitate the analysis of deviations, muscle actions, and postoperative alignments, allowing for highly individualized surgical interventions. This marks a significant shift in enhancing surgical precision and redefining strabismus management standards.

Discussion

The integration of artificial intelligence (AI) in strabismus management represents a significant advancement in ophthalmology, enhancing diagnostic precision and therapeutic efficacy. As AI technologies have begun to permeate every aspect of healthcare, from data collection and integration [41–45] to analysis and treatment [46], they demonstrate a potent synergy with medical professionals, showcasing their immense potential to enhance human health [47]. The advent of large models like ChatGPT has marked a pivotal shift, increasingly evident in the fourth industrial revolution, driving transformative changes in how healthcare is delivered.

While AI's application in healthcare, particularly in ophthalmology, is promising, it faces challenges such as the need for improved data-sharing mechanisms, validation, evaluation, and regulatory frameworks. Despite the impressive achievements of AI in enhancing strabismus screening, diagnosis, and treatment, there are significant limitations regarding the representativeness and generalizability of these advancements in real-world clinical settings. Current research often excludes numerous strabismus types, such as vertical, restrictive, sensory, paralytic strabismus, myasthenia gravis, nystagmus, and Duane syndrome, focusing primarily on pediatric populations and concomitant strabismus patients. This oversight highlights a critical gap, as there is a pressing need for comprehensive screening and precise diagnostic processes that encompass all age groups and subtypes of strabismus. Thus, the utility of these AI models in diverse clinical environments remains questionable. Meanwhile, despite early advantages in AI research facilitated by the digitization in ophthalmology, which amassed extensive imaging and pathological data, the comprehensive integration of multimodal patient data remains scarce, and the reliance on single data sources for AI diagnostics and prognostic assessments presents substantial challenges. Typical methodologies primarily use ocular position photos or eye movement videos for diagnosing strabismus, or electronic health records for predicting surgical outcomes, without considering additional data inputs, such as the sensory exam results, the refractive status, the CT or MRI images, forced duction test, etc. Conversely, clinicians often employ a multimodal data approach, integrating those concurrent data streams to enhance the accuracy of disease diagnosis, prognostic evaluations, and therapeutic strategies. Current AI systems process static, singular time-point data, which fails to capture the dynamic, evolving nature of diseases and overlooks the rich historical context of patient data that could significantly refine predictive accuracies. Theoretically, as AI technologies advance, models should be capable of harnessing all available data sources, including those traditionally inaccessible to clinicians, such as genomics [48]. Moreover, in regions such as China, many hospitals still rely on non-digital, unstructured data collection methods due to a lack of digital resources and personnel, leading to incomplete or inaccurate medical data and hindering widespread AI research. Additionally, the field suffers from a scarcity of AI-driven strabismus management products that extend beyond diagnosis to include essential services such as patient referral and long-term follow-up, which are vital for ensuring sustained care and systematic data collection across various modalities and time points.

Moving forward, research utilizing deep learning in strabismus should embrace a more inclusive approach, incorporating patients of all ages, ethnicities, and all types of the condition. However, the diversity in irrelevant features such as eyelid size, eye color, and skin tone across different age groups and ethnic backgrounds poses additional challenges for model training. Complications such as eyelid ptosis, which require physical assistance during photo acquisition, can disrupt the accurate extraction of features by AI models. Additionally, ensuring privacy protection is critical as AI technologies handle sensitive medical data. Addressing these challenges is essential for maximizing the clinical utility of AI technologies. Future initiatives should focus on easily collectible multimodal data for strabismus research, integrating biosensors, electronic medical records, eye movement videos, ocular photos, and socio-environmental factors throughout the patient care timeline. Large AI models, such as Transformer-based architectures, have the potential to handle the complexity and scale of multimodal data, offering enhanced generalization and predictive power. This integration not only facilitates extensive research but also enables the construction of ophthalmological knowledge graphs and the provision of personalized treatment recommendations, which are becoming increasingly feasible. Meanwhile, the development of an integrated AI-based strabismus management platform that facilitates paperless, comprehensive management of strabismus patients from screening through treatment, and enables the integration and collection of cross-modal patient information, will lay a solid foundation for a specialized, large-scale AI model in strabismus care. The platform should support AI applications in the screening, diagnosis, surgical parameter estimation, and prognosis prediction of strabismus, as well as intelligent follow-up. By leveraging a full-process, multimodal, and multi-timepoint intelligent platform, ophthalmologists can achieve more accurate, personalized, and effective strabismus management, ultimately improving patient outcomes and advancing the field of ophthalmology.

Conclusion

In conclusion, this review has highlighted significant advancements and emerging challenges in integrating AI into strabismus management. AI is revolutionizing screening, diagnosis, and surgical planning through cutting-edge technologies such as deep learning, enhancing accuracy and optimizing outcomes. However, critical gaps are evident, particularly the underrepresentation of diverse strabismus types and age groups in AI studies. These limitations underscore the necessity for AI systems that accommodate broader demographics and clinical scenarios. Additionally, the reliance on single-source data in AI models, compared to the multimodal approach used in clinical settings, reveals an urgent need for integrating more comprehensive data sources, including longitudinal patient data. Addressing these challenges will be pivotal in advancing AI technology in ophthalmology, enhancing patient outcomes, and setting new standards in healthcare delivery.

Author contributions

DW and XH: Writing–original draft, Writing–review and editing, Methodology, Conceptualization, Data curation, Investigation. LC and PH: Writing–original draft, Data curation. GY: Investigation, Methodology, Resources, Supervision, Writing–original draft, Writing–review and editing, Conceptualization. LL: Supervision, Conceptualization, Critical revision of the manuscript. All authors contributed to the article and approved the submitted version.

Funding

The author(s) declare financial support was received for the research, authorship, and/or publication of this article. This work was supported by Project for disciplines of excellence for West China Hospital, Sichuan University, China (No. ZYJC23001).

Conflict of interest

The author(s) declared no potential conflicts of interest with respect to the research, authorship, and/or publication of this article.

References

1. Repka MX, Lum F, Burugapalli B. Strabismus, strabismus surgery, and reoperation rate in the United States: analysis from the IRIS registry. *Ophthalmology* (2018) **125**:1646–53. doi:10.1016/j.ophtha.2018.04.024

2. Mojon-Azzi SM, Mojon DS. Strabismus and employment: the opinion of headhunters. *Acta Ophthalmologica* (2009) **87**:784–8. doi:10.1111/j.1755-3768.2008.01352.x

3. Durnian JM, Noonan CP, Marsh IB. The psychosocial effects of adult strabismus: a review. *Br J Ophthalmol* (2011) **95**:450–3. doi:10.1136/bjo.2010.188425

4. Uretmen O, Egrilmez S, Kose S, Pamukçu K, Akkin C, Palamar M. Negative social bias against children with strabismus. *Acta Ophthalmologica Scand* (2003) **81**:138–42. doi:10.1034/j.1600-0420.2003.00024.x

5. Cotter SA, Tarczy-Hornoch K, Song E, Lin J, Borchert M, Azen SP, et al. Fixation preference and visual acuity testing in a population-based cohort of preschool children with amblyopia risk factors. *Ophthalmology* (2009) **116**:145–53. doi:10.1016/j.ophtha.2008.08.031

6. Wang X, Gao X, Xiao M, Tang L, Wei X, Zeng J, et al. Effectiveness of strabismus surgery on the health-related quality of life assessment of children with intermittent exotropia and their parents: a randomized clinical trial. *J Am Assoc Pediatr Ophthalmol Strabismus* (2015) **19**:298–303. doi:10.1016/j.jaapos.2015.04.007

7. Ambrósio R, Jr, Salomão MQ, Barros L, da Fonseca Filho JBR, Guedes J, Neto A, et al. Multimodal diagnostics for keratoconus and ectatic corneal diseases: a paradigm shift. *Eye Vis* (2023) **10**:45. doi:10.1186/s40662-023-00363-0

8. Zhou Y, Li G, Li H. Automatic cataract classification using deep neural network with discrete state transition. *IEEE Trans Med Imaging* (2020) **39**:436–46. doi:10.1109/tmi.2019.2928229

9. Li B, Chen H, Yu W, Zhang M, Lu F, Ma J, et al. The performance of a deep learning system in assisting junior ophthalmologists in diagnosing 13 major fundus diseases: a prospective multi-center clinical trial. *NPJ Digit Med* (2024) **7**:8. doi:10.1038/s41746-023-00991-9

10. Dong L, He W, Zhang R, Ge Z, Wang YX, Zhou J, et al. Artificial intelligence for screening of multiple retinal and optic nerve diseases. *JAMA Netw Open* (2022) **5**:e229960. doi:10.1001/jamanetworkopen.2022.9960

11. Dave T, Athaluri SA, Singh S. ChatGPT in medicine: an overview of its applications, advantages, limitations, future prospects, and ethical considerations. *Front Artif Intell* (2023) **6**:1169595. doi:10.3389/frai.2023.1169595

12. Harris E. Large Language models answer medical questions accurately, but can't match clinicians' knowledge. *Jama* (2023) **330**:792–4. doi:10.1001/jama.2023.14311

13. Singhal K, Azizi S, Tu T, Mahdavi SS, Wei J, Chung HW, et al. Large language models encode clinical knowledge. *Nature* (2023) **620**:172–80. doi:10.1038/s41586-023-06291-2

14. Long EP, Liu ZZ, Xiang YF, Xu AD, Huang JL, Huang XC, et al. Discrimination of the behavioural dynamics of visually impaired infants via deep learning. *Nat Biomed Eng* (2019) **3**:860–9. doi:10.1038/s41551-019-0461-9

15. Chen W, Li R, Yu Q, Xu A, Feng Y, Wang R, et al. Early detection of visual impairment in young children using a smartphone-based deep learning system. *Nat Med* (2023) **29**:493–503. doi:10.1038/s41591-022-02180-9

16. Miao Y, Jeon JY, Park G, Park SW, Heo H. Virtual reality-based measurement of ocular deviation in strabismus. *Computer Methods Programs Biomed* (2020) **185**: 105132. doi:10.1016/j.cmpb.2019.105132

17. Saisara U, Boonbrahm P, Chaiwiriya A. Strabismus screening by eye tracker and games. In: 14th international joint conference on computer science and software engineering (JCSSE). Nakhon Si Thammarat, Thailand, July 12–14, 2017 (IEEE) (2017).

18. Chen ZH, Fu H, Lo WL, Chi ZR. Eye-Tracking aided digital system for strabismus diagnosis. In: IEEE international conference on systems, man, and cybernetics (SMC), Hong Kong, Peoples R China, October 9–12, 2015 (Hong Kong, China: City Univ Hong Kong, IEEE Computer Soc) (2015). p. 2305–9.

19. Valente TLA, de Almeida JDS, Silva AC, Teixeira JAM, Gattass M. Automatic diagnosis of strabismus in digital videos through cover test. *Computer Methods Programs Biomed* (2017) **140**:295–305. doi:10.1016/j.cmpb.2017.01.002

20. Chen ZH, Fu H, Lo WL, Chi ZR. Strabismus recognition using eye-tracking data and convolutional neural networks. *J Healthc Eng* (2018) **2018**:1–9. doi:10.1155/2018/7692198

21. Ma SX, Guan YQ, Yuan YZ, Tai Y, Wang T. A one-step, streamlined children's vision screening solution based on smartphone imaging for resource-limited areas: design and preliminary field evaluation. *JMIR mHealth uHealth* (2020) **8**:e18226. doi:10.2196/18226

22. Kang YC, Yang HK, Kim YJ, Hwang JM, Kim KG. Automated mathematical algorithm for quantitative measurement of strabismus based on photographs of nine cardinal gaze positions. *Biomed Res Int* (2022) **2022**:1–7. doi:10.1155/2022/9840494

23. Sousa de Almeida JD, Silva AC, Teixeira JAM, Paiva AC, Gattass M. Computer-aided methodology for syndromic strabismus diagnosis. *J Digit Imaging* (2015) **28**:462–73. doi:10.1007/s10278-014-9758-0

24. de Oliveira ST, Carvalho SJ, Sousa de Almeida JD, Correa Silva A, Cardoso de Paiva A. Automatic ocular alignment evaluation for strabismus detection using U-net and ResNet networks. In: 2019 8th Brazilian conference on intelligent systems (BRACIS) proceedings, Salvador, Brazil, October 15–18, 2019, (2019). p. 239–44.

25. Mesquita M, Valente TLA, de Almeida JDS, Teixeira JAM, Medina FM, dos Santos AM. A mhealth application for automated detection and diagnosis of strabismus. *Int J Med Inform* (2021) **153**:6. doi:10.1016/j.ijmedinf.2021.104527

26. De Figueiredo LA, Dias JVP, Polati M, Carricondo PC, Debert I. Strabismus and artificial intelligence app: optimizing diagnostic and accuracy. *Translational Vis Sci and Technol* (2021) **10**:22. doi:10.1167/tvst.10.7.22

27. Huang X, Lee SJ, Kim CZ, Choi SH. An automatic screening method for strabismus detection based on image processing. *PLoS One* (2021) **16**:e0255643. doi:10.1371/journal.pone.0255643

28. Zheng C, Yao Q, Lu JW, Xie XL, Lin SB, Wang ZL, et al. Detection of referable horizontal strabismus in Children's primary gaze photographs using deep learning. *Translational Vis Sci and Technol* (2021) **10**:33. doi:10.1167/tvst.10.1.33

29. Mao KL, Yang YH, Guo C, Zhu Y, Chen C, Chen JC, et al. An artificial intelligence platform for the diagnosis and surgical planning of strabismus using corneal light-reflection photos. *Ann Transl Med* (2021) **9**:374. doi:10.21037/atm-20-5442

30. Wu D, Li Y, Zhang H, Yang X, Mao Y, Chen B, et al. An artificial intelligence platform for the screening and managing of strabismus. *Eye (Lond)* (2024) **38**: 3101–7. doi:10.1038/s41433-024-03228-5

31. Kim D, Joo J, Zhu G, Seo J, Ha J, Kim SC. Ieee. Strabismus classification using convolutional neural networks. In: 3rd international conference on artificial intelligence in information and communication (IEEE ICAIIC), Jeju Island, South Korea, April 20–23, 2021 (IEEE) (2021). p. 216–8.

32. Almeida JDSd, Silva AC, Teixeira JAM, Paiva AC, Gattass M. Surgical planning for horizontal strabismus using Support Vector Regression. *Comput Biol Med* (2015) **63**:178–86. doi:10.1016/j.compbiomed.2015.05.025

33. Leite FHF, Almeida JDSd, Cruz LBd, Teixeira JAM, Junior GB, Silva AC, et al. Surgical planning of horizontal strabismus using multiple output regression tree. *Comput Biol Med* (2021) **134**:104493. doi:10.1016/j.compbiomed.2021.104493

34. Tang R, Wang W, Meng Q, Liang S, Miao Z, Guo L, et al. A strabismus surgery parameter design model with WGAN-GP data enhancement method. *J Phys Conf Ser (Uk)* (2022) **2179**:012009. doi:10.1088/1742-6596/2179/1/012009

35. Lou LX, Huang XR, Sun YM, Cao J, Wang YQ, Zhang QN, et al. Automated photographic analysis of inferior oblique overaction based on deep learning. *Quant Imaging Med Surg* (2023) **13**:329–38. doi:10.21037/qims-22-467

36. Liu YL, Liu CG, Zhang W, Chen X, Zhao KX. Model of a support vector machine to assess the functional cure for surgery of intermittent exotropia. *Sci Rep* (2019) **9**(7):8321. doi:10.1038/s41598-019-38969-x

37. Smola AJ, Schölkopf B. A tutorial on support vector regression. *Stat Comput* (2004) **14**:199–222. doi:10.1023/b:stco.0000035301.49549.88

38. Borchani H, Varando G, Bielza C, Larrañaga P. A survey on multi-output regression. *WIREs Data Mining Knowledge Discov* (2015) **5**:216–33. doi:10.1002/widm.1157

39. Gu JX, Wang ZH, Kuen J, Ma LY, Shahroudy A, Shuai B, et al. Recent advances in convolutional neural networks. *Pattern Recognition* (2018) **77**:354–77. doi:10.1016/j.patcog.2017.10.013

40. Boxuan Y, Junwei F, Jun L. Residual recurrent neural networks for learning sequential representations. *Information (Switzerland)* (2018) **9**(56):14. doi:10.3390/info9030056

41. Bycroft C, Freeman C, Petkova D, Band G, Elliott LT, Sharp K, et al. The UK Biobank resource with deep phenotyping and genomic data. *Nature* (2018) **562**: 203–9. doi:10.1038/s41586-018-0579-z

42. Chen ZM, Chen JS, Collins R, Guo Y, Peto R, Wu F, et al. China Kadoorie Biobank of 0.5 million people: survey methods, baseline characteristics and long-term follow-up. *Int J Epidemiol* (2011) **40**:1652–66. doi:10.1093/ije/dyr120

43. Nagai A, Hirata M, Kamatani Y, Muto K, Matsuda K, Kiyohara Y, et al. Overview of the BioBank Japan Project: study design and profile. *J Epidemiol* (2017) **27**:S2–S8. doi:10.1016/j.je.2016.12.005

44. Gaziano JM, Concato J, Brophy M, Fiore L, Pyarajan S, Breeling J, et al. Million Veteran Program: a mega-biobank to study genetic influences on health and disease. *J Clin Epidemiol* (2016) **70**:214–23. doi:10.1016/j.jclinepi.2015.09.016

45. Saenz A, Chen E, Marklund H, Rajpurkar P. The MAIDA initiative: establishing a framework for global medical-imaging data sharing. *The Lancet Digital Health* (2024) **6**:e6–e8. doi:10.1016/s2589-7500(23)00222-4

46. Bo ZH, Guo YC, Lyu J, Liang HR, He JX, Deng SJ, et al. Relay learning: a physically secure framework for clinical multi-site deep learning. *Npj Digit Med* (2023) **6**:204. doi:10.1038/s41746-023-00934-4

47. Dvijotham K, Winkens J, Barsbey M, Ghaisas S, Stanforth R, Pawlowski N, et al. Enhancing the reliability and accuracy of AI-enabled diagnosis via complementarity-driven deferral to clinicians. *Nat Med* (2023) **14**. doi:10.1038/s41591-023-02437-x

48. Acosta JN, Falcone GJ, Rajpurkar P, Topol EJ. Multimodal biomedical AI. *Nat Med* (2022) **28**:1773–84. doi:10.1038/s41591-022-01981-2

EBM Experimental Biology and Medicine

TYPE Original Research
PUBLISHED 13 December 2024
DOI 10.3389/ebm.2024.10170

Check for updates

OPEN ACCESS

*CORRESPONDENCE
Shaoqing Ju,
jsq814@hotmail.com

†These authors share first authorship

RECEIVED 16 March 2024
ACCEPTED 07 November 2024
PUBLISHED 13 December 2024

CITATION
Yuan J, Gu W, Xu T, Zhang Y, Shen L, Yan J, Guan X, Chu H, Yuan R and Ju S (2024) Dysregulated transfer RNA-derived small RNAs as potential gastric cancer biomarkers.
Exp. Biol. Med. 249:10170.
doi: 10.3389/ebm.2024.10170

Dysregulated transfer RNA-derived small RNAs as potential gastric cancer biomarkers

Jie Yuan[1†], Wenchao Gu[2†], Tianxin Xu[3], Yan Zhang[1], Lei Shen[1], Jianliang Yan[4], Xi Guan[1], Haidan Chu[1], Ruoyu Yuan[1] and Shaoqing Ju[1*]

[1]Department of Laboratory Medicine, Affiliated Hospital of Nantong University, Nantong University, Nantong, China, [2]Department of Special Laboratory Center, Affiliated Hospital of Nantong University, Nantong University, Nantong, China, [3]Department of General Surgery, Affiliated Hospital of Nantong University, Nantong University, Nantong, China, [4]Medical School of Nantong University, Nantong University, Nantong, China

Abstract

Gastric cancer (GC) is the kind of carcinoma that has the highest rates of morbidity and death worldwide. In the early stages of GC, there is currently an absence of sensitive and specific biomarkers. The newly-discovered class of non-coding RNAs (ncRNAs) known as transfer RNA-derived small RNAs (tsRNAs) is highly expressed in bodily fluids and neoplastic cells. High-throughput sequencing was initially employed to identify differentially expressed tsRNAs in early GC patients, followed by validation in patient serum, GC tissues, and cell lines by quantitative real-time polymerase chain reaction (qRT-PCR). We identified dysregulated tsRNAs (the up-regulated tsRNAs included tRF-31-PNR8YP9LON4VD, tRF-30-MIF91SS2P4FI, and tRF-30-IK9NJ4S2I7L7, whereas the down-regulated tsRNAs included tRF-38-W6RM7KYUPRENRHD2, tRF-37-LBRY73W0K5KKOV2, tRF-36-JB59V3WD8YQ84VD, tRF-25-MBQ4NKKQBR, and tRF-36-0KFMNKYUHRF867D) in GC, and we verified that the serum of patients, GC cells and tissues both consistently expressed these tsRNAs. Additionally, GC patients' serum had considerably greater expression levels of the three up-regulated tsRNAs than did healthy controls. Receiver operating characteristic (ROC) curve analysis demonstrated that the sensitivity and specificity of the three up-regulated tsRNAs were superior to those of CEA, CA199, and CA724 in the process of diagnosing GC, particularly in its early stages. This suggests that tsRNAs have great diagnostic efficacy and potential as new "liquid biopsy" biomarkers for the diagnosis of GC. Using bioinformatics software, we predicted that dysregulation of tsRNAs may be a potential regulatory mechanism for the development of GC.

KEYWORDS

tsRNA, gastric cancer, tRF, diagnosis biomarker, ncRNA

Impact statement

Gastric cancer (GC) is a malignancy characterized by a high global death rate and is deficient in sensitive diagnostic markers during its early stages. Recent studies have elucidated several functions of transfer RNA-derived small RNAs (tsRNAs) in many malignancies. The differential expression of tsRNAs in GC tissues and their biological importance were investigated in this study. Initially, we discovered that tsRNAs exhibited differential expression in patients with early gastric cancer by high-throughput sequencing. Moreover, the expression levels of tRF-31-PNR8YP9LON4VD, tRF-30-MIF91SS2P4FI, and tRF-30-IK9NJ4S2I7L7 in the serum of GC patients were significantly elevated compared to healthy controls, suggesting strong diagnostic potential, particularly in the early stages of gastric cancer. tsRNAs are considered to hold significant potential as innovative "liquid biopsy" biomarkers for the detection of GC.

Introduction

Over one million new cases of gastric cancer (GC) are reported each year across the globe, with China being the location of forty percent of these occurrences. GC ranks among the top three malignancies in China in terms of morbidity and mortality [1, 2]. Furthermore, adenocarcinoma is the most common histopathological variant of GC due to the malignant transformation of gastric epithelial cells. Early-stage GC is indiscoverable because of its non-specific clinical symptoms, such as nausea. Upon diagnosis, over 70% of individuals exhibit locally advanced illness [3, 4]. Therefore, improving patient prognosis in GC through early diagnosis and treatment is of great clinical importance. While endoscopic screening is the primary method for early GC detection, early screening depends on the putative GC biomarkers' ability to diagnose the disease. Haematological screening has several advantages, including convenience, cost-effectiveness and non-invasiveness [5]. At present, carcinoembryonic antigen (CEA), carbohydrate antigen 199 (CA199), and carbohydrate antigen 724 (CA724) are commonly used tumor biomarkers, but their specificity and sensitivity are limited [6]. Yu et al [7] showed that CEA had a sensitivity of approximately 13%–35% in diagnosing GC, whereas its specificity was approximately 65% only. Moreover, CA199 had a sensitivity of approximately 40% and specificity of approximately 70%. Consequently, there is an imperative necessity to develop novel clinical indicators for the early identification of GC.

Non-coding RNAs (ncRNAs) are the primary component of the human transcriptome [8]. Numerous research have investigated the involvement of ncRNAs families, including circular RNAs (circRNAs), long non-coding RNAs (lncRNAs), and microRNAs (miRNAs), in cancer formation and progression [9, 10]. Prior research indicated that ncRNAs may serve as biomarkers for diagnosing and prognosticating cancer patients [11]. Transfer RNA (tRNA) is a form of ncRNA that is universally expressed and conserved [12]. tRNA is crucial for maintaining normal homeostasis, cellular stress responses, stem cell formation, carcinogenesis, and the survival of cancer cells, comprising around 10% of total cellular RNA. The initial reports of tRNA-derived compounds originated in the late 1970s, when tRNA fragments were detected in cancer patients [13]. tsRNAs may be classified into two categories according to the cleavage sites of their source tRNA: tRNA-derived fragments (tRFs), which range from 14 to 36 nucleotides, and tRNA halves (tiRNAs), which range from 30 to 40 nucleotides [14, 15].

The importance of tsRNAs in cancer has recently attracted heightened attention due to their potential as innovative biomarkers [16]. Huang et al [17] shown that tDR-7816 expression promotes the growth early-stage breast cancer and was identified as a disease biomarker. Pekarsky et al [18] discovered that in lung cancer and chronic lymphocytic leukemia, ts-4521 and ts-3676 were down-regulated and shown anticancer properties. Shen et al [19] demonstrated that tRF-33-P4R8YP9LON4VDP promoted the proliferation and migration of GC cells while inhibiting cellular apoptosis, whereas Xu et al [20] discovered that tRF-Glu-TTC-027 impeded the progression of GC via modulating the MAPK signaling pathway. Our team's prior research shown that three tsRNAs (tRF-29-RRJ89O9NF5JP, tRF-31-U5YKFN8DYDZDD, and tRF-23-Q99P9P9NDD) shown exceptional stability and specificity for GC patients' dynamic monitoring [21–23].

Building on prior research, we further examined the therapeutic relevance of tsRNAs in GC. This work identified dysregulated tsRNAs using high-throughput sequencing. Through the validation of a significant number of serum and tissue samples, our aim is to identify tsRNAs that have biomarker roles. Furthermore, the specific mechanism of these tsRNAs in GC will be investigated in future experiments.

Materials and methods

Serum and tissue samples from clinical patients

This investigation followed the ethical standards set forth by the World Medical Association throughout the sample collection period from January 2021 to February 2024. Blood samples were collected from 60 patients diagnosed with primary hepatocellular cancer and 60 medical examiners at Affiliated Hospital of Nantong University. Three milliliters of blood were collected from each participant through venipuncture, and serum was isolated via centrifugation. Additionally, 36 pairs of GC tissues and the non-cancerous tissues that surrounded them were taken from our hospital's operating room. All of the aforementioned patients received a pathology-confirmed diagnosis, gave their informed permission in accordance with ethical standards. Ethics committee approval was secured from the Affiliated Hospital of Nantong University (ethics review report number: 2018-L055).

High-throughput sequencing

Total RNA isolation was performed with Trizol, followed by assessment of RNA quality and quantity. The Multi-sample library preparation kits was utilized to prepare a small RNA library using 1 μg total RNA from each sample. The library was sequenced, and the clean reads obtained were analyzed in comparison to MINTbase utilizing MINTmap software, leading to the generation of new tsRNA predictions for reads absent in MINTbase. The analysis of changes in tsRNAs across various groups was conducted using EdgeR software.

Quantitative real-time polymerase chain reaction (qRT-PCR)

The qRT-PCR reaction was conducted utilizing a Bio-Rad CFX96 Real-Time PCR Detection System (Bio-Rad Laboratories, Inc., United States). U6 was utilized as an internal control, while RNA extracted from a pooled serum of 10 healthy donors acted as an external control. The sequences of the primers can be found in Supplementary Table S1. The $2^{-\Delta\Delta CT}$ method was used to analyze the data using the formula: $\Delta\Delta Ct = \Delta Ct_{target} (Ct_{target}-Ct_{reference}) - \Delta Ct_{external\ control} (Ct_{external\ control}-Ct_{reference})$ during the reaction.

The amplification products of each tsRNA underwent verification through Sanger sequencing. The purified amplicons underwent sequencing with Applied Biosystems technology. Sequences underwent analysis with the ABI3730XL DNA Analyzer and were compared to tsRNA on a sequence-by-sequence basis.

Cell culture

A set of human GC cell lines (MGC-803, AGS, MKN-45, SGC-7901, BGC-823) along with human gastric mucosal epithelial cell lines (GES-1) was sourced from the Chinese Academy of Sciences (Shanghai, China). All cells were cultured in RPMI 1640 medium (Corning, Manassas, VA, United States) enriched with 10% fetal bovine serum (Gibco, Waltham, MA, United States) and 1% penicillin and streptomycin (HyClone, Logan, UT, United States) under standard conditions of 37°C and 5% CO_2 in a humidified incubator.

Total RNA extraction and RNA reverse transcription

Total RNA was extracted from serum samples of GC patients utilizing a total RNA purification and isolation kit (BioTeke, Wuxi, Jiangsu, China). In contrast, total RNA from tissue and cell samples was obtained using TRIzol reagent (Invitrogen, Carlsbad, CA, United States). The process of reverse transcription of total RNA to cDNA was executed with a revert aid RT reverse transcription kit (Thermo Fisher Scientific, Waltham, MA, United States). This was carried out in a 10 μL reaction volume, incubated at 42°C for 60 min, and subsequently inactivated at 70°C for 5 min. Prior to the reaction, quantification was necessary.

Bioinformatics analysis

The nomenclature and structures of tsRNAs: MINTbase version 2.0,[1] UCSC Genome Browser database,[2] and Transfer RNA Database.[3]

Identification of tsRNAs and Target Genes: Miranda,[4] and Pictar.[5]

Screening for Differentially Expressed Genes: Kyoto Encyclopedia of Genes and Genomes (KEGG),[6] Gene Ontology enrichment analysis[7] and Reactome Pathway Database.[8]

Statistical analysis

The analysis of high-throughput sequencing results was conducted utilizing the R package edgeR, with significance determined at $p < 0.05$ and $|Log_2FC|>2$. The analysis of data was conducted using SPSS Statistics Version 20.0 (IBM SPSS Statistics, Chicago, IL, United States) and GraphPad Prism 9.0 (GraphPad Software, San Jose, California, United States). Prior to conducting the analysis, the normality of the data was evaluated through normality and lognormality tests, which confirmed that all data adhered to a normal distribution. Group differences were assessed through the application of t-tests. The ROC curve and the area under the curve (AUC) were utilized to assess the diagnostic efficacy of tsRNAs in GC. Prior to plotting the ROC curve, binomial logistic

---

[1] https://cm.jefferson.edu/MINTbase/

[2] https://genome.ucsc.edu/

[3] http://trna.bioinf.unileipzig.de/

[4] http://www.microrna.org/

[5] https://pictar.mdc-berlin.de/

[6] https://www.genome.jp/kegg/

[7] https://geneontology.org/docs/go-enrichment-analysis/

[8] https://reactome.org/

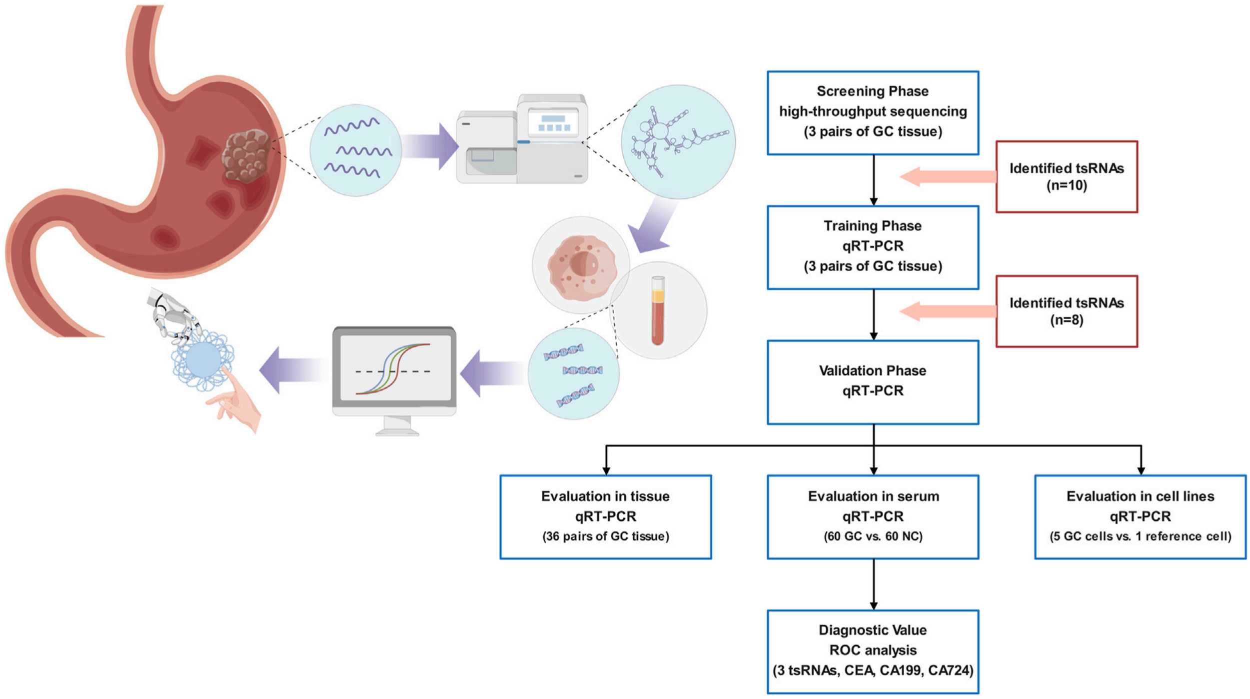

FIGURE 1
An illustration of the research methodology.

regression was conducted. Cox's proportional hazards model was utilized for the multivariate analysis. The risk ratio along with its 95% confidence interval (CI) was documented for each marker. The determination of tsRNA cut-off values utilized the Youden index, whereas the cut-off values for CEA, CA199, and CA724 were established based on the reference range from the Affiliated Hospital of Nantong University, specifically 5 ng/mL, 37 U/mL, and 10 U/mL, respectively. Independent experiments were conducted a minimum of three times, and statistical significance was established when the P-value was less than 0.05.

Results

Expression profiles of tsRNAs in GC and preliminary validation

The deregulation of ncRNA expression is closely associated with the initiation and advancement of cancers. Studies have focused on ncRNAs as potential diagnostic biomarkers because of their tissue specificity and convenient and stable detection in human tissues and body fluids. tsRNAs have been shown to circulate in a very stable, cell-free state inside the serum. The study design is presented in Figure 1. We initially utilized a high-throughput sequencing technique to identify the differentially expressed tsRNAs in GC tissues and adjacent non-cancerous specimens. The identified tsRNAs with $p < 0.05$ and $|Log_2FC| > 2$ were differentially expressed.

Statistical results showed 435 tsRNAs were dysregulated (249 were up-regulated, and 186 were down-regulated). The expression heatmap and volcano plot are presented in Figures 2A, B. Ten candidates were selected from the top five up-regulated and top five down-regulated tsRNAs, based on the average expression level and the uniformity of fluorescence signals within each group (Figure 2C; Supplementary Table S2). To confirm the results of RNA sequencing, we employed the same three pairs of GC tissues for qRT-PCR. The results demonstrated that eight tsRNAs (the up-regulated tsRNAs include: tRF-31-PNR8YP9LON4VD, tRF-30-MIF91SS2P4FI, tRF-30-IK9NJ4S2I7L7, and the down-regulated tsRNAs include: tRF-38-W6RM7KYUPRENRHD2, tRF-37-LBRY73W0K5KKOV2, tRF-36-JB59V3WD8YQ84VD, tRF-25-MBQ4NKKQBR, tRF-36-0KFMNKYUHRF867D, tsRNAs named followed version 2.0 of MINTbase) expression levels were consistent with the high-throughput sequencing (Figure 2D).

Expression of tsRNAs in GC tissues and cell lines

The structure and cleavage site of the eight tsRNAs were visualized in Figure 3A. To further validate the eight tsRNAs

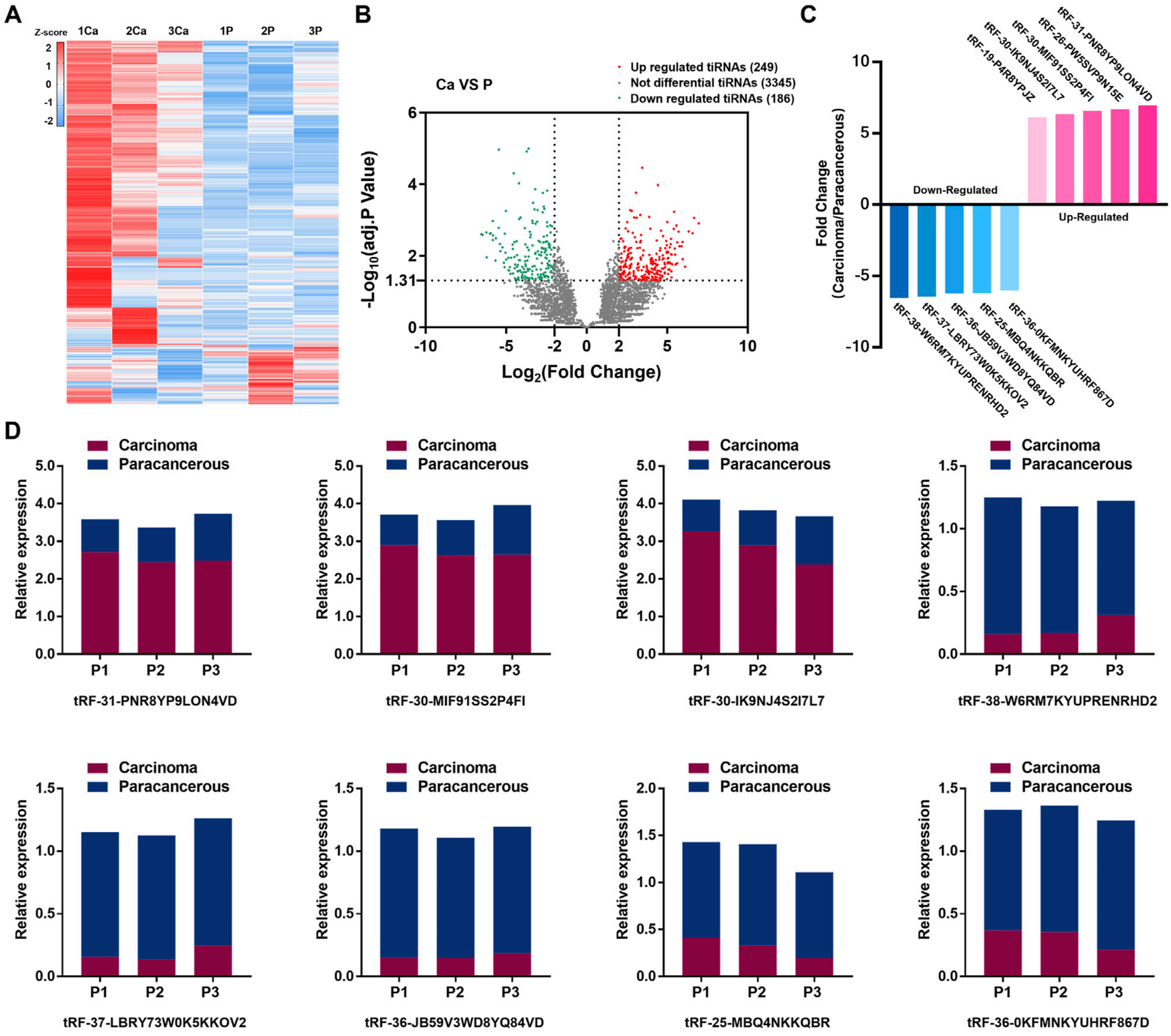

FIGURE 2
Expression profiles of tsRNAs in GC and preliminary validation. **(A)** High-throughput sequencing performed on three pairs of TNM I/II stage GC tissues and adjacent nontumor tissue, the expression heatmap of high-throughput sequencing. **(B)** Volcano plot of tsRNAs distribution. **(C)** 10 candidates selected from the top five up-regulated tsRNAs and top five down-regulated tsRNAs. **(D)** qRT-PCR validated 10 candidates and 8 tsRNAs conformed.

expression levels, we obtained 36 pairs of tissue samples from GC patients and assessed the expression levels of the eight tsRNAs. Results showed that the three up-regulated tsRNAs expressed higher levels in carcinomas than paracancerous specimens, and the five down-regulated tsRNAs were lowly expressed (Figure 3B). The results of unpaired comparisons were consistent with the results of paired comparisons within 36 pairs of tissue samples (Figure 3C). Simultaneously, we observed the expression levels of eight tsRNAs across several GC cell lines and discovered that the three up-regulated tsRNAs were markedly elevated in GC cells relative to GES-1 cell line, whereas the five down-regulated tsRNAs exhibited the inverse pattern (Figure 3D). This section assessed the expression of eight tsRNAs in GC tissue samples and cell lines, revealing that these tsRNAs were dysregulated in GC.

Diagnostic efficiency of tsRNAs in serum of GC patients

The collection of peripheral blood samples from patients for testing is the most convenient diagnostic method; hence, we

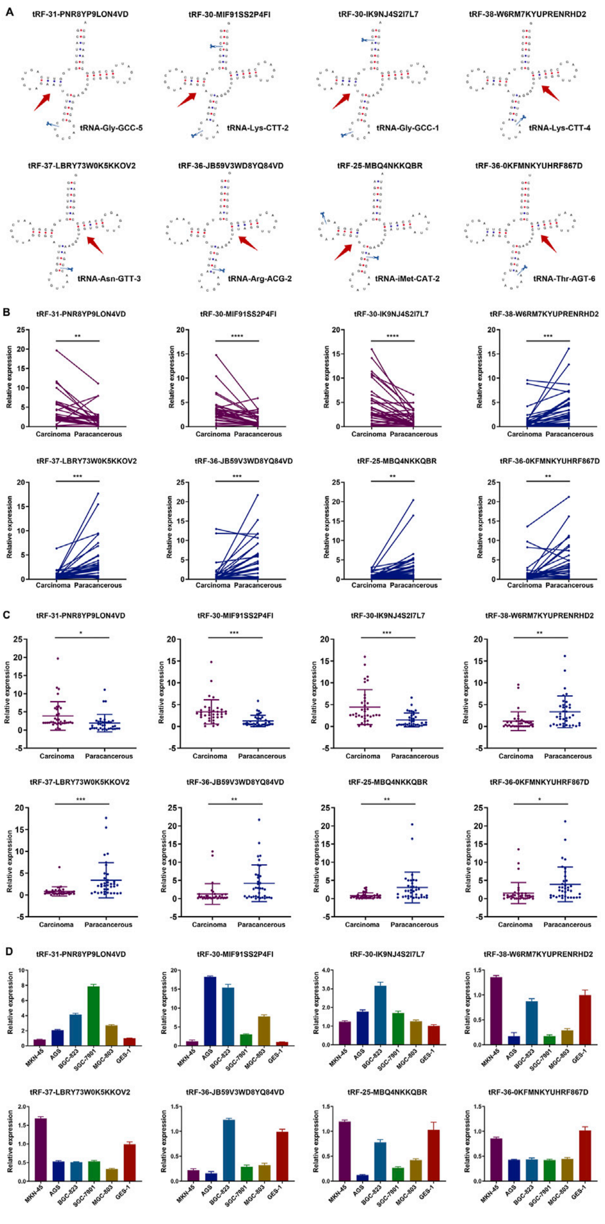

FIGURE 3
Structure of tsRNAs and expression in GC tissues and cell lines. **(A)** The structure and cleavage site of the eight tsRNAs. **(B)** Expression of the eight tsRNAs in 36 pairs of tissue samples from GC patients. Statistics by paired t-tests. **(C)** Expression of the eight tsRNAs in 36 pairs of tissue samples from GC patients. Statistics by unpaired t-tests. **(D)** Expression of the eight tsRNAs in five human GC cell lines (MGC-803, AGS, MKN-45, SGC-7901, BGC-823) and the human gastric epithelial cell line (GES-1). All the values are as mean ± SD. *****P* < 0.0001, ****P* < 0.001, ***P* < 0.01, **P* < 0.05.

sought to determine if these tsRNAs were differentially expressed in the serum of 60 GC patients compared to 60 healthy controls. The serum concentration of tRF-31-PNR8YP9LON4VD, tRF-30-MIF91SS2P4FI, and tRF-30-IK9NJ4S2I7L7 showed a statistically significant increase in GC patients, whereas tRF-

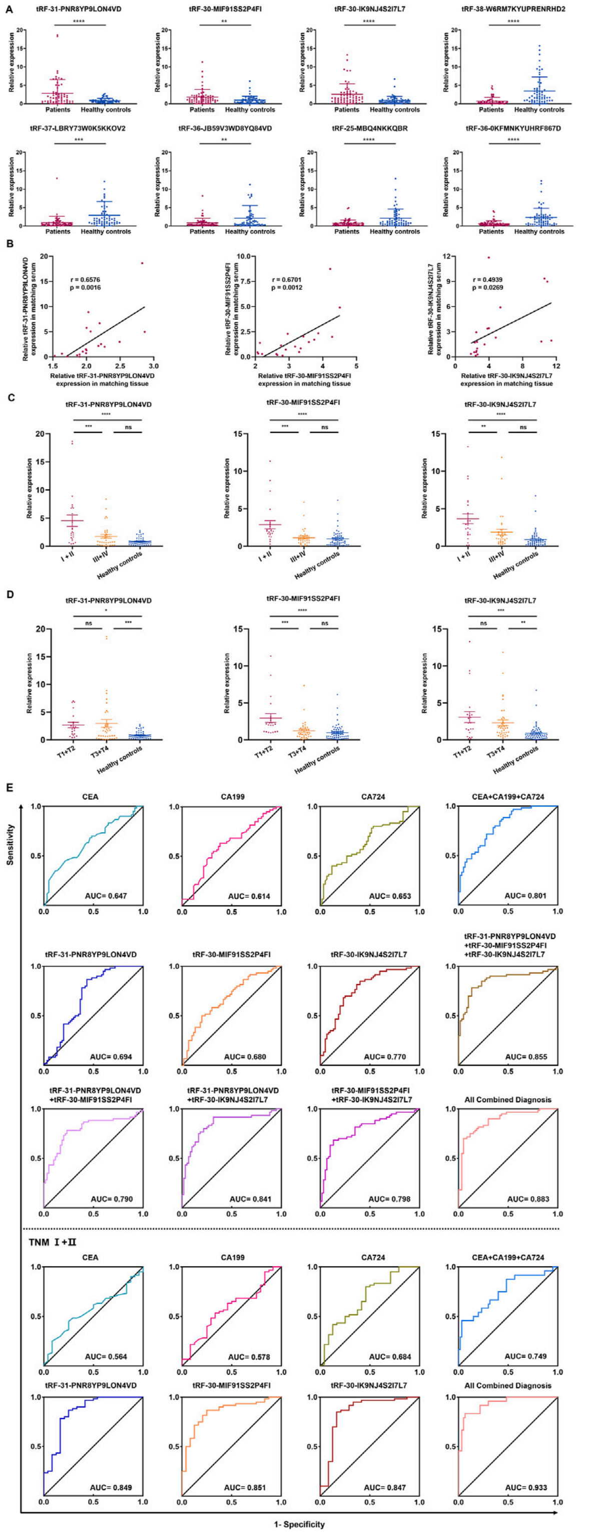

FIGURE 4
Expression and diagnostic efficiency of tsRNAs in serum of GC patients. **(A)** The eight tsRNAs were expressed in 60 GC patient and 60 health evaluation serum samples. **(B)** The expression levels of three up-regulated tsRNAs (tRF-31-PNR8YP9LON4VD,

(*Continued*)

FIGURE 4 (Continued)
tRF-30-MIF91SS2P4FI, and tRF-30-IK9NJ4S2I7L7) were analyzed using Pearson correlation in 20 GC tissues and serum samples from patients with matching diagnoses. **(C)** The expression levels of tRF-31-PNR8YP9LON4VD, tRF-30-MIF91SS2P4FI, and tRF-30-IK9NJ4S2I7L7 in serum of TNM I/II stage GC patients, TNM III/IV stage GC patients, and health examination subjects. **(D)** The expression levels of tRF-31-PNR8YP9LON4VD, tRF-30-MIF91SS2P4FI, and tRF-30-IK9NJ4S2I7L7 in different stages of the depth of tumor invasion and health examination subjects. **(E)** ROC curves for GC diagnosis or TNM I+II stage using serum tRF-31-PNR8YP9LON4VD, tRF-30-MIF91SS2P4FI, tRF-30-IK9NJ4S2I7L7, CEA, CA199, CA724 and combined diagnosis between GC patients and healthy controls. All the values are as mean ± SD. ****$P < 0.0001$, ***$P < 0.001$, **$P < 0.01$, *$P < 0.05$.

38-W6RM7KYUPRENRHD2, tRF-37-LBRY73W0K5KKOV2, tRF-36-JB59V3WD8YQ84VD, tRF-25-MBQ4NKKQBR, and tRF-36-0KFMNKYUHRF867D showed an opposite trend (Figure 4A). The expression levels of tRF-31-PNR8YP9LON4VD, tRF-30-MIF91SS2P4FI, and tRF-30-IK9NJ4S2I7L7 in tissues were correlated with the expression levels in the same patient's serum (Figure 4B).

For each tsRNA group, we split 60 GC patients in half, with 30 patients in the high expression group and 30 in the low expression group, according to the median serum expression of tRF-31-PNR8YP9LON4VD, tRF-30-MIF91SS2P4FI, and tRF-30-IK9NJ4S2I7L7, respectively. Clinicopathological parameters were evaluated the correlations with the three up-regulated tsRNAs expression levels in serum using the χ^2 test. The results demonstrated a strong correlation between gender ($p = 0.0321$), differentiation grade ($p = 0.0062$), and TNM stage ($p = 0.035$) and tRF-31-PNR8YP9LON4VD expression. There was a significant correlation between the expression of tRF-30-MIF91SS2P4FI and age ($p = 0.0242$), TNM stage ($p = <0.0001$), tumor depth ($p = 0.0149$), and lymph node metastasis ($p = 0.0242$). A statistically significant connection ($p = 0.0016$) was found between the expression of tRF-30-IK9NJ4S2I7L7 and TNM stage (Table 1). The elevated expression of tsRNAs may serve as a possible indicator for predicting tumor malignant development. Subsequently, we categorized the substantially varied clinicopathological features into groups to further evaluate the disparities in tsRNA expression levels within each group. The results demonstrated that the expression of three upregulated tsRNAs increased with the early TNM stages (I/II) and T1/T2 tumor depth of gastric cancer (Figures 4C, D).

We further assessed the diagnostic effectiveness of three highly expressed tsRNAs for GC based on their expression levels in patients with GC using ROC analysis. The diagnostic AUC values of tRF-31-PNR8YP9LON4VD, tRF-30-MIF91SS2P4FI, and tRF-30-IK9NJ4S2I7L7 were 0.808 (95% confidence interval, 0.694–0.924), 0.774 (95% CI, 0.657–0.892), and 0.843 (95% CI, 0.747–0.940), respectively (Figure 4E). We compared the diagnostic efficiency of the three up-regulated tsRNAs with GC clinical biomarkers CEA, CA199, and CA724. ROC analysis indicated that the three tsRNAs had better diagnostic efficacy than CEA, CA199, and CA724. AUC increased to 0.956 (95% CI, 0.906–1) when all biomarkers were combined for diagnosis. Additionally, we analysed the diagnostic efficacy of the three tsRNAs in TNM Ⅰ/Ⅱ stage of GC based on the clinicopathological parameters of the patients. We discovered that their diagnostic value increases even further in the early stages of GC. The diagnostic AUC values of tRF-31-PNR8YP9LON4VD, tRF-30-MIF91SS2P4FI, and tRF-30-IK9NJ4S2I7L7 were 0.849, 0.851 and 0.847 (Figure 4E). In contrast, CEA and CA199 have limited diagnostic value (AUC values of 0.564 and 0.578) in the early stages of GC.

Predicted targets and functions of tsRNAs in GC

Consequently, we aimed to further examine and forecast the involvement of these tsRNAs in the advancement of gastric cancer. We predicted downstream target genes of tRF-31-PNR8YP9LON4VD, tRF-30-MIF91SS2P4FI, and tRF-30-IK9NJ4S2I7L7 using miRanda and PicTar databases. The prediction results of the two databases were intersected, and the results showed 1,187 target genes that were most likely bound to tRF-30-IK9NJ4S2I7L7, 445 to tRF-30-MIF91SS2P4FI, and 2,114 to tRF-31-PNR8YP9LON4VD (Figure 5A). Integrating all 3,435 predicted target genes, the KEGG signaling network was shown to be considerably enriched in pathways related to cancer, the MAPK signaling pathway, and the control of the actin cytoskeleton, according to an enrichment analysis (Figure 5B). Gene Ontology functional enrichment study suggested that the up-regulated tsRNAs of GC may play a significant role in histone modification, signal release, and cell growth in biological processes (Figure 5C). The phrase having the highest statistical significance inside a cluster was selected to represent that cluster. The enrichment analysis is depicted in Figure 5D. It is evident that certain genes play a role in multiple functions. Nonetheless, the processes behind tsRNA expression in the control of biological activity in GC cells require additional investigation.

Discussion

GC is among the most aggressive malignancies globally. Notwithstanding advancements in surgical procedures, radiation, and chemotherapy, the incidence and fatality rates of GC persist as the fifth and fourth highest globally, respectively [24]. Early-stage GC frequently presents with vague symptoms, and 80% of patients are discovered at advanced stages, so forfeiting the chance for surgical resection [25]. Currently, there are no biomarkers for GC that fulfill the necessary requirements; thus, efforts are underway to identify novel

TABLE 1 Clinicopathological parameters of gastric cancer patients.

Characteristics	Screening/training phase	Validation phase			tRF-31-PNR8YP9LON4VD			tRF-30-MIF91SS2P4FI			tRF-30-IK9NJ4S2I7L7		
	GC tissue samples (%)	GC tissue samples (%)	NC serum samples (%)	GC serum samples (%)	High	Low	*p* Value	High	Low	*p* Value	High	Low	*p* Value
Number	3	36	60	60	30	30		30	30		30	30	
Gender													
Male	2 (66.7)	23 (63.9)	30 (50.0)	38 (63.3)	23	15	*__0.0321__	21	17	0.2839	21	17	0.2839
Female	1 (33.3)	13 (36.1)	30 (50.0)	22 (36.7)	7	15		9	13		9	13	
Age (Years)													
< 60	1 (33.3)	11 (30.6)	26 (43.3)	18 (30.0)	6	12	0.091	13	5	*__0.0242__	7	11	0.2598
≥ 60	2 (66.7)	25 (69.4)	34 (56.7)	42 (70.0)	24	18		17	25		23	19	
Differentiation grade													
Well-moderate	2 (66.7)	12 (33.3)		20 (33.3)	15	5	**__0.0062__	12	8	0.2733	13	7	0.1003
Poor-undifferentiation	1 (33.3)	24 (66.7)		40 (66.7)	15	25		18	22		17	23	
TNM stage													
I + II	3 (100)	20 (55.6)		24 (40.0)	16	8	*__0.0350__	20	4	****__<0.0001__	18	6	**__0.0016__
III + IV	0 (0)	16 (44.4)		36 (60.0)	14	22		10	26		12	24	
Tumor depth													
T1-T2	3 (100)	16 (44.4)		21 (35.0)	12	9	0.4168	15	6	*__0.0149__	13	8	0.176
T3-T4	0 (0)	20 (55.6)		39 (65.0)	18	21		15	24		17	22	
Lymph node metastasis													
Negative	2 (66.7)	14 (38.9)		18 (30.0)	8	10	0.5731	5	13	*__0.0242__	11	7	0.2598
Positive	1 (33.3)	22 (61.1)		42 (70.0)	22	20		25	17		19	23	
Distant metastasis													
Absence	3 (100)	28 (77.8)		50 (83.3)	26	24	0.4884	23	27	0.1659	26	24	0.4884
Presence	0 (0)	8 (22.2)		10 (16.7)	4	6		7	3		4	6	

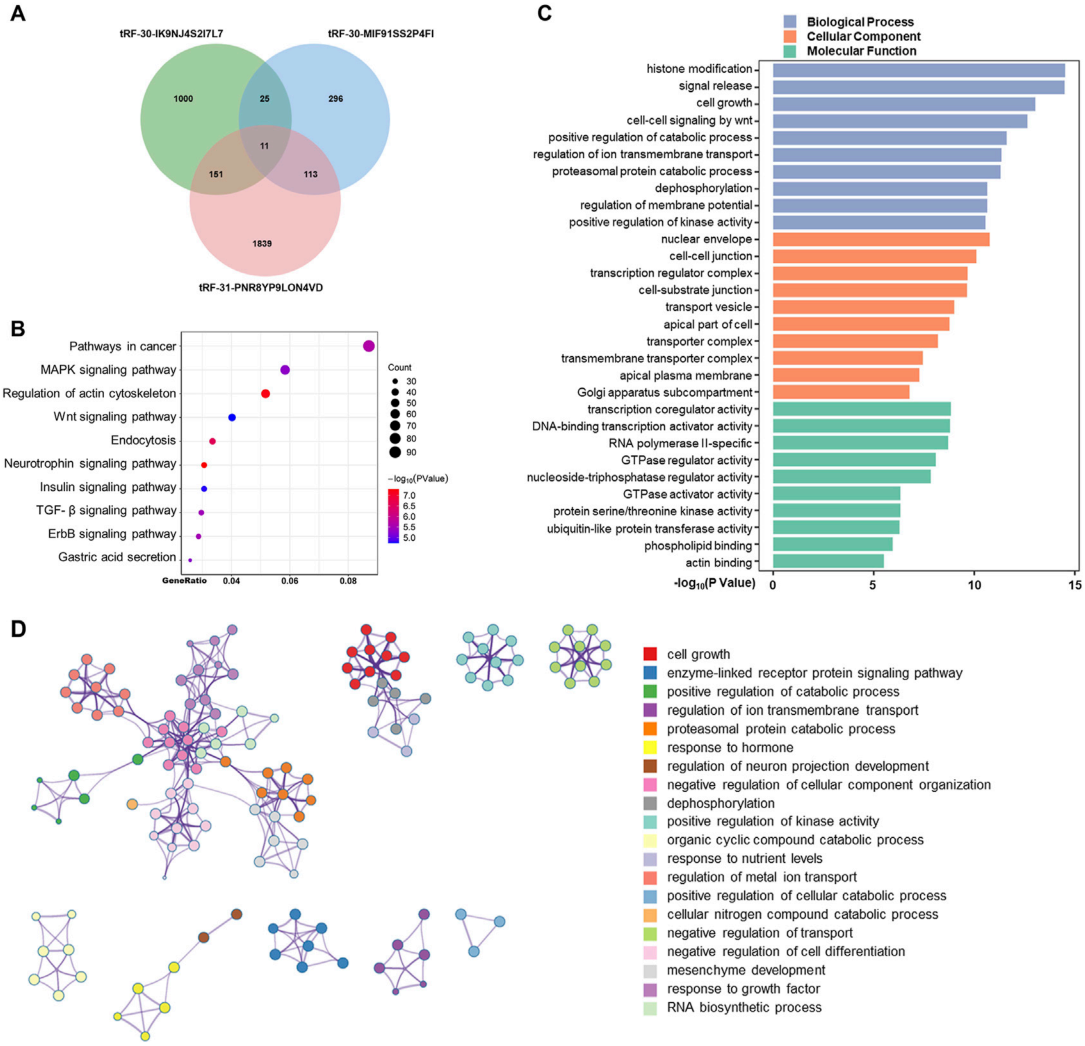

FIGURE 5
Predicted targets and functions of tsRNAs in GC. **(A)** Using miRanda and PicTar databases, predicted downstream target genes of tRF-31-PNR8YP9LON4VD, tRF-30-MIF91SS2P4FI, and tRF-30-IK9NJ4S2I7L Venning diagrams examined the three tsRNAs' target genes' overlap. **(B)** Bubble graphic showing KEGG analysis of pathway-enriched target genes. **(C)** GO analysis of biological processes, cellular components, and molecular functions-enriched target genes. **(D)** Enhanced terminology network. We grouped terms with a p-value < 0.01, a minimum count of 3, and an enrichment factor >1.5 into clusters based on membership similarities. Kappa values of 4 were utilized for hierarchical clustering of enriched phrases, with sub-trees with similarity larger than 0.3 identified as clusters.

biomarkers with enhanced sensitivity and specificity to facilitate early diagnosis of GC [26].

There is mounting evidence from high-throughput sequencing studies linking dysregulated ncRNA expression to tumor formation and progression [11]. ncRNAs were increasingly recognized as a diagnostic tumor marker because of its remarkable tissue specificity and ability to be detected conveniently and robustly in human tissues and body fluids [27–29]. In 1979, tsRNA, a newly discovered family of ncRNA, was first found in patients with cancer, indicating that tsRNAs participate in the gene expression regulation in these patients [13]. Through their interactions with proteins and mRNAs, tsRNAs regulate gene expression, epigenetic changes, and the cell cycle, among other biological processes [30, 31]. A number of studies have identified dysregulated tsRNAs in various tumor types using high-throughput sequencing methods [32–34]. Investigating the particular pathways of dysregulated tsRNAs is crucial for the early detection and treatment of GC.

A total of three sets of tissues were sequenced using high-throughput technology in order to identify tsRNAs that were differently expressed. One set of tissues were from early-stage GC, while the other set came from nearby non-tumor tissues. After that, we used qRT-PCR to confirm in GC tissues and cell lines the top five tsRNAs that were up-regulated and the top five tsRNAs that were down-regulated. Three up-regulated and five down-regulated tsRNAs were consistent with high-throughput sequencing results. Nevertheless, it is expected that down-regulated tsRNAs will be identified in significant quantities in healthy populations due to their probable involvement in cancer development. Nevertheless, we acknowledge the challenge of determining the minimum threshold of the reference value for the down-regulated tsRNAs. Therefore, we intend to concentrate our future investigations on the oncogenic functions of these five tsRNAs in relation to GC. For the present biomarker investigation, our main emphasis was on the three tsRNAs that demonstrated high expression levels.

We collected serum samples from 60 individuals recently diagnosed with GC and 60 healthy controls to determine the expression levels of these tsRNAs in the serum. All three of the up-regulated tsRNAs were highly expressed in GC patients, according to the data.

A large body of research suggests that tsRNAs may serve as biomarkers for GC due to their distinct expression patterns in the blood of people with the disease. Many of these studies examined the expression level of tsRNAs using receiver operating characteristic (ROC) but did not assess the diagnostic effectiveness with widely used diagnostic markers of gastric cancer, such as CEA, CA199, and CA724. In a study conducted by Mao et al. [35], the researchers investigated how well tsRNAs might detect GC in its early stages. The possible advantages for early detection of GC could not be investigated due to the study's tiny sample size. Consequently, we set out to learn more about how well GC may be detected in its early stages. ROC analysis showed that tRF-31-PNR8YP9LON4VD, tRF-30-MIF91SS2P4FI and tRF-30-IK9NJ4S2I7L7 had higher sensitivity and specificity and were superior to the conventional markers (CEA, CA199, and CA724) in the differential diagnosis of GC, particularly in the early stages of the disease. The combination of tRF-31-PNR8YP9LON4VD, tRF-30-MIF91SS2P4FI, and tRF-30-IK9NJ4S2I7L7 with CEA, CA199, and CA724 has enhanced diagnostic efficacy and significant clinical promise.

Similar to microRNAs, tsRNAs have been shown to regulate certain genes or signaling cascades and may act as tumor suppressors or oncogenes. Shen et al [19] observed that tRF-33-P4R8YP9LON4VDP inhibited apoptosis and increased GC cell migration and proliferation, suggesting that this tsRNA represents a viable target for targeted treatment. Xu et al [20] discovered that tRF-Glu-TTC-027 inhibited GC cell growth via regulating the MAPK signaling cascade. In some malignancies, such as breast cancer, the RUNT-related transcription factor can mitigate the effects of ts-112, which cause tumor cells to proliferate at an enhanced pace [36]. In breast cancer, tsRNA-26576 not only promotes tumor cell proliferation but also the invasion and migration [37]. Therefore, we predicted the potential downstream genes regulated by tRF-31-PNR8YP9LON4VD, tRF-30-MIF91SS2P4FI, and tRF-30-IK9NJ4S2I7L7 through miRanda and PicTar databases. There is speculation that GC-enriched tsRNAs may play a role in certain signaling pathways associated with cancer.

Our preliminary study identified three up-regulated and five down-regulated tsRNAs through high-throughput sequencing. Further analysis of the highly expressed tsRNAs revealed a correlation between their serum expression levels and GC TNM stage. ROC curve analysis suggested that these tsRNAs have superior diagnostic value for early-stage GC compared to traditional biomarkers. However, the study has limitations. The samples provided are inadequate, and the clinical use of these biomarkers has not yet been established. Additionally, it is necessary to monitor changes in tsRNA expression levels during disease progression and their potential as prognostic indicators in GC patients. Further investigation into the function of tsRNAs in GC cells and the methods by which they contribute to GC will be carried out in the near future.

Conclusion

Using high-throughput sequencing, we discovered dysregulated tsRNAs in GC tissues. The expression levels of tRF-31-PNR8YP9LON4VD, tRF-30-MIF91SS2P4FI, and tRF-30-IK9NJ4S2I7L7 in the serum of patients with GC were considerably elevated compared to healthy controls, demonstrating substantial diagnostic effectiveness. Therefore, tsRNAs have great potential becoming new "liquid biopsy" biomarkers for the diagnosis of GC. Through bioinformatics software, we predicted that dysregulated tsRNAs have potential regulatory mechanisms for GC development. Our next research will focus on examining the functional role of tsRNAs in GC, and our results lay the theoretical groundwork for that investigation. In conclusion, emerging ncRNAs linked to GC indicate that tsRNAs may serve as biomarkers and predictors of worse prognosis. Dysregulated tsRNAs can be potential therapeutic targets for GC.

Author contributions

WG, XG, and HC collected specimens. LS cultured GC cell lines. RY and JaY extracted total RNA and performed qRT-PCR analysis. YZ and TX analyzed data. JeY wrote the manuscript. The project was conceptualized and funded by SJ. All authors contributed to the article and approved the submitted version.

Data availability

The datasets presented in this study can be found in online repositories. The names of the repository/repositories and accession number(s) can be found in the article/Supplementary Material.

Ethics statement

The studies involving humans were approved by Ethics committee of the Affiliated Hospital of Nantong University. The studies were conducted in accordance with the local legislation and institutional requirements. The participants provided their written informed consent to participate in this study.

Funding

The author(s) declare that financial support was received for the research, authorship, and/or publication of this article. This study was supported by Scientific Research Project of Nantong Municipal Commission of Health and Family Planning (No. QN2023001), Science and Technology to People's Livelihood Program of Nantong (No. MSZ2023207) and National natural science foundation of China (No. 82072363 and No. 82272411).

Conflict of interest

The author(s) declared no potential conflicts of interest with respect to the research, authorship, and/or publication of this article.

Supplementary material

The Supplementary Material for this article can be found online at: https://www.ebm-journal.org/articles/10.3389/ebm.2024.10170/full#supplementary-material

References

1. Ajani JA, D'Amico TA, Bentrem DJ, Chao J, Cooke D, Corvera C, et al. Gastric cancer, version 2.2022, NCCN clinical practice guidelines in oncology. *J Natl Compr Cancer Netw* (2022) **20**:167–92. doi:10.6004/jnccn.2022.0008

2. Smyth EC, Nilsson M, Grabsch HI, van Grieken NC, Lordick F. Gastric cancer. *The Lancet* (2020) **396**:635–48. doi:10.1016/s0140-6736(20)31288-5

3. Joshi SS, Badgwell BD. Current treatment and recent progress in gastric cancer. *CA: A Cancer J Clinicians* (2021) **71**:264–79. doi:10.3322/caac.21657

4. Sexton RE, Al Hallak MN, Diab M, Azmi AS. Gastric cancer: a comprehensive review of current and future treatment strategies. *Cancer Metastasis Rev* (2020) **39**: 1179–203. doi:10.1007/s10555-020-09925-3

5. Matsuoka T, Yashiro M. Biomarkers of gastric cancer: current topics and future perspective. *World J Gastroenterol* (2018) **24**:2818–32. doi:10.3748/wjg.v24.i26.2818

6. Li Y, Yang Y, Lu M, Shen L. Predictive value of serum CEA, CA19-9 and CA72.4 in early diagnosis of recurrence after radical resection of gastric cancer. *Hepatogastroenterology* (2011) **58**:2166–70. doi:10.5754/hge11753

7. Yu J, Zhang S, Zhao B. Differences and correlation of serum CEA, CA19-9 and CA72-4 in gastric cancer. *Mol Clin Oncol* (2016) **4**:441–9. doi:10.3892/mco.2015.712

8. Saw PE, Xu X, Chen J, Song EW. Non-coding RNAs: the new central dogma of cancer biology. *Sci China Life Sci* (2021) **64**:22–50. doi:10.1007/s11427-020-1700-9

9. Yan H, Bu P. Non-coding RNA in cancer. *Essays Biochem* (2021) **65**:625–39. doi:10.1042/ebc20200032

10. Toden S, Zumwalt TJ, Goel A. Non-coding RNAs and potential therapeutic targeting in cancer. *Biochim Biophys Acta (Bba) - Rev Cancer* (2021) **1875**:188491. doi:10.1016/j.bbcan.2020.188491

11. Slack FJ, Chinnaiyan AM. The role of non-coding RNAs in oncology. *Cell* (2019) **179**:1033–55. doi:10.1016/j.cell.2019.10.017

12. Romano G, Veneziano D, Acunzo M, Croce CM. Small non-coding RNA and cancer. *Carcinogenesis* (2017) **38**:485–91. doi:10.1093/carcin/bgx026

13. Speer J, Gehrke CW, Kuo KC, Waalkes TP, Borek E. tRNA breakdown products as markers for cancer. *Cancer* (1979) **44**:2120–3. doi:10.1002/1097-0142(197912)44:6<2120::aid-cncr2820440623>3.0.co;2-6

14. Pekarsky Y, Balatti V, Croce CM. tRNA-derived fragments (tRFs) in cancer. *J Cel Commun Signal* (2023) **17**:47–54. doi:10.1007/s12079-022-00690-2

15. Wang Y, Weng Q, Ge J, Zhang X, Guo J, Ye G. tRNA-derived small RNAs: mechanisms and potential roles in cancers. *Genes and Dis* (2022) **9**:1431–42. doi:10.1016/j.gendis.2021.12.009

16. Xie Y, Zhang S, Yu X, Ye G, Guo J. Transfer RNA-derived fragments as novel biomarkers of the onset and progression of gastric cancer. *Exp Biol Med (Maywood)* (2023) **248**:1095–102. doi:10.1177/15353702231179415

17. Huang Y, Ge H, Zheng M, Cui Y, Fu Z, Wu X, et al. Serum tRNA-derived fragments (tRFs) as potential candidates for diagnosis of nontriple negative breast cancer. *J Cell Physiol* (2020) **235**:2809–24. doi:10.1002/jcp.29185

18. Pekarsky Y, Balatti V, Palamarchuk A, Rizzotto L, Veneziano D, Nigita G, et al. Dysregulation of a family of short noncoding RNAs, tsRNAs, in human cancer. *Proc Natl Acad Sci U S A* (2016) **113**:5071–6. doi:10.1073/pnas.1604266113

19. Shen Y, Yu X, Ruan Y, Li Z, Xie Y, Yan Z, et al. Global profile of tRNA-derived small RNAs in gastric cancer patient plasma and identification of tRF-33-P4R8YP9LON4VDP as a new tumor suppressor. *Int J Med Sci* (2021) **18**: 1570–9. doi:10.7150/ijms.53220

20. Xu W, Zhou B, Wang J, Tang L, Hu Q, Wang J, et al. tRNA-derived fragment tRF-glu-TTC-027 regulates the progression of gastric carcinoma via MAPK signaling pathway. *Front Oncol* (2021) **11**:733763. doi:10.3389/fonc.2021.733763

21. Zhang Y, Gu X, Qin X, Huang Y, Ju S. Evaluation of serum tRF-23-Q99P9P9NDD as a potential biomarker for the clinical diagnosis of gastric cancer. *Mol Med* (2022) **28**:63. doi:10.1186/s10020-022-00491-8

22. Huang Y, Zhang H, Gu X, Qin S, Zheng M, Shi X, et al. Elucidating the role of serum tRF-31-U5YKFN8DYDZDD as a novel diagnostic biomarker in gastric cancer (GC). *Front Oncol* (2021) **11**:723753. doi:10.3389/fonc.2021.723753

23. Gu X, Ma S, Liang B, Ju S. Serum hsa_tsr016141 as a kind of tRNA-derived fragments is a novel biomarker in gastric cancer. *Front Oncol* (2021) **11**:679366. doi:10.3389/fonc.2021.679366

24. Sung H, Ferlay J, Siegel RL, Laversanne M, Soerjomataram I, Jemal A, et al. Global cancer Statistics 2020: GLOBOCAN estimates of incidence and mortality worldwide for 36 cancers in 185 countries. *CA: A Cancer J Clinicians* (2021) **71**: 209–49. doi:10.3322/caac.21660

25. Pasechnikov V, Chukov S, Fedorov E, Kikuste I, Leja M. Gastric cancer: prevention, screening and early diagnosis. *World J Gastroenterol* (2014) **20**: 13842–62. doi:10.3748/wjg.v20.i38.13842

26. Wu D, Zhang P, Ma J, Xu J, Yang L, Xu W, et al. Serum biomarker panels for the diagnosis of gastric cancer. *Cancer Med* (2019) **8**:1576–83. doi:10.1002/cam4.2055

27. Yuan J, Su Z, Gu W, Shen X, Zhao Q, Shi L, et al. MiR-19b and miR-20a suppress apoptosis, promote proliferation and induce tumorigenicity of multiple myeloma cells by targeting PTEN. *Cancer Biomarkers* (2019) **24**:279–89. doi:10.3233/cbm-182182

28. Tang XH, Guo T, Gao XY, Wu XL, Xing XF, Ji JF, et al. Exosome-derived noncoding RNAs in gastric cancer: functions and clinical applications. *Mol Cancer* (2021) **20**:99. doi:10.1186/s12943-021-01396-6

29. Beilerli A, Gareev I, Beylerli O, Yang G, Pavlov V, Aliev G, et al. Circular RNAs as biomarkers and therapeutic targets in cancer. *Semin Cancer Biol* (2022) **83**: 242–52. doi:10.1016/j.semcancer.2020.12.026

30. Balatti V, Nigita G, Veneziano D, Drusco A, Stein GS, Messier TL, et al. tsRNA signatures in cancer. *Proc Natl Acad Sci U S A* (2017) **114**:8071–6. doi:10.1073/pnas.1706908114

31. Park J, Ahn SH, Shin MG, Kim HK, Chang S. tRNA-derived small RNAs: novel epigenetic regulators. *Cancers (Basel)* (2020) **12**:2773. doi:10.3390/cancers12102773

32. Li YK, Yan LR, Wang A, Jiang LY, Xu Q, Wang BG. RNA-sequencing reveals the expression profiles of tsRNAs and their potential carcinogenic role in cholangiocarcinoma. *J Clin Lab Anal* (2022) **36**:e24694. doi:10.1002/jcla.24694

33. Tu M, Zuo Z, Chen C, Zhang X, Wang S, Chen C, et al. Transfer RNA-derived small RNAs (tsRNAs) sequencing revealed a differential expression landscape of tsRNAs between glioblastoma and low-grade glioma. *Gene* (2023) **855**:147114. doi:10.1016/j.gene.2022.147114

34. Fu BF, Xu CY. Transfer RNA-derived small RNAs: novel regulators and biomarkers of cancers. *Front Oncol* (2022) **12**:843598. doi:10.3389/fonc.2022.843598

35. Mao C, Zhang Z, Fang R, Yuan W, Wu Y, Cong H. A novel tRNA-derived fragment tRF-17-18VBY9M works as a potential diagnostic biomarker for gastric cancer. *J Cancer Res Clin Oncol* (2024) **150**:263. doi:10.1007/s00432-024-05792-5

36. Farina NH, Scalia S, Adams CE, Hong D, Fritz AJ, Messier TL, et al. Identification of tRNA-derived small RNA (tsRNA) responsive to the tumor suppressor, RUNX1, in breast cancer. *J Cell Physiol* (2020) **235**:5318–27. doi:10.1002/jcp.29419

37. Zhou J, Wan F, Wang Y, Long J, Zhu X. Small RNA sequencing reveals a novel tsRNA-26576 mediating tumorigenesis of breast cancer. *Cancer Manage Res* (2019) **11**:3945–56. doi:10.2147/cmar.s199281

EBM Experimental Biology and Medicine

TYPE Original Research
PUBLISHED 13 December 2024
DOI 10.3389/ebm.2024.10280

Berberine alleviates AGEs-induced ferroptosis by activating NRF2 in the skin of diabetic mice

Chunjie Jiang[1†], Guojuan Lao[2†], Jianmin Ran[1,3] and Ping Zhu[1,3]*

[1]Institute of Disease-Oriented Nutritional Research, Guangzhou Red Cross Hospital, Jinan University, Guangzhou, China, [2]Department of Endocrinology and Metabolism, Sun Yat-sen Memorial Hospital, Sun Yat-sen University, Guangzhou, China, [3]Department of Endocrinology and Metabolism, Guangzhou Red Cross Hospital, Jinan University, Guangzhou, China

Abstract

Advanced glycation end products (AGEs) have adverse effects on the development of diabetic complications. Berberine (BBR), a natural alkaloid, has demonstrated its ability to promote the delayed healing of skin wounds. However, the impact of BBR on AGEs-induced ferroptosis in skin cells and the underlying molecular mechanisms remains unexplored. This study investigated the involvement of ferroptosis in AGEs-induced keratinocyte death, and the impact of BBR on ferroptosis in a db/db mouse model with long-term hyperglycemia was elucidated. A remarkable reduction in cell viability was observed along with increased malondialdehyde (MDA) production in AGEs-induced HaCaT cells. Intracellular reactive oxygen species (ROS) and iron levels were elevated in cells exposed to AGEs. Meanwhile, the protein expression of glutathione peroxidase 4 (GPX4) and ferritin light chain (FTL) was significantly decreased in AGEs-treated cells. However, pretreatment with BBR markedly protected cell viability and inhibited MDA levels, attenuating the intracellular ROS and iron levels and increased expression of GPX4 and FTL *in vitro*. Significantly diminished antiferroptotic effects of BBR on AGEs-treated keratinocytes were observed upon the knockdown of the nuclear factor E2−related factor 2 (*NRF2*) gene. *In vivo*, GPX4, FTL, and FTH expression in the epidermis of diabetic mice was significantly reduced, accompanied by enhanced lipid peroxidation. Treatment with BBR effectively rescued lipid peroxidation accumulation and upregulated GPX4, FTL, FTH, and NRF2 levels in diabetic skin. Collectively, the findings indicate that ferroptosis may play a significant role in AGEs-induced keratinocyte death. BBR protects diabetic keratinocytes against ferroptosis, partly by activating NRF2.

KEYWORDS

advanced glycation end productions, ferroptosis, berberine, keratinocytes, NRF2

OPEN ACCESS

*CORRESPONDENCE
Ping Zhu,
✉ pingzhu@ext.jnu.edu.cn

†These authors have contributed equally to this work

RECEIVED 08 June 2024
ACCEPTED 07 November 2024
PUBLISHED 13 December 2024

CITATION
Jiang C, Lao G, Ran J and Zhu P (2024) Berberine alleviates AGEs-induced ferroptosis by activating NRF2 in the skin of diabetic mice.
Exp. Biol. Med. 249:10280.
doi: 10.3389/ebm.2024.10280

Impact statement

This study investigated the potential role of ferroptosis in AGEs-induced keratinocyte death and elucidated the impact of berberine on ferroptosis in diabetic skin tissue. We found that exposure to AGEs triggers pronounced oxidative stress and iron overload in keratinocytes, resulting in lipid peroxidation and ferroptosis. Additionally, we identified a novel cytoprotective role of berberine beyond its conventional antidiabetic effects, as it effectively inhibited ferroptosis by upregulating NRF2 activity. Moreover, we also demonstrated a substantial reduction in GPX4, FTL, and FTH expression levels within the epidermis of db/db diabetic mice, along with enhanced lipid peroxidation. Treatment with berberine ameliorated lipid peroxidation accumulation and upregulated GPX4, FTL, FTH, and NRF2 levels in diabetic skin tissues. Overall, we believe that our study makes a significant contribution to the existing literature by shedding light on the involvement of ferroptosis in mediating the protective effects of berberine against hidden damage in diabetic skin.

Introduction

The increasing global prevalence of diabetes is estimated to reach 1.31 billion by 2050, leading to significant socioeconomic burdens [1]. Approximately 18.6 million people worldwide suffer from diabetic foot ulcers yearly [2]. However, the exact mechanisms underlying the pathogenesis of this dysfunction remain inadequately comprehended.

With the onset of diabetes, elevated systemic glucose levels contribute to the formation of advanced glycation end-products (AGEs), which undergo accumulation within the extracellular matrix of the skin [3]. Apoptotic cell death has been recognized as a significant mechanism underlying AGEs-induced cytotoxicity in impaired wound healing [4, 5]. However, the potential contribution of non-apoptotic modes of regulated cell death to developing chronic non-healing wounds remains largely unexplored.

Ferroptosis, a regulated form of cell death, has garnered significant attention in various diseases including cancer [6], degenerative disease [7], and cardiovascular disease [8]. Oxidative stress holds a crucial position in the pathophysiology of diabetes. Increasing evidence has demonstrated that iron overload elevates the likelihood of developing insulin resistance and diabetes progression and exacerbates diabetes complications. This occurs due to the Fenton reaction among individuals with diabetes [9, 10]. Furthermore, in a diabetic model, the local application of ferrostatin-1 (Fer-1) to the wound site reduced the expression of oxidative stress and inflammation markers, leading to accelerated wound healing [11]. Based on this premise, it was hypothesized that ferroptosis might be implicated in the onset of diabetic foot ulcers. Therefore, the present research aimed to elucidate the role of ferroptosis in the mechanisms underlying AGEs-induced regulated cell death.

Berberine (BBR), a natural plant alkaloid, exerts diverse pharmacological effects and can modulate inflammation, oxidative stress, and glucolipid homeostasis [12]. Recent studies have highlighted the remarkable anti-hyperglycemic effects of BBR in type 2 diabetes mellitus. These effects were achieved by enhancing insulin sensitivity and insulin secretion through the upregulation of insulin receptor expression [13, 14]. Moreover, evidence suggests that BBR acts as an effective endogenous antioxidant, promoting the activity of antioxidant enzymes and suppressing the generation of reactive oxygen species (ROS) [15, 16]. Notably, BBR has demonstrated the ability to stimulate cell proliferation, downregulate matrix metalloproteinases-9 expression, and upregulate transforming growth factor-β1 levels. These effects collectively contribute to the accelerated healing of diabetic wounds [17]. However, the involvement of ferroptosis in BBR-mediated alleviation of chronic diabetic wound healing and the specific underlying mechanism remain unknown and require further examination. In addition, in diabetic mouse models, the pharmacological activation of nuclear factor E2-related factor 2 (NRF2) demonstrated reduced oxidative stress and enhanced faster wound healing [18]. However, the exact mechanism *via* which the NRF2 pathway modulates ferroptosis in the presence of BBR has not been entirely elucidated.

The primary goal of the research was to evaluate the involvement of ferroptosis in AGEs-induced keratinocyte death and assess the protective effect of BBR against ferroptosis *in vitro* and *in vivo*. Additionally, the study aimed to scrutinize the involvement of NRF2 in BBR-mediated protection against ferroptosis. The present research findings demonstrated that ferroptosis involves AGE-induced cell death and that BBR protects keratinocytes against AGE-induced cellular damage. This protection effect was achieved partially through the activation of NRF2, thereby inhibiting the onset of ferroptosis.

Materials and methods

Study approval and mouse treatment

Eight-week-old male type 2 diabetic mice (db/db, weighting 40–46g) and age-matched wild-type mice (WT, weighting 22–23g) were obtained from GemPharmatech, Co., Ltd. (T002407; Nanjing, China). The mice were housed in a temperature-controlled room with a 12-hour alternating light/dark cycle and acclimatized for 1 week. Subsequently, eighteen mice were divided into three groups (n = 6): normal mouse group (WT), diabetic mouse group (db/db), and db/db + BBR group (gavage once a day, BBR 100 mg/kg/dose). The WT and db/db groups received daily intragastric administration of 0.5% sodium carboxymethyl cellulose (Na-CMC; Solarbio, Beijing, China) for 5 weeks. Blood glucose levels and body weight were monitored every week throughout the study period. At the end of the experiment, all mice were euthanized by exposure to 100% carbon dioxide gas for 5 min after isoflurane anesthesia induction. The skin from the back was collected for follow-up experiments.

The experimental procedures were conducted in accordance with the Guide for the Care and Use of Laboratory Animals of the National Institutes of Health, as well as the Animal Welfare Act guidelines. The experiment protocols received approval from the Institutional Animal Care and Use Committee of TOP Biotechnology (LFTOP-IACUC-2023-0020).

Cell culture

The human keratinocyte cell line HaCaT was a gift from Prof. Xiaoping Wu (Jinan University, Guangzhou, China). The cell line was cultured at 37°C in Dulbecco's modified Eagle's medium (Corning, VA, United States) supplemented with 10% fetal bovine serum (Gibco-BRL, CA, United States) and 100 U/mL penicillin-streptomycin. Two hours before stimulation with 150 μg/mL of glycolaldehyde-modified AGE-BSA (Cayman Chemical, MI, United States) for 48 h, the cells were subjected to pretreatment with various compounds. These compounds included ferroptosis inhibitor ferrostatin-1 (Fer-1; 1 μM; HY-100579), Z-VAD-FMK (VAD; 10 μM; HY-16658B), and necrosulfonamide (NSA; 30 μM; HY-100573) or the ferroptosis inducer erastin (10 μM; HY-15763; all MedChemExpress, Shanghai, China). Fer-1, VAD, NSA, erastin, and BBR (HY-18258, MedChemExpress) were dissolved in DMSO (Sigma–Aldrich, MO, United States), and 0.1% DMSO was utilized as a vehicle control.

Cell viability assay

During the logarithmic growth phase, HaCaT cells were seeded into 96-well plates at a density of 3×10^3 cells per well. After 24 h of incubation in a normal culture medium, the specified chemicals were administered to the cells. After 48 h, 10 μL of cell counting kit-8 solution (CCK-8; Dojindo, Kumamoto, Japan) was introduced to each well, and the samples were incubated at 37°C for one or 2 h. Subsequently, cell viability percentages were calculated at each designated time point.

Evaluation of intracellular ROS

HaCaT cells were seeded in 6-well plates. The cells underwent pretreatment with Fer-1 (1 μM) or BBR (5 μM) for 2 h, followed by incubation with 150 μg/mL AGEs for 48 h. Afterward, the cells were thoroughly washed thrice with PBS buffer. Then, 10 μM 2′,7′-dichlorofluorescin diacetate (DCFH-DA, S0033M, Beyotime, Shanghai, China), a redox-sensitive fluorescent dye, was introduced into serum-free DMEM. The cells were then incubated at 37°C for 30 min in a dark environment. After washing the cells thrice with PBS buffer, they were mounted using an anti-fading mounting medium and subjected to analysis under a fluorescence microscope (Nikon Corporation, Tokyo, Japan) at excitation wavelengths of 488 nm. The intracellular ROS levels were measured utilizing ImageJ software (NIH, Bethesda, MD).

Assessment of total iron levels

The intracellular total iron levels were assessed using an iron colorimetric assay kit (E-BC-K880-M; Elabscience, Wuhan, China) following the prescribed protocol from the manufacturer. In brief, HaCaT cells (1×10^6) were first rinsed with ice-cold PBS and then homogenized by sonication in 200 μL of iron assay buffer at the appropriate times. The supernatants were then obtained after centrifugation at 15,000 × g for 10 min. Subsequently, 80 μL of the supernatant was introduced into a 96-well plate. Afterward, 80 μL of the chromogenic solution was introduced into each well and incubated for 40 min at 37°C in the darkness. Finally, the absorbance was measured at 593 nm utilizing a microplate reader.

Measurement of malondialdehyde (MDA)

HaCaT cells were treated with Fer-1 or BBR for 2 h and then cultured with 150 μg/mL AGEs for 48 h. MDA levels in cell lysates and mouse skin tissue were assessed by means of a colorimetric MDA assay, following the provided instructions from the manufacturer (BC0025; Solarbio Life Sciences, Beijing, China).

NRF2 siRNA transfection

NRF2 siRNA knockdown assays were carried out utilizing Lipofectamine RNAiMAX Transfection Reagent (Thermo Fisher Scientific, CA, United States), following the guidelines provided by the manufacturer. The cells were transfected with 50 nM commercial siRNA (sc-37030; Santa Cruz, CA, United States) against NRF2 (NRF2 siRNA), control siRNA (Con siRNA) or transfection reagents alone (mock transfection). HaCaT cells were seeded into 6-well plates at a density of 2×10^5 per well and incubated at 37°C until they reached 70% confluence. Subsequently, 150 pmol siRNA was diluted in 250 μL of Opti-MEM serum-free media, and 7.5 μL of Lipofectamine RNAiMAX was diluted in 250 μL of Opti-MEM. Then, these diluted mixtures of siRNA and RNAiMAX were gently mixed and incubated at room temperature for 20 min. After incubation, this mixture was transferred into 6-well plates with 2.5 mL of Opti-MEM serum-free media.

Western blot analysis

The cells, treated as previously mentioned, were collected and subjected to lysis using either RIPA lysis buffer or NE-PER nuclear extraction reagents (Thermo Fisher Scientific) with protease inhibitors (Beyotime). Following lysis, the cell lysates were separated utilizing SDS-polyacrylamide gel electrophoresis (PAGE) and transferred to polyvinylidene difluoride (PVDF) membranes (Millipore, MA, United States). After blocking for 1 h at room temperature, the membranes underwent an overnight incubation with primary antibodies against the following proteins: glutathione peroxidase 4 (GPX4; 1:1000; 67763-1-Ig; Proteintech, Wuhan, China), ferritin light chain (FTL; 1:1000; 10727-1-AP; Proteintech), NRF2 (1:800; 12721; Cell Signaling Technology, Danvers, United States), α-tubulin (1: 20,000; HRP-66031; Proteintech), or lamin B1 (1:10,000; 12987-1-AP; Proteintech). Following primary antibody incubation, the membranes were exposed to the corresponding secondary antibodies and incubated for 1 h. The protein bands were developed using an enhanced chemiluminescence reagent (Millipore). Subsequently, these bands were visualized and quantified with the assistance of ImageJ software.

Immunohistochemical (IHC) and immunofluorescence analysis

The skin tissue sections were washed with PBS and blocked with 10% goat serum at 25°C for 30 min after deparaffinization, rehydration. Antigen retrieval was performed by submerging the slides in EDTA (pH 8.0), and reacting at 95°C for 10 min. Immunohistochemical staining was performed by incubating primary antibodies for GPX4 (1:100; 67763-1-Ig; Proteintech), FTL (1:900; 10727-1-AP; Proteintech), ferritin heavy chain (FTH; 1:100; DF6278; Affinity Biosciences), and 4-Hydroxynonenal (4-HNE; 1:900; bs-6313R; Bioss, Beijing, China) overnight at 4°C. Then, the targeted protein was detected using a secondary antibody at 37°C for 1 h, followed by incubating with horseradish peroxidase (HRP)-DAB reagents (DAB4033; Maxim, Fuzhou, China) and counterstaining with hematoxylin. The images were randomly taken by a NanoZoomer S360 slide scanner (Hamamatsu). Five high-power field images were captured for each section, with a total of 100 cells counted in each image. The immunoreactive reactivity score (IRS) was calculated according to previously reported criteria [19]. Briefly, the IRS is calculated by multiplying the percentage of stained cells (0 = 0% stained cells, 1 = 1%–10%, 2 = 11%–50%, 3 = 51%–80%, 4 = 81%–100%) with the staining intensity (0 = no staining, 1 = weak, 2 = moderate, 3 = strong). The HaCaT cells were initially fixed with 4% paraformaldehyde for 15 min and then permeabilized with 0.2% Triton X-100 at room temperature. Then, the cells were blocked with 10% goat serum for 60 min following an overnight incubation at 4°C with NRF2 primary antibodies (1:400; 12721; Cell Signaling Technology). Subsequently, the cells were washed with PBS and incubated with FITC-conjugated secondary antibodies (P0186; Beyotime) at room temperature for 1 h. To visualize the cell nuclei, DAPI staining was applied. Images were then captured utilizing a fluorescence microscope.

Hematoxylin-eosin (HE) and Masson's trichrome staining

The skin tissues were fixed in 4% paraformaldehyde, paraffin-embedded and cut into 4 μm thick slices. The sections underwent deparaffinization using xylene followed by rehydration through a series of graded alcohol solutions. Masson's trichrome staining was conducted following the manufacturer's protocol to evaluate the collagen deposition (BP028; Biossci, Wuhan, China).

Statistical analysis

The data were expressed as the means ± standard deviation (SD). All experiments were repeated at least three times. Student's t-test was employed for comparisons between two distinct groups, while one-way analysis of variance (ANOVA) was utilized for multiple comparisons. A two-tailed *P*-value of less than 0.05 indicated the statistical significance. Moreover, statistical analysis was carried out using Prism 9.0 software (GraphPad, CA, United States).

Results

AGEs induced ferroptosis in HaCaT cells

AGEs are pivotal pathogenic factors in diabetic skin. Recent studies have highlighted the capacity of AGEs to induce ferroptosis in cardiomyocytes [20]. Therefore, to investigate the impact of AGEs in ferroptosis in HaCaT cells, these cells were treated with AGEs, and a dose- and time-dependent decrease in cell viability was observed (Figure 1A). After 48 h of exposure to 150 μg/mL AGEs, cell viability was reduced by 25%. Furthermore, HaCaT cells were pretreated with several cell death inhibitors for 2 h before being incubated for 48 h with AGEs (150 μg/mL). Moreover, cell viability assays revealed that

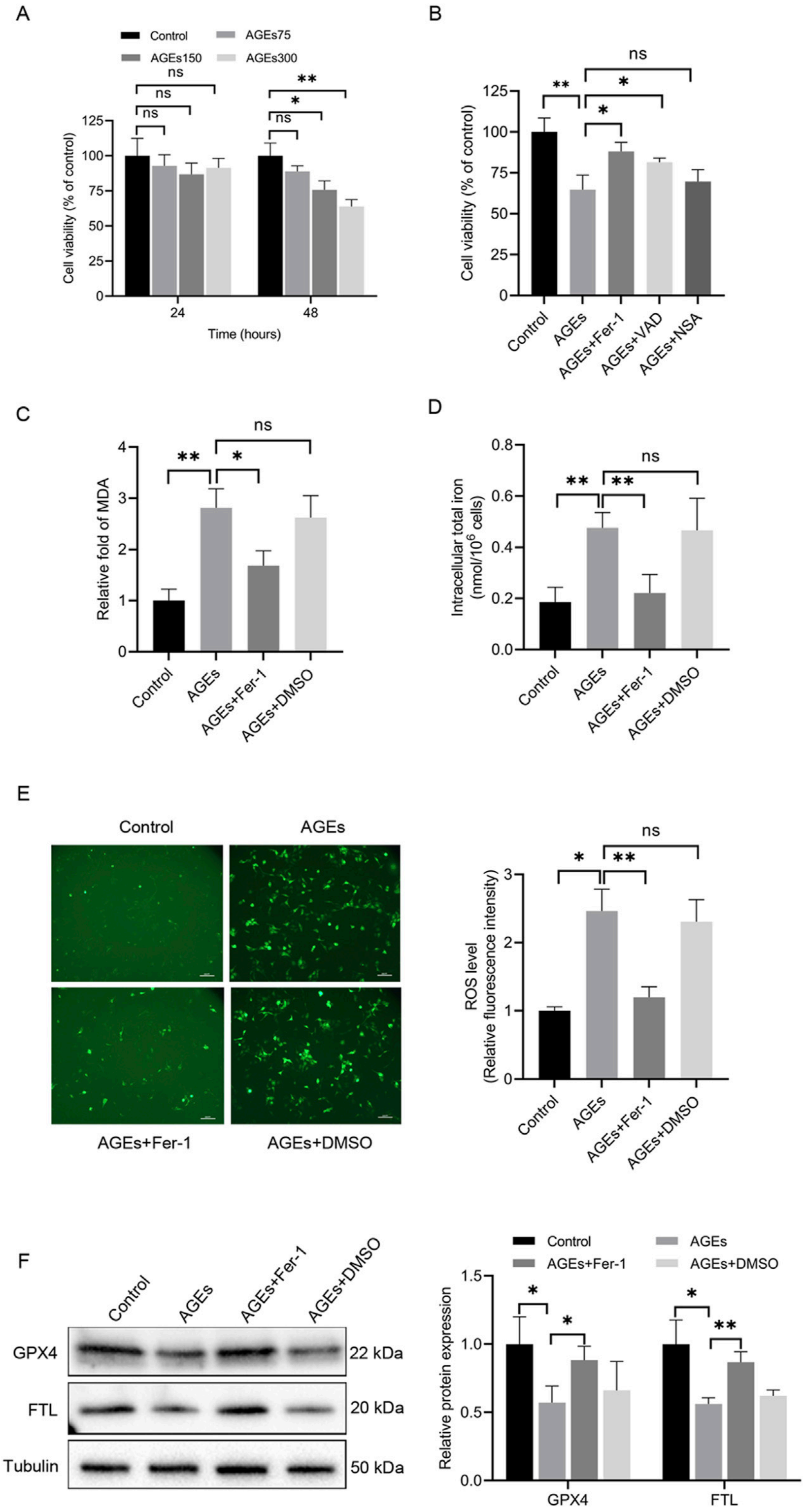

FIGURE 1
AGEs induced alterations in cell activity and key ferroptosis-associated molecules in HaCaT cells. **(A)** HaCaT cells were exposed to various concentrations of AGEs for the indicated times, and CCK-8 assays determined cell viability. **(B)** HaCaT cells were treated with different inhibitors of cell death pathways (Fer-1, 1 μM; VAD, 10 μM; NSA, 30 μM) for 2 h, followed by the addition of AGEs (150 μg/mL) for 48 h. CCK-8 assays determined cell viability. **(C)** After pretreatment with the ferroptosis inhibitor Fer-1 (1 μM) for 2 h, the HaCaT cells were treated with AGEs (150 μg/mL) for

(Continued)

FIGURE 1 (Continued)
48 h to determine lipid peroxidation (MDA). **(D)** Intracellular iron levels were examined in HaCaT cells. **(E)** Representative images and quantitative analysis of intracellular ROS levels using DCFH-DA in HaCaT cells. **(F)** The protein levels of GPX4 and FTL in HaCaT cells were detected by Western blot analysis. The results are expressed as the mean ± SD. Data are representative of three independent experiments. Scale bar, 100 μm. $^{*}P \le 0.05$, $^{**}P \le 0.01$. AGEs, advanced glycation end products; DCFH-DA, 2′, 7′-dichlorofluorescin diacetate; Fer-1, ferrostatin-1; FTL, ferritin light chain; GPX4, glutathione peroxidase 4; MDA, malondialdehyde; ns, no significance; NSA, necrosulfonamide; VAD, Z-VAD-FMK.

Fer-1 and the apoptosis pan-caspase inhibitor VAD partially attenuated AGEs-induced cell death, whereas the necrosis inhibitor NSA had no significant effect (Figure 1B).

Lipid peroxidation and iron levels were evaluated in HaCaT cells to assess the initiation of ferroptosis. Lipid peroxidation is a crucial event in the induction of ferroptosis. The total iron content and MDA levels were measured, and it was noted that AGEs-treated cells exhibited significantly higher iron and MDA levels than untreated cells (Figures 1C, D). Additionally, DCFH-DA staining was performed to examine the production of ROS in HaCaT cells induced by AGEs. Notably, the control group exhibited minimal fluorescence, whereas cells cultured with AGEs exhibited a higher level of fluorescence (Figure 1E).

Given the protective role of GPX4 against lipid peroxide-mediated damage, the impact of AGEs on GPX4 expression was also explored. The results unveiled a remarkable decrease in GPX4 protein expression in HaCaT cells treated with AGEs compared to control cells (Figure 1F). Additionally, the protein expression of FTL was also examined, which is a key component of ferritin involved in the initial stage in iron storage. The results indicated a decrease in FTL protein expression following AGE treatment (Figure 1F). To investigate the role of ferroptosis in these changes, the ferroptosis-specific inhibitor Fer-1 was utilized, demonstrating that it partially rescued the ferroptosis-related alterations (Figures 1C–F). In summary, these findings collectively offer substantial evidence supporting the induction of ferroptosis by AGEs in HaCaT cells *in vitro*.

BBR alleviated AGEs-mediated ferroptosis in HaCaT cells

To investigate the impact of BBR on ferroptosis in HaCaT cells, cell viability was assessed following 48 h of treatment with the ferroptosis inducer erastin, both in the presence and absence of BBR (Figure 2A). The results revealed that erastin administration reduced cell viability, while pretreatment with BBR attenuated this effect. These findings suggest that BBR may act as a negative regulator of ferroptosis. Furthermore, the impact of treatment with 150 μg/mL AGEs for 48 h was investigated, and a substantial reduction in cell viability was observed. However, pretreatment with 5 μM BBR for 2 h before exposure to AGEs effectively attenuated the suppressive effects of AGEs on cell viability (Figure 2B).

Then, the impact of BBR supplementation on iron levels and lipid peroxidation induced by AGEs was investigated. Adding BBR effectively counteracted lipid peroxidation and intracellular iron levels triggered by AGEs (Figures 2C, D). Additionally, the elevation in the accumulation of ROS in AGEs-treated cells was observed. However, the administration of BBR substantially reduced the ROS levels (Figure 2E). Importantly, the decreased expression of GPX4 and FTL, known to be associated with ferroptosis, exhibited a significant restoration in response to treatment with BBR (Figure 2F). Overall, these findings suggest that BBR attenuates AGEs-mediated ferroptosis in keratinocytes.

BBR increased the NRF2 nuclear translocation in HaCaT cells

NRF2, a crucial ferroptosis regulator, is a downstream pathway directly influenced by ROS. However, to elucidate the mechanisms underlying the antiferroptotic impacts of BBR on keratinocytes, NRF2 activity was analyzed. This investigation revealed the upregulation of NRF2 nuclear translocation during AGEs-induced ferroptosis, as confirmed by Western blotting (Figure 3A) and immunofluorescence analysis (Figure 3B). Moreover, treatment with BBR further enhanced the expression of NRF2, suggesting an association between the inhibitory effects of BBR on ferroptosis and NRF2 activity.

BBR protected HaCaT cells against ferroptosis via NRF2 activity

To further explore the involvement of NRF2 activity in AGEs-induced ferroptosis, NRF2-siRNA was utilized to silence NRF2 expression (Figure 4A). The attenuation trend in cell viability caused by AGE treatment could be ameliorated upon BBR exposure. However, the protective effects of BBR were attenuated by NRF2 knockdown (Figure 4B). Additionally, it was observed that BBR effectively suppressed MDA levels in AGEs-treated keratinocytes. However, this inhibitory effect was partially reversed by NRF2 siRNA (Figure 4C). Furthermore, treatment with BBR markedly increased the protein expression of GPX4 and FTL in AGEs-treated cells. Conversely, the knockdown of NRF2 significantly reduced the expression of GPX4 and FTL (Figure 4D). Collectively, these findings

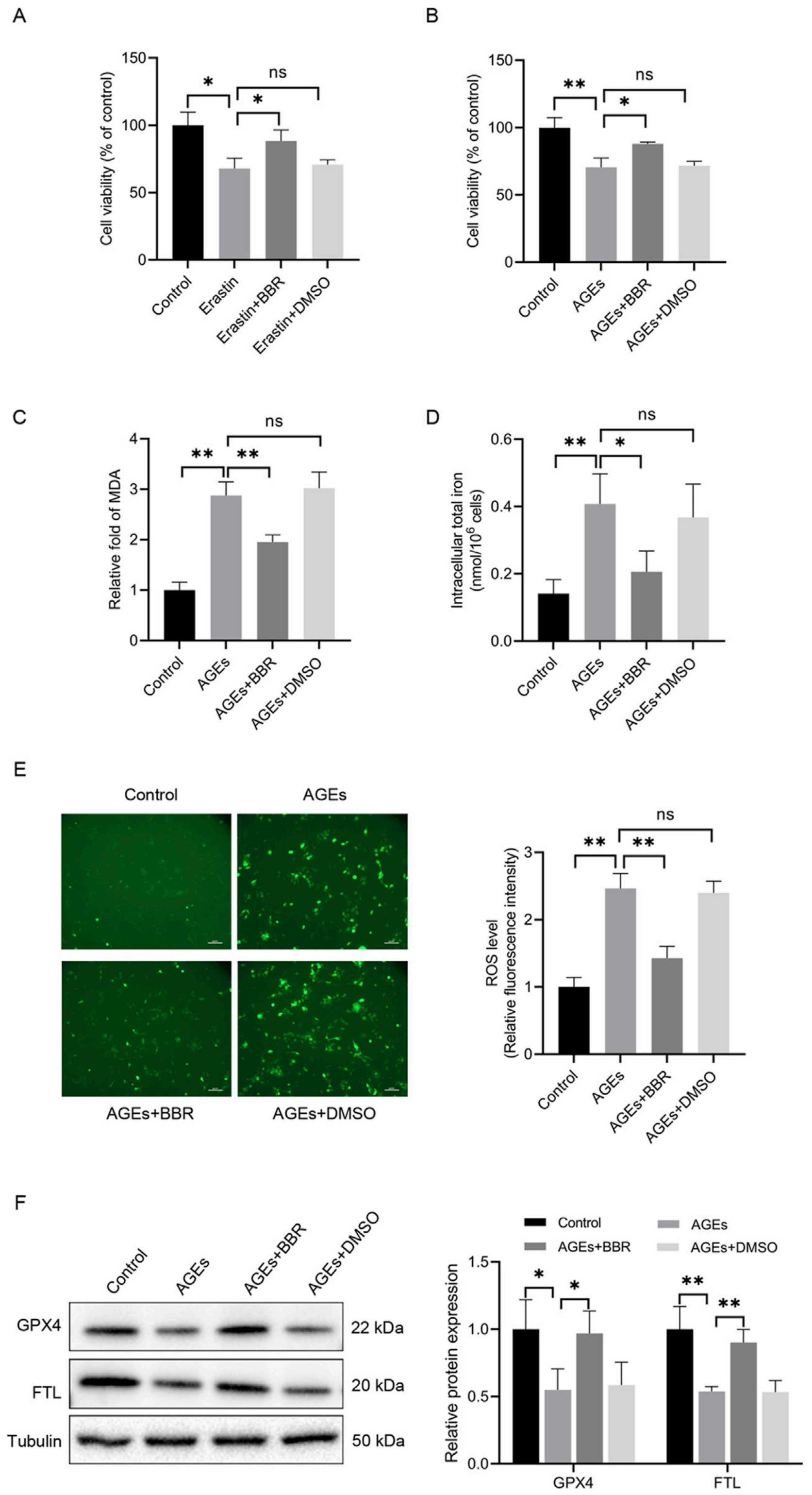

FIGURE 2
BBR alleviated AGEs-mediated ferroptosis in HaCaT cells. **(A)** The cells were treated with erastin (10 μM) with or without BBR (5 μM) for 48 h, and cell viability was quantified by CCK-8 assays. **(B)** Cells were exposed to AGEs (150 μg/mL) with or without BBR for 48 h, and cell viability was investigated. **(C)** HaCaT cells were exposed to BBR (5 μM) followed by AGEs (150 μg/mL) for 48 h, and the relative levels of MDA were measured. **(D)** Intracellular iron levels were examined in HaCaT cells. **(E)** Representative images and quantitative analysis of intracellular ROS levels using

(*Continued*)

FIGURE 2 (Continued)
DCFH-DA in HaCaT cells. **(F)** The protein levels of GPX4 and FTL were measured by Western blot analysis following the exposure of HaCaT cells to AGEs with or without BBR (5 μM). The results are expressed as the mean ± SD. Data are representative of three independent experiments. Scale bar, 100 μm. *$P \le 0.05$, **$P \le 0.01$. AGEs, advanced glycation end products; BBR, berberine; DCFH-DA, 2′, 7′-dichlorofluorescin diacetate; FTL, ferritin light chain; GPX4, glutathione peroxidase 4; MDA, malondialdehyde; ns, no significance.

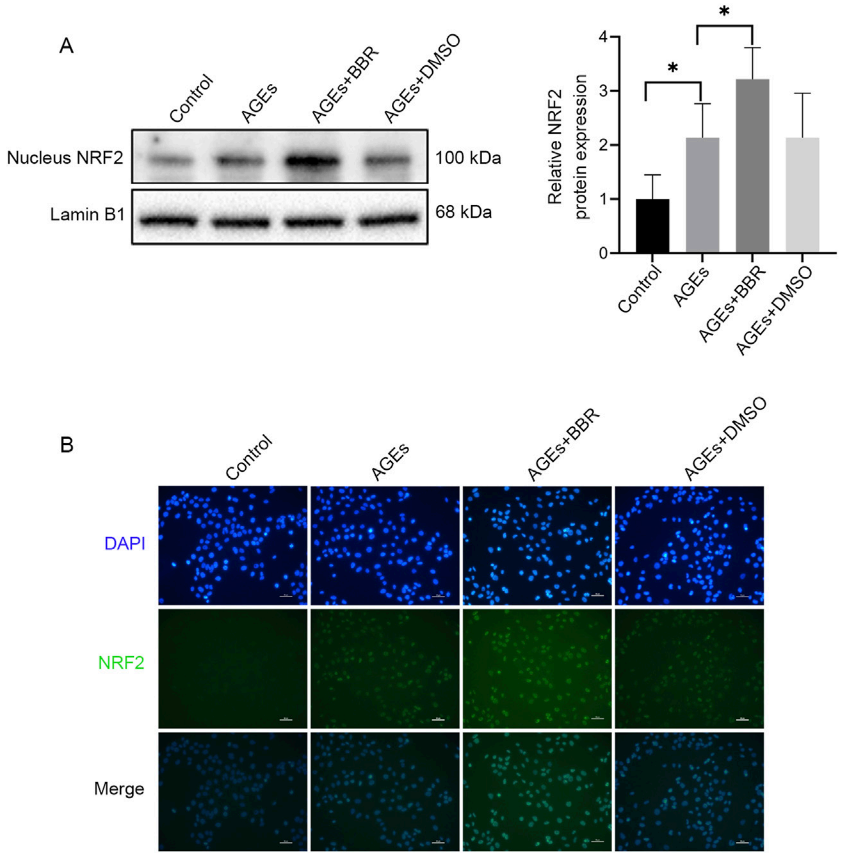

FIGURE 3
BBR increased the NRF2 nuclear translocation in HaCaT cells. **(A)** The HaCaT cells were treated with AGEs (150 μg/mL) with or without BBR (5 μM), and the protein expression levels of NRF2 were determined by Western blot analysis. **(B)** Representative images of immunofluorescence staining of NRF2. Data are representative of three independent experiments. Scale bar, 50 μm. *$P \le 0.05$. AGEs, advanced glycation end products; BBR, berberine; NRF2, nuclear factor E2-related factor 2.

underscore the crucial role of NRF2 activity in mediating the inhibitory effects of BBR on ferroptosis in HaCaT cells.

BBR ameliorated ferroptosis in skin of db/db diabetic mice

To investigate the potential of pharmacologic activation of BBR in preserving the function of diabetic skin, BBR was evaluated for its capacity to improve the ferroptosis-related pathway in db/db mouse skin tissues. As anticipated, db/db diabetic mice had elevated blood glucose levels compared to WT mice at 3 and 5 weeks. Administration of BBR partially decreased blood glucose levels in diabetic mice (Figure 5A). In terms of histology, the skin structure in WT mice exhibited intact layers. The epidermal layers displayed a well-organized arrangement and a rich collagen content with a typical braid pattern. Conversely, in db/db mice, the epidermal cell layers became obscure and some lacked stratified organization. The dermis showed evident atrophy, accompanied by disordered arrangement of connective tissue fiber bundles. However, treatment with BBR significantly ameliorated these aforementioned histological alterations observed in the skin tissue of db/db mice (Figure 5B).

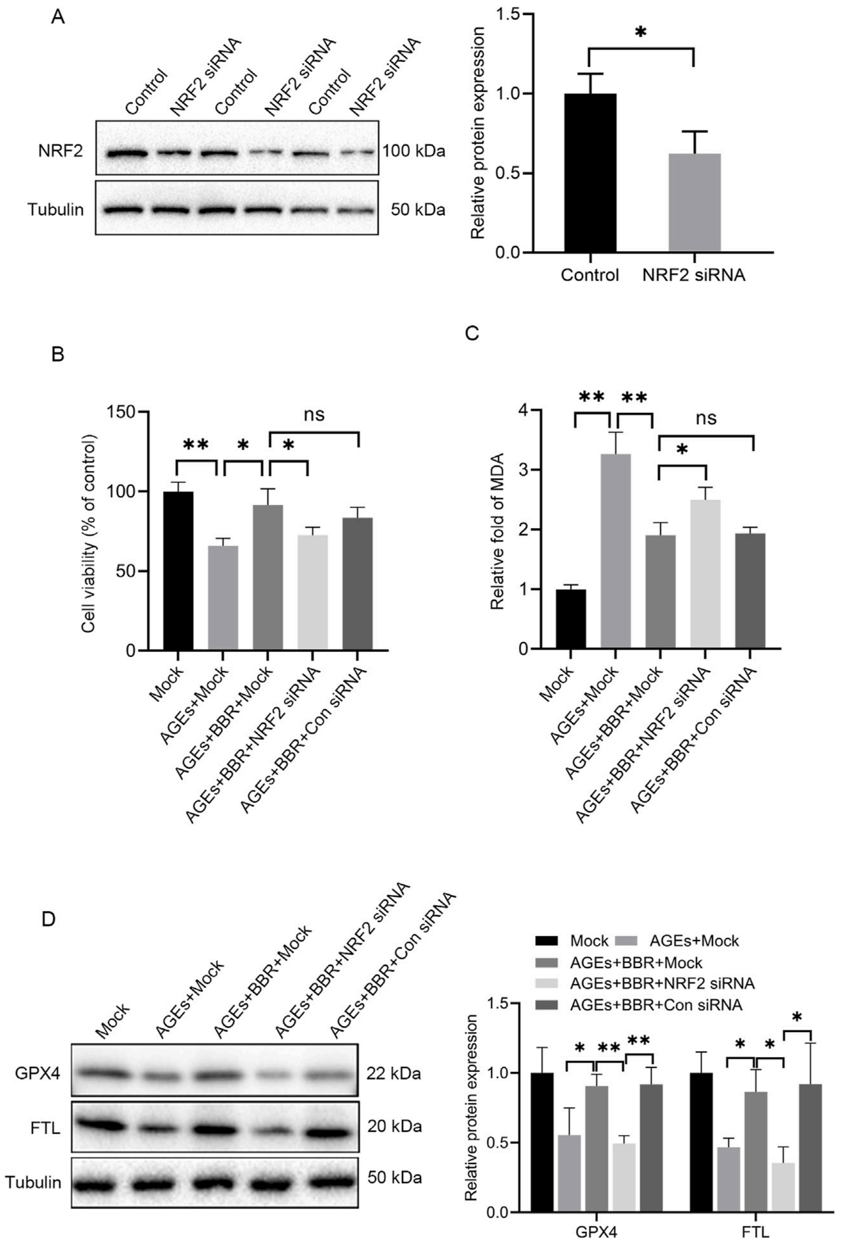

FIGURE 4
BBR protected HaCaT cells against AGEs-induced ferroptosis partially through NRF2 activity. **(A)** Representative Western blot experiments illustrating NRF2 protein expression in HaCaT cells after transfection with NRF2 siRNA. **(B)** The mock-, NRF2 siRNA- or Con siRNA-transfected HaCaT cells were cultured with 150 μg/mL AGEs and 5 μM BBR for 48 h, and cell viability was examined using CCK-8 assays. **(C)** The relative levels of MDA were measured in HaCaT cells after treatment. **(D)** Representative images and quantitative analysis of the protein levels of GPX4 and FTL in HaCaT cells. The results are expressed as the mean ± SD. Data are representative of three independent experiments. *$P \le 0.05$, **$P \le 0.01$. AGEs, advanced glycation end products; BBR, berberine; Con siRNA, control siRNA; FTL, ferritin light chain; GPX4, glutathione peroxidase 4; MDA, malondialdehyde; NRF2, nuclear factor E2-related factor 2; ns, no significance.

Next, we evaluated alterations in key ferroptosis-related molecules, including GPX4, FTL, FTH, NRF2, and 4-HNE, within the epidermis. Consistent with our findings in HaCaT cells, db/db mice exhibited reduced protein expression of GPX4, FTL, and FTH along with elevated levels of 4-HNE and NRF2 in the epidermis of skin sections. However, treatment with BBR significantly enhanced the protein expression of GPX4, FTL, FTH, and NRF2 while decreasing 4-HNE protein adducts in the db/db group (Figures 5C, D, F). Additionally, BBR administration attenuated the increased lipid peroxidation

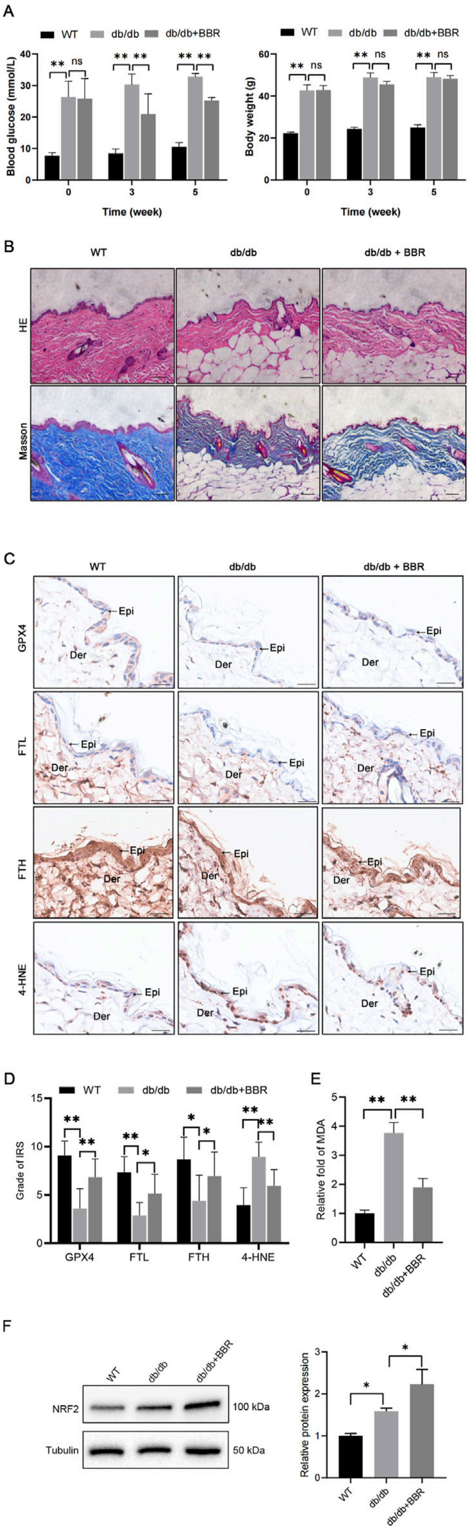

FIGURE 5
BBR mitigated ferroptosis in the epidermis of diabetic mice **(A)** The body weight and blood glucose levels were evaluated in three groups of mice. **(B)** Representative images of HE and Masson's trichrome staining in skin tissues of WT mice, db/db
(*Continued*)

FIGURE 5 (Continued)
mice, and BBR-treated db/db mice. Scale bar, 50 μm. **(C)** Representative immunohistochemical images demonstrate the impact of BBR on protein expression levels of GPX4, FTL, FTH, and 4-HNE in skin tissues of db/db mice. Scale bar, 25 μm. **(D)** Quantitative analysis of GPX4, FTL, FTH, and 4-HNE protein (brown color) levels in the epidermis was conducted according to IRS (n = 5 per group). **(E)** MDA concentrations were measured in skin tissues from the indicated mouse groups (n = 4 per group). **(F)** Representative images and quantitative analysis of the protein levels of NRF2 in skin tissues (n = 3 per group). The results are presented as mean ± SD. $*P \le 0.05$, $**P \le 0.01$. BBR, berberine; Der, dermis; Epi, epidermis; FTL, ferritin light chain; FTH, ferritin heavy chain; GPX4, glutathione peroxidase 4; 4-HNE, 4-Hydroxynonenal; IRS, immunoreactive reactivity score; MDA, malondialdehyde.

product MDA in the skins of db/db mice (Figure 5E). Collectively, these results indicate that BBR may ameliorate ferroptosis within the epidermis of diabetic mice.

Discussion

In this study, we found that exposure of HaCaT cells to AGEs resulted in the induction of ferroptosis, as evidenced by the increase in ROS and intracellular iron levels and the accumulation of MDA, which was accompanied by a decrease in the expression of FTL and GPX4. We further found that BBR protected against AGEs-induced ROS and MDA production, thereby mitigating ferroptosis. Notably, we determined an important role for NRF2 activity in BBR-mediated prevention of AGEs-induced ferroptosis *in vitro*. Moreover, we also demonstrated a significant decrease in GPX4, FTL, and FTH expression in the epidermis of db/db diabetic mice, along with enhanced lipid peroxidation. However, treatment with BBR effectively ameliorated lipid peroxidation accumulation and upregulated GPX4, FTL, and FTH levels in diabetic skin. These findings provide valuable insights into the underlying pathogenic mechanisms that contribute to impaired wound healing in diabetes and propose a new theoretical foundation for utilizing BBR for managing diabetic chronic wounds.

AGEs, comprising glycated proteins or lipids generated by hyperglycemia, are indicative of diabetes [21]. The levels of AGEs are increased in the skin of diabetic patients, and they are considered the foremost pathogenic initiators of impaired wound healing [22]. This impairment occurs through their association with the AGEs receptors and the development of oxidative stress [23]. Ferroptosis, a regulated type of cell death, is distinguished by the iron-dependent buildup of lipid peroxidation products [7]. When cell membranes containing phospholipids undergo ROS-induced lipid peroxidation, it increases MDA production, leading to direct cytotoxicity and the subsequent induction of ferroptosis [24]. In the current study, we found a substantial accumulation of ROS and iron levels in HaCaT cells subjected to AGEs treatment, which was accompanied by enhanced levels of lipid peroxidation products, including MDA.

GPX4, a vital antioxidant enzyme in mammals, is crucial in eliminating lipid peroxidation [25]. The deficiency of GPX4 is recognized as a biomarker for ferroptosis, and the inhibition of GPX4 could induce acute renal failure induced by lipid oxidation, leading to associated ferroptosis [26]. In this study, we observed a remarkable reduction in the expression of GPX4 in HaCaT cells. The reduced expression of GPX4 compromised the ability of the cells to counteract ROS-induced damage, rendering them more susceptible to ferroptosis.

Ferritin is pivotal in regulating iron metabolism, which is closely associated with ferroptosis [27]. Through its oxidase activity, ferritin facilitates the conversion of ferrous iron to ferric iron and the incorporation of iron into ferritin, thereby reducing free iron levels. In this context, we observed a significant reduction in FTL levels, which was accompanied by a notable increase in iron levels and was consistent with prior findings on ferroptosis. In addition, the elevated oxidative stress resulting from iron overload, mediated by the Fenton reaction, promotes the formation of AGEs, thus perpetuating a vicious cycle [28]. Furthermore, treatment with Fer-1 alleviated the detrimental effects of oxidative stress and iron accumulation, leading to improved cell activity. These findings provide compelling evidence for the involvement of ferroptosis in AGEs-induced death in HaCaT cells. Similar observations of AGEs-induced ferroptosis were also reported in diabetic cardiomyopathy and osteoblasts, further supporting our findings [20, 29].

BBR, a traditional plant alkaloid isolated from the Chinese herb *Coptis chinensis*, exerts anti-inflammatory and antioxidant effects [12]. Its beneficial effects are mediated by several signaling pathways, such as nuclear factor-κB, NRF2, the mitogen-activated protein kinase cascade, and various kinases in cellular systems [30, 31]. Recent studies have demonstrated that BBR accelerates wound healing and enhances extracellular matrix synthesis in diabetic rats induced by streptozotocin. Furthermore, BBR has shown significant inhibition of oxidative stress and apoptosis induced by high glucose in HaCaT cells [17, 32]. Additionally, ferroptosis-related characteristic changes were implicated in the pathogenesis of delayed wound healing in diabetic ulcers [33]. Our findings reveal that BBR attenuates AGEs-induced ROS, MDA, and iron accumulation. Moreover, BBR strikingly rescued the decreased expression of GPX4 and FTL in AGEs-treated HaCaT cells. These results demonstrated that BBR treatment alleviates AGEs-induced ferroptosis in HaCaT cells. Interestingly, in a separate study, BBR attenuated liver fibrosis by inducing ferrous redox to activate ROS-mediated ferroptosis in hepatic stellate cells [34]. A possible explanation for the varying effects could be attributed to differences in BBR concentrations used in the study or tissue-specific effects.

NRF2, a well-established transcription factor, a crucial role in the cellular antioxidant response [15, 35]. Furthermore, it is a regulatory factor in ferroptosis and pathological injury across multiple organs. This role is hallmarked by the nuclear translocation of NRF2 and induction of its downstream target proteins [36, 37]. The impact of oxidative stress resulting from AGEs or hyperglycemia on NRF2 activity remains inconsistent. Certain studies have indicated that hyperglycemia or AGEs inhibit NRF2 activity through the ERK pathway or the NRF2-activating mediator Sirt1 [38, 39]. However, conflicting viewpoints exist on this subject [40]. We observed a slight increase in nuclear NRF2 levels after short-term exposure to AGEs in HaCaT cells. This increased nuclear translocation of NRF2 after acute AGE treatment could signify an endogenous self-defense mechanism. However, persistent exposure to AGEs or hyperglycemia could induce oxidative stress, suppressing NRF2 antioxidant activity and potentially triggering ferroptosis. Remarkably, BBR treatment significantly increased nuclear NRF2 levels in AGEs-treated cells, as confirmed by immunofluorescence. This observation indicates that BBR promotes NRF2 nuclear translocation. Interestingly, the inhibitory effects of BBR on lipid ROS accumulation and iron levels were reversed when NRF2 activity was suppressed by siRNA. Furthermore, FTL and GPX4, essential mediators of ferroptosis, are the known targets of NRF2 [37, 41]. We found that downregulating NRF2 expression with NRF2 siRNA abolished the beneficial impact of BBR on GPX4 and FTL levels in AGEs-treated cells. These findings suggest that the protective properties of BBR against ferroptosis induced by AGEs in HaCaT cells are, to some extent, dependent on NRF2 activity.

In fact, most studies on berberine for diabetes or its complications have focused on oral administration, despite the poor oral bioavailability and absorption of berberine in the intestines [42]. An animal study in rats showed a Cmax of 0.26 μg/mL after oral administration of 400 mg/kg berberine [43], while a human study reported a Cmax value of 0.40 ng/mL after administering 400 mg of berberine orally to healthy male volunteers [44]. In order to achieve the same plasma concentration, the dosage of berberine used in mouse models is significantly higher than that in humans. However, due to the potential differences in absorption rate and basal metabolic rate of berberine between animal models and humans, it is challenging to determine an appropriate dosage of berberine based on results from animal studies.

In conclusion, our study demonstrated that exposure to AGEs triggers substantial oxidative stress and iron overload in keratinocytes, resulting in lipid peroxidation and ferroptosis. Furthermore, we showed the novel cytoprotective role of BBR beyond its conventional antidiabetic effects, as it inhibited ferroptosis by upregulating NRF2 activity. These findings introduce a new perspective for the management of delayed diabetic wound healing.

Author contributions

CJ: Conceptualization, Investigation, Data Formal analysis, Writing–original draft, Software. GL: Investigation, Methodology, Resources, Writing–review and editing. JR: Supervision, Project administration, Writing–review and editing. PZ: Conceptualization, Project administration, Supervision, Writing–review and editing, Funding acquisition. All authors contributed to the article and approved the submitted version.

Data availability

The original contributions presented in the study are included in the article/supplementary material, further inquiries can be directed to the corresponding author.

Ethics statement

The animal study was approved by Institutional Animal Care and Use Committee of TOP Biotechnology (LFTOP-IACUC-2023-0020). The study was conducted in accordance with the local legislation and institutional requirements.

Funding

The author(s) declare that financial support was received for the research, authorship, and/or publication of this article. This work was supported by the research grants from the Guangzhou Municipal Science and Technology Project (2023A03J0985).

Conflict of interest

The author(s) declared no potential conflicts of interest with respect to the research, authorship, and/or publication of this article.

References

1. Ong KL, Stafford LK, McLaughlin SA, Boyko EJ, Vollset SE, Smith AE, et al. Global, regional, and national burden of diabetes from 1990 to 2021, with projections of prevalence to 2050: a systematic analysis for the Global Burden of Disease Study 2021. *The Lancet* (2023) **402**:203–34. doi:10.1016/s0140-6736(23)01301-6

2. Armstrong DG, Tan T-W, Boulton AJM, Bus SA. Diabetic foot ulcers: a review. *JAMA* (2023) **330**:62–75. doi:10.1001/jama.2023.10578

3. Arshi B, Chen J, Ikram MA, Zillikens MC, Kavousi M. Advanced glycation end-products, cardiac function and heart failure in the general population: the Rotterdam Study. *Diabetologia* (2023) **66**:472–81. doi:10.1007/s00125-022-05821-3

4. Lao G, Ren M, Wang X, Zhang J, Huang Y, Liu D, et al. Human tissue inhibitor of metalloproteinases-1 improved wound healing in diabetes through its anti-apoptotic effect. *Exp Dermatol* (2019) **28**:528–35. doi:10.1111/exd.13442

5. Alikhani Z, Alikhani M, Boyd CM, Nagao K, Trackman PC, Graves DT. Advanced glycation end products enhance expression of pro-apoptotic genes and stimulate fibroblast apoptosis through cytoplasmic and mitochondrial pathways. *J Biol Chem* (2005) **280**:12087–95. doi:10.1074/jbc.m406313200

6. Dos Santos AF, Fazeli G, Xavier da Silva TN, Friedmann Angeli JP. Ferroptosis: mechanisms and implications for cancer development and therapy response. *Trends Cel Biol* (2023) **33**:1062–76. doi:10.1016/j.tcb.2023.04.005

7. Stockwell BR, Friedmann Angeli JP, Bayir H, Bush AI, Conrad M, Dixon SJ, et al. Ferroptosis: a regulated cell death nexus linking metabolism, redox biology, and disease. *Cell* (2017) **171**:273–85. doi:10.1016/j.cell.2017.09.021

8. Wu X, Li Y, Zhang S, Zhou X. Ferroptosis as a novel therapeutic target for cardiovascular disease. *Theranostics* (2021) **11**:3052–9. doi:10.7150/thno.54113

9. Sun L, Franco OH, Hu FB, Cai L, Yu Z, Li H, et al. Ferritin concentrations, metabolic syndrome, and type 2 diabetes in middle-aged and elderly Chinese. *J Clin Endocrinol and Metab* (2008) **93**:4690–6. doi:10.1210/jc.2008-1159

10. Simcox JA, McClain DA. Iron and diabetes risk. *Cel Metab* (2013) **17**:329–41. doi:10.1016/j.cmet.2013.02.007

11. Li S, Li Y, Wu Z, Wu Z, Fang H. Diabetic ferroptosis plays an important role in triggering on inflammation in diabetic wound. *Am J Physiol Endocrinol Metab* (2021) **321**:E509–E520. doi:10.1152/ajpendo.00042.2021

12. Ma X, Chen Z, Wang L, Wang G, Wang Z, Dong X, et al. The pathogenesis of diabetes mellitus by oxidative stress and inflammation: its inhibition by berberine. *Front Pharmacol* (2018) **9**:782. doi:10.3389/fphar.2018.00782

13. Zhang H, Wei J, Xue R, Wu JD, Zhao W, Wang ZZ, et al. Berberine lowers blood glucose in type 2 diabetes mellitus patients through increasing insulin receptor expression. *Metabolism* (2010) **59**:285–92. doi:10.1016/j.metabol.2009.07.029

14. Semwal DK, Kumar A, Aswal S, Chauhan A, Semwal RB. Protective and therapeutic effects of natural products against diabetes mellitus via regenerating pancreatic*β*-cells and restoring their dysfunction. *Phytotherapy Res* (2021) **35**:1218–29. doi:10.1002/ptr.6885

15. Zhang Q, Liu J, Duan H, Li R, Peng W, Wu C. Activation of Nrf2/HO-1 signaling: an important molecular mechanism of herbal medicine in the treatment of atherosclerosis via the protection of vascular endothelial cells from oxidative stress. *J Adv Res* (2021) **34**:43–63. doi:10.1016/j.jare.2021.06.023

16. Alnuqaydan AM, Almutary AG, Azam M, Manandhar B, De Rubis G, Madheswaran T, et al. Phytantriol-based berberine-loaded liquid crystalline nanoparticles attenuate inflammation and oxidative stress in lipopolysaccharide-induced RAW264.7 macrophages. *Nanomaterials (Basel)* (2022) **12**:4312. doi:10.3390/nano12234312

17. Zhou R, Xiang C, Cao G, Xu H, Zhang Y, Yang H, et al. Berberine accelerated wound healing by restoring TrxR1/JNK in diabetes. *Clin Sci* (2021) **135**:613–27. doi:10.1042/cs20201145

18. Long M, Rojo de la Vega M, Wen Q, Bharara M, Jiang T, Zhang R, et al. An essential role of NRF2 in diabetic wound healing. *Diabetes* (2016) **65**:780–93. doi:10.2337/db15-0564

19. Ilie MD, Tabarin A, Vasiljevic A, Bonneville JF, Moreau-Grangé L, Schillo F, et al. Predictive factors of somatostatin receptor ligand response in acromegaly-A prospective study. *J Clin Endocrinol and Metab* (2022) **107**:2982–91. doi:10.1210/clinem/dgac512

20. Wang X, Chen X, Zhou W, Men H, Bao T, Sun Y, et al. Ferroptosis is essential for diabetic cardiomyopathy and is prevented by sulforaphane via AMPK/NRF2 pathways. *Acta Pharmaceutica Sinica B* (2022) **12**:708–22. doi:10.1016/j.apsb.2021.10.005

21. Khalid M, Petroianu G, Adem A. Advanced glycation end products and diabetes mellitus: mechanisms and perspectives. *Biomolecules* (2022) **12**:542. doi:10.3390/biom12040542

22. Huijberts MS, Schaper NC, Schalkwijk CG. Advanced glycation end products and diabetic foot disease. *Diabetes Metab Res Rev* (2008) **24**(Suppl. 1):S19–24. doi:10.1002/dmrr.861

23. Zhu P, Ren M, Yang C, Hu Y-X, Ran J-M, Yan L. Involvement of RAGE, MAPK and NF-κB pathways in AGEs-induced MMP-9 activation in HaCaT keratinocytes. *Exp Dermatol* (2012) **21**:123–9. doi:10.1111/j.1600-0625.2011.01408.x

24. Chen X, Li J, Kang R, Klionsky DJ, Tang D. Ferroptosis: machinery and regulation. *Autophagy* (2021) **17**:2054–81. doi:10.1080/15548627.2020.1810918

25. Ursini F, Maiorino M. Lipid peroxidation and ferroptosis: the role of GSH and GPx4. *Free Radic Biol Med* (2020) **152**:175–85. doi:10.1016/j.freeradbiomed.2020.02.027

26. Friedmann Angeli JP, Schneider M, Proneth B, Tyurina YY, Tyurin VA, Hammond VJ, et al. Inactivation of the ferroptosis regulator Gpx4 triggers acute renal failure in mice. *Nat Cel Biol* (2014) **16**:1180–91. doi:10.1038/ncb3064

27. Plays M, Müller S, Rodriguez R. Chemistry and biology of ferritin. *Metallomics.* (2021) **13**:mfab021. doi:10.1093/mtomcs/mfab021

28. Kang Q, Yang C. Oxidative stress and diabetic retinopathy: molecular mechanisms, pathogenetic role and therapeutic implications. *Redox Biol* (2020) **37**:101799. doi:10.1016/j.redox.2020.101799

29. Ge W, Jie J, Yao J, Li W, Cheng Y, Lu W. Advanced glycation end products promote osteoporosis by inducing ferroptosis in osteoblasts. *Mol Med Rep* (2022) **25**:140. doi:10.3892/mmr.2022.12656

30. Haftcheshmeh SM, Abedi M, Mashayekhi K, Mousavi MJ, Navashenaq JG, Mohammadi A, et al. Berberine as a natural modulator of inflammatory signaling pathways in the immune system: focus on NF-κB, JAK/STAT, and MAPK signaling pathways. *Phytotherapy Res* (2022) **36**:1216–30. doi:10.1002/ptr.7407

31. Li S, Ding X, Yan X, Qian J, Tan Q. ceAF ameliorates diabetic wound healing by alleviating inflammation and oxidative stress via TLR4/NF-κB and Nrf2 pathways. *J Diabetes Res* (2023) **2023**:1–12. doi:10.1155/2023/2422303

32. Panda DS, Eid HM, Elkomy MH, Khames A, Hassan RM, Abo El-Ela FI, et al. Berberine encapsulated lecithin-chitosan nanoparticles as innovative wound healing agent in type II diabetes. *Pharmaceutics* (2021) **13**:1197. doi:10.3390/pharmaceutics13081197

33. Li S, Li Y, Wu Z, Wu Z, Fang H. Diabetic ferroptosis plays an important role in triggering on inflammation in diabetic wound. *Am J Physiology-Endocrinology Metab* (2021) **321**:E509–E520. doi:10.1152/ajpendo.00042.2021

34. Yi J, Wu S, Tan S, Qin Y, Wang X, Jiang J, et al. Berberine alleviates liver fibrosis through inducing ferrous redox to activate ROS-mediated hepatic stellate cells ferroptosis. *Cel Death Discov* (2021) **7**:374. doi:10.1038/s41420-021-00768-7

35. Hybertson BM, Gao B, Bose SK, McCord JM. Oxidative stress in health and disease: the therapeutic potential of Nrf2 activation. *Mol Aspects Med* (2011) **32**:234–46. doi:10.1016/j.mam.2011.10.006

36. Liu Y, Yang X, Liu Y, Jiang T, Ren S, Chen J, et al. NRF2 signalling pathway: new insights and progress in the field of wound healing. *J Cell Mol Med* (2021) **25**:5857–68. doi:10.1111/jcmm.16597

37. Dodson M, Castro-Portuguez R, Zhang DD. NRF2 plays a critical role in mitigating lipid peroxidation and ferroptosis. *Redox Biol* (2019) **23**:101107. doi:10.1016/j.redox.2019.101107

38. Ko SY, Chang SS, Lin IH, Chen HI. Suppression of antioxidant Nrf-2 and downstream pathway in H9c2 cells by advanced glycation end products (AGEs) via ERK phosphorylation. *Biochimie* (2015) **118**:8–14. doi:10.1016/j.biochi.2015.07.019

39. Li M, Yu H, Pan H, Zhou X, Ruan Q, Kong D, et al. Nrf2 suppression delays diabetic wound healing through sustained oxidative stress and inflammation. *Front Pharmacol* (2019) **10**:1099. doi:10.3389/fphar.2019.01099

40. Zhao S, Lo CS, Miyata KN, Ghosh A, Zhao XP, Chenier I, et al. Overexpression of Nrf2 in renal proximal tubular cells stimulates sodium-glucose cotransporter 2 expression and exacerbates dysglycemia and kidney injury in diabetic mice. *Diabetes* (2021) **70**:1388–403. doi:10.2337/db20-1126

41. Kerins MJ, Ooi A. The roles of NRF2 in modulating cellular iron homeostasis. *Antioxid and Redox Signaling* (2018) **29**:1756–73. doi:10.1089/ars.2017.7176

42. Khoshandam A, Imenshahidi M, Hosseinzadeh H. Pharmacokinetic of berberine, the main constituent of Berberis vulgaris L.: a comprehensive review. *Phytotherapy Res* (2022) **36**:4063–79. doi:10.1002/ptr.7589

43. Yu Q, Li M, Chen H, Xu L, Cheng J, Lin G, et al. The discovery of berberine erythrocyte-hemoglobin self-assembly delivery system: a neglected carrier underlying its pharmacokinetics. *Drug Deliv* (2022) **29**:856–70. doi:10.1080/10717544.2022.2036870

44. Hua W, Ding L, Chen Y, Gong B, He J, Xu G. Determination of berberine in human plasma by liquid chromatography-electrospray ionization-mass spectrometry. *J Pharm Biomed Anal* (2007) **44**:931–7. doi:10.1016/j.jpba.2007.03.022

Experimental Biology and Medicine

TYPE Original Research
PUBLISHED 13 December 2024
DOI 10.3389/ebm.2024.10240

Increased hip fracture risk in the patients with type 2 diabetes mellitus is correlated with urine albumin-to-creatinine ratio (ACR) and diabetes duration in men

Huiru Ding[1,2†], Hongxia Wang[1,2†], Guanghui Liu[1], Yu Wang[1,2], Dongxu Han[1,2], Xiaoya Zhang[1,2] and Lige Song[1,2*]

[1]Department of Endocrinology, Shanghai Tongji Hospital, School of Medicine, Tongji University, Shanghai, China, [2]Institute of Osteoporosis and Metabolic Bone Diseases, School of Medicine, Tongji University, Shanghai, China

OPEN ACCESS

*CORRESPONDENCE
Lige Song,
6songlige@tongji.edu.cn

†These authors have contributed equally to this work

RECEIVED 15 May 2024
ACCEPTED 19 November 2024
PUBLISHED 13 December 2024

CITATION
Ding H, Wang H, Liu G, Wang Y, Han D, Zhang X and Song L (2024) Increased hip fracture risk in the patients with type 2 diabetes mellitus is correlated with urine albumin-to-creatinine ratio (ACR) and diabetes duration in men.
Exp. Biol. Med. 249:10240.
doi: 10.3389/ebm.2024.10240

Abstract

Patients with type 2 diabetes mellitus (T2DM) have increased hip fracture risk. And the association between urine albumin to creatinine ratio (ACR) and an increased risk of hip fracture in patients with T2DM remains controversial. This study aimed to investigate the association between urinary ACR and hip fracture risk in postmenopausal women and aged men with T2DM. The study included 219 postmenopausal women and 216 older men (mean age >60 years) with T2DM. Women and men were divided into control group (ACR<30 mg/g), microalbuminuria group (30 mg/g ≤ ACR<300 mg/g), and macroalbuminuria group (ACR≥300 mg/g) respectively. Demographic characteristics and clinical history were collected in patients. Biochemical indexes and bone turnover-related markers were measured in patients. In the study, we found that several factors, including age, T2DM duration, cerebral infarction history, serum corrected calcium levels and urine ACR were positively associated with hip fracture risk. However, 25-Hydroxyvitamin D and areal BMD were negatively associated with hip fracture risk. Furthermore, multiple regression analysis showed that urinary ACR level ($\beta = 0.003$, $p = 0.044$) and duration of T2DM ($\beta = 0.015$, $p = 0.018$) were positively and independently correlated with hip fracture risk in older men. In contrast, femoral neck BMD ($\beta = -6.765$, $p < 0.001$) was independently and negatively correlated with hip fracture risk in older men. This study indicated that the elevated ACR levels and longer T2DM duration were related to higher hip fracture risk in older men with T2DM, which could be beneficial for developing a predictive model for osteoporotic fractures in patients with type 2 diabetes in the future. However, results were inconsistent in women, hip fracture risk didn't alter by changes in urinary microalbuminuria level in postmenopausal women with T2DM.

KEYWORDS

type 2 diabetes mellitus, fracture risk, hip fracture, urine albumin to creatinine ratio, diabetes duration

Impact statement

1. Hip fracture was related to age, T2DM duration, cerebral infarction history, serum corrected calcium levels, 25-Hydroxyvitamin D, urine ACR and areal BMDs. 2. Urinary ACR level and duration of T2DM were independent predictors of hip fracture risk in older men by multiple linear regression analysis incorporating these correlates. 3. Increased hip fracture risk in older men with T2DM was related to elevated ACR levels and longer T2DM duration.

Introduction

Diabetes mellitus (DM) is a common metabolic disease with increasing prevalence throughout the world. Chronic complications of DM adversely affect multiple organ systems, which cause an enormous medical and economic burden and reduce life span [1]. Apart from the significant complications, such as diabetic nephropathy, diabetic retinopathy and diabetic peripheral neuropathy, diabetic osteopathy is also reported as a severe complication for heightened risk of fractures among diabetic patients [2]. In type 1 diabetes (T1DM), reduced bone mass and bone strength, increase the susceptibility to fractures. In contrast, Type 2 diabetes mellitus also have been reported to be associated with an increased fractures risk, vertebral [3], hip [4] and all non-vertebral fractures. Previous studies have demonstrated that many factors contribute to the increased risk of fractures in type 2 diabetes mellitus, including impaired insulin signaling, decreased incretin effect, increased oxidative stress, accumulation of advanced glycation end products, and microvascular damage [5]. Diabetic nephropathy is recognized as one of the most important microvascular complications of diabetes, which has been reported to increase the risk of fracture in patients with T2DM [6].

Studies confirmed disturbances in serum calcium, phosphate and vitamin D levels, parathyroid hormone (PTH) metabolism, and dysregulation of bone turnover, primarily attributed to progressive eGFR decline associated with diabetic nephropathy [7, 8]. Besides, it is worth noting that persistent albuminuria is a marker of microvascular injury in diabetic nephropathy. Previous studies have demonstrated that microcirculation is vital to bone health [9]. And several clinical studies have demonstrated high urinary ACR levels maybe associated with increased fracture risk in non-diabetic populations [8, 10, 11]. However, patients with T2DM have unique skeletal metabolic features, and the association between ACR and fracture risk among the individuals with T2DM is unclear. Our study mainly explored whether urinary albumin excretion can be used as a risk factor for fractures in patients with type 2 diabetes.

Materials and methods

Study population

This was a cross-sectional study. It enrolled 435 individuals with type 2 diabetes mellitus who came to the Department of Endocrinology of Shanghai Tongji hospital for regular follow-up from January 2019 to December 2020. The enrolled population consisted of 219 post-menopausal women (menopausal status was confirmed by the absence of menses for more than 1 year in a woman over 50 years of age; and, in women with previous hysterectomy or those under 50 years of age, by an elevated value for serum follicle-stimulating hormone (FSH) of >30 IU/L) between 50 and 90 years old and 216 men between 40 and 80 years old. All patients were diagnosed with T2DM based on the criteria of the American Diabetes Association [12].

All patients met the following criteria: (1) all women were post-menopausal, and all men were over 40 years old; (2) the eGFR was greater than 30 mL/min/1.73 m^2 in all patients; and (3) never use any anti-osteoporosis drugs. The exclusion criteria included: (1) severe hepatic dysfunction with alanine aminotransferase >40 U/L or aspartate aminotransferase >40 U/L; (2) severe renal dysfunction with eGFR <30 mL/min/1.73 m^2; (3) malignancy; (4) hyperthyroidism; (5) rheumatoid arthritis; (6) hormone replacement therapy for the last 6 months; (7) prior anti-osteoporotic medicine; (8) previous use of a hypoglycemic agent that can affect bone metabolism such as thiazolidinediones (TZDs); and (9) depression diseases. At last, we selected 435 patients with T2DM who met the above criteria. The study has passed the Ethics Committee of Tongji Hospital and Tongji University School of Medicine and conforms to the Declaration of Helsinki. All participants signed informed consent. This study has been registered in the Chinese Clinical Trials Registry (ID: ChiCTR1800020077).

Demographic information and clinical history

Each patient's medical history was reviewed. The following data were recorded: age, sex, height, weight, current smoking and drinking status (there are many people who drink but who are not consuming excessive amounts of alcohol. Therefore drinking status referes to excessive alcohol consumption, which is defined as drinking alcohol 3 or more units per day.), duration of type 2 diabetes, history of coronary heart disease, hypertension, and cerebral infarction. Body mass index (BMI) (kg/m^2) was calculated as weight (kg)/height (m^2). Drinking status was defined as consuming three or more units of alcohol daily (one unit of alcohol means 8 g of alcohol).

Laboratory measurements

Peripheral venous blood was collected after overnight fast to measure biochemical data, including fasting blood glucose (FBG), fasting insulin, glycosylated haemoglobin (HbA1c), liver and renal function, serum albumin level, lipid profile including total cholesterol (TC), triglyceride (TG), low-density lipoprotein (LDL) and high-density lipoprotein (HDL), electrolyte levels including serum calcium (Ca) and phosphorus (P), bone turnover markers, and bone metabolism-related hormones including bone alkaline phosphatase (BALP), procollagen type I intact N- terminal (P1NP), osteocalcin (OC), tartrate-resistant acid phosphatase-5b (TRACP-5b), C- terminal cross-linking telopeptide of type I collagen (CTX), 25-hydroxy vitamin (D [25(OH)D]), and parathyroid hormone (PTH).

HbA1c was detected using high-performance liquid chromatography with whole blood. Serum OC, CTX, P1NP, [25-(OH)D], and PTH were measured by electrochemiluminescence assay (Roche Diagnostics; coefficient of variation of intra- and inter-assay <10%). The enzyme immunoassay was used to measure the serum BALP and TRACP- 5b levels (IDS Ltd; coefficient of variation of intra- and inter-assay <10%). An automatic chemistry analyzer using serum detected liver function, renal function, albumin, lipid profiles, and electrolytes. Corrected Ca (mmol/L) was calculated according to the following formula: Ca (mmol/L) −0.025*albumin+1. The calcium-phosphorus product was calculated using the following formula: 12.4*Ca (mmol/L) *P (mmol/L). The insulin resistance (homeostatic model assessment for insulin resistance, HOMA-IR) assessment was calculated according to the existing literature formula: FBG (mmol/L) *fasting insulin (mU/L)/ 22.5 [13]. The arterial stiffness index or the atherogenic coefficient was calculated as follows: (TC-HDL-C)/HDL-C [14–16].

The eGFRs (ml/min/1.73 m2) were estimated using the serum creatinine (sCr) levels according to the simplified CKD-MDRD equation as follows [17].

$$\text{For male: eGFR} = 186{*}\text{sCr} - 1.154{*}\text{age}^{-0.203}$$

$$\text{For female: eGFR} = \left(186{*}\text{sCr} - 1.154{*}\text{age}^{-0.203}\right){*}0.742$$

Fasting urine samples were also collected to measure urine albumin and urine creatinine levels using an immunoturbidimetric method. The urine albumin/creatinine ratios (mg/g) were calculated by dividing the urine microalbumin by the urine creatinine concentration. The sensitivity and precision of urine albumin are 93% and 94%, and the sensitivity and precision of urine creatinine are 91% and 97%. According to clinical recommendations from the American Diabetes Association (ADA) for the prevention and control of diabetic nephropathy, study participants were categorized into three groups based on ACR: the normal group (ACR<30 mg/g), the microalbuminuria group (30 mg/g ≤ ACR≤300 mg/g), and macroalbuminuria group (ACR >300 mg/g). Among women, there were 20 patients in the macroalbuminuria group, 79 patients in the microalbuminuria group, and 120 patients in the control group. Among men, there were 33, 45, and 138 patients in the respective groups.

BMD and fracture risk

Bone mineral density (BMD) at lumbar spine 1–4, femoral neck, and total hip was measured using dual-energy X-ray absorptiometry (DXA) at Shanghai Tongji Hospital with a Hologic instrument (Hologic Inc., United States). The coefficient of variation was less than 1.0%. Least significant change (LSC) was 2.31%. The 10-year probability of significant osteoporotic fractures (including the clinical spine, hip, humerus, or wrist) was predicted using the FRAX tool and accessed through the International Osteoporosis Foundation (IOF) website[1]. Fracture risk was calculated based on age, BMI, femoral neck BMD, and dichotomized risk factors [18].

Statistical analysis

We used SPSS version 26.0 (SPSS Inc., Chicago, IL, United States) to perform all statistical-analyses. All continuous variables were analyzed using the Kolmogorov -Smirnov test to test normality of data. Non-normal data generally exhibit a normal distribution after logarithmic transformation. Normally distributed continuous variables were described as mean ± SD. Moreover, the median (p25-p75) was used to describe skewness

---

[1] http://www.shef.ac.uk/FRAX/

TABLE 1 Comparison of characteristics of patients in the normal, microalbuminuria, and macroalbuminuria groups.

Factors	Sex = Female (N = 219)			
	Control (N = 120)	Microalbuminuria (N = 79)	Macroalbuminuria (N = 20)	P-value
Demographic and history				
Age (years)	66.97 ± 9.33	68.84 ± 9.99	67.15 ± 7.53	0.382
BMI (kg/m2)	24.535 ± 3.214	24.721 ± 3.371	24.293 ± 2.452	0.777
Current smoking (%)	4 (3.3%)	3 (3.8%)	0 (0)	0.684
Current drinking (%)	0 (0%)	0 (0%)	0 (0%)	—
DM Duration (years)	11.0 (7.7–20.0)	16.0 (9.0–20.0)[a]	14.0 (10.25–20.0)	0.029*
History of coronary heart disease	29 (24.2%)	30 (38%)	8 (40%)	0.074
History of hypertension	71 (59.2%)	57 (72.1%)	15 (75%)	0.108
History of cerebral infarction	31 (25.8%)	26 (32.9%)	5 (25%)	0.523
Blood biochemical indicators				
HbA1c (%)	8.60 (7.40–10.65)	9.60 (8.30–11.40)[a]	9.30 (7.28–10.70)	0.023*
HOMA-IR	4.46 (2.39–7.59)	6.00 (3.40–11.62)[a]	5.56 (3.19–8.70)	0.021*
TCH (mmol/L)	4.95 ± 1.29	4.93 ± 1.37	5.48 ± 1.95	0.247
TG (mmol/L)	1.61 (1.12–2.11)	1.84 (1.31–2.33)	1.84 (1.38–2.99)	0.064
LDL (mmol/L)	3.34 ± 1.03	3.27 ± 0.98	3.67 ± 1.23	0.284
HDL (mmol/L)	1.14 (1.00–1.36)	1.11 (0.96–1.27)	1.08 (0.92–1.28)	0.140
Atherogenic coefficient	3.241 ± 1.042	3.356 ± 1.038	4.013 ± 1.166[a] [b]	0.011*
Corrected Ca (mmol/L)	2.29 (2.23–2.35)	2.31 (2.26–2.39)	2.41 (2.26–2.45)[a]	0.012*
P (mmol/L)	1.27 ± 1.18	1.27 ± 0.20	1.30 ± 0.23	0.867
The calcium-phosphorus product	35.45 (32.42–40.13)	36.07 (32.79–39.93)	37.15 (31.46–42.56)	0.303
sCr (umol/L)	66.65 (59.90–79.35)	79.00 (61.40–90.60)[a]	75.30 (62.50–94.15)[a]	0.015*
eGFR (ml/min/1.73 m^2)	79.201 ± 20.941	75.042 ± 24.726	67.666 ± 29.823	0.093
Bone metabolism-related markers				
Total ALP(U/L)	76.00 (62.25–92.78)	83.85 (74.33–99.38)[a]	80.00 (63.00–94.05)	0.024
BALP (ug/L)	14.03 (10.70–17.51)	14.24 (10.80–19.07)	15.05 (11.00–19.80)	0.579
P1NP(ng/mL)	38.05 (31.48–49.30)	36.95 (33.05–42.00)	44.65 (28.55–50.25)	0.820
OC(ng/mL)	12.15 (8.53–14.67)	11.20 (8.71–14.40)	13.81 (11.03–17.91)	0.097
TRACP-5b (U/L)	0.964 ± 0.338	0.959 ± 0.322	0.907 ± 0.342	0.776
CTX (ng/mL)	0.373 (0.245–0.483)	0.359 (0.245–0.530)	0.429 (0.254–0.709)	0.657
25(OH)D (nmol/L)	40.60 (32.77–53.99)	39.67 (34.31–51.45)	34.62 (25.87–47.79)	0.205
PTH(pg/mL)	33.780 (15.07)	32.175 (22.96)	42.70 (42.07)	0.139
Bone mineral density by DXA				
Lumbar1-4 BMD (g/cm^2)	0.875 (0.772–0.964)	0.886 (0.799–0.979)	0.852 (0.761–0.987)	0.663
Femur neck BMD (g/cm^2)	0.645 ± 0.116	0.620 ± 0.120	0.605 ± 0.139	0.188
Total hip BMD (g/cm^2)	0.806 ± 0.123	0.773 ± 0.129	0.775 ± 0.126	0.160

(Continued on following page)

TABLE 1 (*Continued*) Comparison of characteristics of patients in the normal, microalbuminuria, and macroalbuminuria groups.

Factors	Sex = Female (N = 219)			
	Control (N = 120)	Microalbuminuria (N = 79)	Macroalbuminuria (N = 20)	P-value
Fracture risk by FRAX tool				
Major osteoporotic fracture	3.90 (3.08–5.90)	4.50 (3.50–5.85)	5.30 (2.80–6.50)	0.327
Hip Fracture	1.00 (0.48–2.33)	1.40 (0.60–2.50)	1.90 (0.33–2.30)	0.123
Factors	**Sex = Male (N = 216)**			
	Control (N = 138)	**Microalbuminuria (N = 45)**	**Macroalbuminuria (N = 33)**	**P-value**
Demographic and history				
Age (years)	63.55 ± 9.85	70.47 ± 8.28[a]	64.61 ± 9.87[b]	0.000***
BMI (kg/m2)	24.293 ± 3.083	23.655 ± 2.915	25.069 ± 3.152	0.133
Current smoking (%)	51 (37%)	15 (33.3%)	15 (45.5%)	0.538
Current drinking (%)	22 (15.9%)	8 (17.8%)	5 (15.2%)	0.944
DM Duration (years)	9.0 (5.0–15.0)	10.0 (5.5–20.0)	15.0 (6.5–20.0)[a]	0.010**
History of coronary heart disease	37 (26.8%)	12 (26.7%)	15 (45.5%)	0.096
History of hypertension	74 (53.6%)	32 (71.1%)	32 (97%)[a b]	0.000***
History of cerebral infarction	32 (23.2%)	23 (51.5%)[a]	9 (27.3%)	0.002**
Blood biochemical indicators				
HbA1c (%)	8.70 (7.20–13.00)	10.05 (8.45–11.50)	9.30 (7.65–11.35)	0.079
HOMA-IR	4.03 (2.22–6.92)	5.59 (3.38–10.24)[a]	6.16 (2.65–9.12)	0.005**
TCH (mmol/L)	4.37 ± 1.04	4.16 ± 0.91	4.58 ± 1.29	0.315
TG (mmol/L)	1.39 (0.97–1.98)	1.31 (1.00–1.85)	1.45 (1.12–2.44)	0.218
LDL (mmol/L)	2.94 ± 0.83	2.78 ± 0.72	2.98 ± 0.91	0.491
HDL (mmol/L)	1.00 (0.86–1.16)	0.98 (0.84–1.11)	1.00 (0.82–1.15)	0.975
Atherogenic coefficient	3.417 ± 1.192	3.228 ± 1.071	3.631 ± 1.218	0.324
Corrected Ca (mmol/L)	2.26 (2.22–2.33)	2.34 (2.24–2.35)[a]	2.32 (2.27–2.37)	0.005**
P (mmol/L)	1.19 ± 0.18	1.15 ± 0.19	1.19 ± 0.22	0.511
The calcium-phosphorus product	33.55 (28.98–37.13)	32.86 (29.05–38.22)	32.86 (29.18–38.04)	0.814
sCr (umol/L)	84.20 (74.00–96.30)	85.00 (73.25–101.75)	89.90 (75.50–126.00)	0.096
eGFR (ml/min/1.73m2)	85.262 ± 20.868	81.789 ± 24.546	78.958 ± 26.756	0.300
Bone metabolism-related markers				
Total ALP(U/L)	76.20 (66.60–90.00)	95.15 (76.30–109.75)[a]	84.40 (64.50–97.35)	0.023
BALP (ug/L)	12.70 (10.55–18.23)	14.79 (10.02–17.30)	12.41 (10.51–16.05)	0.444
P1NP(ng/ml)	36.40 (30.20–42.63)	37.80 (30.90–43.40)	31.90 (29.00–38.95)	0.207
OC(ng/ml)	9.71 (8.23–12.70)	9.70 (8.01–12.32)	10.00 (6.96–12.39)	0.440
TRACP-5b (U/L)	0.874 ± 0.311	0.933 ± 0.256	0.834 ± 0.363	0.349
CTX (ng/ml)	0.305 (0.223–0.476)	0.313 (0.232–0.418)	0.249 (0.190–0.369)	0.745

(Continued on following page)

TABLE 1 (*Continued*) Comparison of characteristics of patients in the normal, microalbuminuria, and macroalbuminuria groups.

Factors	**Sex = Male (N = 216)**			
	Control (N = 138)	**Microalbuminuria (N = 45)**	**Macroalbuminuria (N = 33)**	**P-value**
25(OH)D (nmol/L)	45.23 (34.62–57.09)	40.07 (28.93–46.11)[a]	30.15 (20.60–46.69)[a b]	0.000***
PTH(pg/ml)	40.351 ± 18.555	34.645 ± 13.559	35.962 ± 17.073	0.110
Bone mineral density by DXA				
Lumbar1-4 BMD (g/cm^2)	0.960 (0.885–1.095)	0.991 (0.906–1.095)	1.038 (0.878–1.199)	0.430
Femur neck BMD (g/cm^2)	0.728 ± 0.117	0.681 ± 0.117	0.714 ± 0.126	0.071
Total hip BMD (g/cm^2)	0.900 ± 0.133	0.841 ± 0.150[a]	0.901 ± 0.125	0.035*
Fracture risk by FRAX tool				
Major osteoporotic fracture	2.25 (1.70–2.90)	3.25 (2.50–4.32)	2.40 (1.80–2.98)	0.105
Hip Fracture	0.60 (0.30–1.13)	0.90 (0.60–1.55)[a]	0.70 (0.30–1.50)	0.014*

Values are shown as means ± SD, median (p25-p75), or number (percentage).

[a] $p < 0.05$ compared with the normal group.

[b] $p < 0.05$ compared with the microalbuminuria group.

Abbreviations: BMI, body mass index; DM, diabetes mellitus; HbA1c, glycosylated hemoglobin; HOMA-IR, homeostatic model assessment for insulin resistance; HDL, high density lipoprotein; LDL, low density lipoprotein; TCH, total cholesterol; TG, triglyceride; corrected Ca, corrected calcium; P, phosphorus; sCr, serum creatinine; eGFR, glomerular filtration rate; Total ALP, total alkaline phosphatase; BALP, bone alkaline phosphatase; OC, osteocalcin; TRACP-5b, tartrate-resistant acid phosphatase-5b; CTX, C-terminal cross-linking telopeptide of type I collagen; P1NP, procollagen 1 intact N-terminal; 25(OH)D, 25-hydroxyvitamin D; PTH, parathyroid hormone; DXA, dual-energy X-ray absorptiometry; BMD: bone mineral density. *$p < .05$, **$p < .01$, ***$p < 0.001$.

distribution variables. These skewness distribution variables were transformed using a logarithmic transformation to make them normally distributed and render them suitable for analysis of variance (ANOVA). Categorical variables were reported as numbers and percentages. One-way ANOVA was applied to compare the baseline data among the three groups for continuous variables. The least significant difference (LSD) method was used to compare baseline data between the two groups.

Furthermore, the chi-square test was used to compare the categorical variables. The Pearson correlation was conducted to analyze whether partial discrepant variables were associated with hip fractures in males. Multiple regression analysis was used to assess the independent associations between various clinical factors and the risk of hip fracture. We included variables that showed potential associations ($p < 0.1$ according to Pearson correlation) in the multiple linear regression model. Values of p less than 0.05 were considered statistically significant.

Results

Comparison of characteristics of patients in the control, microalbuminuria, and macroalbuminuria groups

Table 1 showed the clinical characteristics of 219 post-menopausal women and 216 men. The average age of all patients was over 65 years old, and there were no differences observed among the three groups of females. In men, the mean age of the microalbuminuria group (70.47 ± 8.28) was higher than that of the control group (63.55 ± 9.85) and the macroalbuminuria group (64.61 ± 9.87) ($p < 0.001$), while there was no significant difference between the control and macroalbuminuria groups. In addition, at baseline, the duration of diabetes, homeostatic model assessment for insulin resistance (HOMA-IR), serum corrected calcium level, and serum total alkaline phosphatase (ALP) level were significantly different among three groups both in women and men (all $p < 0.05$; Table 1). In women, the microalbuminuria group had longer T2DM duration [16.0 (9.0–20.0), $p = 0.029$] and HOMA-IR [6.0 (3.40–11.62), 0.021] than control group. For men, the macroalbuminuria group had longer T2DM duration [15.0 (6.5–20.0), $p = 0.010$] than control group. Regardless of sex, individuals with T2DM with microalbuminuria had higher total ALP levels [women: 83.85 (74.33–99.38) U/L, $p = 0.024$; 95.15 (76.30–109.75)U/L, $P = 0.023$] than control groups. However, the macroalbuminuria group of women had higher corrected Ca [2.41 (2.26–2.45) mmol/L, $p = 0.012$] level than control group and the microalbuminuria group of men had had higher corrected Ca [2.34 (2.24–2.35) mmol/L, $p = 0.005$] level than control group. The significant differences in atherogenic coefficient, glycosylated haemoglobin and serum creatinine levels were found among the three groups of post-menopausal women (all $p < 0.05$; Table 1), no finding in men. In women, the macroalbuminuria group had higher atherogenic coefficient

TABLE 2 Correlation analysis of different characteristics with Hip Fracture in male.

Indexes	r	P
Age	0.463	<0.001***
DM Duration	0.154	0.023*
History of hypertension	0.043	0.526
History of cerebral infarction	0.223	0.001***
Corrected Ca	0.140	0.040*
HOMA-IR	−0.067	0.325
Total ALP	0.064	0.351
25(OH)D	−0.134	0.050*
ACR	0.176	0.010**
Lumbar 1-4 BMD	−0.428	<0.001***
Femur neck BMD	−0.909	<0.001***
Total hip BMD	−0.720	<0.001***

Abbreviations: DM, diabetes mellitus; corrected Ca, corrected calcium; P, phosphorus; sCr, serum creatinine; eGFR, glomerular filtration rate; Total ALP, total alkaline phosphatase; 25(OH)D, 25-hydroxyvitamin D; ACR, albumin/creatinine ratio; BMD, bone mineral density. *p < .05, **p < .01, ***p < 0.001.

TABLE 3 Multiple regression analysis of Hip Fracture in male.

Indexes	β	Lower limit of 95% CI	Upper limit of 95% CI	P-value
Age	0.009	−0.002	0.020	0.102
DM Duration	0.015	0.003	0.028	0.018*
History of cerebral infarction	0.021	−0.196	0.237	0.850
corrected Ca	0.104	−0.446	0.653	0.711
25(OH)D	−0.002	−0.007	0.004	0.509
ACR	0.003	0.000	0.006	0.044*
Lumbar 1-4 BMD	0.098	−0.625	0.821	0.790
Femur neck BMD	−6.765	−8.247	−5.283	<0.001***
Total hip BMD	0.336	−0.997	1.669	0.620

Abbreviations: DM, diabetes mellitus; corrected Ca, corrected calcium; 25(OH)D, 25-hydroxyvitamin D; ACR, albumin/creatinine ratio; BMD, bone mineral density. *p < .05, ***p < 0.001.

(4.013 ± 1.166, p = 0.011) than other two groups, the microalbuminuria group had higher glycosylated haemoglobin level [9.6%, (8.30%–11.40%) p = 0.023] than control group and the macroalbuminuria group had higher serum creatinine level [75.30 (62.50–94.15) μmol/L, p = 0.015) than control group. Intergroup differences in hypertension, history of cerebral infarction, serum 25(OH)D level, total hip BMD measurements, and hip fracture were observed in men but not in women (Table 1). In men, the microalbuminuria group had lower total hip BMD (0.841 ± 0.150 g/cm^2, p = 0.035), higher history of cerebral infarction prevalence (71.1%, p < 0.001) and a higher hip fracture risk [0.90 (0.60–1.55), p = 0.014] compared to the other tow groups. In both women and men, there were no significant differences observed in other indices among the control, microalbuminuria, and macroalbuminuria groups (all p > 0.05; Table 1).

Correlation analysis of clinical characteristics with hip fracture in men

Bivariate correlation analysis showed that several clinical characteristics in men with type 2 diabetes mellitus, including age (r = 0.463, p < 0.001), duration of type 2 diabetes mellitus (r = 0.154, p = 0.023), history of cerebral infarction (r = 0.223, p = 0.050), serum corrected calcium level (r = 0.140, p = 0.040), and

ACR ($r = 0.176$, $p = 0.010$) were positively related to hip fracture. Bone mineral density (BMD) measurements at the lumbar vertebrae ($r = -0.428$, $p < 0.001$), femoral neck ($r = -0.909$, $p < 0.001$) and total hip ($r = -0.720$, $p < 0.001$), as well as with serum 25(OH)D levels ($r = -0.134$, $p = 0.050$) showed negative association with hip fractures. However, history of hypertension, HOMA-IR, and serum total ALP level were not significantly correlated with the total hip fracture in men ($p > 0.05$) (Table 2).

Multiple linear regression analysis of hip fracture in men

For men with type 2 diabetes mellitus, multiple linear regression analysis was performed to identify independent influence factors of hip fracture. Femoral neck BMD was negatively correlated with hip fracture risk ($\beta = -6.765$, $p < 0.001$) (Table 3). In contrast, T2DM duration ($\beta = 0.015$, $p = 0.018$) and ACR ($\beta = 0.003$, $p = 0.044$) were positively associated with hip fracture risk. And the results remained statistically significant after further adjustment by age, history of cerebral infarction, serum corrected Ca and 25(OH)D levels, urinary ACR level, and areal BMDs (Table 3).

Results were inconsistent in women, hip fracture risk didn't alter by changes in urinary microalbuminuria level in postmenopausal women with T2DM.

Discussion

Type 2 diabetes mellitus has been reported to be associated with an increased risk of fracture [19–21], and the increased hip fracture risk appears to be the most obvious [19]. However, the underlying causes and risk factors still require further investigation. Several large clinical studies have found an increased fracture risk among individuals with T2DM. One Women's Health Initiative Observational Study (WHI-OS), involving 93,676 postmenopausal women with T2DM, adjusted for frequent falls and increased areal BMDs, revealing heightened risk of hip, foot, and spine fractures [22]. Secondly, conducted in 5994 men (≥65 years), found that non-vertebral fracture risk was higher in patients with diabetes who were using insulin compared with non-diabetic patients (HR1.74; 95%CI:1.31–2.69) [23]. In addition, in a recent meta-analysis of 15 studies ($n = 852705$), people with type 2 diabetes had a 35% higher incidence of fracture [24].

One of the goals of this cross-sectional study was to investigate the relationship between urinary ACR levels and fracture risk among elderly patients with T2DM, who had an eGFR greater than 30 mL/min/1.73 m^2 and average serum creatine levels less than 100 mmol/L. We found that urinary ACR levels were associated with a slight but statistically significant increase in hip fracture risk among men with T2DM. Specifically, hip fracture risk appeared higher in men with ACR levels equal to or greater than 30 mg/g but less than 300 mg/g compared to those with levels below 30 mg/g. However, so few men had macroalbuminuria that we found no difference in the risk of hip fracture between the group with macroalbuminuric group and the other two groups in our study.

The urinary albumin-to-creatinine ratio (ACR) reflects the status of diabetic microangiopathy [25]. Microcirculation significantly influences bone health [26, 27]. Previous large clinical studies have shown a correlation between urinary ACR levels and fracture risk. A mean follow-up of 4.6 years from the ONTARGET and TRANSCEND trials found that baseline albuminuria levels were associated with increased risk of hip and pelvic fractures. Importantly, this association was consistent across sexes and between diabetic and non-diabetic populations [28]. Barzilay et al. found that urinary microalbumin levels were linked to an increased risk of hip fractures in older women, but not in men [29]. A prospective study of community-dwelling older men aged ≥65 years found no independent association of urine albumin with the risk of incident fracture [10]. The risk estimates from our current study are not fully consistent with previous studies. The current study focused on individuals with type 2 diabetes, whose distinctive metabolic characteristics may alter fracture susceptibility compared to older adults without type 2 diabetes. Despite including a limited number of patients with macroalbuminuria, we still found a dose-dependent relationship between urinary ACR levels and the risk of hip fractures, thereby substantiating our finding. However, the effect of macroalbuminuria ACR levels on hip fracture risk observed in this study was too small to be used for clinical prognostic purposes. Further research may explore its potential role in larger cohorts populations.

The impact of urinary ACR levels on fracture risk in patients with type 2 diabetes can be attributed to several key factors. Firstly, inadequate blood flow in the bone microvasculature can lead to increased cortical porosity. This change in bone microarchitecture results in reduced bone strength and an increased likelihood of fractures [30, 31]. Secondly, when microalbuminuria occurs, levels of inflammatory cytokines are typically elevated [32]. While elevated levels of inflammatory cytokines are associated with osteoporosis [33], which indirectly increases the risk of fracture. Thirdly, microangiopathy contributes to muscle and nerve damage, thereby increasing the risk of falls.

At the same time, the conclusion of our study corroborates previous findings indicating that the duration of type 2 diabetes independently contributes to the fracture risk of patients with T2DM [6, 34, 35]. A prospective study involving 3,654 subjects aged 49 years and older found that longer duration of diabetes is associated with an increased fracture risk [36]. Another retrospective, population-based matched cohort study spanning from 1984 to 2004 found that long-term diabetes is associated with an increased fracture risk, whereas newly diagnosed diabetes is associated with a reduced fracture risk [37]. The reason why the duration of type 2 diabetes remains associated with fracture risk after adjusting for effects such as bone density may be multifactorial. Firstly, patients with longer disease duration tend to have more comorbidities and poorer nutritional status, including decreased muscle strength and muscle mass, leading to an increased risk of falls [38]. Secondly, as the disease progresses, there is an increase in advanced glycation end products in bones, leading to decreased bone strength.

However, we didn't observe the similar results in post-menopausal women. Hip fracture risk didn't alter by changes in urinary microalbuminuria level in postmenopausal women with T2DM. This may be attributed to the following factors. Firstly, there is a significant disparity in fracture risk between men and women. Previous studies have shown that osteoporotic or fragility fractures affect one in two women and one in five men who are older than 50 [39]. Men usually have a higher peak bone mass compared to women. This means that, all else being equal, men start with a stronger skeletal structure, reducing their fracture risk. Women, especially postmenopausal women, experience a rapid decline in bone density due to hormonal changes (mainly the decrease in estrogen levels), which makes them more prone to osteoporosis and fractures. In addition to lower bone mineral density, women, especially older women, are more susceptible to falls due to decreased muscle strength, balance issues and other factors like a higher body fat percentage, all of which increase their risk of fractures [40]. This rationale also underpinned the separate analysis of fracture risk for men and women in this study. Secondly, the effect of ACR on fracture risk in women is diminished by other key factors, such as the post-menopausal decline in bone mineral density due to reduced estrogen levels, as well as the heightened fracture risk linked to decreased muscle mass. Thus, future studies with larger sample sizes and more rigorous methodologies should aim to incorporate as many relevant fracture risk factors as possible to more accurately assess their individual contributions and facilitate the development of a more comprehensive fracture risk assessment model.

In addition, we observed the HbA1c and HOMA-IR levels were high. HOMA-IR in the controls was >4 and even higher in the other groups. While HbA1c% was >8.6 in all groups. These findings suggested that patients didn't achieve optimal diabetes management, placing them at an increased risk of both non-fatal and fatal cardiovascular events. This could be attributed to that this study included patients who visited Tongji Hospital in Shanghai. They typically sought medical care due to symptoms related to poor blood glucose control. Consequently, we observed that patients generally had suboptimal blood glucose levels. Moreover, recent research indicates that achieving a single blood glucose control target is no longer the sole goal in managing diabetes. Preventing non-fatal and fatal cardiovascular events is a key goal in managing type 2 diabetes patients [41]. In recent years, there has also been increasing concern about the high risk of fractures in diabetic patients. Therefore, reducing the risk of fractures in diabetic patients is also becoming one of the management goals for diabetes.

Here are several strengths of this study: (1) We analyzed bone metabolism and fracture risk separately for men and women to rule out the influence of gender differences; (2) Cases with eGFR>30 mL/min/1.73 m^2 were selected; (3) Study participants were categorized into three groups based on ACR: the normal group (ACR<30 mg/g), the microalbuminuria group (30 mg/g ≤ ACR≤300 mg/g), and macroalbuminuria group (ACR >300 mg/g), which may well reflect the severity of diabetic nephropathy; (4) BMD is a crucial factor determining bone strength and fracture susceptibility, but most brittle fractures occur in individuals without osteoporosis. Therefore, we chose the FRAX tool to calculate the probability better.

There are limitations to this study: (1) We have taken too few cases, especially people with T2DM with macroalbuminuria; (2) The medical history may be incomplete and associated with other undetected diseases; (3) Brittle fractures were not documented; (4) Urine ACR was grouped according to a single measurement. An abnormal level of ACR was confirmed with at least one further measurement because ACR has high within-person variability from day to day [42, 43]. (5) Fracture risk assessment tool (FRAX) widely used in the past underestimates fracture risk in people with T2DM [44], so our analyses may underestimate the impact of urinary ACR level on fracture. (6) Whether urine ACR directly affects bone microarchitecture is still unknown.

Conclusion

In conclusion, we found that increased urinary ACR level and duration of T2DM were associated with an increased hip fracture risk among older men with T2DM. In addition, there was no difference between BMD and fracture risk among the three groups by urinary ACR level in postmenopausal women. In the future, it may be possible to reduce fracture risk in patients with T2DM by delaying the process of albuminuria and avoiding factors that increase fracture risk.

Author contributions

LS, HD, and HW designed the experiment. HD, HW, GL, YW, DH, and XZ performed the experiments. HD wrote the draft manuscript. HW, XZ, and LS revised the manuscript. All authors contributed to the article and approved the submitted version.

Data availability

The original contributions presented in the study are included in the article/supplementary material, further inquiries can be directed to the corresponding author.

Ethics statement

The study has passed the Ethics Committee of Tongji Hospital and Tongji University School of Medicine and conforms to the Declaration of Helsinki. All participants signed informed consent. The studies were conducted in accordance with the local legislation and institutional requirements. Written informed consent for participation in this study was provided by the participants' legal guardians/next of kin.

Funding

The author(s) declare that financial support was received for the research, authorship, and/or publication of this article. Clinical Research Project of Tongji Hospital of Tongji University (Grant No. ITJ(QN)2002) to GL, Clinical Research Project of Tongji Hospital of Tongji University to LS (Grant No. ITJ(ZD)1904), Shanghai Science and Technology Foundation to LS (19ZR1448600) and Medical Innovation Research Project of Shanghai Municipal Commission of Science and Technology (22Y11904600) to LS.

Conflict of interest

The author(s) declared no potential conflicts of interest with respect to the research, authorship, and/or publication of this article.

References

1. Sun H, Saeedi P, Karuranga S, Pinkepank M, Ogurtsova K, Duncan BB, et al. IDF Diabetes Atlas: global, regional and country-level diabetes prevalence estimates for 2021 and projections for 2045. *Diabetes Res Clin Pract* (2022) **183**:109119. doi:10.1016/j.diabres.2021.109119

2. Hofbauer LC, Busse B, Eastell R, Ferrari S, Frost M, Müller R, et al. Bone fragility in diabetes: novel concepts and clinical implications. *The Lancet Diabetes & Endocrinol* (2022) **10**(3):207–20. doi:10.1016/s2213-8587(21)00347-8

3. Wang J, You W, Jing Z, Wang R, Fu Z, Wang Y. Increased risk of vertebral fracture in patients with diabetes: a meta-analysis of cohort studies. *Int Orthopaedics* (2016) **40**(6):1299–307. doi:10.1007/s00264-016-3146-y

4. Norris R, Parker M. Diabetes mellitus and hip fracture: a study of 5966 cases. *Injury* (2011) **42**(11):1313–6. doi:10.1016/j.injury.2011.03.021

5. Papatheodorou K, Papanas N, Banach M, Papazoglou D, Edmonds M. Complications of diabetes 2016. *J Diabetes Res* (2016) **2016**:1–3. doi:10.1155/2016/6989453

6. Dede AD, Tournis S, Dontas I, Trovas G. Type 2 diabetes mellitus and fracture risk. *Metabolism* (2014) **63**(12):1480–90. doi:10.1016/j.metabol.2014.09.002

7. Hampson G, Elder GJ, Cohen-Solal M, Abrahamsen B. A review and perspective on the assessment, management and prevention of fragility fractures in patients with osteoporosis and chronic kidney disease. *Endocrine* (2021) **73**(3):509–29. doi:10.1007/s12020-021-02735-9

8. Daya N, Voskertchian A, Schneider ALC, Ballew S, McAdams DeMarco M, Coresh J, et al. Kidney function and fracture risk: the atherosclerosis risk in communities (ARIC) study. *Am J Kidney Dis* (2016) **67**(2):218–26. doi:10.1053/j.ajkd.2015.06.020

9. Saran U, Gemini Piperni S, Chatterjee S. Role of angiogenesis in bone repair. *Arch Biochem Biophys* (2014) **561**:109–17. doi:10.1016/j.abb.2014.07.006

10. Fink HA, Vo TN, Langsetmo L, Barzilay JI, Cauley JA, Schousboe JT, et al. Association of increased urinary albumin with risk of incident clinical fracture and rate of hip bone loss: the osteoporotic fractures in men study. *J Bone Mineral Res* (2017) **32**(5):1090–9. doi:10.1002/jbmr.3065

11. Barzilay JI, Bůžková P, Fink HA, Cauley JA, Robbins JA, Garimella PS, et al. Systemic markers of microvascular disease and bone mineral density in older adults: the cardiovascular health study. *Osteoporos Int* (2016) **27**(11):3217–25. doi:10.1007/s00198-016-3649-9

12. American Diabetes Association. 2. Classification and diagnosis of diabetes: standards of medical care in diabetes-2021. *Diabetes Care* (2021) **44**(Suppl. 1):S15–s33. doi:10.2337/dc21-s002

13. Matthews DR, Hosker JP, Rudenski AS, Naylor BA, Treacher DF, Turner RC. Homeostasis model assessment: insulin resistance and beta-cell function from fasting plasma glucose and insulin concentrations in man. *Diabetologia* (1985) **28**(7):412–9. doi:10.1007/bf00280883

14. Ahmadvand H, Ghasemi-Dehnoo M. Antiatherogenic, hepatoprotective, and hypolipidemic effects of coenzyme Q10 in alloxan-induced type 1 diabetic rats. *ARYA Atheroscler* (2014) **10**(4):192–8.

15. Wu L, Gong Q, Na R, Mao X, Zheng X, Liu Q, et al. Dipeptidyl peptidase 4 concentration influenced by serum insulin levels rather than arterial stiffness index in type 2 diabetics. *Int J Clin Exp Med* (2015) **8**(4):6236–41.

16. Aziz N, Mehmood MH, Mandukhal SR, Bashir S, Raoof S, Gilani AH. Antihypertensive, antioxidant, antidyslipidemic and endothelial modulating activities of a polyherbal formulation (POL-10). *Vasc Pharmacol* (2009) **50**(1-2):57–64. doi:10.1016/j.vph.2008.09.003

17. Fotschki B, Juśkiewicz J, Jurgoński A, Kosmala M, Milala J, Zduńczyk Z, et al. Grinding levels of raspberry pomace affect intestinal microbial activity, lipid and glucose metabolism in Wistar rats. *Food Res Int* (2019) **120**:399–406. doi:10.1016/j.foodres.2019.03.014

18. Kanis JA, Johansson H, Harvey NC, McCloskey EV. A brief history of FRAX. *Arch Osteoporos* (2018) **13**(1):118. doi:10.1007/s11657-018-0510-0

19. Hamann C, Kirschner S, Günther KP, Hofbauer LC. Bone, sweet bone--osteoporotic fractures in diabetes mellitus. *Nat Rev Endocrinol* (2012) **8**(5):297–305. doi:10.1038/nrendo.2011.233

20. Napoli N, Chandran M, Pierroz DD, Abrahamsen B, Schwartz AV, Ferrari SL. Mechanisms of diabetes mellitus-induced bone fragility. *Nat Rev Endocrinol* (2017) **13**(4):208–19. doi:10.1038/nrendo.2016.153

21. Vilaca T, Schini M, Harnan S, Sutton A, Poku E, Allen IE, et al. The risk of hip and non-vertebral fractures in type 1 and type 2 diabetes: a systematic review and meta-analysis update. *Bone* (2020) **137**:115457. doi:10.1016/j.bone.2020.115457

22. Bonds DE, Larson JC, Schwartz AV, Strotmeyer ES, Robbins J, Rodriguez BL, et al. Risk of fracture in women with type 2 diabetes: the women's health initiative observational study. *The J Clin Endocrinol & Metab* (2006) **91**(9):3404–10. doi:10.1210/jc.2006-0614

23. Napoli N, Strotmeyer ES, Ensrud KE, Sellmeyer DE, Bauer DC, Hoffman AR, et al. Fracture risk in diabetic elderly men: the MrOS study. *Diabetologia* (2014) **57**(10):2057–65. doi:10.1007/s00125-014-3289-6

24. Koromani F, Oei L, Shevroja E, Trajanoska K, Schoufour J, Muka T, et al. Vertebral fractures in individuals with type 2 diabetes: more than skeletal complications alone. *Diabetes Care* (2020) **43**(1):137–44. doi:10.2337/dc19-0925

25. Wukich DK. Diabetes and its negative impact on outcomes in orthopaedic surgery. *World J Orthopedics* (2015) **6**(3):331–9. doi:10.5312/wjo.v6.i3.331

26. Prisby RD, Ramsey MW, Behnke BJ, Dominguez JM, 2nd, Donato AJ, Allen MR, et al. Aging reduces skeletal blood flow, endothelium-dependent vasodilation, and NO bioavailability in rats. *J Bone Mineral Res* (2007) **22**(8):1280–8. doi:10.1359/jbmr.070415

27. Shanbhogue VV, Hansen S, Frost M, Brixen K, Hermann AP. Bone disease in diabetes: another manifestation of microvascular disease? *The Lancet Diabetes & Endocrinol* (2017) **5**(10):827–38. doi:10.1016/s2213-8587(17)30134-1

28. Barzilay JI, Gao P, Clase CM, Mente A, Mann JF, Sleight P, et al. Albuminuria and rapid loss of GFR and risk of new hip and pelvic fractures. *Clin J Am Soc Nephrol* (2013) **8**(2):233–40. doi:10.2215/cjn.06640712

29. Barzilay JI, Bůžková P, Chen Z, de Boer IH, Carbone L, Rassouli NN, et al. Albuminuria is associated with hip fracture risk in older adults: the cardiovascular health study. *Osteoporos Int* (2013) **24**(12):2993–3000. doi:10.1007/s00198-013-2389-3

30. Samakkarnthai P, Sfeir JG, Atkinson EJ, Achenbach SJ, Wennberg PW, Dyck PJ, et al. Determinants of bone material strength and cortical porosity in patients with type 2 diabetes mellitus. *The J Clin Endocrinol & Metab* (2020) **105**(10): e3718–3729. doi:10.1210/clinem/dgaa388

31. Samelson EJ, Demissie S, Cupples LA, Zhang X, Xu H, Liu CT, et al. Diabetes and deficits in cortical bone density, microarchitecture, and bone size: framingham HR-pQCT study. *J Bone Mineral Res* (2018) **33**(1):54–62. doi:10.1002/jbmr.3240

32. Barzilay JI, Peterson D, Cushman M, Heckbert SR, Cao JJ, Blaum C, et al. The relationship of cardiovascular risk factors to microalbuminuria in older adults with or without diabetes mellitus or hypertension: the cardiovascular health study. *Am J Kidney Dis* (2004) **44**(1):25–34. doi:10.1053/j.ajkd.2004.03.022

33. Redlich K, Smolen JS. Inflammatory bone loss: pathogenesis and therapeutic intervention. *Nat Rev Drug Discov* (2012) **11**(3):234–50. doi:10.1038/nrd3669

34. Compston J. Type 2 diabetes mellitus and bone. *J Intern Med* (2018) **283**(2): 140–53. doi:10.1111/joim.12725

35. Janghorbani M, Feskanich D, Willett WC, Hu F. Prospective study of diabetes and risk of hip fracture: the Nurses' Health Study. *Diabetes Care* (2006) **29**(7): 1573–8. doi:10.2337/dc06-0440

36. Ivers RQ, Cumming RG, Mitchell P, Peduto AJ. Diabetes and risk of fracture: the blue mountains eye study. *Diabetes Care* (2001) **24**(7):1198–203. doi:10.2337/diacare.24.7.1198

37. Leslie WD, Lix LM, Prior HJ, Derksen S, Metge C, O'Neil J. Biphasic fracture risk in diabetes: a population-based study. *Bone* (2007) **40**(6):1595–601. doi:10.1016/j.bone.2007.02.021

38. Ganz DA, Latham NK. Prevention of falls in community-dwelling older adults. *N Engl J Med* (2020) **382**(8):734–43. doi:10.1056/nejmcp1903252

39. Rizzoli R, Biver E, Brennan-Speranza TC. Nutritional intake and bone health. *The Lancet Diabetes & Endocrinol* (2021) **9**(9):606–21. doi:10.1016/s2213-8587(21)00119-4

40. Hong C, Choi S, Park M, Park SM, Lee G. Body composition and osteoporotic fracture using anthropometric prediction equations to assess muscle and fat masses. *J Cachexia Sarcopenia Muscle* (2021) **12**(6):2247–58. doi:10.1002/jcsm.12850

41. Kristensen SL, Rørth R, Jhund PS, Docherty KF, Sattar N, Preiss D, et al. Cardiovascular, mortality, and kidney outcomes with GLP-1 receptor agonists in patients with type 2 diabetes: a systematic review and meta-analysis of cardiovascular outcome trials. *The Lancet Diabetes & Endocrinol* (2019) **7**(10): 776–85. doi:10.1016/s2213-8587(19)30249-9

42. American Diabetes Association. Standards of medical care in diabetes--2009. *Diabetes Care* (2009) **32**:S13–61. doi:10.2337/dc09-s013

43. Miller WG, Bruns DE, Hortin GL, Sandberg S, Aakre KM, McQueen MJ, et al. Current issues in measurement and reporting of urinary albumin excretion. *Clin Chem* (2009) **55**(1):24–38. doi:10.1373/clinchem.2008.106567

44. Schwartz AV, Vittinghoff E, Bauer DC, Hillier TA, Strotmeyer ES, Ensrud KE, et al. Association of BMD and FRAX score with risk of fracture in older adults with type 2 diabetes. *Jama* (2011) **305**(21):2184–92. doi:10.1001/jama.2011.715

Experimental Biology and Medicine

TYPE Original Research
PUBLISHED 15 January 2025
DOI 10.3389/ebm.2024.10281

*CORRESPONDENCE
Dingwen Xu,
✉ dingwenxu@bjmu.edu.cn

RECEIVED 11 June 2024
ACCEPTED 12 December 2024
PUBLISHED 15 January 2025

CITATION
Su L, Li J, Qin L, Feng Y and Xu D (2025) Function of formyl peptide receptor 2 in adriamycin resistance of breast cancer. *Exp. Biol. Med.* 249:10281.
doi: 10.3389/ebm.2024.10281

Function of formyl peptide receptor 2 in adriamycin resistance of breast cancer

Landi Su, Jingjing Li, Li Qin, Yang Feng and Dingwen Xu*

School of Medicine, Yangzhou Polytechnic College, Yangzhou, Jiangsu, China

Abstract

FPRL2 has been shown to be associated with a variety of tumours but has not been well studied in breast cancer. In this study, We combine molecular biology techniques with bioinformatics to analyze the role of FPRL2 in breast cancer and adriamycin resistance. By utilizing bioinformatics, we mine TCGA and GEO public databases to assess FPRL2 expression in breast cancer patients and its correlation with patient prognosis. Additionally, we employ the DepMap tool to probe the CCLE database, examining the relationship between FPRL2 gene effects and adriamycin sensitivity. Chemosensitivity of Adriamycin in breast cancer cells was tested by CCK-8 method. The apoptosis of breast cancer cells was determined by flow cytometry assay. Expression of p-ERK5 and p-AKT was determined by Western blot assay. Our results indicate that the expression level of FPRL2 in tumor tissues of breast cancer patients is significantly higher than that in normal tissues, and it correlates with poor prognosis in patients. Furthermore, the expression level of FPRL2 in tumor tissues of adriamycin-resistant breast cancer patients is also significantly higher than that in adriamycin-sensitive patients. The IC_{50} (Inhibitory Concentration 50). Of Adriamycin was significantly lower in FPRL2 silenced cells than those control cells. The apoptosis was markedly increased in FPRL2-silenced cells. p-ERK5 and p-AKT in breast cancer cells was significantly reduced after FPRL2 knocked down. In Conclusion, FPRL2 mediates Adriamycin resistance in breast cancer cells, and knockdown of FPRL2 increased apoptosis and decreased Adriamycin resistance in breast cancer cells.

KEYWORDS

FPRL2, breast cancer, adriamycin resistance, apoptosis, molecular docking

Impact statement

Our results demonstrate for the first time that FPRL2 is highly expressed in breast cancer and adriamycin-resistant breast cancer cells and that knockdown of FPRL2 increases adriamycin-induced apoptosis in breast cancer cells. Our results provided clues for overcoming adriamycin resistance in breast cancer.

Introduction

Breast cancer ranks as the most prevalent cancer type among women. Recent data indicates approximately 2.3 million new cases globally. In 112 countries, breast cancer serves as a leading cause of cancer-related deaths. Furthermore, estimates suggest that by 2040, this figure will surpass 3 million cases [1]. Breast cancer surgery plus chemotherapy is still the primary means of treatment for breast cancer. Surgical treatment of breast cancer has made significant progress, and minimally invasive treatment of breast cancer has dramatically improved the quality of life of patients without affecting the efficacy of surgery [2]. However, resistance to chemotherapy drugs is still a significant cause of breast cancer recurrence, metastasis, and death [3, 4].

The family of G protein-coupled receptors (GPCRs) is involved in a variety of physiological functions, including tumor growth and metastasis, and aberrantly expressed or aberrantly activated GPCRs are involved in various aspects of cancer progression such as tumor growth, invasion, migration, survival, and metastasis [5], which has led to the emergence of GPCRs as an essential target for tumor drug resistance [6]. Formyl peptide receptors (FPRs) are cell surface pattern recognition receptors (PRRs) that belong to the evolutionarily conserved family of G protein-coupled receptors (GPCRs). The formyl peptide receptor family consists of the Formyl peptide receptor (FPR), the Formyl peptide receptor-like 1 (FPRL1), and the Formyl peptide receptor-like 2 (FPRL2). Formyl peptide receptors are highly expressed in phagocytic leukocytes, and activation of the receptors by agonists triggers a series of signaling events that result in leukocyte activation, cell chemotaxis, phagocytosis, release of inflammatory mediators, and other biological effects, thus playing an essential role in the host defense response against pathogen infection [7]. The distribution of the formyl peptide receptor is not limited to phagocytosis of leukocytes but is also expressed in tumor cells such as colon cancer, which enhances drug resistance, and knockdown of FPR2 reduces the tumorigenicity of colon cancer [8, 9]. However, its expression on breast cancer tissues and its biological role have been little studied. This study investigates the expression of FPRL2 in breast cancer and explores the relationship between FPRL2 and doxorubicin resistance in breast cancer.

Materials and methods

Materials

Cell lines

The human breast adenocarcinoma resistant to Adriamycin cell line MCF-7/ADM and human adenocarcinoma cell line MCF-7 were purchased from the Shanghai Institute of Biochemistry and Cell Technology, Chinese Academy of Sciences.

Reagents and consumables

Adriamycin for injection was purchased from Shanghai Yuan Ye Company; DMEM medium and fetal bovine serum were purchased from Gibco, USA; RNA extraction kit was purchased from Qiagen, United States; CCK-8 (cell counting kit-8) kit was purchased from Tongrentang, Japan; Lipofectamine™ RNAiMAX was purchased from Thermo Electron, United States; RevertAidTM First Strand cDNA Synthesis Kit was purchased from Fermentas, Canada; Realtime PCR Kit ABI SYBR Green Master Mix was purchased from Invitrogen, United States; Realtime PCR Kit ABI SYBR Green Master Mix was purchased from Invitrogen, United States; Reverse Transcription RevertAidTM First Strand cDNA Synthesis Kit was purchased from Fermentas, Canada; Real-time PCR kit ABI SYBR Green Master Mix was purchased from Invitrogen, United States; RNase and propidium iodide (PI) were purchased from Sigma; rabbit anti-AKT, p-AKT and GAPDH were purchased from Cell Signaling, United States; rabbit anti-FPRL2 antibody, FPRL2 siRNA and its control siRNA, and HRP-labeled goat-anti-rabbit IgG were purchased from Santa Cruz, United States; immunohistochemistry assay SuperPictureTM 3rd Gen IHC Detection kit was purchased from Invitrogen, United States. The IHC Detection kit was purchased from Invitrogen, United States.

Methodology

Bioinformatics analysis

TCGA breast cancer data and METABRIC breast cancer data were downloaded by cBioportal, and then FPRL2 expression was analyzed. The correlation between FPRL2 and the prognosis of breast cancer patients was analyzed by KM-plotter[1]. The correlation of gene effects with drug sensitivity in CCLE (Cancer Cell Line Encyclopedia) database was analyzed using the DepMap platform[2]. Molecular docking was performed by AutodockVina 1.2.2[3] to analyze protein-molecule binding energy and interaction patterns.

Cell culture and siRNA transfection

The above cell lines were routinely cultured in DMEM medium containing 10% fetal bovine serum and dual antibodies at 37°C, 5% CO_2, and 1 μg/mL of Adriamycin was added to the medium of MCF-7/AMD to maintain its resistance. To knock down endogenous FPRL2, cells were transiently transfected with 100 nM mouse siRNA targeting FPRL2 (si-FPRL2) or non-silencing control siRNA (si-NC) in the

---

1 http://www.kmplot.com/

2 https://depmap.org/portal/interactive/

3 http://autodock.scripps.edu/

antimicrobial-free medium using Lipofectamine™ RNAiMAX in both cell lines.

Real-time PCR

After the above cell lines were routinely cultured, RNA extraction and reverse transcription were performed. PCR reactions were performed according to the instructions, respectively, with 5′-ACTACTACGCCAAGGAGGTCAC-3′ as the upstream primer, 5′-GAGCAACACGGGGTTCAGGT-3 ′ as the downstream primer to amplify the mRNA of FPRL2, 5′- TGC ACCACCAACTGCTTAGC-3′ as the upstream primer, 5′- GGC ATGGGACTGTGGTCATGAG-3 ′ as downstream primer amplified GAPDH mRNA as internal reference.$2^{-\Delta\Delta CT}$ method was used to process the amplified data.

IC50 of adriamycin measurements

Cell Counting Kit-8 was performed according to the instructions of Cell Counting Kit-8. PRRL2 knockdown and non-knockdown cell lines were planted in 96-well plates (100 μL, 2×10^3/well) and treated with 0, 5, 10, 20, and 40 μg/mL of adriamycin (5 replicate wells per group) for 72 h. After that, the cell lines were added to CCK-8 solution and incubated at 37°C for 3 hours. The cell lines' OD values were determined using an enzyme marker (Bio-Tek, Elx800, United States) at 450 nm. The half-maximal inhibitory concentration of the drug (IC_{50}) was calculated from the absorbance report.

Western blot

First, treat the cells with an LC50 dose of doxorubicin for 24 h to obtain standard cell lysates. Next, perform SDS-PAGE electrophoresis followed by membrane transfer. After the transfer, incubate the membrane overnight at 4°C with primary antibodies (FPRL2, p-ERK5, p-AKT, GAPDH). The following day, wash the membrane three times with PBST, then incubate it at room temperature for 2 h with HRP-conjugated sheep anti-rabbit secondary antibodies. Finally, detect protein bands using ECL chemiluminescence.

Flow cytometry

Cells (5×10^6 cells/tube) from various treatments were washed in cold PBS and fixed in 70% ethanol at 4°C. After PBS washing, RNase (500 U/mL) was treated at 37°C for 15 min, and DNA was stained with 50 μg/mL propidium iodide (PI) (dissolved in PBS). Apoptosis analysis was performed using a Becton Dickinson flow cytometer (BD-FACS Aria II, California, United States) and the included software. Approximately 15,000 cells were counted per assay.

Statistical methods

GraphPad Prism 10 was used for statistical analysis of the data. The unpaired t-test was applied for comparisons between two groups of data that followed a normal distribution. For data that did not follow a normal distribution, the rank-sum test was used. A significance level of $p < 0.05$ was set as the criterion for significant differences.

Results

Bioinformatics analysis of FPRL2 expression and prognosis in breast cancer

Through the TCGA database and METABRIC database, we found that FPRL2 expression was significantly elevated in breast cancer ($P < 0.05$) (Figure 1A), and the expression was higher in recurrent breast cancer than in non-recurrent breast cancer tissues ($P < 0.05$) (Figure 1B). By KM-plotter analysis, FPRL2 expression was found to be not significantly correlated with disease progression-free survival in breast cancer patients ($P > 0.05$) (Figure 1C). Interestingly, it was significantly correlated with disease progression-free rate in patients treated with chemotherapy ($P < 0.05$) (Figure 1D). This suggests that FPRL2 may affect the prognosis of patients by influencing the effect of chemotherapy.

Expression analysis of FPRL2 in adriamycin-resistant breast cancer

FPRL2 was significantly elevated ($P < 0.05$) in the GEO datasets GSE20271 and GSE20194, which were resistant to Adriamycin chemotherapy (Figures 2A, C). The ROC curve analysis revealed that FPRL2 could be used as an indicator for determining Adriamycin resistance in breast cancer ($P < 0.05$) (Figures 2B, D).

Correlation between the FPRL2 gene effect and breast cancer cell adriamycin sensitivity

Analysis of the FPRL2 gene effect and breast cancer cell Adriamycin sensitivity by DepMap revealed a positive correlation between the FPRL2 gene effect and breast cancer cell Adriamycin sensitivity in two computational models, CERES and Chronos (Figures 3A, B). This indicates that the dependence on FPRL2 increases in Adriamycin-resistant breast cancer tissues.

Molecular docking to validate the interaction of FPRL2 with adriamycin

The molecular docking results showed that the affinity energy of Adriamycin to FPRL2 was −7.928 kcal/mol and that

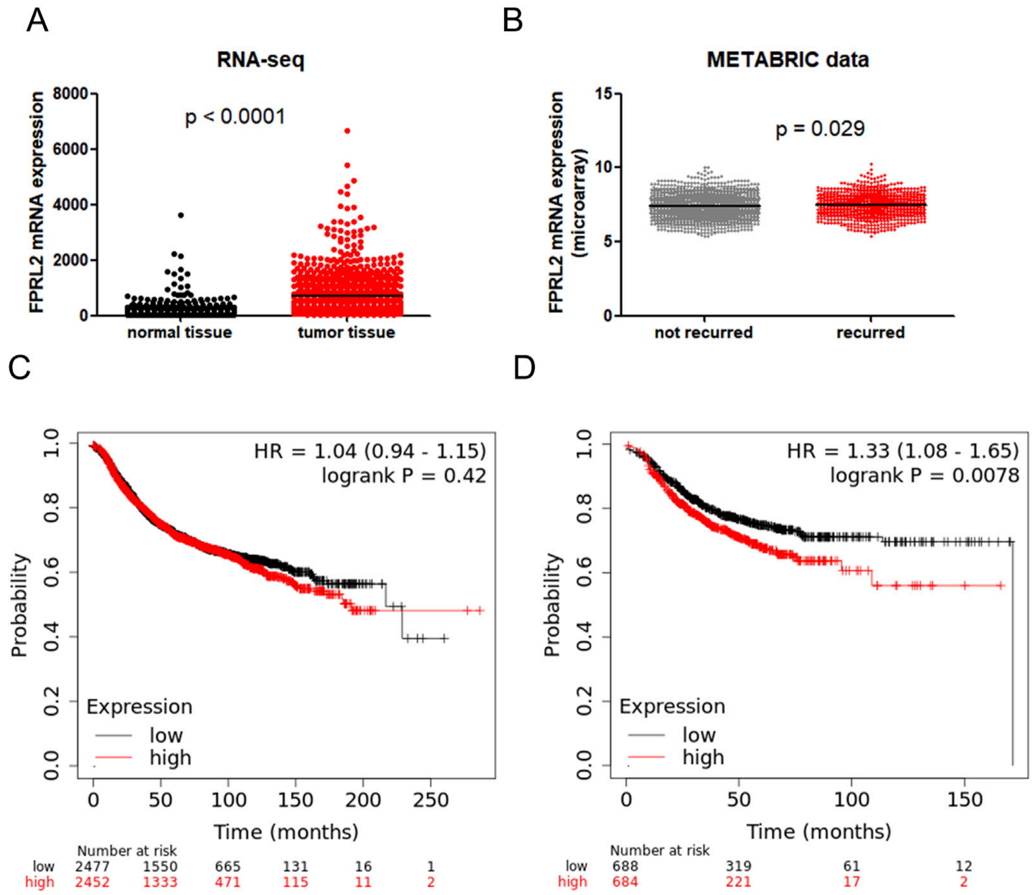

FIGURE 1
Bioinformatics analysis of FPRL2 expression and prognosis in breast cancer. **(A)** Data in TCGA and GTex breast cancer patients show that FPR3 is elevated in breast cancer. **(B)** The METABRIC database shows that FPR3 expression is higher in patients with recurrent breast cancer. **(C)** Correlation of FPR3 expression with disease progression-free survival in all breast cancers. **(D)** Correlation of FPR3 expression with disease progression-free survival in breast cancer treated with chemotherapy.

there were hydrogen bonding connections (hydrogen bonding) between Adriamycin and phenylalanine at position 5 (Phe 5), phenylalanine at position 178 (Phe 178), and aspartate at position 179 (Asn 179) of FPRL2 (indicated by arrows in Figure 4). bonds) (indicated by arrows in Figure 4). This implies that Adriamycin interacts with FPRL2.

FPRL2 expression in breast cancer cell lines

The results of Western Blot showed that FPRL2 was significantly higher in resistant MCF-7 cells (MCF7/ADM) than in the sensitive group (MCF7) ($P< 0.05$). In addition, Adriamycin treatment did not affect the protein expression of FPRL2 in both MCF-7 and MCF7/ADM tumor cells (Figure 5).

IC_{50} of Adriamycin and Adriamycin-induced apoptosis of breast cancer cells after FPRL2 knockdown

As shown in Figure 7, the IC_{50} of Adriamycin on breast cancer cells after FPRL2 knockdown was significantly lower than that of the non-knockdown, both in resistant and non-resistant MCF-7 cells ($P < 0.0001$) (Figures 6A, B). In the same time, flow cytometry results showed that Adriamycin-induced apoptosis in breast cancer cells was significantly increased in both MCF7 and MCF7/ADM cell lines after FPRL2 knockdown ($P < 0.0001$) (Figures 6C, D).

Expression of p-AKT and p-ERK5 in Adriamycin-treated breast cancer cells after FPRL2 knockdown

Western blot results showed that the expression levels of p-AKT and p-ERK5 in Adriamycin-treated breast cancer cells

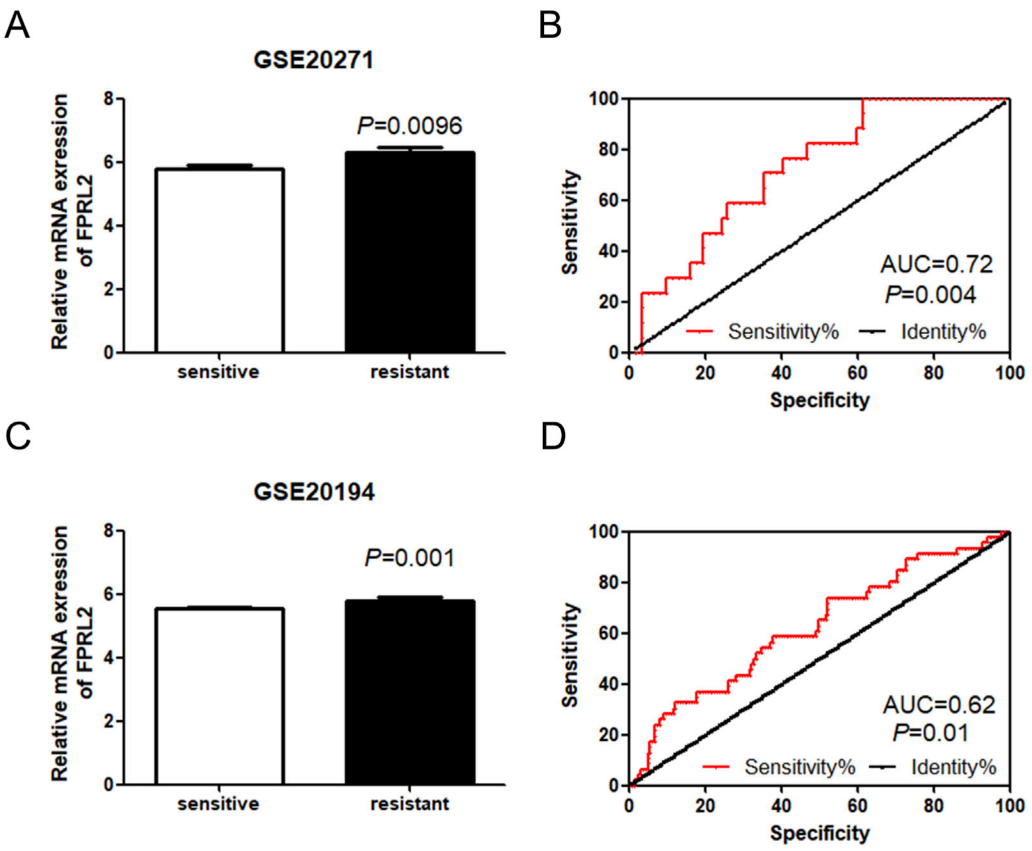

FIGURE 2
Expression analysis of FPRL2 in Adriamycin-resistant breast cancer. **(A, B)**: Expression of FPRL2 in Adriamycin-sensitive and drug-resistant **(A, B)**: Expression of FPRL2 in Adriamycin-sensitive and drug-resistant breast cancer samples in GSE20271 sample **(A)** and ROC curve analysis **(B)**. **(C, D)**: Expression of FPRL2 in Adriamycin-sensitive and drug-resistant breast cancer samples in GSE20194 sample **(C)** and ROC curve analysis **(D)**.

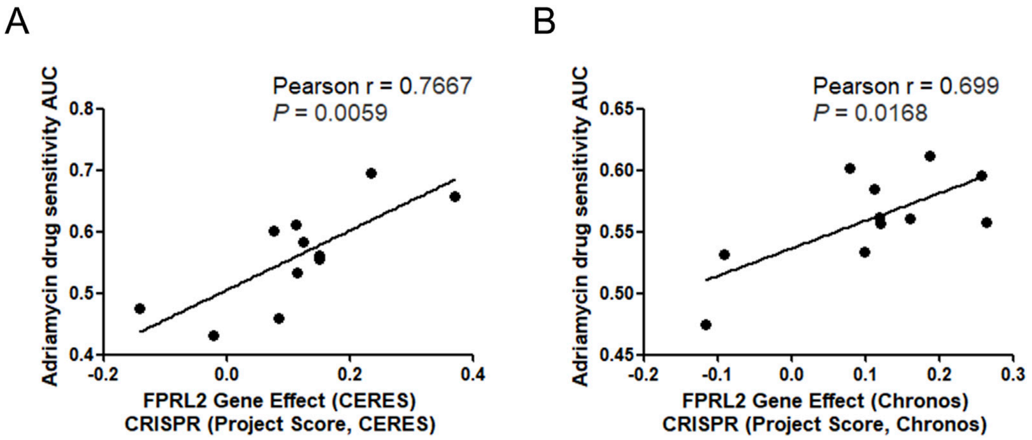

FIGURE 3
FPRL2 gene effect and Adriamycin sensitivity analysis. **(A)** FPRL2 gene effect and Adriamycin sensitivity analysis of breast cancer cells in CERES model. **(B)** FPRL2 gene effect and Adriamycin sensitivity analysis of breast cancer cells in Chronos model.

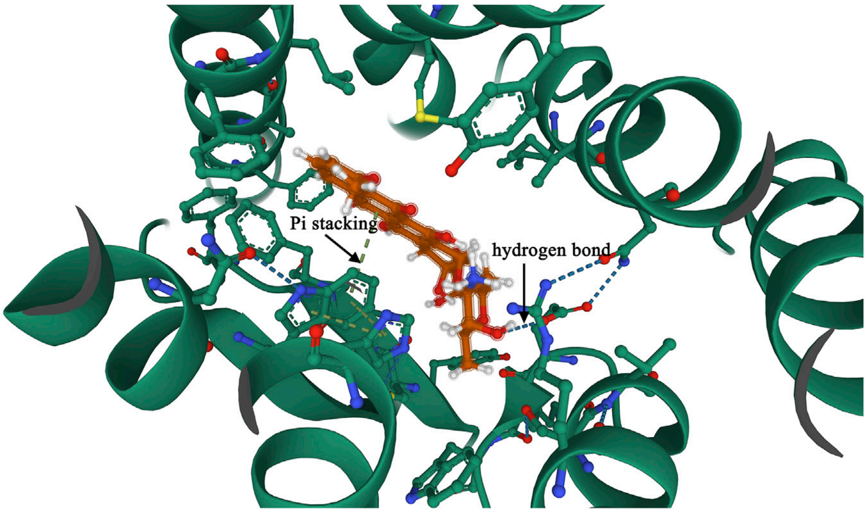

FIGURE 4
Molecular docking to verify the interaction of FPRL2 with Adriamycin. Note: FPRL2 protein in red and Adriamycin in green. Dashed lines are hydrogen bonding connections.

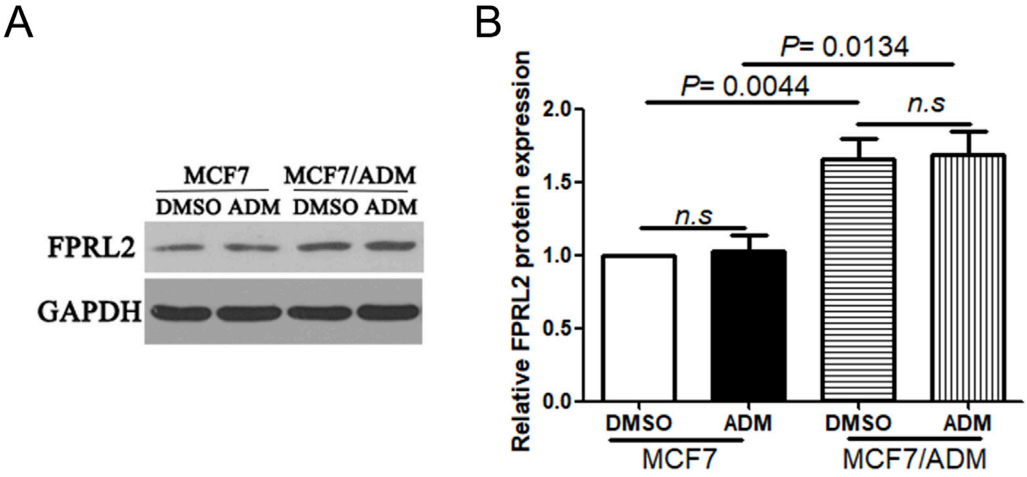

FIGURE 5
FPRL2 protein expression in breast cancer cell lines. **(A)** Protein expression of FPRL2 in Adriamycin-sensitive and drug-resistant cell lines of breast cancer tumors. **(B)** WB quantitative analysis.

were lower after FPRL2 knockdown, in both MCF-7 and MCF-7/ADM (Figure 7).

Discussion

Breast cancer is one of the common female malignant tumors, and the incidence and deaths have been increasing significantly in recent years [1]. In-depth research on breast cancer drug resistance can help to find ways to fight this common tumor. In this study, we reported for the first time that FPRL2 mediates Adriamycin resistance in breast cancer using public database mining, and breast cancer cell lines and utilizing a combination of bioinformatics and molecular biology experimental techniques.

Three subtypes of the formyl peptide receptor family are highly expressed in inflammatory cells, including FPR, FPRLl, and FPRL2. At the amino acid level, FPRLl shares 69% homology with FPR, and FPRL2 shares 56% and 83% homology with FPR and FPRLI, respectively. Numerous agonists of the formyl peptide receptor

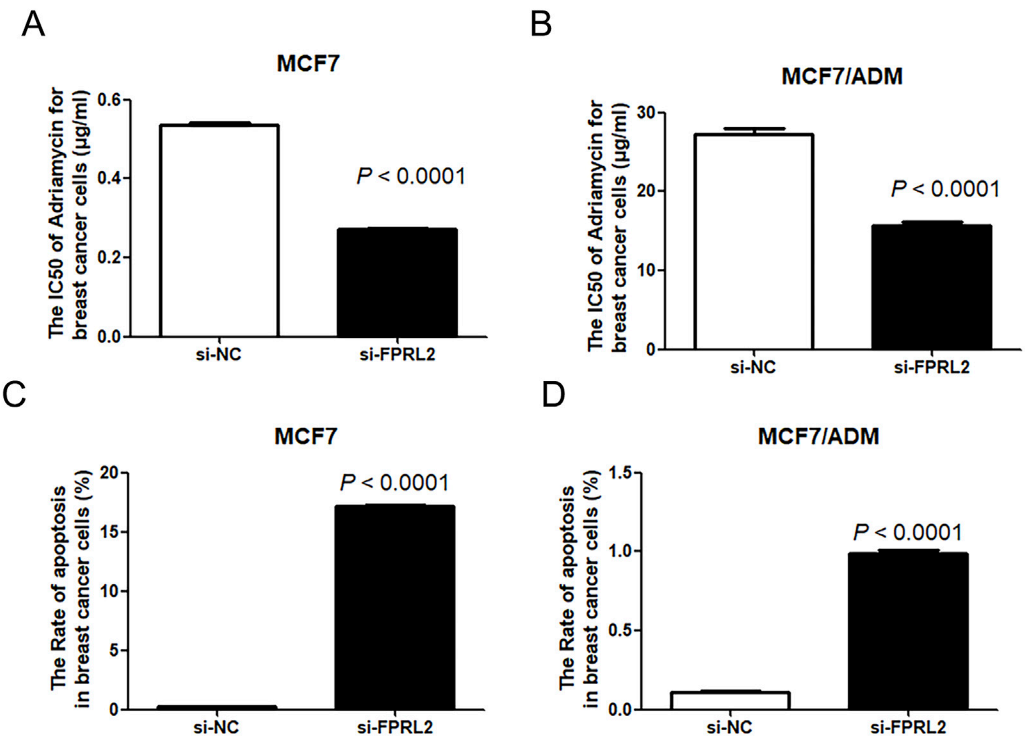

FIGURE 6
IC50 of Adriamycin and Adriamycin-induced apoptosis of breast cancer cells after FPRL2 knockdown. **(A)** The IC50 of Adriamycin in MCF7 after FPRL2 knockdown. **(B)** The IC50 of Adriamycin in MCF7/ADM after FPRL2 knockdown. **(C)** The Adriamycin-induced apoptosis rate of MCF7 after FPRL2 knockdown. **(D)** The Adriamycin-induced apoptosis rate of MCF7/AMD after FPRL2 knockdown.

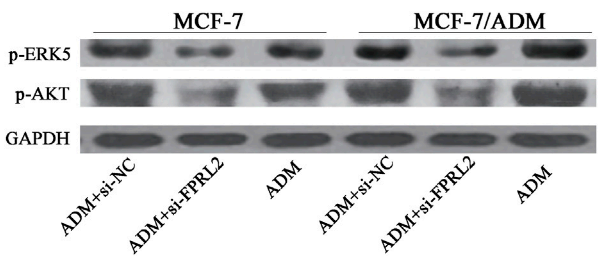

FIGURE 7
Expression of p-AKT and p-ERK5 in Adriamycin-treated breast cancer cells after FPRL2 knockdown.

family of receptors include pathogen-derived, synthetic peptides, and endogenous substances from the host [10, 11]. Currently, the FPR family serves as an important pharmacological target for treating many inflammation-related diseases such as inflammatory lung disease, ischemia-reperfusion injury, neuroinflammation, and cancer [12–14]. Formyl peptide receptors are also expressed in breast cancer and are biomarkers for targeted therapies in the immune microenvironment of breast cancer [15]. The present study confirms the expression of FPRL2, a member of the formyl peptide receptor family, in breast cancer tissues and cell lines.

The formyl peptide receptor is a transmembrane G protein-coupled receptor that, upon activation, causes Ca^{2+} endocytosis and mediates cellular responses. It has been reported in the literature that the activation of the formyl peptide receptor mainly activates the ERK, AKT, and STAT signaling pathways, among which the ERK and AKT pathways are closely related to apoptosis and tumor cell resistance. The activation of the ERK signaling pathway leads to doxorubicin resistance in a breast cancer nude mouse model [16]. L-amino acid oxidase enhances the cytotoxicity of doxorubicin against breast and pancreatic cancer cells by attenuating ERK and AKT activities [17]. Ivermectin binds to the extracellular domain of EGFR, inhibiting the activation of EGFR and its downstream signaling cascade ERK/Akt/NF-κB, thereby enhancing the antitumor efficacy of doxorubicin against breast cancer cells [18]. So we speculated that the formyl peptide receptor might be related to the drug resistance of the tumor cells, and the results of our experiments confirmed our speculation. In this study, the formyl peptide receptor was highly expressed in drug-resistant breast cancer tissues. The apoptosis of MCF-7 and MCF-7/ADM with knockdown of FPRL2 were significantly higher than those of control cells in response to Adriamycin. The p-ERK and p-AKT protein levels were decreased after FPRL2 knocked down. The above results indicate that the FPRL2 is involved in at least part of the function of cellular drug resistance through ERK and AKT pathways, consistent with previous reports [19].

This study confirmed that the knockdown of the FPRL2 can reverse the drug resistance of breast cancer cells, thus there is possibility that FPRL2 can be used as a target for adjuvant breast cancer therapy. Since the ligands of the formyl peptide receptor are numerous but of small molecular weight, it is favorable to synthesize small molecule compounds as antagonists or agonists of the formyl peptide receptor for the adjuvant therapy of breast cancer [20].

Author contributions

LS: data curation, data analysis, data interpretation, and writing-original draft. JL: data interpretation, and writing–review. LQ: data interpretation, writing–review and editing. YF: writing–review. DX: conceptualization, data interpretation and confirmation of authenticity, project administration and supervision, writing–original draft, review and editing, and funding acquisition. All authors contributed to the article and approved the submitted version.

Data availability

The original contributions presented in the study are included in the article/supplementary material, further inquiries can be directed to the corresponding author.

Funding

The author(s) declare that financial support was received for the research, authorship, and/or publication of this article. This work was supported by grants from the Innovation and Entrepreneurship Program for College Students in Jiangsu Province (202111462005Y).

Conflict of interest

The author(s) declared no potential conflicts of interest with respect to the research, authorship, and/or publication of this article.

References

1. Coles CE, Earl H, Anderson BO, Barrios CH, Bienz M, Bliss JM, et al. The lancet breast cancer commission. *The Lancet* (2024) **403**:1895–950. doi:10.1016/s0140-6736(24)00747-5

2. Chan CWH, Law BMH, So WKW, Chow KM, Waye MMY. Novel strategies on personalized medicine for breast cancer treatment: an update. *Int J Mol Sci* (2017) **18**:2423. doi:10.3390/ijms18112423

3. Rani A, Stebbing J, Giamas G, Murphy J. Endocrine resistance in hormone receptor positive breast cancer-from mechanism to therapy. *Front Endocrinol* (2019) **10**:245. doi:10.3389/fendo.2019.00245

4. Cheng X, Li D, Sun M, He L, Zheng Y, Wang X, et al. Co-delivery of DOX and PDTC by pH-sensitive nanoparticles to overcome multidrug resistance in breast cancer. *Colloids Surf B, Biointerfaces* (2019) **181**:185–97. doi:10.1016/j.colsurfb.2019.05.042

5. O'Hayre M, Degese MS, Gutkind JS. Novel insights into G protein and G protein-coupled receptor signaling in cancer. *Curr Opin Cel Biol* (2014) **27**:126–35. doi:10.1016/j.ceb.2014.01.005

6. Chaudhary PK, Kim S. An insight into GPCR and G-proteins as cancer drivers. *Cells* (2021) **10**:3288. doi:10.3390/cells10123288

7. Weiß E, Kretschmer D. Formyl-peptide receptors in infection, inflammation, and cancer. *Trends Immunology* (2018) **39**:815–29. doi:10.1016/j.it.2018.08.005

8. Xiang Y, Yao X, Chen K, Wang X, Zhou J, Gong W, et al. The G-protein coupled chemoattractant receptor FPR2 promotes malignant phenotype of human colon cancer cells. *Am J Cancer Res* (2016) **6**:2599–610.

9. Su LD, Peng JM, Ge YB. Formyl peptide receptor 2 mediated chemotherapeutics drug resistance in colon cancer cells. *Eur Rev Med Pharmacol Sci* (2018) **22**:95–100. doi:10.26355/eurrev_201801_14105

10. Devosse T, Dutoit R, Migeotte I, De Nadai P, Imbault V, Communi D, et al. Processing of HEBP1 by cathepsin D gives rise to F2L, the agonist of formyl peptide receptor 3. *The J Immunol* (2011) **187**:1475–85. doi:10.4049/jimmunol.1003545

11. Rabiet MJ, Macari L, Dahlgren C, Boulay F. N-formyl peptide receptor 3 (FPR3) departs from the homologous FPR2/ALX receptor with regard to the major processes governing chemoattractant receptor regulation, expression at the cell surface, and phosphorylation. *J Biol Chem* (2011) **286**:26718–31. doi:10.1074/jbc.m111.244590

12. Li Z, Li Y, Han J, Zhu Z, Li M, Liu Q, et al. Formyl peptide receptor 1 signaling potentiates inflammatory brain injury. *Sci translational Med* (2021) **13**:eabe9890. doi:10.1126/scitranslmed.abe9890

13. Lee C, Han J, Jung Y. Formyl peptide receptor 2 is an emerging modulator of inflammation in the liver. *Exp & Mol Med* (2023) **55**:325–32. doi:10.1038/s12276-023-00941-1

14. Prevete N, Poto R, Marone G, Varricchi G. Unleashing the power of formyl peptide receptor 2 in cardiovascular disease. *Cytokine* (2023) **169**:156298. doi:10.1016/j.cyto.2023.156298

15. Qi J, Liu Y, Hu J, Lu L, Dou Z, Dai H, et al. Identification of FPR3 as a unique biomarker for targeted therapy in the immune microenvironment of breast cancer. *Front Pharmacol* (2020) **11**:593247. doi:10.3389/fphar.2020.593247

16. Christowitz C, Davis T, Isaacs A, van Niekerk G, Hattingh S, Engelbrecht AM. Mechanisms of doxorubicin-induced drug resistance and drug resistant tumour growth in a murine breast tumour model. *BMC cancer* (2019) **19**:757. doi:10.1186/s12885-019-5939-z

17. Min C, Zhao Y, Romagnoli M, Trackman PC, Sonenshein GE, Kirsch KH. Lysyl oxidase propeptide sensitizes pancreatic and breast cancer cells to doxorubicin-induced apoptosis. *J Cell Biochem* (2010) **111**:1160–8. doi:10.1002/jcb.22828

18. Jiang L, Wang P, Sun YJ, Wu YJ. Ivermectin reverses the drug resistance in cancer cells through EGFR/ERK/Akt/NF-κB pathway. *J Exp & Clin Cancer Res* (2019) **38**:265. doi:10.1186/s13046-019-1251-7

19. Zhao L, Wang Y, Jiang L, He M, Bai X, Yu L, et al. MiR-302a/b/c/d cooperatively sensitizes breast cancer cells to adriamycin via suppressing P-glycoprotein(P-gp) by targeting MAP/ERK kinase kinase 1 (MEKK1). *J Exp & Clin Cancer Res* (2016) **35**:25. doi:10.1186/s13046-016-0300-8

20. Vergelli C, Khlebnikov AI, Crocetti L, Guerrini G, Cantini N, Kirpotina LN, et al. Synthesis, biological evaluation, molecular modeling, and structural analysis of new pyrazole and pyrazolone derivatives as N-formyl peptide receptors agonists. *Chem Biol & Drug Des* (2021) **98**:582–603. doi:10.1111/cbdd.13913

TYPE Original Research
PUBLISHED 19 November 2024
DOI 10.3389/ebm.2024.10361

OPEN ACCESS

*CORRESPONDENCE
Hyacinth I. Hyacinth,
hyacinhi@ucmail.uc.edu

†These authors share first authorship

RECEIVED 01 September 2024
ACCEPTED 17 October 2024
PUBLISHED 19 November 2024

CITATION
DeVeaux SA, Vyshnya S, Propsom K, Gbotosho OT, Singh AS, Horning RZ, Sharma M, Jegga AG, Niu L, Botchwey EA and Hyacinth HI (2024) Neuroinflammation underlies the development of social stress induced cognitive deficit in male sickle cell mice. *Exp. Biol. Med.* 249:10361.
doi: 10.3389/ebm.2024.10361

Neuroinflammation underlies the development of social stress induced cognitive deficit in male sickle cell mice

S'Dravious A. DeVeaux[1,2†], Sofiya Vyshnya[1,2†], Katherine Propsom[3], Oluwabukola T. Gbotosho[3], Asem S. Singh[3], Robert Z. Horning[3], Mihika Sharma[4], Anil G. Jegga[4], Liang Niu[5], Edward A. Botchwey[1,2] and Hyacinth I. Hyacinth[3]*

[1]The Wallace H. Coulter Department of Biomedical Engineering, Georgia Tech and Emory, Atlanta, GA, United States, [2]Petit Institute of Bioengineering and Biosciences, Georgia Institute of Technology, Atlanta, GA, United States, [3]Department of Neurology and Rehabilitation Medicine, University of Cincinnati College of Medicine, Cincinnati, OH, United States, [4]Division of Biomedical Informatics, Department of Pediatrics, Cincinnati Children's Hospital Medical Center, University of Cincinnati College of Medicine Cincinnati, Cincinnati, OH, United States, [5]Department of Environmental and Public Health Sciences, University of Cincinnati College of Medicine, Cincinnati, OH, United States

Abstract

Cognitive deficit is a debilitating complication of sickle cell disease (SCD), with a multifactorial etiopathogenesis. Here we show that neuroinflammation and dysregulation in lipidomics and transcriptomics profiles are major underlying mechanisms of social stress-induced cognitive deficit in SCD. Male Townes sickle cell (SS) mice and controls (AA) were exposed to social stress using the repeat social defeat (RSD) paradigm concurrently with or without treatment with minocycline. Mice were tested for cognitive deficit using novel object recognition and fear conditioning tests. SS mice exposed to RSD without treatment had worse performance on cognitive tests compared to SS mice exposed to RSD with treatment or to AA controls, irrespective of their RSD or treatment disposition. Additionally, compared to SS mice exposed to RSD with treatment, SS mice exposed to RSD without treatment had significantly more cellular evidence of neuroinflammation coupled with a significant shift in the differentiation of neural progenitor cells towards astrogliogenesis. Additionally, brain tissue from SS mice exposed to RSD was significantly enriched for genes associated with blood-brain barrier dysfunction, neuron excitotoxicity, inflammation, and significant dysregulation in sphingolipids important to neuronal cell processes. We demonstrate in this study that social stress induces cognitive deficit in SS mice, concurrently with neuroinflammation and lipid dysregulation.

KEYWORDS

sickle cell disease, neuroinflammation, cognitive function, social stress, minocycline

Impact statement

We show for the first time that neuroinflammation along with changes in the brain lipidome and transcriptome, are underlying biological mechanisms contributing to the development and potentially progression of cognitive impairment in SCD mice. These findings also provide for the first time, a potential mechanistic basis for an earlier reported observation of a higher likelihood of having lower intelligence quotient scores among children with sickle cell disease exposed to social stress in the form of low parental socioeconomic status.

Introduction

Sickle cell disease (SCD) is a common inherited blood disorder that affects approximately 100,000 Americans and millions more worldwide [1, 2]. SCD is caused by a point mutation in the gene for the β-globin subunit of hemoglobin. This mutation causes the hemoglobin to polymerize in conditions of low oxygen tension, causing the red blood cells (RBCs) to assume a sickle morphology [2, 3]. Sickle RBCs are more fragile and prone to hemolysis, leading to anemia; the resulting free heme also initiates and propagates an inflammatory cascade that leads to vaso-occlusion [2, 3], and end organ damage [4].

The cerebrovascular effects of SCD include silent cerebral infarctions (SCIs) found in ~39% of children by 18 years of age and >50% of adults by 30 years of age, stroke, cerebral macro- and microvascular abnormalities [5]. Strokes and SCIs have been linked to cognitive impairment in SCD. However, recent studies have found cognitive dysfunction in children [6–8] and adults [9, 10] even in the absence of MRI-detectable cerebral injury. Children with SCD typically have lower full-scale IQ scores, poorer academic achievement, and impaired processing speed [6, 7]. Similarly, adults with SCD exhibit impairments in processing speed, working memory, global cognitive function, and executive function.

The mechanism underlying cognitive impairment in SCD is not well understood, and one possibility is that individuals with SCD are hypersensitive to social stressors (to which individuals with SCD are exposed), which interact with biological factors leading to the development of cognitive deficit. Individuals with SCD often belong to lower socioeconomic classes with associated lower family educational attainment and income. The impact of social stress on cognitive function in SCD was recently demonstrated by several studies [5, 11–13]. In a study by King *et al.*, they reported that social stressors in the form of lower parental education levels and lower family income – had a similar albeit slightly more severe impact on cognitive function compared to biological factors – such as the presence of SCI, anemia, and age [14, 15]. Studies in the general human population and in non-sickle cell mouse models have shown a link between social stress and neuroinflammation. The functional effects of neuroinflammation on the brain include the development of cognitive impairment as well as neuropsychological abnormalities, such as anxiety and depression [16]. As well as learning and memory impairments [17–19]. Hence, neuroinflammation may be a possible mechanism for stress-induced cognitive abnormalities in SCD.

Neuroinflammation is also mediated by multiple factors, including sphingolipids and genetics. Sphingolipids are a class of bioactive lipids that participate in cell signaling. In the brain, sphingolipids modulate cytokine release and astroglia activation [20]. Studies have shown that imbalances in the sphingolipid metabolism and distribution of lipids in the brain are associated with impaired memory and learning in both humans and animal models [21–26]. Furthermore, enzymes in the sphingolipid pathway – such as sphingosine kinases, sphingosine-1-phosphate lyase, and sphingomyelinases – are involved in synaptic communication, learning, and memory, as well as in the regulation of other enzymes (e.g., COX2) that synthesize both pro-inflammatory and anti-inflammatory lipid mediators. Changes in the enzymatic activity have been implicated in the development of neuroinflammation and neurodegenerative diseases, such as Alzheimer's and amyotrophic lateral sclerosis [27, 28].

We have previously shown that aging and neuroinflammation contribute to cognitive impairment in the SCD mouse model [29]. In the present study, we demonstrate the role of sociological stress in cognitive and neurobehavioral deficits in SCD and show that neuroinflammation is a likely underlying mechanism. We used the repeat social defeat (RSD) paradigm as a social stress model, as previously described [17]. Our overall hypothesis is that *stress-related cognitive impairment in sickle cell disease is mediated by neuroinflammation and inimical changes in the brain lipidomic and transcriptomic profiles compared to controls.* Furthermore, treatment with minocycline, an "anti-neuroinflammatory" drug, during RSD exposure in mice will reduce neuroinflammation and improve cognitive and behavioral function.

Materials and Methods

Animals

We used humanized Townes sickle cell mouse model (SS or HbSS) and humanized control mice (AA or HbAA) [30]. Mice were provided food and water *ad libitum*, housed in a 12-h light and dark cycle, and their health statuses were monitored closely throughout the study. All experiments were approved by the Institutional Animal Use Committee at Emory University.

Study design and overall methods

This study aims to examine the mechanism underlying the development of cognitive deficit in SCD with exposure to social stress, by using the repeat social defeat (RSD) paradigm in male SS mice. RSD was carried out by introducing a male intruder mouse (an aggressor) into an established cage containing three 6-month-old male SS mice (N = 10) or AA mice (N = 10) every day for 2 hours (5–7 p.m.) for six consecutive days. Age- and sex-matched control [SS (N = 10) and AA (N = 10) mice] cages were set up but without aggressor mice. On the seventh day, mice were tested for cognitive/behavioral deficit using novel object recognition (NOR) and fear conditioning (FC) test paradigms. Except for the aggressors, all mice used were Townes humanized SS and AA mice.

To test the hypothesis that neuroinflammation is an underlying mechanism, a second cohort of SS (N = 35) and AA (N = 32) mice were randomly assigned to receive oral (administered in drinking water) minocycline treatment (90 mg/kg) or placebo (plain drinking water). We assigned 2 mice to the minocycline plus stress arm (due to the potential for injury and mortality from the RSD paradigm) for every 1 mouse assigned to the other arms, from each genotype group. Mice within each treatment arm were randomly assigned to RSD exposure or no RSD exposure. Minocycline treatment was started 1 day prior to the day of commencing RSD and co-terminated on the same day as the final RSD session. The minocycline dose was kept constant by adjusting the amount administered daily, using the water/drug consumption from the previous day. Cognitive/behavioral testing was performed as before, starting the next day after day 6 of RSD and day 7 of treatment.

In both experiments, the mice were randomized to histological analysis or molecular (bulk RNA sequencing and lipidomics) studies and sacrificed 1-2 days after the completion of behavioral testing. Their brains were extracted for the assigned analysis. Cellular evidence of neuroinflammation in the hippocampus/dentate gyrus was determined using immunohistochemistry to quantify peripheral immune cell infiltrates:CD45$^+$ (bone marrow-derived microglia), CD3$^+$ (T-cell density), B220$^+$ (B-cell density), and Iba1$^+$ (activated microglia).

A more detailed description of the study methods is in the methods section of the Online Supplementary Material. Data reporting is in accordance with the ARRIVE guidelines.

Results

All studies were conducted using male mice. Experimental groups in this study are defined as follows: humanized control mice (AA) and Townes sickle (SS) mice, and also denote animals not exposed to stress or treated with minocycline; AA + RSD and SS + RSD denote mice exposed to stress (RSD); AA + minocycline and SS + minocycline denote mice not exposed to RSD but treated with minocycline; AA + RSD + minocycline and SS + RSD + minocycline denote mice treated with minocycline 1 day prior to and during exposure to stress.

Figure 1 shows comparison of the groups on measures of anxiety (open-field test) and cognitive function (percent preference or freezing). In Figures 1A, B, overall, we see that SS mice that were not exposed to RSD or drug treatment showed more evidence of anxiety compared to AA mice that were not exposed to RSD, indicated by the shorter distance traveled (Figure 1A, day 1: 19,116 mm in AA vs. 12,593 mm in SS, n.s.) and relatively shorter time spent in the middle of the open field (Figure 1B, day 1: 33.94 s in AA vs. 24.06 s in SS, n.s.). Furthermore, SS mice exposed to RSD showed more evidence of anxiety compared to AA mice exposed to RSD (distance traveled: day 1: 12,593 mm in SS vs. 9,274 cm in SS + RSD; time in the middle of the open field: day 1: 24.1 s in SS vs. 32.3 s in SS + RSD) or to SS or AA mice. Treatment with minocycline abrogated the development of anxiety in SS mice exposed to RSD (distance traveled: day 1: 13,276 mm in SS + RSD + Minocycline vs. 9,274 mm in SS + RSD; time in open field: day 1: 39.6 s in SS + RSD + Minocycline vs. 32.28 s in SS + RSD: Figures 1A, B).

Furthermore, evaluation of hippocampus-dependent non-associative as well as associative learning and memory, was carried out using NOR and fear conditioning, respectively. In the NOR test, (Figure 1C), SS and AA mice had similar percent preference (56.1 ± 14% vs. 53.1 ± 13%), indicating comparable non-associative memory. However, SS + RSD mice showed some evidence of cognitive impairment as demonstrated by lower percent preference (36.1 ± 18% SS + RSD vs. 56.1 ± 14% SS, $p = 0.06$) compared to SS mice, indicating impaired non-associative memory function. Additionally, we also noted that SS + RSD + minocycline mice had significantly higher percent preference (67.1 ± 18% vs. 36.1 ± 18%, $p = 0.0007$) compared to SS + RSD mice, suggesting that minocycline treatment led to a sparing of non-associative memory in the treated mice despite exposure to RSD. On the other hand, in the AA group, neither stress nor minocycline treatment were associated with significant changes in cognitive function.

Likewise, the fear conditioning tests (Figures 1D–F) showed that overall, sickle and non-sickle mice, irrespective of treatment or exposure disposition, trained similarly during the acquisition phase (Figure 1D). As shown in Figure 1E, RSD exposure resulted in significant impairment in contextual (associative) fear memory (evidenced by significantly lower percent freezing) in SS + RSD mice, compared to SS mice. As in Figures 1C, E shows that SS + RSD + minocycline mice had significantly better contextual fear memory, compared to SS + RSD mice, $p = 0.025$ to $p < 0.0001$ across all time points except at 240 s. The abnormal contextual fear memory indicates possible molecular disturbance and/or “overt or covert”

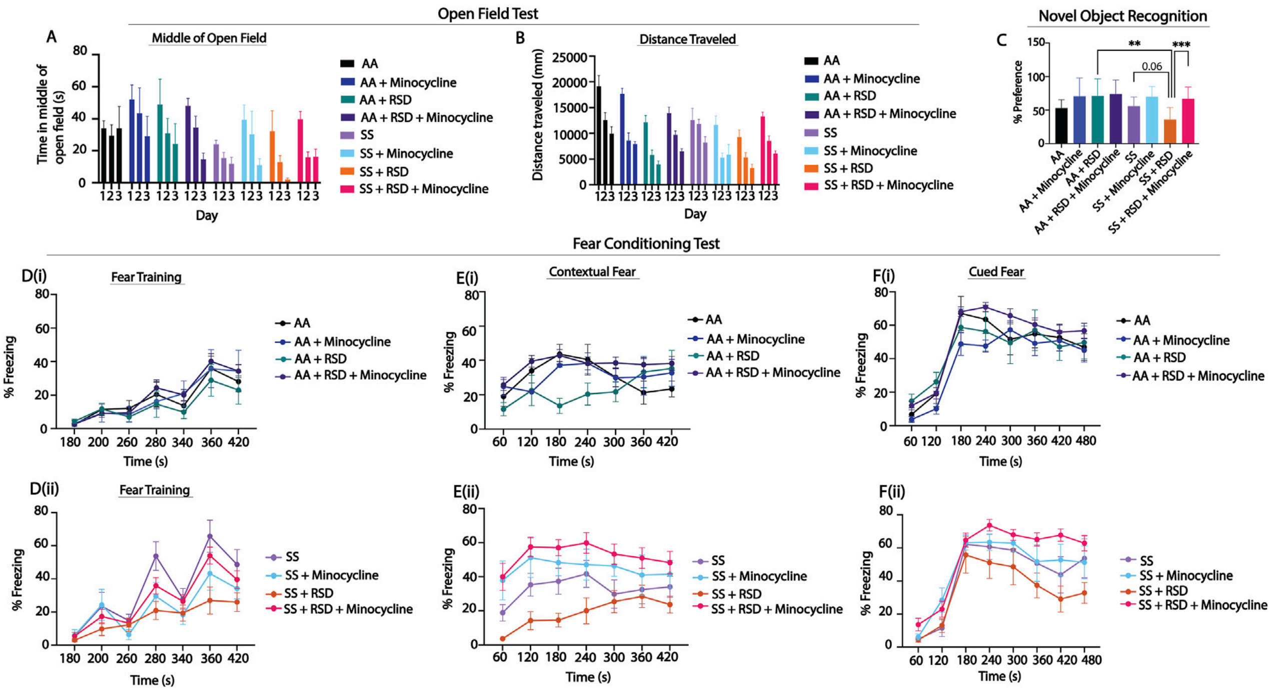

FIGURE 1
Sickle mice display significant cognitive and neurobehavioral deficits under stress compared to control mice. **(A, B)** illustrate the results for the open field test, depicting distance traveled through the open field arena and time spent in the middle of the arena. Statistical comparisons were conducted using a two-way ANOVA (using a mixed effect model) with Tukey's multiple comparisons test. **(C)** depicts preference for the novel object in the NOR test; analysis was with a one-way ANOVA with multiple comparisons (using Fisher's LSD) conducted to compare object preference between groups. **(D, F)** illustrate results for the fear conditioning studies (a measure of associative memory). **(Di,ii)** represents the training phase, where mice acquired a fear response to an 85 dB tone that was paired with a shock through classical conditioning. **(Ei,ii)** and **(Fi,ii)** test the strength of the animals' conditioned fear response by observing freezing behavior (indicative of fear) after being placed in the same environment where the shock had been administered during the learning phase or after hearing the 85 db tone that was associated with the shock, respectively. Freezing behavior was compared between groups using a two-way ANOVA (using a mixed effect model) with Holm-Sidak's adjustment for multiple comparisons for the contextual and cued fear assessments. All groups (AA and SS) were analyzed together. The figures **(E, F)** were split based on genotype to enhance the clarity of the presentation of the result. AA mice (n = 7–9), AA + RSD mice (n = 6–9), AA + minocylcine mice (n = 6), AA + RSD + minocycline (n = 13–21), SS mice (n = 6–7), SS + RSD mice (n = 6–10), SS + minocycline mice (n = 7), SS + RSD + minocycline mice (n = 15–22). *p < 0.05, **p < 0.01, ***p < 0.001. Data are presented as *mean* ± *SEM*.

lesion of the amygdala resulting from exposure to RSD and its abrogation by minocycline treatment.

Similarly, on cued fear testing (Figure 1F), there was no significant difference in response from the unperturbed AA or SS mice. However, SS + RSD mice showed significant impairment in hippocampus-mediated cued (associative) fear memory compared to SS + RSD + minocycline mice (p = 0.016 to <0.0001) across different time points. In contrast, neither RSD nor minocycline had significant effects on cognitive function among the AA genotypes.

Next, we evaluated the density of peripheral immune cell infiltrates (known from here on as $CD45^+$ "bone-marrow derived" microglia [BMDM]), $Iba1^+$ activated microglia (activation state determined based on morphological features), $CD3^+$ T cells, and $B220^+$ B cells in the hippocampus/dentate gyrus (DG). We focused on the hippocampus/DG because of its critical role in cognitive function as well as adult neurogenesis [31]. In Figure 2A, we show that overall, SS mice had a higher density of activated microglia (233.6 ± 44.6 cells/mm^2 vs. 179.3 ± 47.0 cells/mm^2, $p \leq 0.0001$) compared to AA mice. Furthermore, SS + minocycline mice had a significantly lower density of activated microglia (164.4 ± 56.6 cells/mm^2 vs. 233.6 ± 44.6 cells/mm^2, $p \leq 0.0001$) compared to SS mice. Similarly, SS + RSD mice had a significantly higher density of activated microglia (260.2 ± 44.3 cells/mm^2 vs. 233 ± 44.6 cells/mm^2, $p \leq 0.0001$) compared to SS mice. Finally, we observed that SS + RSD + minocycline mice showed a 35% decrease (p ≤ 0.0001) in activated microglia density compared to SS + RSD mice. As shown in Figure 2A, the results for the comparison within the AA groups were similar to those described for the SS mice. Figures 2B, C are representative images. Additionally, except for the control (non-perturbed group), there were no significant differences between the AA and SS mice based on RSD exposure or minocycline treatment.

Results of the examination of the contribution of peripheral immune cell ($CD45^+$) infiltrate to the observed cognitive deficit

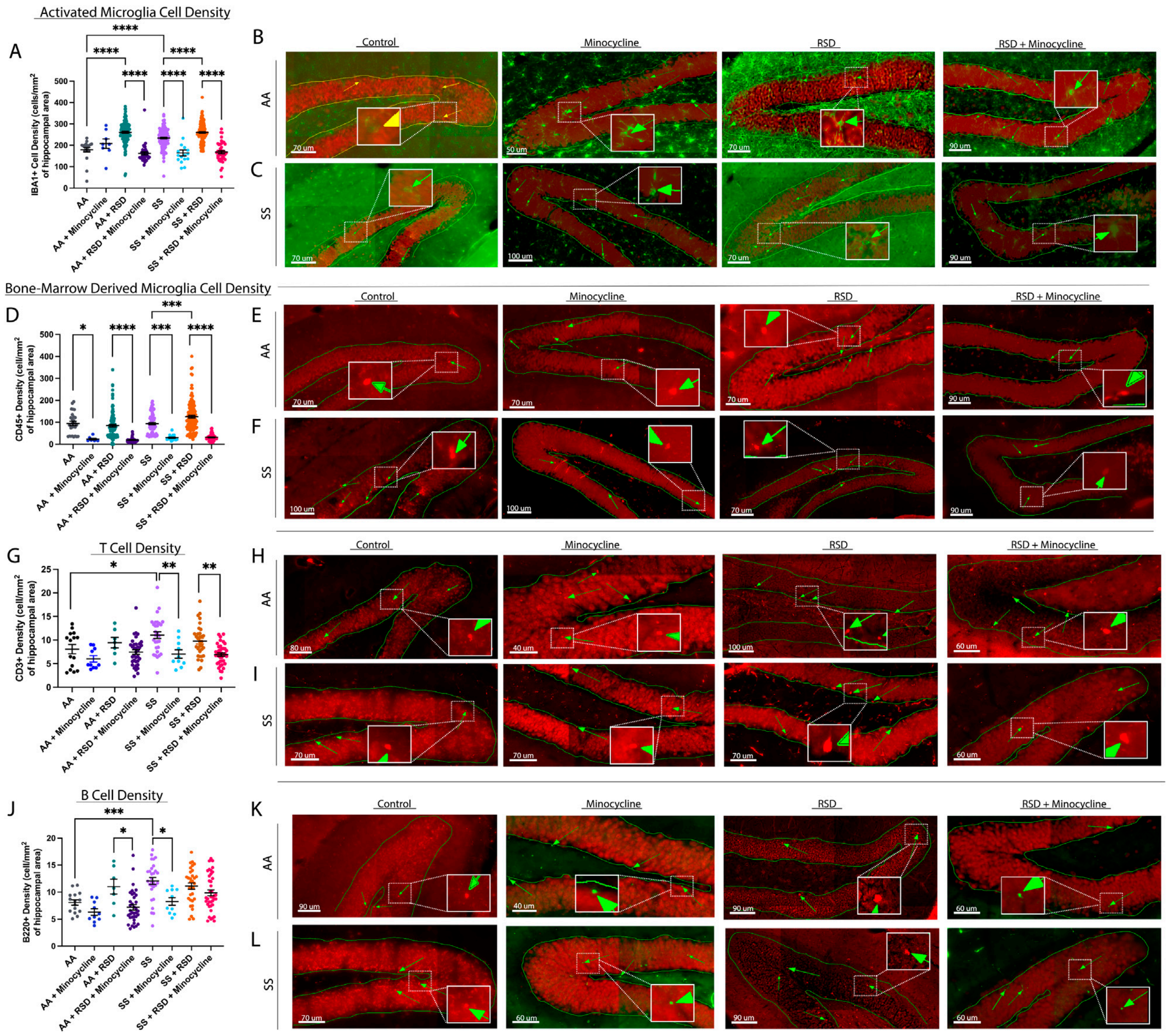

FIGURE 2
Sickle cell mice exposed to RSD have a higher density of activated microglia and B and T cell infiltrates in the hippocampus while minocycline reduces the density of immune cell infiltrates. **(A)** IBA-1+ activated microglia cell density. **(B)** Immunohistochemistry images showing IBA-1+ activated microglia in AA control mice (n = 10 sections), AA mice treated with minocycline (n = 8 sections), AA mice exposed to RSD (n = 27 sections), and AA mice exposed to RSD and treated with minocycline (n = 40 sections). **(C)** Immunohistochemistry images showing IBA-1+ activated microglia in SS control mice (n = 22 sections), SS mice treated with minocycline (n = 18 sections), SS mice exposed to RSD (n = 41 sections), and SS mice exposed to RSD and treated with minocycline (n = 49 sections). **(D)** CD45$^+$ "bone-marrow-derived" microglia cell density. **(E)** Immunohistochemistry images showing CD45$^+$ bone-marrow microglia in AA control mice (n = 10 sections), AA mice treated with minocycline (n = 8 sections), AA mice exposed to RSD (n = 27 sections), and AA mice exposed to RSD and treated with minocycline (n = 40 sections). **(F)** Immunohistochemistry images showing CD45$^+$ bone-marrow microglia in SS control mice (n = 22 sections), SS mice treated with minocycline (n = 18 sections), SS mice exposed to RSD (n = 41 sections), and SS mice exposed to RSD and treated with minocycline (n = 49 sections). **(G)** B220 + B cell density. **(H)** Immunohistochemistry images showing B220 + B cells in AA control mice (n = 16 sections), AA mice treated with minocycline (n = 10 sections), AA mice exposed to RSD (n = 8 sections), and AA mice exposed to RSD and treated with minocycline (n = 36 sections). **(I)** Immunohistochemistry showing B220+ B cells in SS control mice (n = 32 sections), SS mice treated with minocycline (n = 10 sections), SS mice exposed to RSD (n = 32 sections), and SS mice exposed to RSD and treated with minocycline (n = 40 sections). **(J)** CD3$^+$ T cell density. **(K)** Immunohistochemistry images showing CD3$^+$ T cells in AA control mice (n = 16 sections), AA mice treated with minocycline (n = 10 sections), AA mice exposed to RSD (n = 8 sections), and AA mice exposed to RSD and treated with minocycline (n = 36 sections). **(L)** Immunohistochemistry images showing CD3$^+$ T cells in SS control mice (n = 32 sections), SS mice treated with minocycline (n = 10 sections), SS mice exposed to RSD (n = 32 sections), and SS mice exposed to RSD and treated with minocycline (n = 40 sections). Cell density was compared between groups with a one-way ANOVA and Fisher's LSD multiple comparisons test. **p < 0.05, **p < 0.01, ***p < 0.001. Data are presented as mean ± SEM. The "n" in brackets after each group represents the total number of hippocampal brain tissue sections evaluated.*

and impact of minocycline treatment are shown in Figure 2D. There was no significant difference between SS and AA mice with respect to the density of $CD45^+$ BMDM cells in the hippocampus/DG. However, both AA + RSD and SS + RSD mice had a significantly higher density of $CD45^+$ BMDM compared to their non-perturbed controls, with SS + RSD mice having about 1.5-fold ($p < 0.0001$) more $CD45^+$ BMDM than AA + RSD mice. Additionally, we found a 75% ($p = 0.013$) and 77% ($p < 0.0001$) decrease in $CD45^+$ BMDM density in AA mice and AA + RSD treated with minocycline, respectively, compared to their non-treated controls. Similarly, stress exposure significantly increased the density of $CD45^+$ BMDM in SS mice (from 93.7 ± 45.8 cells/mm^2 to 125.4 ± 70.3 cells/mm^2, $p = 0.0004$), while minocycline treatment reduced the density in unperturbed SS mice by 3.1-fold ($p = 0.0002$) and in SS + RSD mice by 3.9-fold ($p < 0.0001$). Figures 2E, F are representative images. Furthermore, we quantified the density of B cells ($B220^+$) and T cells ($CD3^+$) as shown in Figures G. Notably, AA + RSD mice had a significantly higher density of B cells (11.0 ± 3.7 cells/mm^2 vs. 7.2 ± 3.0 cells/mm^2, $p = 0.037$) compared to AA + RSD + minocycline mice. There was also a slight decrease in B cell density in AA + minocycline mice compared to AA mice, though not significant. This suggests that minocycline may be suppressing B-cell-mediated neuroinflammation by limiting peripheral immune cell infiltration into the brain. Furthermore, when compared to AA mice, SS mice had a significantly higher density of B cells (12.1 ± 3.4 cells/mm^2 vs. 8.1 ± 1.9 cells/mm^2, $p = 0.0009$), and when SS mice were treated with minocycline, the density of B cells decreased by 31% ($p = 0.012$). Figures 2H, I are representative images. Surprisingly, exposure of SS mice to RSD with or without minocycline treatment did not result in a significant change in B cell density, contrary to our observation in AA mice. This result suggests that B cell infiltration might play a smaller role in RSD-induced neuroinflammation as an underlying mechanism for the development of cognitive deficits in SCD.

Further analysis, as shown in Figure 2J, indicates that SS mice had significantly higher T cell density (11.1 ± 3.8 cells/mm2 vs. 8.1 ± 3.8 cells/mm2, $p = 0.032$) compared to AA mice. Minocycline treatment decreased T cell density in AA mice by 26% ($p = 0.032$), while T cell density in AA + RSD and AA + RSD + minocycline mice was similar. Among sickle cell groups, minocycline treatment resulted in a 1.6-fold ($p = 0.005$) reduction in T cell density in unperturbed SS mice and about a 30% reduction in SS + RSD mice compared to their untreated controls. Figures 2K, L are representative images of the plot. However, there was no significant difference in T cell density between SS mice and SS + RSD mice. This indicates a possible but slightly lesser role for T cells in cognitive impairment in SCD in the setting of exposure to social stress.

Given the reported role of neurogenesis in social stress-induced cognitive deficits [18, 32] due to neuroinflammation, we quantified and compared the densities of neural progenitor cells (NPCs; DCX^+), adult-born neurons (DCX^+NeuN^+), and "newly formed" astrocytes (DCX^+GFAP^+) in the dentate gyrus and reported our findings in Figure 3. As shown in Figure 3A, we observed a higher density of NPCs in AA + minocycline mice (20.8 ± 4.8 cells/mm^2 vs. 17.1 ± 5.7 cells/mm^2) compared to AA mice, while the NPC density was lower among AA + RSD mice (13.3 ± 3.6 cells/mm^2, $p = 0.06$) compared to AA mice. Additionally, AA + RSD mice had significantly lower NPC density compared to AA + RSD + minocycline mice (18.7 ± 5.3 cells/mm^2, $p < 0.0001$). We also observed that SS mice had slightly lower NPC density compared to AA mice and that minocycline treatment significantly reduced NPC density in SS mice compared to treated AA mice ($p = 0.006$). Furthermore, as seen in the AA groups, SS + RSD mice had a significantly lower NPC density (11.9 ± 3.9 cells/mm^2 vs.15.8 ± 5.6 cells/mm^2, $p = 0.005$) compared to SS + RSD + minocycline mice. Figures 3D–F are representative images. We also noted that SS + RSD + minocycline mice have essentially the same NPC density as SS mice, indicating that minocycline might be limiting the gliogenic shift that seems to result from exposure to RSD (see Figure 3B; Supplementary Figure S1), leading to the development of cognitive deficit.

Furthermore, as shown in Figure 3B, SS mice had more newly generated astrocytes (5.0 ± 1.9 cells/mm^2 vs. 3.3 ± 1.9 cells/mm^2) than AA mice, and exposure to RSD increased the density of new astrocytes in both AA and SS mice, though not significantly when compared to their respective unperturbed controls. However, there was a 35% increase ($p = 0.0011$) in the density of new astrocytes in SS + RSD mice compared to AA + RSD. Interestingly, minocycline treatment reduced the density of new astrocytes in SS mice and AA + RSD mice, with the most significant decrease of 55% observed in the treated SS + RSD mice. Taken together, this indicates that the exposure to RSD alone might be shifting the differentiation of NPCs towards astrocytes. And that treatment with minocycline reduces that shift as seen in the SS + RSD + minocycline and AA + RSD + minocycline mice when compared to their untreated but stressed counterparts.

Results of the quantification of the density of adult-born neurons (DCX^+NeuN^+) are shown in Figure 3C; Supplementary Figure S1. Overall, we show that AA mice, irrespective of treatment or RSD status, had similar adult-born neuron densities. Among the SS mice, SS + RSD mice had significantly lower adult-born neuron density compared with SS mice (1.8 ± 1.7 cells/mm^2 vs. 4.8 ± 2.9 cells/mm^2, $p < 0.0001$). In contrast to similarly stressed AA mice, SS mice also displayed a more pronounced effect of RSD exposure on adult-born neuron density, with a 2.5-fold ($p < 0.0001$) decrease. However, treatment of SS + RSD mice with minocycline resulted in a 50% ($p = 0.0031$) increase in adult-born neurons. Supplementary Figure S1 provides the percentage distribution of these cells (DCX^+GFAP^+ and DCX^+NeuN^+) as a percentage of the total NPCs (DCX^+) counted.

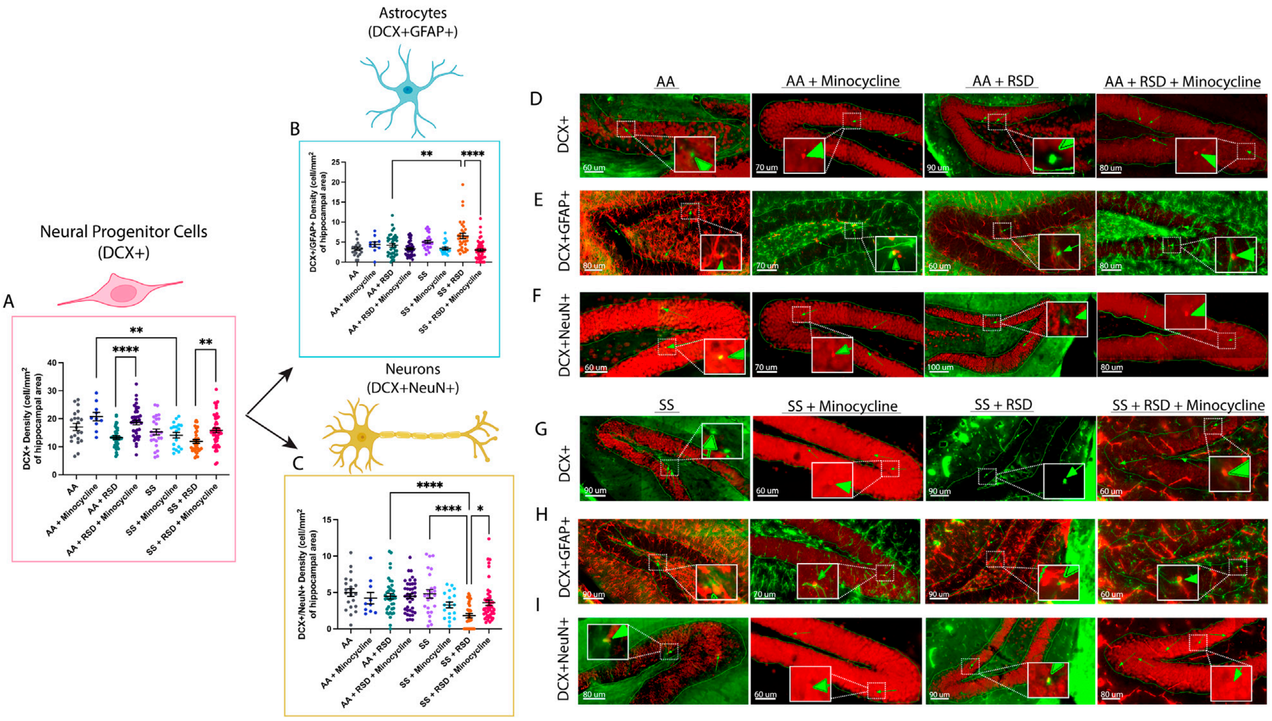

FIGURE 3
Sickle cell mice exposed to RSD have a higher density of DCX$^+$GFAP$^+$ astrocytes while having decreased densities of DCX$^+$ neural progenitor cells and DCX$^+$NeuN$^+$ neurons in the hippocampus. **(A)** DCX$^+$ neural progenitor cell density. **(B)** DCX$^+$GFAP$^+$ astrocyte cell density. **(C)** DCX$^+$NeuN$^+$ neuron cell density **(D)** Immunohistochemistry images showing DCX$^+$ neural progenitor cells in AA control mice (n = 21 sections), AA mice treated with minocycline (n = 10 sections), AA mice exposed to RSD (n = 40 sections), and AA mice exposed to RSD and treated with minocycline (n = 41 sections). **(E)** Immunohistochemistry images showing DCX$^+$GFAP$^+$ astrocytes in AA control mice (n = 21 sections), AA mice treated with minocycline (n = 10 sections), AA mice exposed to RSD (n = 40 sections), and AA mice exposed to RSD and treated with minocycline (n = 41 sections). **(F)** Immunohistochemistry images showing DCX$^+$NeuN$^+$ neurons cells in AA control mice (n = 21 sections), AA mice treated with minocycline (n = 10 sections), AA mice exposed to RSD (n = 40 sections), and AA mice exposed to RSD and treated with minocycline (n = 41 sections). **(G)** Immunohistochemistry images showing DCX$^+$ neural progenitor cells in SS control mice (n = 23 sections), SS mice treated with minocycline (n = 20 sections), SS mice exposed to RSD (n = 40 sections), and SS mice exposed to RSD and treated with minocycline (n = 49 sections). **(H)** Immunohistochemistry images showing DCX$^+$GFAP$^+$ astrocytes in SS control mice (n = 23 sections), SS mice treated with minocycline (n = 20 sections), SS mice exposed to RSD (n = 40 sections), and SS mice exposed to RSD and treated with minocycline (n = 49 sections). **(I)** Immunohistochemistry images showing DCX$^+$NeuN$^+$ neurons cells in SS control mice (n = 23 sections), SS mice treated with minocycline (n = 20 sections), SS mice exposed to RSD (n = 40 sections), and SS mice exposed to RSD and treated with minocycline (n = 49 sections). Statistical comparisons were performed with a one-way ANOVA with Fisher's LSD multiple comparisons test. *$p < 0.05$, **$p < 0.01$, ****$p < 0.0001$. Data are presented as mean ± SEM. ****$p < 0.0001$. The "n" in brackets after each group represents the total number of hippocampal brain tissue sections evaluated.*

We then performed bulk RNA sequencing and gene set enrichment analysis (GSEA) to identify the pathways underlying RSD-linked cognitive deficit and neuroinflammation in SCD (Figure 4). Most of the differentially expressed gene sets in the cortex were involved in cognitive function, synaptic structures, neuronal signaling, and inflammation (Figure 4A). Differences between SS and AA healthy control mice were evident both at baseline and after RSD exposure. We observed that genes connected with blood-brain barrier dysfunction, depressive disorders, and inflammation (*CCR7*, *FOXF1*) were enriched in SS relative to AA mice. SS + RSD mice show enrichment for genes related to neurodegenerative disease processes (*CTNNB1*, [33] *CSF1R*, *VCP* [34–36]), while sirtuins, which prevent aging and neurocognitive diseases [37, 38], were less enriched. In contrast, no significant changes in gene expression were observed in the AA + RSD group. Additionally, *LDLR* expression (associated with long-term memory) was downregulated in the SS + RSD group compared to the AA + RSD group. Together, these findings support our hypothesis that SS mice might have greater susceptibility to the effects of social stressors such as RSD. Furthermore, SS + RSD + minocycline mice showed enrichment for genes related to synaptic structure and plasticity processes (*BDNF*, *ENTPD1*), while genes associated with cell signaling, immune infiltration, and lipid membrane trafficking (*Adora1*, *ABDH6*, and *Akt1/2*) were downregulated. Notably, excitatory signaling through serotonin receptors (5-HTR 4, 6, and 7), glutamatergic, and dopaminergic synapses was decreased, suggesting

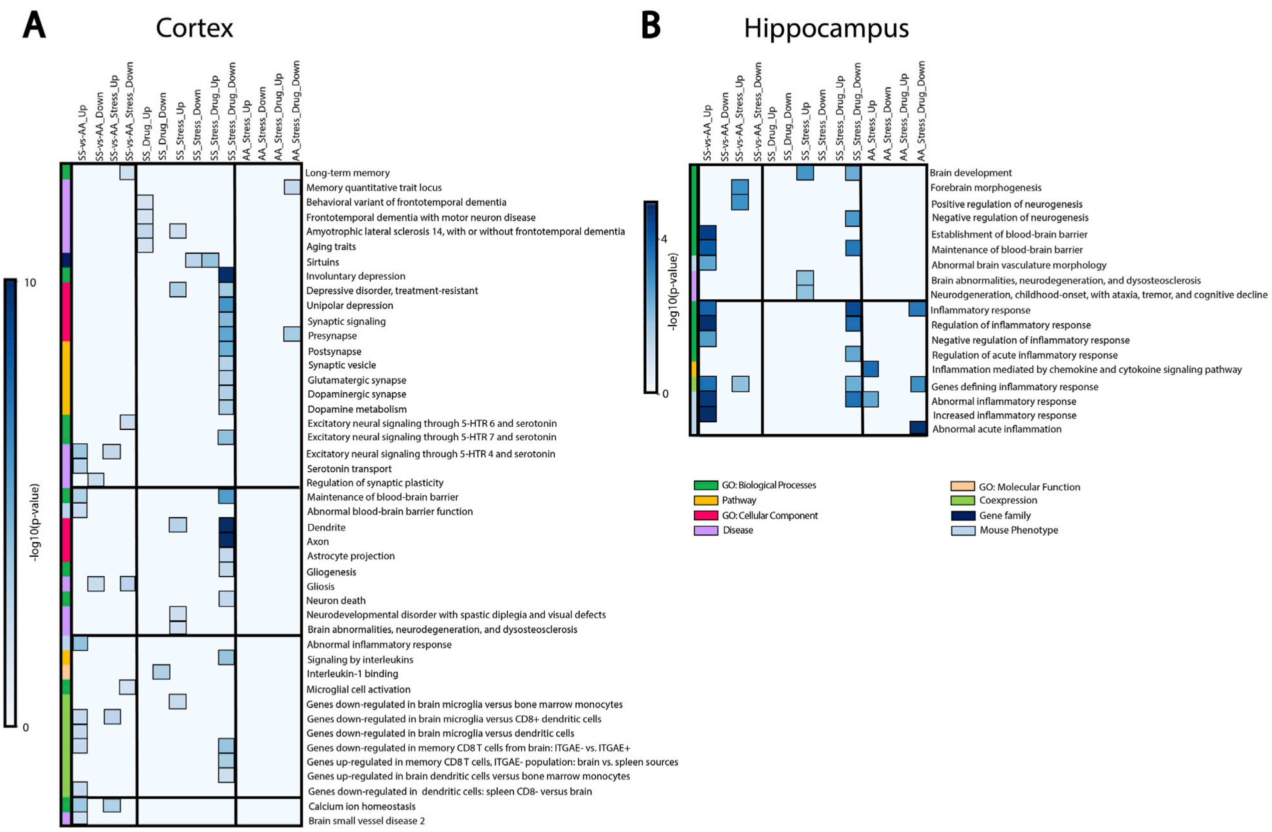

FIGURE 4
Gene set enrichment analysis showing how RSD and minocycline affect pathways, biological processes, and diseases related to cognitive function, brain development, and inflammation. SS-vs-AA_UP: genes enriched in control SS mice compared to control AA mice. SS-vs-AA_DOWN: genes downregulated in control SS mice compared to control AA mice. SS-vs-AA_Stress_UP: genes enriched in SS mice exposed to RSD compared to AA mice exposed to RSD. SS-vs-AA_Stress_DOWN: genes downregulated in SS mice exposed to stress compared to AA mice exposed to stress. SS_Drug_UP: genes enriched in SS mice treated with minocycline compared to control SS mice. SS_Drug_DOWN: genes downregulated in SS mice treated with minocycline compared to control SS mice. SS_Stress_UP: genes enriched in SS mice exposed to RSD compared to control SS mice. SS_Stress_DOWN: genes downregulated in SS mice exposed to RSD compared to control SS mice. SS_Stress_Drug_UP: genes enriched in SS mice exposed to stress and treated with minocycline compared to SS mice exposed to stress only. SS_Stress_Drug_DOWN: genes downregulated in SS mice exposed to stress and treated with minocycline compared to SS mice exposed to stress only. AA_Stress_UP: genes enriched in AA mice exposed to RSD compared to control AA mice. AA_Stress_DOWN: genes downregulated in AA mice exposed to RSD compared to control AA mice. AA_Stress_Drug_UP: genes enriched in AA mice exposed to stress and treated with minocycline compared to AA mice exposed to stress only. AA_Stress_Drug_DOWN: genes downregulated in AA mice exposed to stress and treated with minocycline compared to AA mice exposed to stress only.

minocycline's role in preventing stress-linked excitotoxicity and neurodegeneration [39, 40]. Pathways linked to inflammation, gliogenesis, and neuronal death were less enriched in SS + RSD + minocycline animals, while sirtuin-related pathways and processes were enriched. In the hippocampus, similar trends were observed (Figure 4B), with genes related to abnormal cerebral vasculature, blood-brain barrier dysfunction, and inflammatory processes being more enriched in SS compared to AA mice. In SS + RSD mice, genes related to brain development (*MAOB*) and neurodegeneration were significantly enriched compared to AA + RSD mice. Furthermore, SS + RSD mice showed significant enrichment of genes negatively associated with forebrain morphogenesis and neurogenesis and positively associated with inflammation. Taken together, our results suggest that minocycline may help prevent imbalances in synaptic activity and functional decline in SS mice exposed to stress.

Because sphingolipids play important roles in neurological function and immune signaling, we investigated their potential connection to neuroinflammation and cognitive deficits induced by social stress in SCD. GSEA analysis was performed to evaluate enrichment of sphingolipid-related pathways in the cortex (Figure 5A) and hippocampus (Figure 5C), while liquid chromatography-mass spectrometry (LC-MS) was used to quantify the concentrations of sphingolipids found in these two brain regions (Figures 5B, D).

In the cortex (Figure 5A), AA and SS mice have significantly different gene expression profiles with and without stress

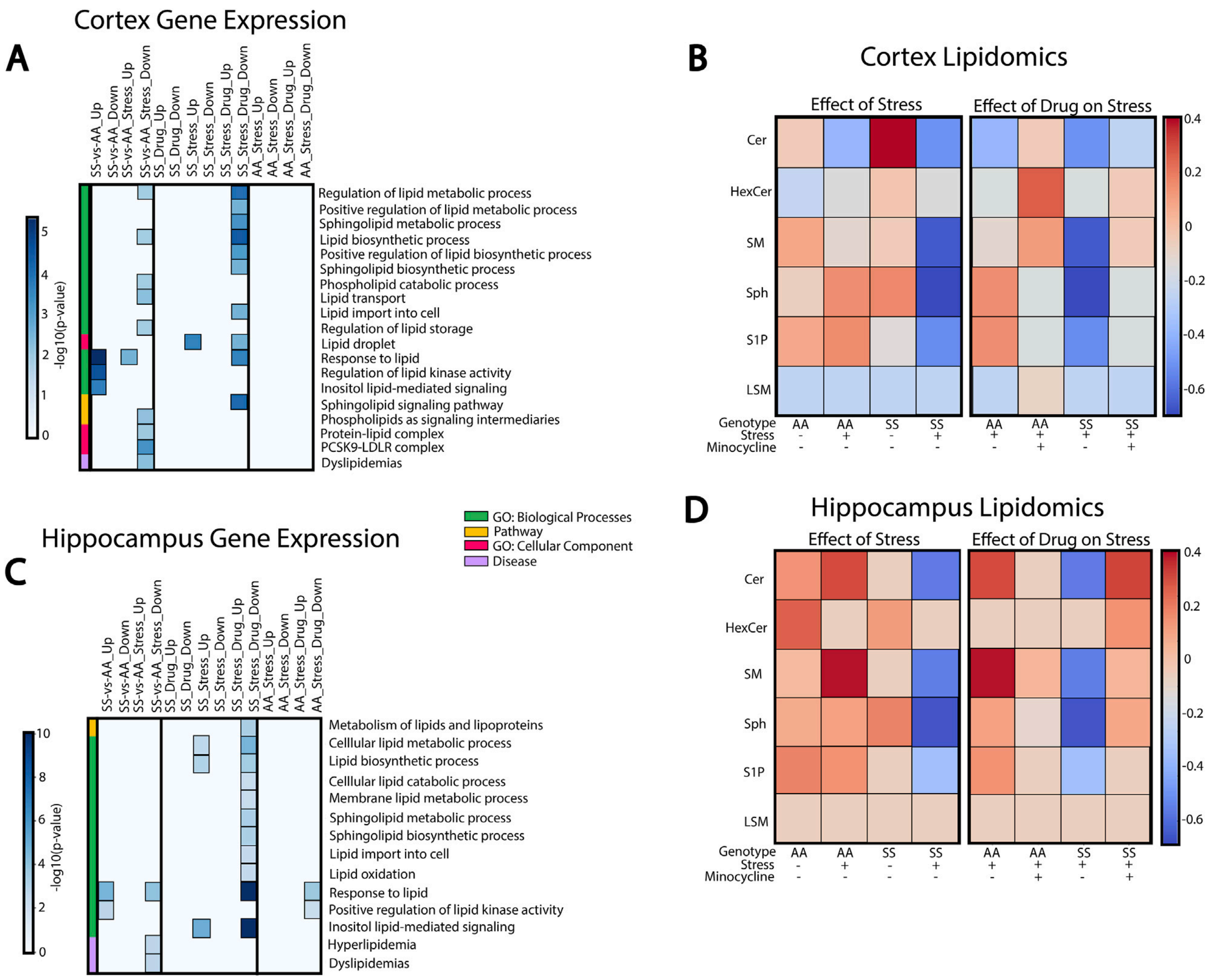

FIGURE 5
Sphingolipids and lipid metabolism in RSD-mediated inflammation and cognitive impairment. **(A)** Cortex GSEA results of RSD exposure and minocycline-treated mice. **(B)** Mass spectrometry characterization of sphingolipid species found in the cortex. **(C)** Hippocampus GSEA results of RSD exposure and minocycline-treated mice. **(D)** Mass spectrometry characterization of sphingolipid species in the hippocampus.

exposure. SS mice exhibit enriched processes related to lipid stimulus responses and lipid kinase activity regulation compared to AA mice. Conversely, processes related to lipid synthesis, metabolism, transport, and storage were downregulated in SS mice. In SS + RSD + minocycline mice, we observed substantial changes in sphingolipid-related pathways and processes. Processes governing lipid metabolism, transport, and storage, including sphingolipids, are downregulated in SS + RSD + minocycline mice compared to SS + RSD mice. Overall, genes associated with sphingolipid signaling and metabolism pathways were also downregulated. In particular, SS + RSD + minocycline mice showed lower expression of genes associated with ceramide (Cer) metabolism, including *de novo* cer synthesis (*Elovl4*, *Slc1a4*) [41], degradation of sphingomyelin (SM) into cer via the salvage pathway (*SMPD1*), and synthesis of ceramide-derived sphingolipids like sphingosine-1-photphate (S1P) (via *Sphk1*) and complex gangliosides (via *ST3GAL2*) [42].

We analyzed LC-MS results to identify a link between pathway enrichment/gene expression and lipidomics profile in the cerebral cortex or hippocampus. In Figure 5B, we found that AA mice had higher levels of Cer and SM and lower levels of hexosylceramide (HexCer), sphingosine (Sph), and S1P compared to AA + RSD mice. Interestingly, SS mice, with or without exposure to RSD, had the highest level of Cer of the two genotypes compared to their AA counterparts. Also, SS mice had higher levels of HexCer, SM, Sph, and S1P compared to SS + RSD mice. This later point may indicate that exposure to RSD/social stress alters the sphingolipid profile by potentially decreasing enzymatic activity in the sphingolipid and thus sphingomyelin biosynthetic and degradation pathways. Minocycline treatment had a significant impact on the sphingolipid profile. Minocycline treatment significantly impacted the sphingolipid profile, with AA + RSD + minocycline mice showing increased Cer, HexCer, SM, and LSM levels and decreased Sph and S1P levels compared to AA + RSD mice. Similarly, SS + RSD + minocycline mice had higher SM, Sph, and S1P levels and lower LSM levels compared to SS + RSD. Overall, these findings suggest that minocycline may restore sphingolipid enzymatic activity perturbed by social stress, which could be one mechanism of its benefit.

Likewise, GSEA and LC-MS analyses of hippocampal tissue showed differential expression of genes involved in critical biological processes between AA and SS mice, as well as between SS + RSD and SS mice (Figure 5C). Specifically, SS + RSD + minocycline mice exhibited downregulation of processes related to lipid metabolism, synthesis, and transport of lipid species (including sphingolipids) and responses to lipid stimuli compared to SS + RSD mice. Notably, several genes responsible for inhibiting (1) *de novo* ceramide synthesis (*ORMDL2*/*ORMDL3*) [43], (2) breaking down lysosomal sphingomyelin to ceramide (*SMPD1*), (3) synthesizing gangliosides from ceramide (*ST3GAL2*/*ST3GAL3*) [42], and (4) converting S1P to sphingosine (*PLPP3*) were significantly less enriched compared to SS + RSD [44]. We noted that some genes involved in the response to lipid stimuli process (*CD38*, *CX3CR1*, and *TLR2*) and downregulated in SS + RSD + minocycline mice encode surface receptors found on microglia and lymphoid cells [45–48], potentially explaining the reduced neuroinflammation, neurodegeneration, and improved cognitive function observed in the treated mice in our study [48, 49].

As before, we examined the link between gene-set enrichment and concentrations of sphingolipid, this time in the hippocampus. Results from the LC-MS analyses of hippocampal tissue showed contrasting levels compared to the cortex, especially in AA mice, with higher sphingolipid levels (Figure 5D). AA + RSD mice had elevated Cer and SM levels but lower HexCer, Sph, and S1P levels. Also, SS mice had lower levels of Cer, HexCer, SM, and S1P, except Sph, compared to AA mice. SS + RSD mice had reduced levels of all sphingolipids, particularly Sph. AA + RSD + minocycline mice showed decreased levels of Cer, SM, Sph, and S1P. SS + RSD + minocycline mice exhibited higher levels of all sphingolipids compared to SS + RSD mice, except for LSM, which remained consistent across all groups.

Discussion

In this study, we sought to understand how RSD affects cognitive function (with or without treatment) in male humanized Townes sickle mice compared to control (treated and untreated) mice. Our findings presented above and the online Supplementary Material support our stated hypothesis and show that social stressors (RSD) impair cognitive functions in sickle mice, similar to what was described among children with SCD by King et al. [14, 15] It also provides some mechanistic insight in showing that neuroinflammation and possibly depression of neurogenesis (Figure 3), with a shift towards astrogliogenesis (Supplementary Figure S2), may be among the underlying mechanisms. In our prior work, we showed that 13-month-old Townes sickle mice had more severe cognitive and neurobehavioral deficits and abnormal neuroplasticity [29]. The findings from that study motivated this work in understanding why children with SCD living in a socially stressful environment have more severe manifestations of cognitive deficit. Thus, we additionally showed that minocycline treatment alleviates neuroinflammation, improved neurogenesis and thus, leads to better cognitive and neurobehavioral functions as well as improvement in relevant molecular and cellular phenotypes.

It is known that individuals with SCD experience cognitive and neurobehavioral (anxiety and depression) deficits observed in early childhood, adolescents, and adults [50, 51]. We saw sickle mice exhibit cognitive and neurobehavioral deficits after being exposed to social stress, recapitulating what was described in children with SCD. In these children, it was shown that the presence of cognitive deficit was associated with "biological factors" such as severity of anemia and presence of silent cerebral infarct (SCI) or stroke [52–54]. However, King et al [14, 15] demonstrated more severe evidence of cognitive deficit in children without SCI but who were exposed to social stress in the form of low parental socioeconomic status. This and the report by Andreotti et al. [55], were essentially recapitulated in our study, which showed one or more mechanisms that may underlie the development of cognitive deficit in children with SCD.

In our study, evaluating the hippocampus and dentate gyrus revealed the presence of evidence of neuroinflammation in sickle mice at baseline, i.e., without exposure to RSD. We noted that sickle cell mice exposed to stress had higher densities of "activated microglia" and CD45^{+} "bone-marrow-derived" microglia compared to control mice or sickle cell mice exposed to stress and treated with minocycline. These findings are of particular interest as increased microglia activation or overactive microglia undergoes phenotypical and functional changes, often resulting in increased pro-inflammatory cytokine secretion and increased phagocytosis. These activities have been shown to be involved in the mechanism of cognitive impairment and cause neurobehavioral changes (anxiety and anhedonia) [56–58]. Additionally, studies have shown that peripheral mononuclear cells aka "bone-marrow-derived" microglia, infiltrate the brain parenchyma after psychological stress and further lead to neuroinflammation, anxiety, and memory deficit [59]. Taken together, this suggests that social stress promotes peripheral immune cell infiltration regardless of genotype, but more so in sickle cell, which is already in a pro-inflammatory state. In our study, we did not see increased lymphocyte densities in sickle mice exposed to stress; however, we did note that sickle mice overall, without exposure to RSD, had higher T and B cell densities as well as a higher density of "bone-marrow-derived" microglia compared to AA control mice. These observations support our assertion of a background neuroinflammation in SCD, which was accentuated by exposure to RSD, leading to cognitive deficit. Additionally, recent studies have reported that B cells contribute to neuroinflammation via peripheral immune mechanisms through the production of pro-inflammatory cytokines and antibodies, while effector T cells interaction with microglia can further promote inflammation [60, 61]. This may explain why we observed a higher density of T cells with RSD exposure but did not observe a higher density of B cells. Furthermore, the presence of a higher density of peripheral immune cells in the brain in sickle cell mice indicates their possible role in SCD-related neuroinflammation even in the absence of social stress. We did not adequately examine the presence of T or B cells, for instance, in our prior study; however, it is conceivable to assume they were involved in our observation [29]. Overall, these findings illustrate the potential cellular mechanisms that contribute to cognitive deficits in sickle cell mice exposed to stress and could underlie the observation among SCD patients exposed to social stress, such as lower individual or parental socioeconomic status.

Chronic social stress modulates neurogenesis by decreasing neuron proliferation, resulting in modifications to hippocampal synaptic signaling and plasticity [62]. However, the effect of stress on neurogenesis in SCD is still unknown. In our study, we noted that neural progenitor cells (NPCs) in the dentate gyrus of sickle mice exposed to RSD shifted more (in their differentiation) towards astrogliogenesis as opposed to mature neurons. It has been documented that minocycline improves neurogenesis and mitigates the gliogenic effect of inflammatory cytokines on NPCs [63–66]. This was also observed in our study, where we noted that SS + RSD + minocycline mice had significantly higher densities of adult-born neurons, lower densities of new astrocytes, and lower densities of proinflammatory cells in the hippocampus/DG compared to SS + RSD mice. Intriguingly, minocycline treatment of AA mice led to increased NPC density as well, but not on density of adult-born neurons. The analysis of bulk RNA sequencing and lipidomics supported our other findings that exposure to RSD/social stressors negatively affects the brain, leading to structural remodeling, particularly in SS mice. Treatment with minocycline led to a unique enrichment signature in the cortex of SS mice exposed to stress, where genes associated with cerebral structure remodeling, blood-brain barrier integrity, brain development, neurogenesis, and inflammation were down-regulated in SS + RSD + minocycline mice.

Together, these results support minocycline's function in preventing neuroinflammation, evidence of neurodegeneration, and cognitive deficit in SS mice exposed to stress and suggest that these might underly the mechanism of social stress-related cognitive deficit in SCD.

Conclusions and limitations

We have attempted to show some of the underlying mechanisms of how RSD affects cognitive deficits in SCD mice exposed to social stress. We showed that the development of cognitive deficit is in part driven by "activation" of resident immune cells and/or infiltration of peripheral immune cells, astrogliogenesis, changes to lipid metabolism, and the transcriptome. Finally, we demonstrated that treatment with minocycline (which is anti-neuroinflammatory and a sphingomyelinase inhibitor) mitigated the presence of cognitive deficit, possibly by blocking neuroinflammation and shifting NPCs towards neurogenesis. It also supports a favorable lipidomics and transcriptomic profile that promotes neurogenesis and synaptogenesis as well as synaptic plasticity but is anti-excitotoxic and anti-neuroinflammatory.

One limitation of our study is that we used the RSD paradigm, which is likely not representative of the way individuals with sickle cell disease are exposed to social stress in everyday life. Related to this is the fact that this form of stress is more easily carried out in male mice, limiting the conclusions that could be drawn from our study. To the later point, we are now working on a chronic stress model using the social disruption paradigm, which allows us to use both male and female mice. We hope to share the result of this new approach in future publications. Another limitation is the imbalance in the number of mice. There was sample attrition due to mortality; however, this did not confound the direction of the observation.

Author contributions

SAD, SV, and OTG wrote and edited the initial draft of the manuscript, HH designed the study, carried out some of the experiments, RH and AS performed immunohistochemistry and carried out microscopy imaging and KP, RH, and HH performed analyses of immunohistochemistry images. LN performed alignment and analysis of RNA sequencing data, MS, AJ, SV, and HH performed bioinformatics and gene-set enrichment analysis. SAD performed lipidomics assay and EB, SAD, and SV performed lipidomic analyses. HH and OTG performed critical review of the manuscript. All authors contributed to the article and approved the submitted version.

Data availability

The datasets presented in this study can be found in online repositories. The names of the repository/repositories and accession number(s) can be found in the article/Supplementary Material

Ethics statement

The animal study was approved by the Emory University Institutional Animal Care and Use Committee. The study was conducted in accordance with the local legislation and institutional requirements.

Funding

The author(s) declare that financial support was received for the research, authorship, and/or publication of this article. This was supported in part by the following awards: S'DD was supported by the National Institutes of Health (T32 GM145735). OG was supported by the American Society of Hematology Scholar Award and the Parker B. Francis Fellowship in Pulmonary Research Award. HH is supported by grants from the National Institutes of Health (R01 HL138423, R01 HL156024, and 3R01 HL138423-05S).

Conflict of interest

The author(s) declared no potential conflicts of interest with respect to the research, authorship, and/or publication of this article.

Supplementary material

The Supplementary Material for this article can be found online at: https://www.ebm-journal.org/articles/10.3389/ebm.2024.10361/full#supplementary-material

References

1. Steiner CA, Miller JL. Statistical brief #21: sickle cell disease patients in U.S. Hospitals. In: *Healthcare cost and utilization project*. Rockville (MD): Agency for healthcare research and quality. (2004).

2. Kato GJ, Piel FB, Reid CD, Gaston MH, Ohene-Frempong K, Krishnamurti L, et al. Sickle cell disease. *Nat Rev Dis Primers* (2018) **4**:18010–22. doi:10.1038/nrdp.2018.10

3. Nader E, Romana M, Connes P. The red blood cell—inflammation vicious circle in sickle cell disease. *Front Immunol* (2020) **11**:454. doi:10.3389/fimmu.2020.00454

4. Lettre G. Blocking HbS polymerization in SCD. *Cell* (2020) **180**:819. doi:10.1016/j.cell.2020.01.019

5. DeBaun M, Jordan L, King A, Schatz J, Vichinsky E, Fox C, et al. American Society of Hematology 2020 guidelines for sickle cell disease: prevention, diagnosis, and treatment of cerebrovascular disease in children and adults. *Blood Adv* (2020) **4**:1554–88. doi:10.1182/bloodadvances.2019001142

6. Heitzer AM, Cohen DL, Okhomina VI, Trpchevska A, Potter B, Longoria J, et al. Neurocognitive functioning in preschool children with sickle cell disease. *Pediatr Blood and Cancer* (2022) **69**:e29531. doi:10.1002/pbc.29531

7. Heitzer AM, Okhomina VI, Trpchevska A, MacArthur E, Longoria J, Potter B, et al. Social determinants of neurocognitive and academic performance in sickle cell disease. *Pediatr Blood and Cancer* (2023) **70**:e30259. doi:10.1002/pbc.30259

8. Heitzer AM, Hamilton L, Stafford C, Gossett J, Ouellette L, Trpchevska A, et al. Academic performance of children with sickle cell disease in the United States: a meta-analysis. *Front Neurol* (2021) **12**:786065. doi:10.3389/fneur.2021.786065

9. Portela GT, Butters MA, Brooks MM, Candra L, Rosano C, Novelli EM. Comprehensive assessment of cognitive function in adults with moderate and severe sickle cell disease. *Am J Hematol* (2022) **97**:E344–e346. doi:10.1002/ajh.26643

10. Oluwole O, Fertrin KY, Kruse-Jarres R. Neurocognitive assessment of adults with sickle cell disease: a descriptive study. *Blood* (2021) **138**:4172. doi:10.1182/blood-2021-145808

11. Asnani MR, Knight Madden J, Reid M, Greene L-G, Lyew-Ayee P. Socio-environmental exposures and health outcomes among persons with sickle cell disease. *PLoS One* (2017) **12**:e0175260. doi:10.1371/journal.pone.0175260

12. Khan SA, AlSiny F, Makki A, Ali A, AlAnsari I, Khan S. Socioeconomic status dependent medical complexities in children with sickle cell disease in Saudi Arabia. *Saudi J Biol Sci* (2020) **27**:1781–7. doi:10.1016/j.sjbs.2020.03.008

13. Jesus ACS, Konstantyner T, Lôbo IKV, Braga JAP. Características socioeconômicas e nutricionais de crianças e adolescentes com anemia falciforme: uma revisão sistemática. *Revista Paulista de Pediatria* (2018) **36**:491–9. doi:10.1590/1984-0462/;2018;36;4;00010

14. King AA, Rodeghier MJ, Panepinto JA, Strouse JJ, Casella JF, Quinn CT, et al. Silent cerebral infarction, income, and grade retention among students with sickle cell anemia. *Am J Hematol* (2014) **89**:E188–192. doi:10.1002/ajh.23805

15. King AA, Strouse JJ, Rodeghier MJ, Compas BE, Casella JF, McKinstry RC, et al. Parent education and biologic factors influence on cognition in sickle cell anemia. *Am J Hematol* (2014) **89**:162–7. doi:10.1002/ajh.23604

16. Finnell JE, Wood SK. Putative inflammatory sensitive mechanisms underlying risk or resilience to social stress. *Front Behav Neurosci* (2018) **12**:240. doi:10.3389/fnbeh.2018.00240

17. Wohleb ES, Powell ND, Godbout JP, Sheridan JF. Stress-induced recruitment of bone marrow-derived monocytes to the brain promotes anxiety-like behavior. *The J Neurosci* (2013) **33**:13820–33. doi:10.1523/jneurosci.1671-13.2013

18. McKim DB, Niraula A, Tarr AJ, Wohleb ES, Sheridan JF, Godbout JP. Neuroinflammatory dynamics underlie memory impairments after repeated social defeat. *J Neurosci* (2016) **36**:2590–604. doi:10.1523/JNEUROSCI.2394-15.2016

19. Wohleb ES, Patterson JM, Sharma V, Quan N, Godbout JP, Sheridan JF. Knockdown of interleukin-1 receptor type-1 on endothelial cells attenuated stress-induced neuroinflammation and prevented anxiety-like behavior. *J Neurosci* (2014) **34**:2583–91. doi:10.1523/JNEUROSCI.3723-13.2014

20. Lee JY, Jin HK, Bae J-s. Sphingolipids in neuroinflammation: a potential target for diagnosis and therapy. *BMB Rep* (2020) **53**:28–34. doi:10.5483/bmbrep.2020.53.1.278

21. Asle-Rousta M, Oryan S, Ahmadiani A, Rahnema M. Activation of sphingosine 1-phosphate receptor-1 by SEW2871 improves cognitive function in Alzheimer's disease model rats. *EXCLI J* (2013) **12**:449–61.

22. Brodowicz J, Przegalinski E, Muller CP, Filip M. Ceramide and its related neurochemical networks as targets for some brain disorder therapies. *Neurotoxicity Res* (2018) **33**:474–84. doi:10.1007/s12640-017-9798-6

23. Efstathopoulos P, Kourgiantaki A, Karali K, Sidiropoulou K, Margioris AN, Gravanis A, et al. Fingolimod induces neurogenesis in adult mouse hippocampus and improves contextual fear memory. *Translational psychiatry* (2015) **5**:e685. doi:10.1038/tp.2015.179

24. Kanno T, Nishizaki T, Proia RL, Kajimoto T, Jahangeer S, Okada T, et al. Regulation of synaptic strength by sphingosine 1-phosphate in the hippocampus. *Neuroscience* (2010) **171**:973–80. doi:10.1016/j.neuroscience.2010.10.021

25. Saleem M, Ratnam Bandaru VV, Herrmann N, Swardfager W, Mielke MM, Oh PI, et al. Ceramides predict verbal memory performance in coronary artery disease patients undertaking exercise: a prospective cohort pilot study. *BMC Geriatr* (2013) **13**:135. doi:10.1186/1471-2318-13-135

26. Saleem M, Herrmann N, Dinoff A, Mielke MM, Oh PI, Shammi P, et al. A lipidomics approach to assess the association between plasma sphingolipids and verbal memory performance in coronary artery disease patients undertaking cardiac rehabilitation: a C18:0 signature for cognitive response to exercise. *J Alzheimer's Dis* (2017) **60**:829–41. doi:10.3233/JAD-161292

27. Ayub M, Jin H-K, Bae J-s. Novelty of sphingolipids in the central nervous system physiology and disease: focusing on the sphingolipid hypothesis of neuroinflammation and neurodegeneration. *Int J Mol Sci* (2021) **22**:7353. doi:10.3390/ijms22147353

28. Henriques A, Croixmarie V, Bouscary A, Mosbach A, Keime C, Boursier-Neyret C, et al. Sphingolipid metabolism is dysregulated at transcriptomic and metabolic levels in the spinal cord of an animal model of amyotrophic lateral sclerosis. *Front Mol Neurosci* (2017) **10**:433. doi:10.3389/fnmol.2017.00433

29. Hardy RA, Rached NA, Jones JA, Archer DR, Hyacinth HI. Role of age and neuroinflammation in the mechanism of cognitive deficits in sickle cell disease. *Exp Biol Med* (2021) **246**:106–20. doi:10.1177/1535370220958011

30. Ryan TM, Ciavatta DJ, Townes TM. Knockout-transgenic mouse model of sickle cell disease. *Science* (1997) **278**:873–6. doi:10.1126/science.278.5339.873

31. Jonas P, Lisman J. Structure, function, and plasticity of hippocampal dentate gyrus microcircuits. *Front Neural Circuits* (2014) **8**:107. doi:10.3389/fncir.2014.00107

32. Ben Menachem-Zidon O, Goshen I, Kreisel T, Ben Menahem Y, Reinhartz E, Ben Hur T, et al. Intrahippocampal transplantation of transgenic neural precursor cells overexpressing interleukin-1 receptor antagonist blocks chronic isolation-induced impairment in memory and neurogenesis. *Neuropsychopharmacology* (2008) **33**:2251–62. doi:10.1038/sj.npp.1301606

33. Cheng M, Luk H-m, Lo IF, Chung BH. *CTNNB1 neurodevelopmental disorder* (1993).

34. Hu B, Duan S, Wang Z, Li X, Zhou Y, Zhang X, et al. Insights into the role of CSF1R in the central nervous system and neurological disorders. *Front Aging Neurosci* (2021) **13**:789834. doi:10.3389/fnagi.2021.789834

35. Wong TH, Pottier C, Hondius DC, Meeter LH, Van Rooij JG, Melhem S, et al. Three VCP mutations in patients with frontotemporal dementia. *J Alzheimer's Dis* (2018) **65**:1139–46. doi:10.3233/jad-180301

36. Smith C, Badadani M, Nalbandian A, Dec E, Vesa J, Donkervoort S, et al. Valosin-containing protein (VCP) disease and familial Alzheimer's disease: contrasts and overlaps. In: *The clinical spectrum of alzheimer's disease-the charge toward comprehensive diagnostic and therapeutic strategies*. IntechOpen (2011). doi:10.5772/18811

37. Bonda DJ, Lee H-g, Camins A, Pallàs M, Casadesus G, Smith MA, et al. The sirtuin pathway in ageing and Alzheimer disease: mechanistic and therapeutic considerations. *The Lancet Neurol* (2011) **10**:275–9. doi:10.1016/s1474-4422(11)70013-8

38. Madeo F, Carmona-Gutierrez D, Hofer SJ, Kroemer G. Caloric restriction mimetics against age-associated disease: targets, mechanisms, and therapeutic potential. *Cell Metab* (2019) **29**:592–610. doi:10.1016/j.cmet.2019.01.018

39. Andrews M, Tousi B, Sabbagh MN. 5HT6 antagonists in the treatment of Alzheimer's dementia: current progress. *Neurol Ther* (2018) **7**:51–8. doi:10.1007/s40120-018-0095-y

40. Ciranna L. Serotonin as a modulator of glutamate-and GABA-mediated neurotransmission: implications in physiological functions and in pathology. *Curr neuropharmacology* (2006) **4**:101–14. doi:10.2174/157015906776359540

41. Esch BM, Limar S, Bogdanowski A, Gournas C, More T, Sundag C, et al. Uptake of exogenous serine is important to maintain sphingolipid homeostasis in *Saccharomyces cerevisiae*. *PLoS Genet* (2020) **16**:e1008745. doi:10.1371/journal.pgen.1008745

42. Olsen AS, Færgeman NJ. Sphingolipids: membrane microdomains in brain development, function and neurological diseases. *Open Biol* (2017) **7**:170069. doi:10.1098/rsob.170069

43. Bugajev V, Halova I, Demkova L, Cernohouzova S, Vavrova P, Mrkacek M, et al. ORMDL2 deficiency potentiates the ORMDL3-dependent changes in mast cell signaling. *Front Immunol* (2020) **11**:591975. doi:10.3389/fimmu.2020.591975

44. Kono M, Hoachlander-Hobby LE, Majumder S, Schwartz R, Byrnes C, Zhu H, et al. Identification of two lipid phosphatases that regulate sphingosine-1-phosphate cellular uptake and recycling. *J Lipid Res* (2022) **63**:100225. doi:10.1016/j.jlr.2022.100225

45. Levy A, Bercovich-Kinori A, Alexandrovich AG, Tsenter J, Trembovler V, Lund FE, et al. CD38 facilitates recovery from traumatic brain injury. *J neurotrauma* (2009) **26**:1521–33. doi:10.1089/neu.2008.0746

46. Morandi F, Horenstein AL, Costa F, Giuliani N, Pistoia V, Malavasi F. CD38: a target for immunotherapeutic approaches in multiple myeloma. *Front Immunol* (2018) **9**:2722. doi:10.3389/fimmu.2018.02722

47. Liu H, Wang X, Chen L, Chen L, Tsirka SE, Ge S, et al. Microglia modulate stable wakefulness via the thalamic reticular nucleus in mice. *Nat Commun* (2021) **12**:4646–16. doi:10.1038/s41467-021-24915-x

48. Fiebich BL, Batista CRA, Saliba SW, Yousif NM, de Oliveira ACP. Role of microglia TLRs in neurodegeneration. *Front Cell Neurosci* (2018) **12**:329. doi:10.3389/fncel.2018.00329

49. Hickman SE, Allison EK, Coleman U, Kingery-Gallagher ND, El Khoury J. Heterozygous CX3CR1 deficiency in microglia restores neuronal β-amyloid clearance pathways and slows progression of alzheimer's like-disease in PS1-APP mice. *Front Immunol* (2019) **10**:2780. doi:10.3389/fimmu.2019.02780

50. Thompson RJ, Jr, Gustafson KE, Bonner MJ, Ware RE. Neurocognitive development of young children with sickle cell disease through three years of age. *J Pediatr Psychol* (2002) **27**:235–44. doi:10.1093/jpepsy/27.3.235

51. Graves JK, Hodge C, Jacob E. Depression, anxiety, and quality of life in children and adolescents with sickle cell disease. *Pediatr Nurs* (2016) **42**:113–44.

52. DeBaun MR, Armstrong FD, McKinstry RC, Ware RE, Vichinsky E, Kirkham FJ. Silent cerebral infarcts: a review on a prevalent and progressive cause of neurologic injury in sickle cell anemia. *Blood* (2012) **119**:4587–96. doi:10.1182/blood-2011-02-272682

53. DeBaun MR, Gordon M, McKinstry RC, Noetzel MJ, White DA, Sarnaik SA, et al. Controlled trial of transfusions for silent cerebral infarcts in sickle cell anemia. *N Engl J Med* (2014) **371**:699–710. doi:10.1056/NEJMoa1401731

54. Schatz J, Brown RT, Pascual JM, Hsu L, DeBaun MR. Poor school and cognitive functioning with silent cerebral infarcts and sickle cell disease. *Neurology* (2001) **56**:1109–11. doi:10.1212/wnl.56.8.1109

55. Andreotti C, King AA, Macy E, Compas BE, DeBaun MR. The association of cytokine levels with cognitive function in children with sickle cell disease and normal MRI studies of the brain. *J child Neurol* (2015) **30**:1349–53. doi:10.1177/0883073814563140

56. Zhang D, Li S, Hou L, Jing L, Ruan Z, Peng B, et al. Microglial activation contributes to cognitive impairments in rotenone-induced mouse Parkinson's disease model. *J Neuroinflammation* (2021) **18**:4. doi:10.1186/s12974-020-02065-z

57. Wang Q, Chen G, Schindler SE, Christensen J, McKay NS, Liu J, et al. Baseline microglial activation correlates with brain amyloidosis and longitudinal cognitive decline in alzheimer disease. *Neurol - Neuroimmunology Neuroinflammation* (2022) **9**:e1152. doi:10.1212/NXI.0000000000001152

58. Schramm E, Waisman A. Microglia as central protagonists in the chronic stress response. *Neurol - Neuroimmunology Neuroinflammation* (2022) **9**:e200023. doi:10.1212/NXI.0000000000200023

59. Wohleb ES, Powell ND, Godbout JP, Sheridan JF. Stress-induced recruitment of bone marrow-derived monocytes to the brain promotes anxiety-like behavior. *J Neurosci* (2013) **33**:13820–33. doi:10.1523/JNEUROSCI.1671-13.2013

60. Ahn JJ, Abu-Rub M, Miller RH. B cells in neuroinflammation: new perspectives and mechanistic insights. *Cells* (2021) **10**:1605. doi:10.3390/cells10071605

61. Schetters STT, Gomez-Nicola D, Garcia-Vallejo JJ, Van Kooyk Y. Neuroinflammation: microglia and T cells get ready to tango. *Front Immunol* (2017) **8**:1905. doi:10.3389/fimmu.2017.01905

62. Smith KE, Pollak SD. Early life stress and development: potential mechanisms for adverse outcomes. *J Neurodevelopmental Disord* (2020) **12**:34. doi:10.1186/s11689-020-09337-y

63. Giri PK, Lu Y, Lei S, Li W, Zheng J, Lu H, et al. Pretreatment with minocycline improves neurogenesis and behavior performance after midazolam exposure in neonatal rats. *Neuroreport* (2018) **29**:153–9. doi:10.1097/wnr.0000000000000937

64. Kohman RA, Bhattacharya TK, Kilby C, Bucko P, Rhodes JS. Effects of minocycline on spatial learning, hippocampal neurogenesis and microglia in aged and adult mice. *Behav Brain Res* (2013) **242**:17–24. doi:10.1016/j.bbr.2012.12.032

65. Mattei D, Djodari-Irani A, Hadar R, Pelz A, de Cossio LF, Goetz T, et al. Minocycline rescues decrease in neurogenesis, increase in microglia cytokines and deficits in sensorimotor gating in an animal model of schizophrenia. *Brain Behav Immun* (2014) **38**:175–84. doi:10.1016/j.bbi.2014.01.019

66. Vay SU, Blaschke S, Klein R, Fink GR, Schroeter M, Rueger MA. Minocycline mitigates the gliogenic effects of proinflammatory cytokines on neural stem cells. *J Neurosci Res* (2016) **94**:149–60. doi:10.1002/jnr.23686

EBM Experimental Biology and Medicine

TYPE Retraction
PUBLISHED 09 January 2025
DOI 10.3389/ebm.2024.10441

OPEN ACCESS

*CORRESPONDENCE
EBM Editorial Office,
ebm@ebm-journal.org

RECEIVED 19 November 2024
ACCEPTED 29 November 2024
PUBLISHED 09 January 2025

CITATION
EBM Editorial Office (2025) Retraction: Pyridoxal 5′ phosphate protects islets against streptozotocin-induced beta-cell dysfunction – *in vitro* and *in vivo*. *Exp. Biol. Med.* 249:10441. doi: 10.3389/ebm.2024.10441

Retraction: Pyridoxal 5′ phosphate protects islets against streptozotocin-induced beta-cell dysfunction – *in vitro* and *in vivo*

EBM Editorial Office*

A Retraction of the Original Research Article

Pyridoxal 5′ phosphate protects islets against streptozotocin-induced beta-cell dysfunction – *in vitro* and *in vivo*

by Kiran SG, Dorisetty RK, Umrani MR, Boindala S, Bhonde RR, Chalsani M, Singh H and Venkatesan V (2011). Exp Biol Med. 236(4):456–465. doi: 10.1258/ebm.2011.010361

Following publication, concerns were raised on the PubPeer platform regarding the reuse of certain images. Particularly, in the β-Actin band in Figure 6A, two sets of western blots appear to be duplicated if reversed horizontally. Further, in the Glut2 band in the same Figure 6A, two sets of western blots appear to be duplicated as well. The authors failed to provide a satisfactory explanation during the investigation, which was conducted in accordance with Experimental Biology and Medicine's policies. Therefore, the article has been retracted.

This retraction was approved by the Editor-in-Chief of Experimental Biology and Medicine. The authors received communication regarding the retraction.

EBM would like to thank the users on PubPeer for bringing the published article to our attention.

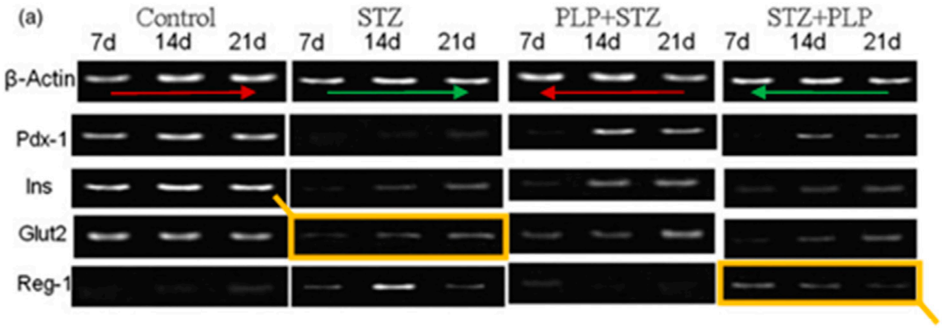

FIGURE 6
Reverse transcriptase-polymerase chain reaction analysis. **(A)** Expression of Pdx1, Insulin and Glut2 was eventually the same throughout the experimental period in the controls. With STZ treatment the expression of Insulin, Pdx1 and Glut2 was reduced marginally with Reg1 being upregulated also seen in STZ þ PLP group. There was a comparison in the expression of these genes between PLP þ STZ and controls by 21 days.

Scope

Experimental Biology and Medicine (EBM) is a global, peer-reviewed journal dedicated to the publication of multidisciplinary and interdisciplinary research in the biomedical sciences. The journal covers the spectrum of translational research from T0, basic research, to T4, population health. Articles in EBM represent cutting edge research at the overlapping junctions of the biological, physical and engineering sciences that impact upon the health and welfare of the world's population. EBM is particularly appropriate for publication of papers that are multidisciplinary in nature, are of potential interest to a wide audience, and represent experimental medicine in the broadest sense of the term. However, manuscripts reporting novel findings on any topic in the realm of experimental biology and medicine are most welcome.

EBM publishes Research, Reviews, Mini Reviews, and Brief Communications in the following categories.

- Anatomy/Pathology
- Artificial Intelligence/ Machine Learning Applications to Biomedical Research
- Biochemistry and Molecular Biology
- Bioimaging
- Biomedical Engineering
- Bionanoscience
- Cell and Developmental Biology
- Clinical Trials
- Endocrinology and Nutrition
- Environmental Health/Biomarkers/ Precision Medicine
- Genomics, Proteomics, and Bioinformatics
- Immunology/Microbiology/Virology
- Mechanisms of Aging
- Neuroscience
- Pharmacology and Toxicology
- Physiology and Pathophysiology
- Population Health
- Stem Cell Biology
- Structural Biology
- Synthetic Biology
- Systems Biology and Microphysiological Systems
- Translational Research

Submit your work to Experimental Biology and Medicine at
ebm-journal.org/submission

More information
ebm-journal.org/journals/experimental-biology-and-medicine

EBM Experimental Biology and Medicine

EBM is the official journal of the Society for Experimental Biology and Medicine

Led by Dr Steven Goodman, Experimental Biology and Medicine (EBM) is a global, peer-reviewed journal dedicated to the publication of multidisciplinary and interdisciplinary research in the biomedical sciences.

Discover more of our Special Issues

See more →

Contact

development@ebm-journal.org

See more

ebm-journal.org
publishingpartnerships.frontiersin.org/our-partners

frontiers | Publishing Partnerships